frontiers | Research Topics

Sustainable treatment methods for wastewater and biosolids

Edited by
Tao Zhang, Sabry Mohamed Shaheen, Shengsen Wang
and Zheng-Yang Huo

Published in
Frontiers in Environmental Science

ISSN 1664-8714
ISBN 978-2-8325-3012-2
DOI 10.3389/978-2-8325-3012-2

About Frontiers

Frontiers is more than just an open access publisher of scholarly articles: it is a pioneering approach to the world of academia, radically improving the way scholarly research is managed. The grand vision of Frontiers is a world where all people have an equal opportunity to seek, share and generate knowledge. Frontiers provides immediate and permanent online open access to all its publications, but this alone is not enough to realize our grand goals.

Frontiers journal series

The Frontiers journal series is a multi-tier and interdisciplinary set of open-access, online journals, promising a paradigm shift from the current review, selection and dissemination processes in academic publishing. All Frontiers journals are driven by researchers for researchers; therefore, they constitute a service to the scholarly community. At the same time, the *Frontiers journal series* operates on a revolutionary invention, the tiered publishing system, initially addressing specific communities of scholars, and gradually climbing up to broader public understanding, thus serving the interests of the lay society, too.

Dedication to quality

Each Frontiers article is a landmark of the highest quality, thanks to genuinely collaborative interactions between authors and review editors, who include some of the world's best academicians. Research must be certified by peers before entering a stream of knowledge that may eventually reach the public - and shape society; therefore, Frontiers only applies the most rigorous and unbiased reviews. Frontiers revolutionizes research publishing by freely delivering the most outstanding research, evaluated with no bias from both the academic and social point of view. By applying the most advanced information technologies, Frontiers is catapulting scholarly publishing into a new generation.

What are Frontiers Research Topics?

Frontiers Research Topics are very popular trademarks of the *Frontiers journals series*: they are collections of at least ten articles, all centered on a particular subject. With their unique mix of varied contributions from Original Research to Review Articles, Frontiers Research Topics unify the most influential researchers, the latest key findings and historical advances in a hot research area.

Find out more on how to host your own Frontiers Research Topic or contribute to one as an author by contacting the Frontiers editorial office: frontiersin.org/about/contact

Sustainable treatment methods for wastewater and biosolids

Topic editors
Tao Zhang — China Agricultural University, China
Sabry Mohamed Shaheen — Kafrelsheikh University, Egypt
Shengsen Wang — Yangzhou University, China
Zheng-Yang Huo — Renmin University of China, China

Citation
Zhang, T., Shaheen, S. M., Wang, S., Huo, Z.-Y., eds. (2023). *Sustainable treatment methods for wastewater and biosolids*. Lausanne: Frontiers Media SA.
doi: 10.3389/978-2-8325-3012-2

Table of contents

frontiers | Frontiers in Environmental Science

ORIGINAL RESEARCH
published: 21 June 2022
doi: 10.3389/fenvs.2022.942263

Adsorption Characteristics of Three Types of Soils on Biogas Slurry Ammonium Nitrogen

*Zichen Wang[1,2], Liping Zhang[1], Guofeng Sun[1], Wei Zhou[1], Jing Sheng[1], Xiaomei Ye[1], Ademola O. Olaniran[2] and E. B. Gueguim Kana[2]**

[1]Key Laboratory of Crop and Livestock Integrated Farming, Ministry of Agriculture and Rural Affairs, Institute of Agricultural Resources and Environment, Jiangsu Academy of Agricultural Sciences, Nanjing, China, [2]Discipline Microbiology, School of Life Sciences, University of KwaZulu-Natal, Pietermaritzburg, South Africa

Using farmland to digest biogas slurry is an effective measure to overcome the bottleneck of sewage treatment in livestock and poultry farms. However, there is limited research on the soil adsorption characteristics of biogas slurry ammonium nitrogen (NH_4^+-N). In addition, the maximum adsorption capacity (Q_m) of farm soil is unclear. In this study, three typical farmland tillage layer soils (silty loam, loam, and sandy loam) were used to analyze adsorption characteristics through adsorption kinetics experiments (adsorption for 0.25, 0.5, 1, 2, 4, 6, 12, 18, or 24 h with NH_4^+-N concentrations of 42.90 mg/L) and thermodynamic experiments (adsorption for 3 days with NH_4^+-N concentrations of 54.25, 88.66, 105.85, 133.71, 178.80, 273.54, and 542.87 mg/L). The Q_m value was fitted by models, and its relationship with soil properties was discussed. The results showed the following: 1) the adsorption of biogas slurry NH_4^+-N by the three types of soils was a composite kinetic process that comprised two stages of rapid and slow reactions. Rapid adsorption predominantly occurred within 0–1 h, and the adsorption capacity accounted for 35.24%–43.55% of the total adsorption. The ExpAssoc equation produced a good fit for the adsorption kinetic behavior in the three soil types. 2) The equilibrium adsorption could be described by the Langmuir equation, the Freundlich equation, the PlPlatt model, and the Langevin model isotherm, among which the Langevin model had the best fit, with a coefficient of determination R^2 close to 1. The theoretical saturated Q_m fitting results of NH_4^+-N were 1038.41–1372.44 mg/kg in silty loam, 840.85–1157.60 mg/kg in loam, and 412.33–481.85 mg/kg in sandy loam. The optimal values were 1108.55, 874.86, and 448.35 mg/kg for silty loam, loam, and sandy loam, respectively. 3) The Q_m value was significantly positively correlated with soil organic matter, total nitrogen, available phosphorus, available potassium, cation exchange capacity, and particle content of 0.02–0.002 mm ($p < 0.01$), but significantly negatively correlated with soil pH ($p < 0.05$). This study can provide a reference for the safe application of biogas slurry on farmland.

Keywords: biogas slurry, wastewater, ammonium nitrogen, soil absorption, kinetics, thermodynamics

Edited by:
Tao Zhang,
China Agricultural University, China

Reviewed by:
Hamou Moussout,
Ibn Tofail University, Morocco
Jale Gülen,
Yıldız Technical University, Turkey
Maulidan Firdaus,
Sebelas Maret University, Indonesia
Vaneet Kumar,
CT Group of Institutions, India

***Correspondence:**
E. B. Gueguim Kana
kanag@ukzn.ac.za

Specialty section:
This article was submitted to Water and Wastewater Management, a section of the journal Frontiers in Environmental Science

Received: *12 May 2022*
Accepted: *06 June 2022*
Published: *21 June 2022*

Citation:
Wang Z, Zhang L, Sun G, Zhou W, Sheng J, Ye X, Olaniran AO and Kana EBG (2022) Adsorption Characteristics of Three Types of Soils on Biogas Slurry Ammonium Nitrogen. Front. Environ. Sci. 10:942263. doi: 10.3389/fenvs.2022.942263

GRAPHICAL ABSTRACT |

INTRODUCTION

Biogas slurry is the residual liquid substance produced by anaerobic fermentation in biogas engineering using biodegradable organic wastes, such as human and livestock manure or various agricultural and forestry wastes. It is produced together with methane, carbon dioxide, and other gases under certain conditions of water content, temperature, and the action of methane bacteria in closed containers (Han et al., 2014). Biogas production has become an important energy-saving and emission-reduction technology for the harmless treatment and energy utilization of livestock and poultry manure in China. According to recent estimates, the biogas slurry produced by the anaerobic fermentation of livestock and poultry manure is more than 1.3 billion tons each year (Lu et al., 2010; Zhu and Huang, 2010). Returning biogas slurry to farmland soil as fertilizer is an effective method of economical use (Bradford et al., 2008; Ning et al., 2019; Liu et al., 2020). However, unreasonable application will not only reduce the use efficiency of biogas slurry, but it will also cause the environmental pollution of farmland water and the reduction of crop yields (Gao et al., 2011; Chen et al., 2013; Wang et al., 2016). The safe utilization of biogas slurry resources is expected to become an increasingly important topic in agriculture, energy use, and environmental protection and thus urgently needs to be investigated.

Biogas slurry is rich in a variety of nutrients required for plant growth and development, such as nitrogen, phosphorus, potassium, copper, zinc, organic acids, hydrolases, and amino acids. The total nitrogen (TN) content of biogas slurry is 0.53–3.24 g/kg (Jin et al., 2011; Ni and Zhang, 2017). Many researchers have studied the use of biogas slurry nitrogen as a measurement parameter for farmland reuse and discussed the safe dosage for fertility enhancement, yield, quality improvement, and environmental emission reduction. For example, Wang et al. (2010) found that applying biogas slurry equivalent to 2–3 times the amount of chemical fertilizer could obtain a pepper yield similar to that of conventional chemical fertilizer treatment, as well as improve pepper quality, increase the contents of soil organic matter (SOM), TN, available nitrogen, phosphorus, and potassium, and save on fertilizer costs. Yang et al. (2017) showed that compared with chemical fertilizer, the application of an equal amount of biogas slurry nitrogen led to no significant differences in the rice yield, nitrogen utilization rate, or soil residual inorganic nitrogen, while the ammonia volatilization per unit rice yield was significantly reduced by 22.6%. Most of these studies were based on the nitrogen fertilizer required for crop growth and replaced chemical nitrogen fertilizer with different

FIGURE 1 | Site image of manure and sewage treatment facilities in the pig farm.

TABLE 1 | Chemical composition of biogas slurry.

	pH	TN (mg/L)	NH_4^+-N (mg/L)	NO_3^--N (mg/L)	TP (mg/L)	TK (mg/L)	COD (mg/L)	EC (mS/cm)	TS (g/L)
Biogas slurry (unfiltered)	7.95	630.29	558.72	42.40	23.97	380	636.67	5.15	2.25
Biogas slurry (filtered through a 0.25-mm mesh screen)	7.97	624.53	550.41	42.36	23.70	375	626.67	5.12	2.24

TN, total nitrogen; NH_4^+-N, ammonium nitrogen; NO_3^--N, nitrate nitrogen; TP, total phosphorus; TK, total potassium; COD, chemical oxygen demand; EC, electrical conductivity; TS, total solid.

proportions of biogas slurry nitrogen, but they did not consider whether the applied biogas slurry nitrogen exceeded the maximum nitrogen adsorption capacity of the topsoil.

Ammonium nitrogen (NH_4^+-N) is the main component of biogas slurry nitrogen, accounting for 46.42%–92.86% of TN (Ham and DeSutter, 1999; Jin et al., 2012; Ni and Zhang, 2017). In addition to being consumed and retained by ammonia volatilization, biological absorption (Li X. et al., 2021), and soil adsorption, a considerable portion of NH_4^+-N over-applied to soil can leach into deep soil through nitrification or into the water table along with surface runoff, thus causing nitrogen pollution in groundwater and surface water (Kithome et al., 1998; Wang et al., 2016; He et al., 2021). A large number of studies reported that the nitrate content in the areas adjacent to concentrated animal feeding operations exceeded the safety standards, thereby creating a bottleneck for livestock and poultry feeding development (Ciravolo et al., 1979; Feinerman et al., 2004). Considering the environmental behavior of NH_4^+-N, adsorption is an important process that can block and delay the further migration and transformation of nitrogen in order to inhibit nitrogen loss (Li W. et al., 2021). Studies of the soil adsorption of NH_4^+-N have focused on the use of a single chemical ammonium salt solution to explore the adsorption mode, deduce the adsorption mechanism, and estimate the adsorption capacity, generally using NH_4Cl solution (Xue et al., 1996; Li et al., 2009; Tian, 2011; Cong et al., 2017). Solutions of NH_4NO_3, $(NH_4)_2SO_4$, and $NH_4H_2PO_4$ have also been used (Dalal, 1975). Furthermore, the soils used in previous research were mostly vermiculitic-type clay loam, kaolinitic sandy soils, and some tropical soils (Dalal, 1975; Lumbanraja and Evangelou, 1994; Wang and Alva, 2000; Kumar and Kothiyal, 2011). There are few studies on the adsorption characteristics of ammonium nitrogen biogas slurry solutions co-existing with complex components (Kumar and Kothiyal, 2012; Zhao et al., 2013), and there is a lack of research on the adsorption characteristics of ammonium nitrogen from biogas slurry in common agricultural production land topsoil.

TABLE 2 | Soil particle composition of three soils.

Soil number	2–0.2 mm (%)	0.2–0.05 mm (%)	0.05–0.02 mm (%)	0.02–0.002 mm (%)	<0.002 mm (%)	Soil texture	Soil classification system of China	Sampling point
Xinbei	0.64	29.90	22.54	30.39	16.54	Silty loam	Wushan soil	Dongnancun, Xixiashu, Xinbei
Jintan	0.53	34.96	19.70	30.64	14.17	Loam	Permeable paddy soil	Luocun, Xuebu, Jintan
Taixing	0.27	61.56	22.58	10.14	5.45	Sandy loam	High sandy soil	Lidangcun, Xinjie, Taixing

TABLE 3 | Physical and chemical characteristics of three soils.

Soil number	pH	SOM (g/kg)	TN (g/kg)	NH_4^+-N (mg/kg)	NO_3^--N (mg/kg)	TP (g/kg)	AP (mg/kg)	AK (mg/kg)	CEC (cmol/kg)	EC (μS/cm)
Xinbei	6.45	29.09	1.16	8.93	56.97	0.57	13.10	122.91	16.27	492.67
Jintan	5.43	19.70	0.79	25.58	26.26	0.31	7.98	126.45	9.57	244.67
Taixing	8.19	5.27	0.16	3.17	10.50	0.54	6.29	65.70	5.83	174.97

SOM, soil organic matter; TN, total nitrogen; TP, total phosphorus; AP, available phosphorus; AK, available potassium; CEC, cation exchange capacity; EC, electrical conductivity.

Studying the adsorption characteristics of biogas slurry ammonium nitrogen in typical farmland soils and predicting the maximum adsorption capacity of the cultivated layer soil are significant for guiding the safe digestion of biogas slurry in farmland. In this study, three types of common farmland soils were collected: silty loam, loam, and sandy loam. Through analyses of adsorption kinetics and adsorption thermodynamics, the adsorption characteristics of these soils for biogas slurry ammonium nitrogen were analyzed, kinetic models were fitted, and the relationships between soil physical and chemical properties and adsorption capacity were explored to provide a scientific basis for the safe application of biogas slurry in farmland and the prevention and control of water pollution.

MATERIALS AND METHODS

Materials

Biogas slurry was collected from a large pig farm (Jiangsu Yangyu Ecological Agriculture Co., Ltd.) in Xinjie Town of Taixing City, China (**Figure 1**). The pig farm has 138 standardized brick-and-concrete pens with a structure area of more than 100,000 m^2. The farm produces around 120,000 commercial pigs annually. It has sewage collection tanks of 1,200 m^3, fermentation tanks of 4,000 m^3, oxidation ponds of 35,000 m^3, one sewage treatment system, and a high-efficiency organic fertilizer farm with an annual output of more than 10,000 tons. The biogas slurry sample was generated from pig feces through primary anaerobic fermentation in a continuous stirred tank reactor (CSTR) and a secondary anaerobic fermentation using a black-film-sealed storage process. Once collected, the samples were stored in sealed plastic barrels and were mixed well and filtered through a 0.25-mm mesh screen before the analysis. Samples were then diluted corresponding to the NH_4^+-N concentration with deionized water for backup use. The basic quality indices of the biogas slurry are shown in **Table 1**.

The experimental soils were collected from the 0–20 cm plough layer of basic farmland in the plain water network area of the Yangtze River Basin in China. The soil textures were silty loam, loam, and sandy loam. The soils were dried naturally, while stones, plant roots, and other DEBRIS found in the soils were removed. The soils were then crushed with a round wooden stick, sieved through a 2-mm mesh screen, and finally fully mixed and placed into a clean plastic storage box for future use. The particle composition and basic physical and chemical properties of the soils are listed in **Tables 2**, **3**.

Adsorption Kinetics Experiments

Soil samples (10 g) were weighed and placed in 250-ml conical bottles. Two hundred milliliters of biogas slurry (NH_4^+-N concentration 42.90 ± 0.66 mg/L) was added to each conical bottle at a soil:water ratio of 1:20, and three drops of toluene were added to inhibit microbial activity. Biogas slurry without soil was used as a blank control. The conical bottles were sealed with a silica gel plug, placed in a thermostatic oscillator (set temperature 25 ± 1°C), and oscillated at 140 r/min for 0.25, 0.5, 1, 2, 4, 6, 12, 18, or 24 h. The conical bottles were taken out for biogas slurry sample collection, and a 20-ml biogas slurry sample was taken each time. The biogas slurry sample was centrifuged at a speed of 3800 r/min for 10 min. The concentration of NH_4^+-N in the supernatant was determined by an automatic flow analyzer (SKALAR SAN^{++}). The above experiments were carried out through destructive sampling. Three batches of experiments were set up. Each batch was set up with nine replicates for each treatment, and one bottle was taken out from the thermostatic oscillator for each round of sampling, which was

TABLE 4 | Four models of soil adsorption kinetics.

Model	Equation
Elovich equation	$Q_t = a + b \ln t$. ………………………….. (2)
Parabolic diffusion equation	$Q_t = a + bt^{1/2}$. ………………………….. (3)
First-order reaction equation	$\ln (Q_e - Q_t) = \ln Q_e - kt$. ………………………….. (4)
ExpAssoc equation	$Q_t = y_0 + A_1 (1 - e^{-t/a}) + A_2 (1 - e^{-t/b})$. ………………..(5)

Q_t is the adsorption capacity of NH_4^+-N at time t (mg/kg); Q_e is the adsorption capacity of NH_4^+-N at adsorption equilibrium (mg/kg); and a, b, k, y_0, A_1, and A_2 are constants used to characterize the adsorption coefficient, where their size indicates the adsorption strength.

TABLE 5 | Four thermodynamic models.

Model	Equation	Adjustable model parameters
Langmuir	$\frac{C_e}{Q_e} = \frac{1}{Q_m K_l} + \frac{C_e}{Q_m}$. ………………….. (6)	K_l is a constant used to characterize the adsorption performance of the soil; and MBC = $Q_m \times K_l$, representing the maximum buffer capacity of the soil (mg/kg).
Freundlich	$Q_e = K_f C_e^{1/n}$. …………………….. (7)	K_f is a constant that represents the strength of soil adsorption force; and 1/n represents the heterogeneity factor related to adsorption strength or surface heterogeneity, reflecting the nonlinear degree of adsorption.
Plplatt	$Q_e = Q_m \cdot \tanh (\frac{A \cdot C_e}{Q_m})$. ……………………….. (8)	A is a constant.
Langevin	$Q_e = a + b \cdot (coth (\frac{C_e - k}{s}) - \frac{s}{C_e - k})$.………….(9)	a, b, k, and s are constants, Q_m = a + b.

Q_e is the adsorption capacity of NH_4^+-N at adsorption equilibrium (mg/kg); C_e is the NH_4^+-N concentration of biogas slurry at adsorption equilibrium (mg/L); and Q_m is the theoretical saturated adsorption capacity of NH_4^+-N per unit soil (mg/kg), representing the capacity factor. MBC, maximum buffer capacity of the soil.

TABLE 6 | Biogas slurry ammonium nitrogen (NH_4^+-N) adsorption rate of three types of soils.

Soils	Adsorption rate at different stage (mg/(kg•h))								
	0–0.25 h	0.25–0.5 h	0.5–1 h	1–2 h	2–4 h	4–6 h	6–12 h	12–18 h	18–24 h
Silty loam (Xinbei)	279.20	131.04	41.65	18.30	17.68	9.47	5.47	3.47	5.61
Loam (Jintan)	165.65	34.85	53.84	22.23	19.82	7.94	1.54	1.59	3.80
Sandy loam (Taixing)	136.91	81.92	25.40	21.65	9.81	7.90	3.33	1.98	2.67

then discarded after sampling. The average value was taken, and the amount of NH_4^+-N adsorbed onto the biogas slurry was calculated after the blank was deducted according to the difference in NH_4^+-N concentration before and after adsorption.

Adsorption Thermodynamic Experiments

A 2.5 g soil sample was mixed with 50 ml biogas slurry with initial diluted concentrations of NH_4^+-N of 54.25, 88.66, 105.85, 133.71, 178.80, 273.54, and 542.87 mg/L in a polyethylene centrifuge tube. Two drops of toluene were added to inhibit microbial activity, and different concentrations of biogas slurry without soil samples were used as blank controls. The sealing cover of the centrifuge tube was tightened, and samples were mixed with a vortex oscillator and oscillated at 180 r/min on a thermostatic oscillator (set temperature 25 ± 1°C) for 1 h. Samples were then incubated in a thermostat at the same temperature for 3 days, oscillating twice a day at an interval of 12 h for 1 h each time. After cultivation, the samples were centrifuged at 3800 r/min for 10 min. The concentration of supernatant NH_4^+-N was measured by an automatic flow analyzer (SKALAR SAN^{++}). Each experiment was repeated three times. The amount of NH_4^+-N absorbed by the tested soil was calculated based on the differences between the initial and final NH_4^+-N concentration in the supernatant.

Calculation Methods

Adsorption Capacity Calculation Formula

$$Q = \frac{(C_0 - C_t) \cdot V}{M}. \tag{1}$$

In the formula, Q is the adsorption capacity of NH_4^+-N (mg/kg); C_0 is the initial concentration (mg/L); C_t is the concentration of the solution at the time of measurement (mg/L); V is the volume of the solution (ml); and M is the soil sample weight (g).

Adsorption Fitting Equations

The fitting equations of adsorption kinetics are shown in **Table 4**. Fitting equations for adsorption thermodynamics are shown in **Table 5**.

Data Processing

Microsoft Office Excel (2010) software was used for test data processing and table drawing, Origin 2017 software was used for drawing and curve fitting, and the significance of Pearson correlations between variables was tested by IBM SPSS Statistics 13.0 version (IBM Corp., NY, United States).

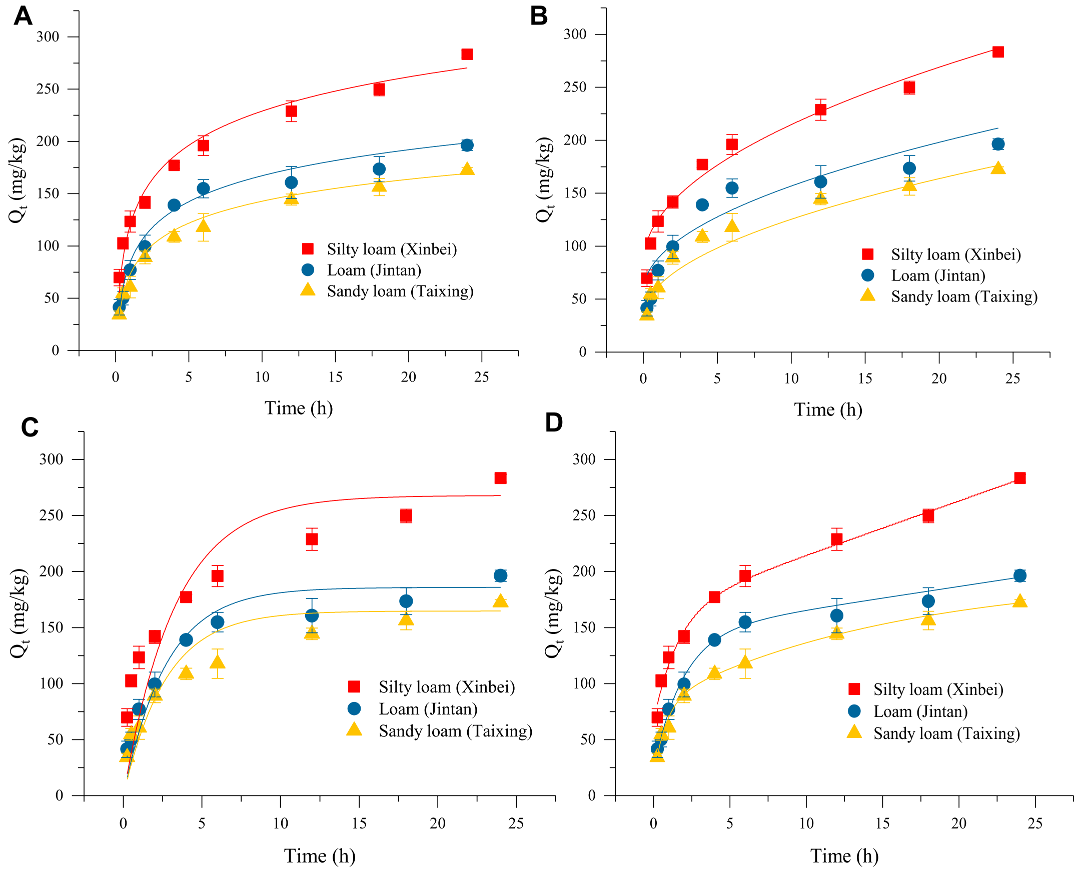

FIGURE 2 | Fitting of adsorption kinetics models: **(A–D)** show the fitting results for the adsorption kinetics of NH_4^+-N in the three kinds of soils obtained by the Elovich equation, a parabolic diffusion equation, a first-order reaction equation, and the ExpAssoc equation, respectively.

TABLE 7 | Fitted parameters in the adsorption kinetics fitting equations.

Soils	Elovich equation			Parabolic diffusion equation			First-order reaction equation			ExpAssoc equation					
	A	b	R^2	a	b	R^2	Q_e	k	R^2	y_0	A_1	a	A_2	b	R^2
Silty loam (Xinbei)	120.38	108.62	0.97	83.86	41.39	0.97	267.93	0.30	0.78	66.29	8.70	1.79	99.76	1.62	0.99
Loam (Jintan)	84.73	82.49	0.98	57.14	31.51	0.81	185.88	0.37	0.92	23.66	1.23	5.92	121.64	1.93	0.99
Sandy loam (Taixing)	73.17	69.66	0.99	32.74	29.30	0.96	164.82	0.37	0.91	15.73	65.84	0.79	114.37	15.30	1.00

RESULTS AND ANALYSIS

Adsorption Kinetic Characteristics

The adsorption rates of three types of soils on biogas slurry ammonium nitrogen (NH_4^+-N) are shown in **Table 6**. The adsorption process of NH_4^+-N from biogas slurry was a composite kinetic process comprising two stages of initial rapid adsorption followed by slow adsorption. The initial rapid adsorption generally occurred within 0–1 h. The ratio of the rapid adsorption amounts to the total amount of adsorption was 35.24%–43.55%. After 1 h, the process entered the slow adsorption stage. The total adsorption amounts in order from highest to least were adsorbed onto silty loam, loam, and sandy loam.

Adsorption Kinetic Model Fitting

Figures 2A–D shows the fitting results for the adsorption kinetics of NH_4^+-N in the three kinds of soils obtained by the Elovich equation, a parabolic diffusion equation, a first-order reaction equation, and the ExpAssoc equation. The four equations could effectively simulate the dynamic adsorption process. The fit of the ExpAssoc equation with relevant parameters produced a confidence interval for R^2 ($0.9923 < R^2 < 0.9966$) that was

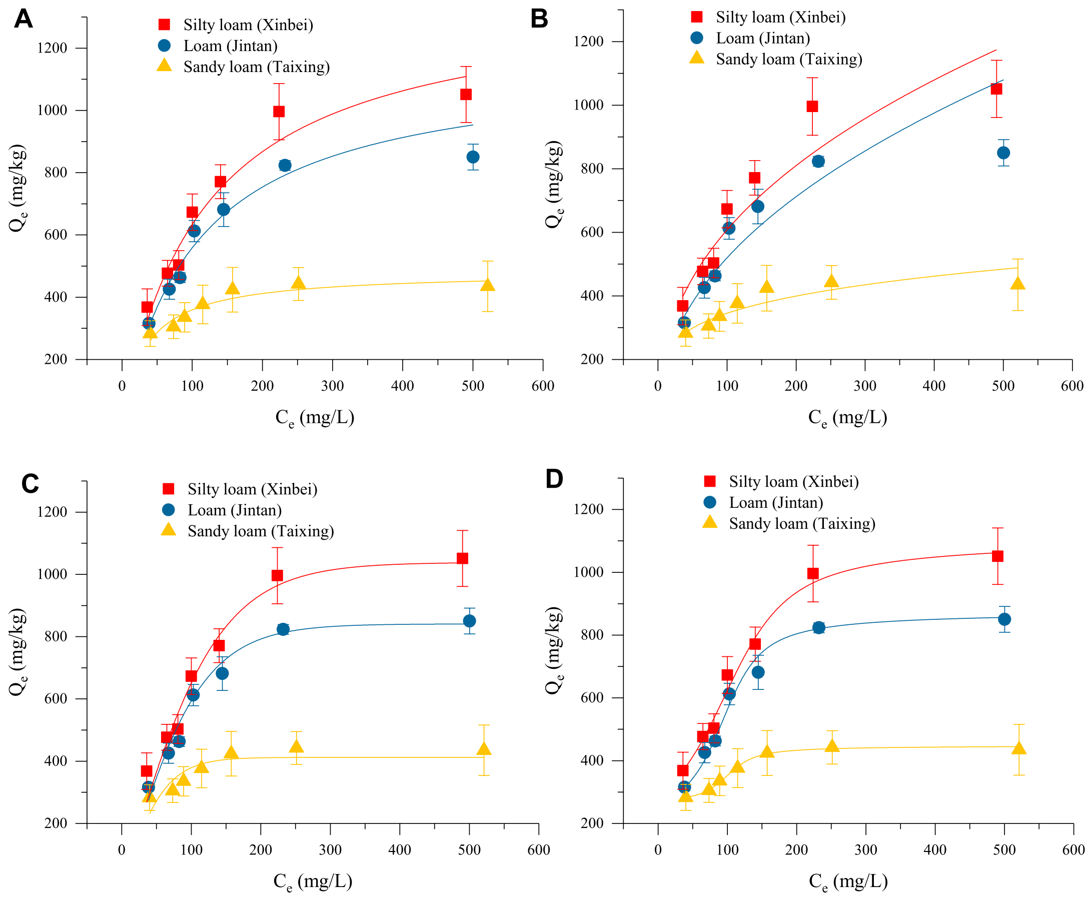

FIGURE 3 | Fitting effects of adsorption thermodynamic models: **(A–D)** show the fitting results for the adsorption thermodynamics of NH_4^+-N in the three kinds of soils obtained by the Langmuir equation, the Freundlich equation, the Plplatt equation, and the Langevin model, respectively, at a temperature of 25 ± 1°C.

TABLE 8 | Related parameters in the adsorption thermodynamic fitting equation.

Soils	Langmuir equation				Freundlich equation			Plplatt equation			Langevin Model				
	Q_m	K_l	MBC	R^2	K_f	1/n	R^2	Q_m	A	R^2	a	k	b	s	R^2
Silty loam	1372.44	0.0086	11.79	0.95	90.13	0.41	0.89	1038.41	7.64	0.94	606.06	96.24	502.49	36.31	0.98
Loam	1157.60	0.0093	10.80	0.98	64.25	0.45	0.93	840.85	7.39	0.96	529.26	93.68	345.60	21.83	1.00
Sandy loam	481.85	0.0294	14.18	0.89	131.39	0.21	0.86	412.33	6.52	0.65	352.64	99.99	95.71	16.05	1.00

better than for the other models (**Table 7**). Therefore, the ExpAssoc equation was used to fit the adsorption kinetics of NH_4^+-N in the three kinds of soils.

Adsorption Thermodynamic Characteristics

The isothermal adsorption curves of the three soils for biogas slurry NH_4^+-N at a temperature of 25 ± 1°C are shown in **Figure 3**. With the increase of the initial biogas slurry NH_4^+-N concentration, the adsorption isotherms of three soils on NH_4^+-N increased, primarily due to the increase of initial biogas slurry NH_4^+-N concentration and the increase of the driving force of the soil itself as an adsorbent, an effect that was conducive to the generation of adsorption. When the initial biogas slurry NH_4^+-N concentration was less than 200 mg/L, the NH_4^+-N adsorption capacity of the three soils increased significantly with the increase of initial concentration; when the initial concentration of NH_4^+-N in biogas slurry was greater than 200 mg/L, the NH_4^+-N adsorption capacity increased slowly and tended to balance with the increase of initial concentration. When the initial biogas slurry NH_4^+-N concentration was low, the adsorption sites of the soil itself were not completely occupied. As the

TABLE 9 | Correlation between adsorption characteristic parameters and soil properties (r, n = 9).

	pH	SOM	TN	NH_4^+-N	NO_3^--N	TP	AP	AK	CEC	EC	Soil particle size distribution (%)			
											2–0.2 mm	0.2–0.02 mm	0.02–0.002 mm	<0.002 mm
Q_m	−0.763*	0.993**	0.974**	0.558	0.785*	0.081	0.974**	0.951**	0.896**	0.792*	−0.64	−0.335	0.912**	−0.34
K_l	0.877**	−0.952**	−0.917**	−0.713*	−0.644	0.119	−0.909**	−0.994**	−0.791*	−0.654	0.566	0.445	−0.944**	0.377
MBC	0.983**	−0.808**	−0.751*	−0.898**	−0.371	0.423	−0.732**	−0.979**	−0.559	−0.382	0.402	0.581	−0.917**	0.403

*SOM, soil organic matter; TN, total nitrogen; TP, total phosphorus; AP, available phosphorus; AK, available potassium; CEC, cation exchange capacity; EC, electrical conductivity. *–P<0.05; **–P<0.01.*

initial biogas slurry NH_4^+-N concentration increased, the unused adsorption sites were gradually occupied and thus were unable to be used, ultimately reaching a saturated state so that the soil and the NH_4^+-N solution tended to balance, and the soil adsorption capacity of NH_4^+-N reached its maximum value.

Adsorption Thermodynamic Model Fitting

The Langmuir equation and Freundlich equation are classical models used to study the thermodynamic characteristics of soil NH_4^+-N adsorption. The Plplatt equation and the Langevin model were the equations selected in this experiment to achieve better fitting. **Figures 3A–D** shows the fitting results of four equations on the adsorption thermodynamics of biogas slurry NH_4^+-N at a temperature of 25 ± 1°C. When fitting the theoretical saturated maximum adsorption capacity (Q_m) values of biogas slurry NH_4^+-N for the three kinds of soils, the Q_m value fitted by the Langmuir equation was highest, and the Q_m value fitted by the Plplatt equation was closer to the measured average value. From the R^2 values (**Table 8**), the adsorption thermodynamic behavior of biogas slurry NH_4^+-N in this experiment was best fitted by the Langevin Model. The optimal theoretical saturated Q_m values calculated by the sum of the parameters a and b were 1108.55, 874.86, and 448.35 mg/kg for silty loam, loam, and sandy loam, respectively.

Correlation Between Adsorption Capacity and Soil Physical and Chemical Properties

Correlations between adsorption characteristic parameters and soil properties are shown in **Table 9**. The Q_m of the soil for biogas slurry NH_4^+-N was positively correlated with SOM, TN, available phosphorus (AP), available potassium (AK), cation exchange capacity (CEC), and the proportion of 0.02–0.002 mm particles ($p < 0.01$), while it was negatively correlated with soil pH ($p < 0.05$). The adsorption constant K_l was negatively correlated with SOM, TN, AP, AK, and the content of particles with the particle size of 0.02–0.002 mm ($p < 0.01$), negatively correlated with soil NH_4^+-N and CEC ($p < 0.05$), and positively correlated with soil pH ($p < 0.01$). The maximum buffer capacity (MBC) of the soil was negatively correlated with SOM, NH_4^+-N, AP, AK, and the content of particles with the particle size of 0.02–0.002 mm ($p < 0.01$), negatively correlated with soil TN ($p < 0.05$), and positively correlated with soil pH ($p < 0.01$).

DISCUSSION

Adsorption Mechanism

Adsorption can be defined as the accumulation of solutes at the solid–liquid interface. This process includes the transfer of solute molecules from the solution, the removal of solvent molecules from the solid surface, and the process of solute molecules attaching to the solid surface (Stumm, 1992). Farmland soil media are heterogeneous aggregates with complex structures.

A large number of organic and inorganic colloids and oxides are interlaced and mixed (Li W. et al., 2021). There are electric fields and residual force fields on the surface of the media that have extremely high surface energy. They can interact with ions, protons, and molecules in the soil liquid and gas phases, and they have strong adsorption on ammonium nitrogen. There are many kinds of active groups in the media, and all kinds of organic and inorganic groups can interact with ammonium. Therefore, the adsorption behavior of ammonium nitrogen in farmland soil media is complex, and the adsorption behavior in different types of media is significantly different (Krishnamoorthy and Overstreet, 1950). At present, the adsorption mechanism of ammonium nitrogen in soil media is mainly discussed at the macro and micro levels. Most macroscopic research has focused on distinguishing the different active surfaces of soil media using the differences in the extraction capacity of different extractants (Lumbanraja and Evangelou, 1994; Wang and Alva, 2000). Microscopically, the occurrence of ammonium in the medium can be identified at the molecular level using X-ray diffraction (XRD), Fourier transform infrared spectroscopy (FTIR), and other spectral means (Sherman and Smulovitch, 1970; Saruchi and Kumar, 2020). Generally, the adsorption mechanism cannot be accurately described through only a single means. The present study characterized the adsorption characteristics of the three soils, and conducted a preliminary discussion based on the factors affecting the adsorption (Shen et al., 1997), but did not conduct an in-depth study of the adsorption mechanism. This will require further study.

Characteristics of Adsorption Kinetics

Soil is an important site for nitrogen circulation and transformation, and the only way for nitrogen to enter groundwater (He et al., 2021; Li X. et al., 2021). The adsorption of NH_4^+-N in the soil shows corresponding regularity with time change, which is one of the important characteristics of soil chemical reaction kinetics. The study of kinetics can reveal the limiting factors and control conditions that affect the adsorption rate. Commonly used adsorption kinetics equations include first-order reaction equations, second-order reaction equations, the Elovich equation, the parabolic diffusion equation, and the ExpAssoc equation. The Elovich equation reflects not only a simple adsorption process but also a complex process involving soil expansion, the activation and deactivation of adsorption sites, and surface diffusion (Sparks and Jardine, 1984). In the present experiment, the coefficient R^2 for the three types of soil adsorption data was the highest for the Elovich equation, indicating that adsorption was a heterogeneous diffusion process. Further analyzing the restrictive factors of the process revealed that the goodness of fit of the parabolic diffusion equation ($0.81 < R^2 < 0.97$) was higher than that of the first-order reaction equation ($0.78 < R^2 < 0.92$) (**Table 7**), indicating that the chemical adsorption process was not the rate-limiting step of the process, while the intra-particle diffusion was the main rate-limiting step. Due to the differences in soil media and environmental conditions, the relationship between adsorption capacity and time often differed during the adsorption process. Previous studies have shown that different kinetics models or the same model have different fits with different soils. In the present study, the best fitting models for the soil adsorption of NH_4^+-N were the first-order reaction equation and the Elovich equation (Xue et al., 1996). The adsorption of NH_4^+-N in silty sand, sandy silt, silt, and silty clay of four typical soils primarily occurred during 0–2 h, and the adsorption kinetics conformed to the second-order reaction equation (Tian, 2011). However, the fitting effect of the adsorption kinetics curve with the ExpAssoc equation was the best (Zhao et al., 2013). The results of this study were consistent with those of Zhao et al. (2013).

Adsorption Thermodynamic Characteristics

The adsorption of NH_4^+-N by soil is a dynamic equilibrium process. Under the same constant temperature, the curve of the adsorption amount (Q) with the equilibrium concentration (C) of the solution is normally referred to as the adsorption isotherm, and the corresponding mathematical expression is called the adsorption isothermal formula. This equation reflects the specific relationship between the adsorbent and the adsorption capacity, as well as the influence of different NH_4^+-N concentrations on the ability of the soil to adsorb NH_4^+-N. At present, the Langmuir equation, the Freundlich equation, the Henry equation, and the Temkin equation are commonly used to describe the adsorption of NH_4^+-N in soil. The Langmuir equation assumes that the medium surface is uniform and the adsorption is performed by single molecules; this model can be used to calculate the corresponding maximum saturated adsorption capacity, adsorption coefficient, and MBC, as well as to evaluate and predict the adsorption of NH_4^+-N in the soil. In this experiment, the Langmuir equation had a high degree of fit, indicating that the isothermal adsorption of NH_4^+-N in the three soils was mainly monolayer adsorption, while multi-molecular layer adsorption was of secondary importance. The Freundlich equation is often used to describe the adsorption of non-uniform surfaces, but the maximum saturated adsorption capacity cannot be calculated. The fitting parameter 1/n of the Freundlich equation in this study was between 0 and 1, indicating that the isothermal adsorption of NH_4^+-N by the three kinds of soils was relatively efficient. The Henry equation is suitable for low concentrations and weak adsorption, while the Temkin equation is only suitable for chemical adsorption. As the latter two models had poor fits to the experimental data, the fitting of these two equations was not presented in this paper. At the same time, in order to further improve the application and evaluation of the fitting results, for the maximum saturated adsorption capacity, the analysis screened out the Plplatt equation whose fitting Q_m value was close to the measured average value, and the Langevin model whose fitting curve was more optimal. Although the adaptability of the assumptions that the adsorption model established to soil adsorption characteristics of NH_4^+-N was worthy of further validation, the law summarized by the analysis of the experimental data was basically consistent with the adsorption characteristics reflected by the empirical adsorption isotherm. Therefore, it was effective to use empirical adsorption isotherms to quantitatively describe the thermodynamic behavior of the soil adsorption of NH_4^+-N.

Soil Factors Affecting Adsorption

The NH_4^+-N Q_m of soil is affected by soil texture, environmental temperature and humidity, artificial fertilization, and crop rotation. The Q_m obtained by the Langmuir equation reflected the maximum saturated adsorption capacity of NH_4^+-N in the soil, as well as the number of soil adsorption sites. Li et al. (2009) found that Q_m was significantly negatively correlated with soil pH and CEC, while it was significantly positively correlated with soil C:N. Research by Cong et al. (2017) showed that Q_m was significantly positively correlated with soil pH and CEC, while it was significantly negatively correlated with SOM and TN content. Wang et al. (2015) reported that the greater the organic matter content, the greater the NH_4^+-N adsorption capacity of albic soil. Xue et al. (1996) found that the adsorption capacity of NH_4^+-N increased with the increase of soil CEC and soil clay content to varying degrees. The results of the present study showed that the Q_m value was significantly negatively correlated with soil pH, consistent with the results of Li et al. (2009). A possible reason was that the biogas slurry was alkaline, and the pH values of weakly acidic soils in Xinbei and Jintan were neutralized, resulting in the release of adsorption sites originally occupied by H^+ and thereby reducing the competition between H^+ and NH_4^+ for adsorption sites. There was a significant positive correlation between the Q_m value and CEC, consistent with the results of Cong et al. (2017), Xue et al. (1996), and Shen et al. (1997). Q_m was positively correlated with SOM, consistent with the results of Li et al. (2009) and Wang et al. (2015). This might be because organic matter had a large number of different functional groups (Liu et al., 2010), a higher CEC, and a larger specific surface area (Khorram et al., 2015; Acosta et al., 2016; Kumar, et al., 2016); these were all factors that could increase the adsorption capacity of NH_4^+-N through surface complexation, ion exchange, and surface precipitation. These results have been verified in many studies aimed at the improving soil adsorption of NH_4^+ by biochar (Yao et al., 2012).

Jiang (2004) showed that the finer the soil particles, the lower the percentage of sand powder with a particle size of ≥0.01 mm, while the higher the percentage of clay particles with a particle size of <0.005 mm, the stronger the adsorption. Xue et al. (1996) reported that NH_4^+-N adsorption capacity was mainly affected by clay content, with clay > loam > sandy soil. Cong et al. (2017) showed that the NH_4^+-N adsorption capacity of soil was in the order of light clay > light loam. The results of this study showed that the Q_m value of silty loam > loam > sandy loam was consistent with the above research results. Wan et al. (2004) found that there was a very significant positive correlation between fixed ammonium and clay content <0.01 mm, with clay content of 0.005–0.01 mm, and with clay content of 0.001–0.005 mm, but there was no significant correlation with clay content <0.001 mm. The results of this study showed that there was a significant positive correlation between the Q_m value and the content of particles with particle size of 0.02–0.002 mm in the soil. The same trend was observed in the results of Wan et al. (2004). Therefore, it is speculated that the increase of soil fixed ammonium content is a characteristic that can be further verified based on the fact that the fixed ammonium soil content increased with the increase of ammonium ion concentration (Liang and MacKenzie, 1994; Juang et al., 2001). In addition, there was a very significant positive correlation between the Q_m value and soil TN content, as well as a significant correlation with soil nitrate nitrogen. This may be the reason for the positive and negative electrical adsorption, and may be responsible for maintaining the balance between soil new ammonium nitrogen and nitrate nitrogen. The Q_m value was positively correlated with the soil AK. This was because active K^+ ions could provide adsorption sites and interlayer solid localization for NH_4^+ ions in external soil, which was in line with cation exchange theory (Rich and Black, 1964; Kittrick, 1966). The Q_m value was positively correlated with soil AP in this experiment. There were two possible reasons: the positive and negative charge adsorption, and the combination of NH_4^+ ions and PO_4^{3-} ions to form $[(NH_4)\ PO_4]^{2-}$, subsequently forming complex precipitates $Mg(NH_4)[PO_4]\cdot 6H_2O$ with the Mg^{2+} and Ca^{2+} plasma in the soil, thereby increasing the adsorption of NH_4^+-N. The correlation between the Langmuir equation adsorption constant K_l value, the MBC value, and soil property-related indicators, and the correlation between the Q_m value and soil property-related indicators were opposite (Li et al., 2009; Cong et al., 2017), indicating that the adsorption strength and the adsorption capacity were complementary. In other words, when the adsorption capacity is high, the adsorption strength is low. In addition, the fitted Q_m values of the NH_4^+-N adsorption of the soils in this study were lower than the fitted value of a single chemical ammonium salt solution, thus indicating that the rich complex components of the biogas slurry interfered with the adsorption of ammonium nitrogen in the soil as described in Zhao et al. (2013). While a preliminary demonstration has been achieved in the present research, the specific mechanism of action requires further study.

CONCLUSION

The soil adsorption of biogas slurry NH_4^+-N predominantly occurred within 0–1 h, and the adsorption capacity within 0–1 h accounted for 35.24%–43.55% of the total adsorption. The ExpAssoc equation produced a good fit for the adsorption kinetic behavior. The optimal theoretical saturated adsorption capacity (Q_m) values fitted by the Langevin model were 1108.55, 874.86g, and 448.35 mg/kg for silty loam, loam, and sandy loam, respectively. The Q_m was significantly positively correlated with SOM, TN, AP, AK, CEC, and particle content of 0.02–0.002 mm, but significantly negatively correlated with soil pH.

DATA AVAILABILITY STATEMENT

The raw data supporting the conclusion of this article will be made available by the authors, without undue reservation.

AUTHOR CONTRIBUTIONS

ZW: conceptualization, methodology, investigation, data curation, writing—original draft, and funding acquisition. LZ: investigation and data curation. GS and WZ: data curation. JS: conceptualization, data curation, supervision, and funding acquisition. XY: methodology and funding acquisition. AO: conceptualization, supervision, and funding acquisition. EK: conceptualization, methodology, writing—review and editing.

FUNDING

This work was supported by the National Key Research and Development Program of China (2018YFD0800105); the Jiangsu Agricultural Science and Technology Innovation Fund of China (CX(20)2014); the Jiangsu Province Key Research and Development Project (Modern Agriculture) of China (BE2019395); and the Collaborative Extension Plan of Jiangsu Major Agricultural Technologies of China (2020-SJ-047-04-01).

ACKNOWLEDGMENTS

We thank LetPub (www.letpub.com) for its linguistic assistance during the preparation of this manuscript.

REFERENCES

Acosta, R., Fierro, V., Martinez de Yuso, A., Nabarlatz, D., and Celzard, A. (2016). Tetracycline Adsorption onto Activated Carbons Produced by KOH Activation of Tyre Pyrolysis Char. *Chemosphere* 149, 168–176. doi:10.1016/j.chemosphere.2016.01.093

Bradford, S. A., Segal, E., Zheng, W., Wang, Q., and Hutchins, S. R. (2008). Reuse of Concentrated Animal Feeding Operation Wastewater on Agricultural Lands. *J. Environ. Qual.* 37, S97–S115. doi:10.2134/jeq2007.0393

Chen, D., Jiang, L., Huang, H., Toyota, K., Dahlgren, R. A., and Lu, J. (2013). Nitrogen Dynamics of Anaerobically Digested Slurry Used to Fertilize Paddy Fields. *Biol. Fertil. Soils.* 49 (6), 647–659. doi:10.1007/s00374-012-0752-8

Ciravolo, T. G., Martens, D. C., Hallock, D. L., Collins, E. R., Kornegay, E. T., and Thomas, H. R. (1979). Pollutant Movement to Shallow Ground Water Tables from Anaerobic Swine Waste Lagoons. *J. Environ. Qual.* 8 (1), 126–130. doi:10.2134/jeq1979.00472425000800010027x

Cong, R., Zhang, L., Lu, Y., Huang, Q., Shi, X., Li, X., et al. (2017). Adsorption-Desorption Characteristics of Soil Ammonium under Long-Term Straw Returning Condition. *J. Plant Nutr. Fert.* 23 (2), 380–388. doi:10.11674/zwyf.16307

Dalal, R. C. (1975). Effect of Associated Anions on Ammonium Adsorption by and Desorption from Soils. *J. Agric. Food Chem.* 23 (4), 684–687. doi:10.1021/jf60200a026

Feinerman, E., Bosch, D. J., and Pease, J. W. (2004). Manure Applications and Nutrient Standards. *Am. J. Agric. Econ.* 86 (1), 14–25. doi:10.1111/j.0092-5853.2004.00559.x

Gao, T., Chen, N., Li, W., Li, B., and Yuan, H. (2011). Effect of Highly Efficient Nutrient Solution of Biogas Slurry on Yield and Quality of Vegetables. *Agric. Sci. Technol.* 12 (4), 567–570. doi:10.3969/j.issn.1009-4229-B.2011.04.026

Ham, J. M., and DeSutter, T. M. (1999). Seepage Losses and Nitrogen Export from Swine-Waste Lagoons: A Water Balance Study. *J. Environ. Qual.* 28 (4), 1090–1099. doi:10.2134/jeq1999.00472425002800040005x

Han, M., Liu, K., Wang, S., Qin, L., and Gao, C. (2014). Definition, Ingredient, Approaches and Risks for Reuse in Biogas Slurry. *J. Agric.* 4 (10), 54–57.

He, G., Liu, X., and Cui, Z. (2021). Achieving Global Food Security by Focusing on Nitrogen Efficiency Potentials and Local Production. *Glob. Food Secur.* 29, 100536. doi:10.1016/j.gfs.2021.100536

Jiang, G. (2004). Discussion about NH_4^+-N Adsorptive Ability in Soils. *J. Chang'an Univ. Archit. Environ. Sci. Ed.* 21 (2), 32–34,38. doi:10.3321/j.issn:1673-2049.2004.02.009

Jin, H., Chang, Z., Ye, X., Ma, Y., and Jin, Z. (2011). Physical and Chemical Characteristics of Anaerobically Digested Slurry from Large-Scale Biogas Project in Jiangsu Province. *Trans. Chin. Soc. Agric. Eng.* 27 (1), 291–296. doi:10.3969/j.issn.1002-6819.2011.01.047

Jin, H., Fu, G., Chang, Z., Ye, X., Chen, G., and Du, J. (2012). Distribution of Nitrogen in Liquid and Solid Fraction of Pig and Dairy Manure in Anaerobic Digestion Reactor. *Trans. Chin. Soc. Agric. Eng.* 28 (21), 208–214. doi:10.3969/j.issn.1002-6819.2012.21.029

Juang, T. C., Wang, M. K., Chen, H. J., and Tan, C. C. (2001). Ammonium Fixation by Surface Soils and Clays. *Soil Sci.* 166 (5), 345–352. doi:10.1097/00010694-200105000-00005

Khorram, M. S., Wang, Y., Jin, X., Fang, H., and Yu, Y. (2015). Reduced Mobility of Fomesafen through Enhanced Adsorption in Biochar-Amended Soil. *Environ. Toxicol. Chem.* 34 (6), 1258–1266. doi:10.1002/etc.2946

Kithome, M., Paul, J. W., Lavkulich, L. M., and Bomke, A. A. (1998). Kinetics of Ammonium Adsorption and Desorption by the Natural Zeolite Clinoptilolite. *Soil Sci. Soc. Am. J.* 62 (3), 622–629. doi:10.2136/sssaj1998.03615995006200030011x

Kittrick, J. A. (1966). Forces Involved in Ion Fixation by Vermiculite. *Soil Sci. Soc. Am. J.* 30 (6), 801–803. doi:10.2136/sssaj1966.03615995003000060040x

Krishnamoorthy, C., and Overstreet, R. (1950). An Experimental Evaluation of Ion-Exchange Relationships. *Soil Sci.* 69 (1), 41–54. doi:10.1097/00010694-195001000-00003

Kumar, V., and Kothiyal, N. C. (2012). Distribution Behavior and Carcinogenic Level of Some Polycyclic Aromatic Hydrocarbons in Roadside Soil at Major Traffic Intercepts Within a Developing City of India. *Environ. Monit. Assess.* 184, 6239–6252. doi:10.1007/s10661-011-2416-9

Kumar, V., and Kothiyal, N. C. (2011). Distribution Behavior of Polycyclic Aromatic Hydrocarbons in Roadside Soil at Traffic Intercepts within Developing Cities. *Int. J. Environ. Sci. Technol.* 8, 63–72. doi:10.1007/BF03326196

Kumar, V., Kothiyal, N. C., and Saruchi (2016). Analysis of Polycyclic Aromatic Hydrocarbon, Toxic Equivalency Factor and Related Carcinogenic Potencies in Roadside Soil within a Developing City of Northern India. *Polycycl. Aromat. Compd.* 36 (4), 506–526. doi:10.1080/10406638.2015.1026999

Li, H., Han, Y., and Cai, Z. (2009). Equilibrium of Ammonium Adsorption in Paddy Soils of Taihu Region of China under Different Reaction Conditions. *Chin. J. Soil Sci.* 40 (1), 89–95. doi:10.3321/j.issn:0564-3945.2009.01.026

Li, W., Shi, Y., Zhu, D., Wang, W., Liu, H., Li, J., et al. (2021). Fine Root Biomass and Morphology in a Temperate Forest are Influenced More by the Nitrogen Treatment Approach Than the Rate. *Ecol. Indic.* 130, 108031. doi:10.1016/j.ecolind.2021.108031

Li, X., Zhang, C., Zhang, B., Wu, D., Zhu, D., Zhang, W., et al. (2021). Nitrogen Deposition and Increased Precipitation Interact to Affect Fine Root Production and Biomass in a Temperate Forest: Implications for Carbon Cycling. *Sci. Total Environ.* 765, 144497. doi:10.1016/j.scitotenv.2020.144497

Liang, B. C., and MacKenzie, A. F. (1994). Fertilization Rates and Clay Fixed Ammonium in Two Quebec Soils. *Plant Soil* 163, 103–109. doi:10.1007/bf00033946

Liu, C., Chen, Y., Li, X., Zhang, Y., Ye, J., Huang, H., et al. (2020). Temporal Effects of Repeated Application of Biogas Slurry on Soil Antibiotic Resistance Genes and Their Potential Bacterial Hosts. *Environ. Pollut.* 258, 113652. doi:10.1016/j.envpol.2019.113652

Liu, H., Dong, Y., Wang, H., and Liu, Y. (2010). Ammonium Adsorption from Aqueous Solutions by Strawberry Leaf Powder: Equilibrium, Kinetics and

Effects of Coexisting Ions. *Desalination* 263 (1-3), 70–75. doi:10.1016/j.desal.2010.06.040

Lu, J., Zhu, L., Hu, G., and Wu, J. (2010). Integrating Animal Manure-Based Bioenergy Production with Invasive Species Control: A Case Study at Tongren Pig Farm in China. *Biomass Bioenergy* 34 (6), 821–827. doi:10.1016/j.biombioe.2010.01.026

Lumbanraja, J., and Evangelou, V. P. (1994). Adsorption-Desorption of Potassium and Ammonium at Low Cation Concentrations in Three kentucky Subsoils. *Soil Sci.* 157 (5), 269–278. doi:10.1097/00010694-199405000-00001

Ni, Z., and Zhang, M. (2017). Chemical Compositions of Nitrogen, Phosphorus, and Potassium in Biogas Slurry and Their Bio-Availability. *Chin. J. Soil Sci.* 48 (5), 1114–1118. doi:10.19336/j.cnki.trtb.2017.05.13

Ning, J., Zhou, M., Pan, X., Li, C., Lv, N., Wang, T., et al. (2019). Simultaneous Biogas and Biogas Slurry Production from Co-Digestion of Pig Manure and Corn Straw: Performance Optimization and Microbial Community Shift. *Bioresour. Technol.* 282, 37–47. doi:10.1016/j.biortech.2019.02.122

Rich, C. I., and Black, W. R. (1964). Pottasium Exchange as Affected by Cation Size, pH, and Mineral Structure. *Soil Sci.* 97 (6), 384–390. doi:10.1097/00010694-196406000-00004

Saruchiand Kumar, V. (2020). Effective Degradation of Rhodamine B and Congo Red Dyes over Biosynthesized Silver Nanoparticles-Imbibed Carboxymethyl Cellulose Hydrogel. *Polym. Bull.* 77, 3349–3365. doi:10.1007/s00289-019-02920-x

Shen, S., Tu, S.-I., and Kemper, W. D. (1997). Equilibrium and Kinetic Study of Ammonium Adsorption and Fixation in Sodium-Treated Vermiculite. *Soil Sci. Soc. Am. J.* 61 (6), 1611–1618. doi:10.2136/sssaj1997.03615995006100060011x

Sherman, W. F., and Smulovitch, P. P. (1970). Pressure-Scanned Fermi Resonance in the Spectrum of NH4+ Isolated in CsBr. *J. Chem. Phys.* 52, 5187–5193. doi:10.1063/1.1672759

Sparks, D. L., and Jardine, P. M. (1984). Comparison of Kinetic Equations to Describe Potassium-Calcium Exchange in Pure and in Mixed Systems. *Soil Sci.* 138 (2), 115–122. doi:10.1097/00010694-198408000-00004

Stumm, W. (1992). *Chemistry of the Solid-Water Interface*. New York: John Wiley & Sons.

Tian, H. (2011). Ammonia-Nitrogen Adsorption Characteristics onto Vadose Zone Soils in Luanhe Delta. *Chin. J. Environ. Eng.* 5 (3), 507–510.

Wan, D., Zhang, Y., Feng, Y., and Huang, Y. (2004). Fixed Ammonium Content of Soils on Cultivated Upland in Hunan Province and its Affecting Factors. *Acta Pedol. Sin.* 41 (3), 480–483. doi:10.3321/j.issn:0564-3929.2004.03.025

Wang, F. L., and Alva, A. K. (2000). Ammonium Adsorption and Desorption in Sandy Soils. *Soil Sci. Soc. Am. J.* 64 (5), 1669–1674. doi:10.2136/sssaj2000.6451669x

Wang, S., Wang, N., Zhang, J., and Fan, C. (2015). Influencing Factors of NH4+ Adsorption Characteristics on Albic Soil. *Soil Fert. Sci. China.* 2, 22–28. doi:10.11838/sfsc.20150205

Wang, Y., Fu, J., Wang, Q., Wang, J., Ma, J., and Jiang, L. (2010). Effect of Biogas Slurry Farmland Disposal and Utilization on Pepper´s Yield, Quality and Soil Fertility. *Acta Agric. Zhejiangensis.* 22 (6), 859–863. doi:10.3969/j.issn.1004-1524.2010.06.030

Wang, Z., Liang, Y., Sheng, J., Guan, Y., Wu, H., Chen, L., et al. (2016). Analysis of Water Environment Risk on Biogas Slurry Disposal in Paddy Field. *Trans. Chin. Soc. Agric. Eng.* 32 (5), 213–220. doi:10.11975/j.issn.1002-6819.2016.05.030

Xue, Q., Wei, Q., Gao, Y., Shi, H., and Qu, D. (1996). Kinetic Characteristics of NH_4^+ Adsorption-Desorption for Five Major Soils in Shanxi Province. *Acta Pedol. Sin.* 32 (2), 129–136.

Yang, R., Sun, Q., Zhao, H., Zou, G., Liu, B., and Li, L. (2017). Precision Application of Biogas Slurry and its Environmental Effects in Paddy Fields. *J. Agro-Environ. Sci.* 36 (8), 1566–1572. doi:10.11654/jaes.2016-1617

Yao, Y., Gao, B., Zhang, M., Inyang, M., and Zimmerman, A. R. (2012). Effect of Biochar Amendment on Sorption and Leaching of Nitrate, Ammonium, and Phosphate in a Sandy Soil. *Chemosphere* 89 (11), 1467–1471. doi:10.1016/j.chemosphere.2012.06.002

Zhao, W., Li, Y., Zhao, Q., Ning, Z., Zhou, C., Wang, H., et al. (2013). Adsorption and Desorption Characteristics of Ammonium in Eight Loams Irrigated with Reclaimed Wastewater from Intensive Hogpen. *Environ. Earth Sci.* 69 (1), 41–49. doi:10.1007/s12665-012-1932-4

Zhu, J., and Huang, T. (2010). *New Processing Technologies in Livestock Wastewater Treatment*. Beijing: Chemical Industry Press.

Conflict of Interest: The authors declare that the research was conducted in the absence of any commercial or financial relationships that could be construed as a potential conflict of interest.

frontiers | Frontiers in Environmental Science

TYPE Original Research
PUBLISHED 05 August 2022
DOI 10.3389/fenvs.2022.949618

OPEN ACCESS

EDITED BY
Shengsen Wang,
Yangzhou University, China

REVIEWED BY
Chuan Chen,
Harbin Institute of Technology, China
Lingzhao Kong,
Chinese Academy of Sciences (CAS),
China

*CORRESPONDENCE
Shuguang Zhu,
zhushuguang@ahjzu.edu.cn

SPECIALTY SECTION
This article was submitted to Water and Wastewater Management,
a section of the journal
Frontiers in Environmental Science

RECEIVED 21 May 2022
ACCEPTED 29 June 2022
PUBLISHED 05 August 2022

CITATION
Mao J, He M, Qin Y, Chen Y, Wang X, Che H, Cheng C, Wang T, Wang W, Sun B and Zhu S (2022), Resource utilization of waste tailings: Simulated removal of nitrogen from secondary effluent by autotrophic denitrification based on pyrite tailings.
Front. Environ. Sci. 10:949618.
doi: 10.3389/fenvs.2022.949618

Resource utilization of waste tailings: Simulated removal of nitrogen from secondary effluent by autotrophic denitrification based on pyrite tailings

Jie Mao[1,2,3], Mengqi He[2,3], Ying Qin[4], You Chen[3], Xinyu Wang[5], Haojie Che[2,3], Chun Cheng[2,3], Tiantian Wang[3], Wenliang Wang[6], Bai Sun[1,2,3] and Shuguang Zhu[1,2,7]*

[1]Engineering Research Center of Ministry of Education, Anhui Jianzhu University, Hefei, China, [2]Key Laboratory of Water Pollution Control and Wastewater Recycling of Anhui Province, Hefei, China, [3]School of Environmental and Energy Engineering, Anhui Jianzhu University, Hefei, China, [4]School of Mechanical and Electrical Engineering, Anhui Jianzhu University, Hefei, China, [5]Nanjing University Environmental Planning and Design Research Institute Group Co., Nanjing, China, [6]Anhui Magang Zhangzhuang Mining Co., Ltd., Luan, China, [7]Energy Saving Research Institute, Anhui Jianzhu University, Hefei, China

In this report, eco-friendly and low-cost pyrite tailings are utilized as denitrification materials, while pyrite and magnetite are used as the control experimental groups to explore the denitrification performance of pyrite tailings. The results show that the removal effect of pyrite tailings on NO_3^- is slightly lower than that of pyrite. However, the concentration of NH_4^+ decreased, and the effluent SO_4^{2-} concentration was lower than that of pyrite. In addition, pyrite with different particle sizes is prepared by the ball milling method, and the effect of particle size on the denitrification performance of pyrite is studied. The results show that with the decrease in particle size, microorganisms are more likely to use S in tailings as electron donors, the denitrification rate is faster, and the denitrification effect was better at the same time.

KEYWORDS

pyrite tailings, denitrification, ball milling, secondary effluent, resource utilization

Introduction

Lake eutrophication is a global water ecological environment problem (Hans W. Paerl, et al., 2015), and it is also one of the main challenges to water ecological environment governance and protection in China (Chen and Li. 2006). In recent years, lake eutrophication caused by excessive input of nitrogen and phosphorus has become increasingly prominent, seriously threatening the ecological security and drinking water security of lake basins (Farshad Shafiei. 2021). At present, although domestic sewage treatment has reached the drainage standard, there is no nitrogen and phosphorus environmental capacity for the eutrophic water (Chen. 2020). Therefore, with the development of cheap and efficient denitrification and dephosphorization materials and technology (Song. 2021), the municipal sewage treatment plant secondary effluent more strict denitrification and dephosphorization processes can ensure the ecological environment of water (Cao, et al., 2020).

Secondary effluent of municipal wastewater treatment plants is typical low C/N wastewater (Sun et al., 2019). The conventional heterotrophic denitrification process requires the addition of external carbon sources, which increases the treatment cost and complexity of operation (Fu, 2022). However, autotrophic denitrification does not require organic carbon sources and can use inorganic carbon and reducing sulfur compounds as electronic donors, which can reduce the operating cost of municipal wastewater treatment plants and effectively remove NO_3^- in secondary effluent with low treatment cost. According to different electron donors, autotrophic denitrification can be divided into hydrogen autotrophic denitrification, iron autotrophic denitrification, and sulfur autotrophic denitrification (Zhou et al., 2022). Sulfur autotrophic denitrification with elemental sulfur as the electron donor has a fast denitrification rate, but a large amount of reaction by-product SO_4^{2-} will be produced during the reaction process, which affects its promotion in practical application (Jiaoyang, 2014). In recent years, pyrite (FeS_2) has also been found to be an electron donor for chemical autotrophic denitrification (Pang, et al., 2020). Garcia-Gil et al. (Garcia-Gil, et al., 1993) found that adding FeS to the sediments of the Rhone Delta in France could change the denitrification rate and monitor the oxidation process of S^{2-} in FeS. Haaijer et al. (Haaijer et al., 2007) reported that autotrophic denitrification based on iron sulfide can remove nitrate in freshwater system and compared the denitrification of two different iron sulfides (pyrite and ferrous sulfide) as substrates, proving that ferrous sulfide can remove nitrate more effectively under the action of denitrifying bacteria. Bosch et al. (Bosch et al., 2012) proposed that while thiobacillus denitrificans use sulfur in iron sulfide as an electron donor, they may also use iron in iron sulfide as an electron donor to reduce nitrate. Yang et al. (Zhang et al., 2020) also found that synthetic or natural pyrrhotite (FeS) autotrophic denitrification (PAD) had excellent simultaneous nitrogen and phosphorus removal performance. At present, many scholars have turned their attention toward the autotrophic denitrification technology using pyrite as the electron donor to remove NO_3^- in water (Kong, et al., 2015), or the autotrophic denitrification and heterotrophic denitrification combined with pyrite and elemental sulfur or other mineral materials to remove nitrogen and phosphorus in sewage (Wang, et al., 2019). However, pyrite is an important mineral resource, and if directly used in a large amount of water treatment, there is also a large economic cost. Mine tailings have become the most produced and stored solid waste in China. The total amount of metal mine tailings accounts for 34% of general industrial solid waste and is a major hazard and pollution source (Kong, et al., 2016). A large number of tailings are piled up in the tailings pond and cannot be used, resulting in a large amount of waste of resources. The accumulation of these wastes also seriously affects the ecological environment and threatens people's health (Theo. 2021). Pyrite tailings, by-products after mining, contain the same effective components as pyrite, which can provide electrons for autotrophic denitrification, while tailings, as substrates for denitrification reaction, provide a new way for waste utilization of tailings (Tong, et al., 2021). Therefore, in this study, pyrite tailings were selected as autotrophic denitrifying electron donors, and pyrite and magnetite were used as control groups to explore the feasibility of removing nitrogen and phosphorus substances from secondary effluent from tailings. At the same time, this study obtained pyrite tailings with different particle size scales using the ball milling method and discussed the influence of particle size scales on their nitrogen and phosphorus removal performance.

Materials and methods

Materials

Raw pyrite and pyrite tailings were obtained from Longqiao Mine in Tongling, Anhui province, China, while magnetite tailings were collected from Zhangzhuang Mine in Huqiu, Anhui Province, China. Then, the tailings were grounded into particles with a size of 0.10–0.15 mm using a high-speed blender, washed in deionized water several times to clarify the supernatant, followed by ultrasonic shock for 1 h, and washed in deionized water again. Finally, the mineral particles were dried at 70°C for 6 h in the oven. Nitrogen removal reaction system with pyrite, pyrite tailings, and magnetite tailings as the substrate was denoted by PM, PT, and MT, respectively.

Preparation of materials

Preparation of pyrite tailings

The pyrite tailings were mixed with water at the mass ratio of 1:1, and the mixed solution was poured into the planetary ball mill and mixed with large beads (3 mm) and small beads (2 mm) at a ratio of 1:1. Three kinds of pyrite tailings with different particle sizes were prepared by different operation settings of the ball mill. The mixture was transferred into the beaker after the ball grinding and made to stand for half an hour, then the supernatant was collected and washed in deionized water several times to clarify, and then, the mineral particles were dried at 70°C.

TABLE 1 Water quality analysis methods.

Analysis indicator	Analysis method	Analytical instrument	Instrument model
NO_3^--N	UV spectrophotometry	Ultraviolet-visible spectrophotometer	UV-5100
NO_2^--N	N-1-Naphthylethylenediamine dihydrochloride spectrophotometry		
NH_4^+-N	Nessler reagent spectrophotometry		
PO_4^{3-}-P	Molybdenum antimony resistance spectrophotometry		
SO_4^{2-}	Ion chromatography	Ion chromatography	ICS-900DionexIonPac

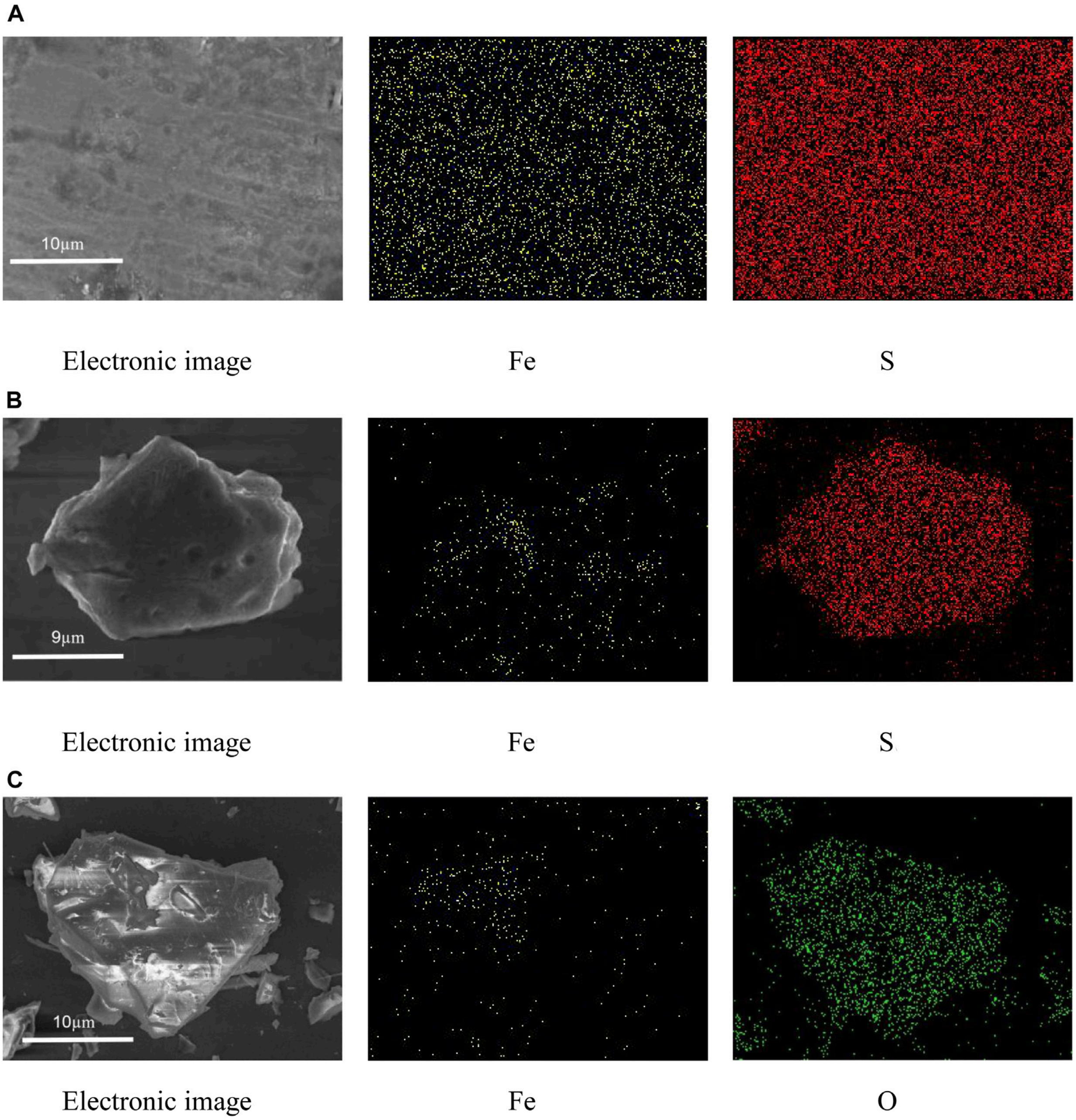

FIGURE 1
SEM images and elemental mappings of pyrite **(A)**, pyrite tailings **(B)**, and magnetite tailings **(C)**.

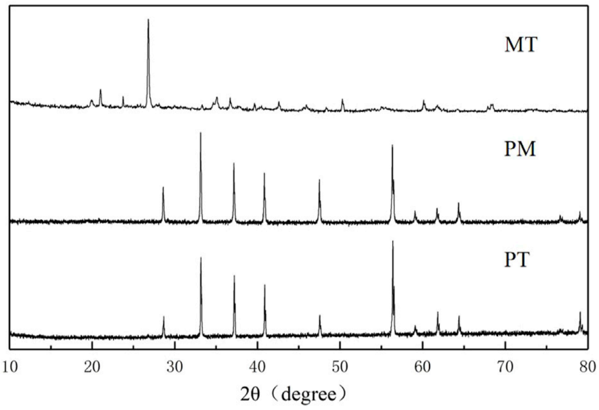

FIGURE 2
XRD spectrum of pyrite, pyrite tailings, and magnetite.

Simulation of sewage quality

The secondary effluent of the laboratory simulated sewage plant was prepared with deionized water. The simulated sewage quality was configured according to the actual secondary effluent concentration of the sewage plant. The concentration of nitrate–nitrogen in the experimental sewage prepared by potassium nitrate was 15 mg/L; and the concentration of ammonia nitrogen prepared by ammonium chloride was 10 mg/L. Sodium bicarbonate was used as an autotrophic denitrification carbon source with a concentration of 90 mg/L.

Methods

A total of 800 ml synthetic sewage was added to a 1000 ml conical flask, and 30 g mineral particles and 5 ml cleaned sludge were added to the flask, respectively. After the rubber plug was fastened, the flask was placed in a constant temperature shaker, which continued to run at 150 r/min and 30°C. Samples were taken at 0, 12, 24, 36, 48, 60, 84, 108, and 132 h, respectively, and the concentrations of NO_3^--N, NH_4^+-N, NO_2^--N, and SO_4^{2-} in the water were measured. Three parallel experiments were set up for each group.

Thirty grams of mineral particles with different particle sizes were weighed and placed in a 1000 ml conical flask, 800 ml simulated secondary effluent was added, and then 5 ml cleaned sludge was added. After the rubber plug was fastened, the particles were placed in a constant temperature shaker, which continued to run at 150 r/min and 30°C. Samples were taken at 0, 12, 24, 36, 48, 60, 84, 108, and 132 h, respectively, and the concentrations of NO_3^--N, NH_4^+-N, NO_2^--N, and SO_4^{2-} in the water were measured. Three parallel experiments were set up.

Characterization

To analyze the structure and element composition of the three minerals, the micromorphology and the element composition of the three mineral particles were observed using scanning electron microscopy equipped with an energy dispersive spectrometer (SEM-EDS). The mineral particles mixed with water after drying were collected, and the mixed solution was slowly added to the laser particle size analyzer at a speed of 2200 r/min. The dried mineral particles were placed in an X-ray powder diffractometer (XRD) for crystal structure analysis, and the angle of diffraction (2θ) was set in the range of 10–80°. The dried mineral particles were mixed with deionized water, and the mineral surface potential was determined using the Zeta potential analyzer.

Water sample analysis was performed according to Water and Water Monitoring Analysis Method 4th Edition (2002). The specific indicators and analysis methods are shown in Table 1.

Results and discussions

Study on nitrogen removal from the secondary effluent by autotrophic denitrification of three minerals

Characterization of three minerals

SEM images and elemental mappings of PM, PT, and MT are shown in Figure 1. SEM images clearly indicated that PM has a smooth, crystalline surface with large particles, while PT has a rough, granular surface with small particles. Meanwhile, elemental mappings verified that the areas of S in PM and PT were significantly larger than that of Fe, further confirming the pyrite structure. In addition, the surface of MT was rough, granular, and larger, and the mineral contained less Fe, which was due to the fact that the tailings contained less Fe_2O_3.

XRD analysis of PT, PM, and MT was conducted for crystal structure analysis, and it can be seen from Figure 2 that all of the three minerals have obvious crystal structures. The diffraction peaks (2θ) of PT and PM at 28.6°, 33.1°, 37.2°, 40.9°, 47.6°, and 56.4° are assigned to the (111), (200), (210), (211), (220), and (311) crystal planes of FeS_2 (JCPDS card no. 01-1295), respectively. Moreover, the diffraction peak position (2θ) of MT is 15.2°, 24.8°, 26.7°, 26.8°, 28.7°, 47.0°, 57.6°, and 50.4°, corresponding to the orthorhombic crystal structure; all the diffraction peaks were well matched with JCPDS card no: 89-2810.

Variation of effluent nitrogen and sulfate concentration

In order to explore the denitrification effect of pyrite tailings, we conducted a comparative study on the NO_3^--N,

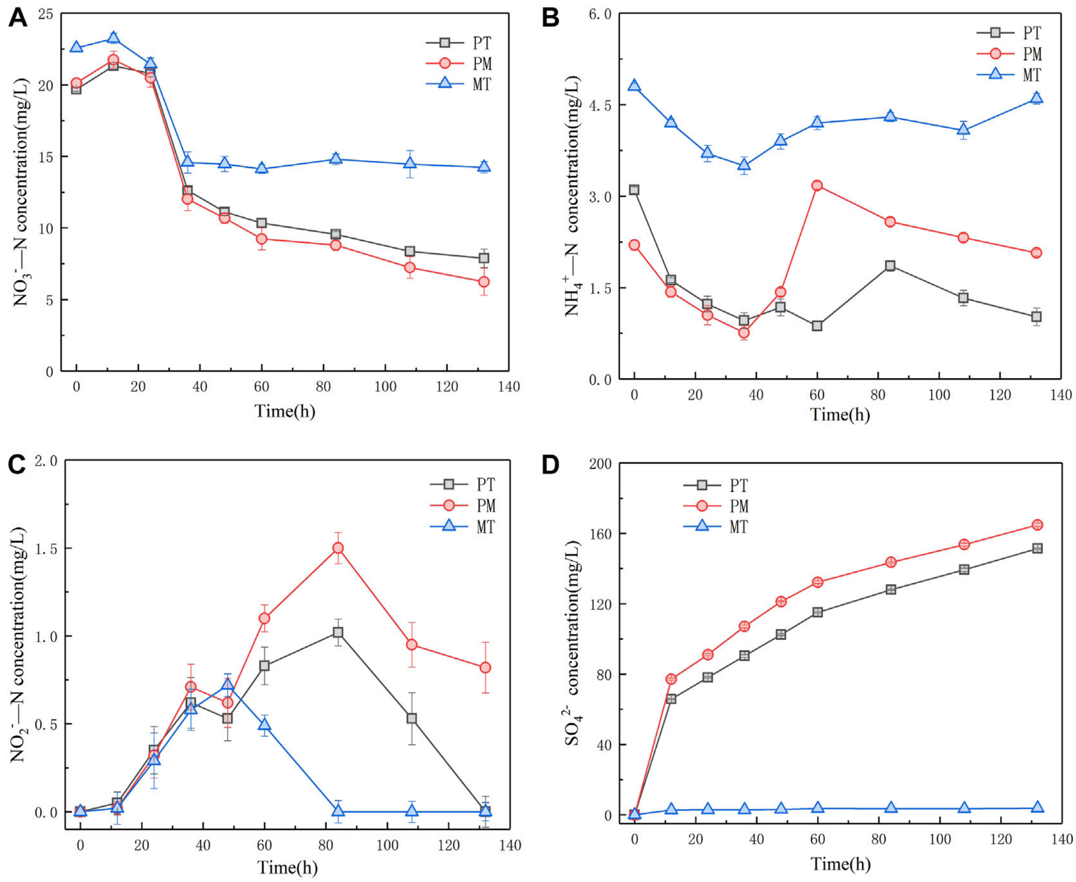

FIGURE 3
Variation of NO_3^--N concentration **(A)**, NH_4^+-N concentration **(B)**, NO_2^--N concentration **(C)**, and SO_4^{2-}concentration **(D)** in denitrification system of three minerals.

NO_2^--N, and NH_4^+-N removal performance of simulated sewage by three reaction systems of PM, MT, and PT. It can be seen from Figure 3A that the concentration of NO_3^--N in PT, PM, and MT reaction systems first increased and then decreased at the initial stage of microbial growth and adaptation. During the 24–36 h period, the concentration of NO_3^--N in the three systems reduced rapidly for a short time, which is probably due to the heterotrophic denitrification caused by the sewage with a low content of organic carbon. Subsequently, the concentration of NO_3^--N in PT and PM shows a stable downward trend, while the concentration of NO_3^--N in MT shows no significant change. After 132 h of reaction, the NO_3^--N removal rates of PT, PM, and MT were 60.0, 69.0, and 36.94%, respectively. Figure 3B reveals the variation of effluent NH_4^+-N concentration over time in the reaction system. The effluent NH_4^+-N concentration of the three reaction systems shows a great difference. During the 24–36 h stage, the concentration of NH_4^+-N in PT, PM, and MT decreased from 3.10, 2.20, and 4.80 mg/L to 0.96, 0.76, and 3.50 mg/L, respectively. After 36h, the concentration of NH_4^+-N in the three reaction systems increased, which may result from the increase in NH_4^+ concentration caused by the death of heterotrophic microorganisms after the completion of heterotrophic denitrification. Furthermore, the autotrophic denitrification of PT and PM requires partial utilization of NH_4^+; so, the concentration of NH_4^+ in PT and PM gradually descended at the later stage of the reaction. Moreover, compared with PT, PM has a high content of FeS_2 and more electron donors, and its demand for NH_4^+ is lower. Therefore, it can be seen from Figure 3B that PT has higher removal efficiency for NH_4^+-N. We simultaneously recorded the NO_2^--N changes of three reaction systems. It can be observed from Figure 3C that NO_2^- was first accumulated and then reduced in all three systems, mainly because microorganisms reduced NO_3^- preferentially, and NO_3^- had an inhibitory effect on the synthesis and activity of NO_2^- reductase. However, at the end of the reaction, the

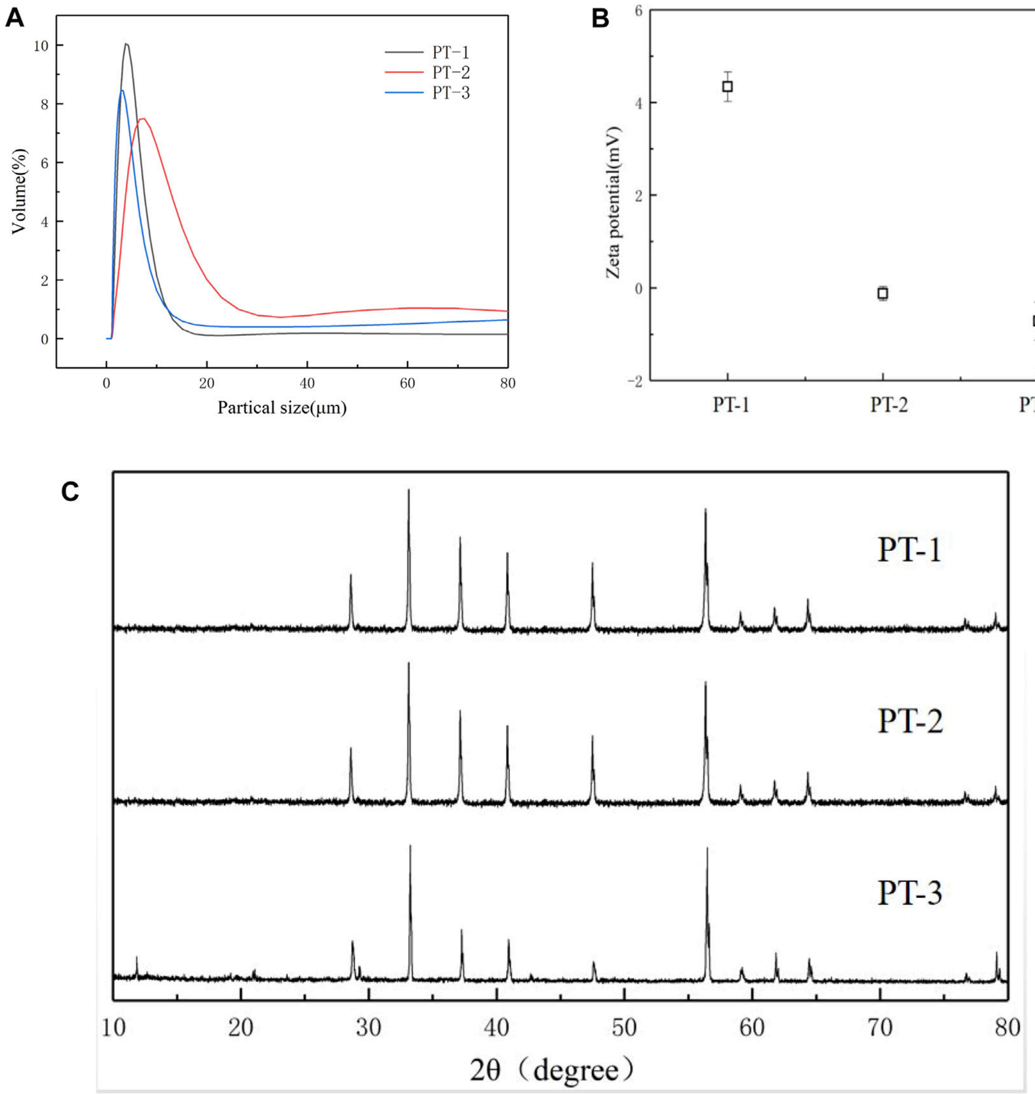

FIGURE 4
Particle size distribution spectrum **(A)** and XRD spectrum **(B),** Zeta potential **(C)** of pyrite tailings with different sizes.

accumulation of NO_2^--N in PT and PM was 1.02 mg/L and 1.50 mg/L, respectively. The concentration of NO_2^--N in MT was reduced to below the detection limit, and MT had the best removal effect on NO_2^--N. Figure 3D reveals the concentration of SO_4^{2-}- in the three systems. As one of the products in the process of sulfur autotrophic denitrification, the massive accumulation of SO_4^{2-} is the limitation for the application of elemental sulfur autotrophic denitrification. In consequence, we monitored the concentration of SO_4^{2-} in the three reaction systems, and the experimental results implied that the concentration of SO_4^{2-} in MT did not change significantly over time, which was attributed to the fact that MT contained no sulfur element and could not undergo autotrophic denitrification of sulfur. On the contrary, the concentration of SO_4^{2-} in PT and PM ascended gradually along with time, but the formation of SO_4^{2-} in PT declined relatively, indicating that the use of pyrite tailings as nitrogen and phosphorus removal materials can reduce the amount of SO_4^{2-}, without changing the water quality significantly.

Influence of particle size on nitrogen removal

Characterization of three tailings with different particle sizes

Based on the fact that pyrite tailings have a certain nitrogen removal effect, we were then interested in

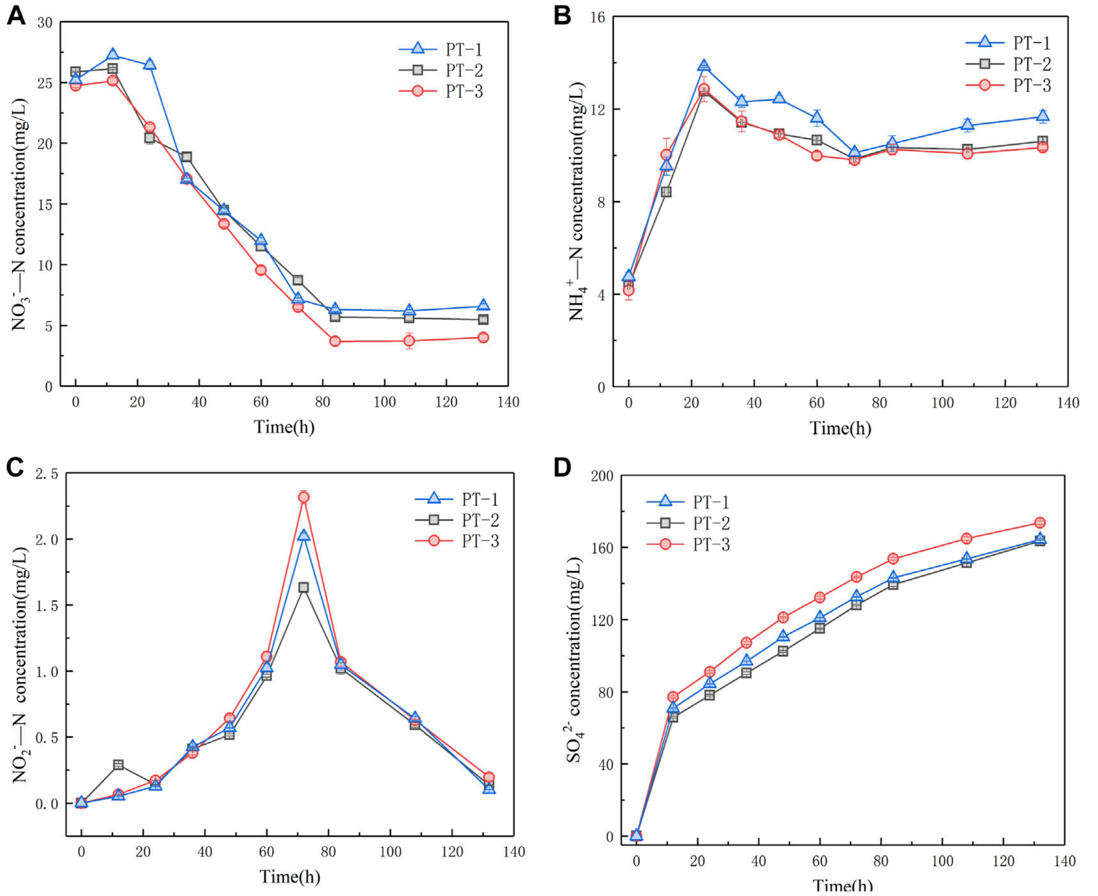

FIGURE 5
Variation of NO_3^--N concentration **(A)**, NH_4^+-N concentration **(B)**, NO_2^--Nconcentration **(C)**, and SO_4^{2-}concentration **(D)** in three granular denitrification systems of pyrite tailings.

studying the effect of particle size of tailings on nitrogen removal from effluent. By grinding the mineral for 30, 25, and 20 min, three tailing samples with different particle sizes were obtained (denoted as PT-1, PT-2, and PT-3, respectively). The particle size distribution is shown in Figure 4A, and the particle sizes (D_{50}) of three kinds of minerals are 3.80, 7.59, and 2.89 μm, respectively. As the ball milling process is accompanied by high temperature and high pressure, the crystal structure of the minerals may be changed; so, XRD analysis was conducted on three kinds of minerals. It can be seen from Figure 4B that all of the minerals had obvious crystal structure, and the diffraction peaks (2θ) at 28.6°, 33.1°, 37.2°, 40.9°, 47.6°, and 56.4° correspond to the (111), (200), (210), (211), (220), and (311) crystal planes of FeS_2, respectively. XRD results indicated that particle size had no influence on the crystal structure of the minerals. However, Zeta data (Figure 4C) demonstrated that the surface potential of the three groups of minerals was 4.34 mV, −0.12 mV, and −0.72 mV, respectively, indicating that the surface charge distribution of minerals would be changed during the mechanical stripping process of minerals by ball milling.

Variation of effluent nitrogen and sulfate concentration

According to the XRD results, we confirmed that the change in particle size had no effect on the crystal structure of pyrite tailings. Therefore, we further investigated the feasibility and difference of NO_3^--N, NO_2^--N, and NH_4^+-N removal from secondary effluent of tailings with three different particle sizes. Variations in NO_3^--N concentration of the three systems are shown in Figure 5A. At the initial stage of microbial growth and adaptation, the reaction rates of the three systems are relatively low. During 36–84 h period, the concentrations of NO_3^--N in the three systems show a stable decreasing trend, and the reduction rates are 1.95, 2.40, and 2.43 mg/(L*d), respectively. The NO_3^--N reduction rate decreased with the increase in pyrite particle size. At this stage, a heterotrophic denitrification reaction mainly occurred. The results indicate that the larger the pyrite tailing particles are, the more difficult it is to be utilized by autotrophic microorganisms, which leads to the slowdown of autotrophic denitrification rate and affects the NO_3^--N removal in the water. As the reaction progressed, the death of some heterotrophic microorganisms was due to the inadaptability to the solution, releasing nitrate nitrogen and slightly increasing the concentration of NO_3^--N in the solution. According to these results, we consider that particle size has no significant impact on the NO_3^--N removal ability of pyrite tailing particles. Figure 5B displays that the change in NH_4^+-N concentration in the three systems is similar, and it rises at the initial stage of the reaction. Subsequently, the concentrations of NH_4^+-N in the three systems decrease because a part of NH_4^+ is consumed in the heterotrophic denitrification stage, while a part of NH_4^+ is also consumed by the growth of microorganisms themselves. At the end of the reaction, the concentrations of NH_4^+-N in the three systems rise, which is attributed to the fact that the dissimilatory nitrate reduction to ammonium (DNRA) process occurs in the autotrophic denitrification stage, which transforms NO_3^- into NH_4^+. In the system, the processes affecting the concentration of NH_4^+ mainly include the synthesis and utilization of microorganisms and the DNRA. It can be seen that the particle size of pyrite has no significant influence on the abovementioned processes. The accumulation amount of NO_2^--N is shown in Figure 5C. All of the concentrations of NO_2^--N in the three systems reach the maximum accumulation amount at 72 h, and there is little difference in NO_3^--N concentration in the three systems at this time, indicating that the particle size of pyrite tailings did not affect the concentration of NO_3^--N, which may inhibit the synthesis and activity of NO_2^- reductase in the denitrification system. As can be seen from Figure 5D, the accumulation amounts of SO_4^{2-} in the three systems within 12–132 h are 93.46, 97.64, and 96.52 mg/L, respectively. With the decrease in particle size, the larger the contact surface between particles and air, the more easily S on the surface is oxidized into SO_4^{2-}, leading to the higher concentration of SO_4^{2-} in the initial reaction. Therefore, at the end of the experiment, more SO_4^{2-} particles were produced.

Conclusion

In conclusion, we compare the denitrification effects of three kinds of mineral materials. The results show that magnetite had a limited ability to remove nitrogen in water and mainly depended on heterotrophic denitrification. Pyrite has the best effect on NO_3^- removal in water, but there is still a certain amount of NO_2^- in water after the reaction, and the concentration of NH_4^+ in water fluctuates within a certain range, which is almost the same as the initial value. However, the NO_3^- removal effect of pyrite tailings is slightly worse than that of pyrite, but the overall NH_4^+ concentration in the reaction process shows a downward trend, and the effluent SO_4^{2-} concentration is lower than that of the pyrite experimental group. Therefore, in view of the economic benefits of pyrite tailings, it has greater potential in the application of denitrification and nitrogen removal in wastewater. In addition, pyrite tailings with different particle sizes are prepared using the ball milling method to study the effect of particle sizes on nitrogen removal. Through XRD and Zeta potential analysis, it can be seen that the main composition of the pyrite tailings after ball milling process does not change except particle size. With the decrease in particle size, microorganisms are more likely to use S in tailings as electron donors, and the denitrification rate will be faster and the denitrification effect will be better at the same time.

Data availability statement

The original contributions presented in the study are included in the article/Supplementary Material, and further inquiries can be directed to the corresponding author.

Author contributions

Conceptualization: JM and SZ; formal analysis: JM, MH, HC, CC, YQ, YC, TW, WW, BS, and SZ; funding acquisition: JM and BS; investigation: MH, HC, CC, YQ, YC, TW, WW, BS, and SZ; methodology: JM, MH, HC, CC, YQ, YC, TW, WW, XW, and SZ; project administration: SZ; validation: SZ; visualization: JM; writing—original draft, JM, MH, and XW; and writing—review and editing, HC, CC, YQ, YC, TW, WW, and BS.

Funding

This research was supported by the Project of the National Key Research and Development Program (2019YFC0408505); the National Natural Science Foundation of China (52103104); the Scientific Research Start-up Foundation for Introduction of Talent, Anhui Jianzhu University (2020QDZ30); the Natural Science Research Project of the Higher Education Institutions of Anhui Province (KJ 2021A0616); the Fujian Provincial Key Laboratory of Fire Retardant Materials, College of Materials, Xiamen University (FH202103); the 2021 National Innovation Training Program for College Students (202110878024); and the 2021 National Innovation Training Program for College Students (202210878026).

Conflict of interest

XW was employed by the company Nanjing University Environmental Planning and Design Research Institute Group Co., and WW was employed by the company Anhui Magang Zhangzhuang Mining Co., Ltd.

The remaining authors declare that the research was conducted in the absence of any commercial or financial relationships that could be construed as a potential conflict of interest.

Publisher's note

References

Bosch, J., Lee, K. Y., Jordan, G., Kim, K. W., and Meckenstock, R. U. (2012). Anaerobic, nitrate-dependent oxidation of pyrite nanoparticles by thiobacillus denitrificans. *Environ. Sci. Technol.* 46 (4), 2095–2101. doi:10.1021/es2022329

Cao, Shenbin, Du, R., Peng, Y., Li, B., and Wang, S. (2020). Corrigendum to "Novel two stage partial denitrification (PD)-Anammox process for tertiary nitrogen removal from low carbon/nitrogen (C/N) municipal sewage" [Chem. Eng. J. 362 (2019) 107–115]. *Chem. Eng. J.* 395, 124810. doi:10.1016/j.cej.2020.124810

Chen, Jing. (2020). Research on technical problems of urban domestic sewage treatment under environmental protection form. *IOP Conf. Ser. Earth Environ. Sci.* 450, 012066. doi:10.1088/1755-1315/450/1/012066

Chen, Xiaoying, and Li, Shijie (2006). An analysis on the evolvement processes of lake eutrophication and their characteristics of the typical lakes in the middle and lower reaches of Yangtze River. *Chin. Sci. Bull.* 51 (13), 1603–1613. doi:10.1007/s11434-006-2005-4

Fu, X. (2022). Application of external carbon source in heterotrophic denitrification of domestic sewage: A review. *Sci. total Environ.*, 817. doi:10.1016/J.SCITOTENV.2022.153061

Garcia-Gil, L. J., and Golterman, H. (1993). Kinetics of FeS-mediated denitrification in sediments from the Camargue (Rhone delta, southern France). *FEMS Microbiol. Ecol.* 13 (2), 85–91. doi:10.1111/j.1574-6941.1993.tb00054.x

Haaijer, S. C. M., Lamers, L. P. M., Smolders, A. J. P., Jetten, M. S. M., and Op den Camp, H. J. M. (2007). Iron sulfide and pyrite as potential electron donors for microbial nitrate reduction in freshwater wetlands. *Geomicrobiol. J.* 24 (5), 391–401. doi:10.1080/01490450701436489

Jiaoyang, P. (2014). Pyrite-based autotrophic denitrification for remediation of nitrate contaminated groundwater. *Bioresour. Technol.* 173, 113. doi:10.1016/j.biortech.2014.09.092

Kong, Zhe, Li, L., Feng, C., Chen, N., Dong, S., and Hu, W. (2015). Soil infiltration bioreactor incorporated with pyrite-based (mixotrophic) denitrification for domestic wastewater treatment. *Bioresour. Technol.* 187, 14–22. doi:10.1016/j.biortech.2015.03.052

Kong, Zhe, Li, L., Feng, C., Dong, S., and Chen, N. (2016). Comparative investigation on integrated vertical-flow biofilters applying sulfur-based and pyrite-based autotrophic denitrification for domestic wastewater treatment. *Bioresour. Technol.* 211, 125–135. doi:10.1016/j.biortech.2016.03.083

Paerl, Hans W., Xu, H., Hall, N. S., Rossignol, K. L., Joyner, A. R., Zhu, G., et al. (2015). Nutrient limitation dynamics examined on a multi-annual scale in lake taihu, China: Implications for controlling eutrophication and harmful algal blooms. *J. Freshw. Ecol.* 30, 5–24. doi:10.1080/02705060.2014.994047

Pang, Y., and Wang, J. (2020). Insight into the mechanism of chemoautotrophic denitrification using pyrite (FeS_2) as electron donor. *Bioresour. Technol.* 318, 124105. doi:10.1016/j.biortech.2020.124105

Shafiei, Farshad (2021). Nutrient mass balance of a large riverine reservoir in the context of water residence time variability. *Environ. Sci. Pollut. Res.* 28, 39082–39100. doi:10.1007/S11356-021-13297-8

Song, Tao (2021). A review of research progress of heterotrophic nitrification and aerobic denitrification microorganisms (HNADMs). *Sci. Total Environ.* 801, 149319. doi:10.1016/J.SCITOTENV.2021.149319

Sun, S., Lin, H., Lin, J., Quan, Z., Zhang, P., and Ma, R. (2019). Underground sewage treatment plant: A summary and discussion on the current status and development prospects. *Water Sci. Technol.* 80, 1601–1611. doi:10.2166/wst.2019.429

Theo, Henckens (2021). Scarce mineral resources: Extraction, consumption and limits of sustainability. *Resour. Conserv. Recycl.* 169, 105511. doi:10.1016/J.RESCONREC.2021.105511

Tong, Liu, Hu, Y., Chen, N., He, Q., and Feng, C. (2021). High redox potential promotes oxidation of pyrite under neutral conditions: Implications for optimizing pyrite autotrophic denitrification. *J. Hazard. Mater.* 416, 125844. doi:10.1016/J.JHAZMAT.2021.125844

Wang, Wei, Wei, D., Li, F., Zhang, Y., and Li, R. (2019). Sulfur-siderite autotrophic denitrification system for simultaneous nitrate and phosphate removal: From feasibility to pilot experiments. *Water Res.* 160, 52–59. doi:10.1016/j.watres.2019.05.054

Zhang, Yang, Yu, J., Wu, Y., Li, M., Zhao, Y., Zhu, H., et al. (2020). Efficient production of chemicals from microorganism by metabolic engineering and synthetic biology. *Chin. J. Chem. Eng.* 13, 14–28. doi:10.1016/J.CJCHE.2020.12.014

Zhou, Q., Sun, H., Jia, L., Wu, W., and Wang, J. (2022). Simultaneous biological removal of nitrogen and phosphorus from secondary effluent of wastewater treatment plants by advanced treatment: A review. *Chemosphere* 296, 134054. doi:10.1016/J.CHEMOSPHERE.2022.134054

frontiers | Frontiers in Environmental Science

TYPE Original Research
PUBLISHED 19 September 2022
DOI 10.3389/fenvs.2022.1002372

OPEN ACCESS

EDITED BY
Tao Zhang,
China Agricultural University, China

REVIEWED BY
Mouez Gouasmia,
University of Gafsa, Tunisia
Yuanzheng Zhai,
Beijing Normal University, China

*CORRESPONDENCE
Yuezan Tao,
taoyuezan@126.com

SPECIALTY SECTION
This article was submitted to Water and Wastewater Management,
a section of the journal
Frontiers in Environmental Science

RECEIVED 25 July 2022
ACCEPTED 24 August 2022
PUBLISHED 19 September 2022

CITATION
Lin F, Ren H, Yang J, Li Y, Kang B and Tao Y (2022), Tracking chlorinated contaminants in the subsurface using analytical, numerical and geophysical methods.
Front. Environ. Sci. 10:1002372.
doi: 10.3389/fenvs.2022.1002372

Tracking chlorinated contaminants in the subsurface using analytical, numerical and geophysical methods

Fei Lin[1,2], Honglei Ren[1], Jie Yang[1], Yucheng Li[2], Bo Kang[3] and Yuezan Tao[1]*

[1]College of Civil Engineering, Hefei University of Technology, Hefei, China, [2]School of Resources and Environmental Engineering, Anhui University, Hefei, China, [3]School of Resources and Environmental Engineering, Hefei University of Technology, Hefei, China

In recent years, many research methods have been developed for the traceability of groundwater contamination source, in which the numerical simulation and analytical methods are the most common methods to study on groundwater flow and solute transport. However, the establishment and solution of an optimization model is a very complex inverse problem. Given that many decision variables are needed to be identified, two relatively simple analytical and numerical methods are applied for the prediction of chloride migration range and duration process in source area, then the geophysical prospecting and drilling sampling analysis are also used for the verification, moreover, the source center is determined based on the difference between predicted results and measured results. In addition, the influence of the observation points layout, hydrodynamic dispersion parameters and groundwater flow rate on the traceability effect are also analyzed. The results show that located observation points can reflect the chloride distribution accurately, hydrodynamic dispersion parameters and groundwater flow rate have more significant impacts on the traceability effect compared with other factors. Lastly, the proposed model application process is also discussed in the limited scale site, and it provides the reference for source traceability and subsequent remediation design under the similar hydrogeological conditions.

KEYWORDS

analytical solution, numerical simulation, contamination range, traceability, geophysical methods

1 Introduction

Generally, the distribution of contamination sources and the emission of contamination concentration need to be found out before the contamination is treated and remediated effectively. However, groundwater contamination has the characteristics of concealment, hysteresis and irreversibility, which makes it impossible to detect contamination sources in time after contamination occurs with continuous spreading. Therefore, tracing, locating and removing contamination sources are important steps for the site risk management. The key problem is to determine the contamination sources accurately and timely. Therefore, it is important to identify the location of groundwater contamination sources, contaminant emission concentration and development history, so as to take effective measures to cut off the contamination sources and avoid the contamination of groundwater in a wider range, furthermore, it has an important impact on the efficiency and cost of subsequent remediation (Mangold and Tsang, 1991; Bashi-Azghadi et al., 2010; Lapworth et al., 2012; Mahsa and Bithin, 2013).

Traceability of groundwater contamination is to trace the history of contaminant discharge and determine the location of contamination sources through limited observation data (Mahar and Datta, 1997; Alexander et al., 2006; Zoi and George, 2009). At present, the main methods of groundwater contamination traceability are mathematical analysis method (Gongsheng et al., 2006; Yu et al., 2012; Long et al., 2014; Gurarslan and Karahan, 2015), simulation optimization method (Ellen and Pierre, 2007; Mirghani et al., 2009; Manish and Bithin, 2013; Xiao et al., 2016; Li et al., 2017; Chakraborty and Prakash, 2020), hydrochemical traceability analysis (; Rashid et al., 2019), isotope traceability analysis (Palau et al., 2014; Sturchio et al., 2014; Nigro et al., 2017; Wang and Zhang, 2019; Zimmermann et al., 2020) and geostatistics method (Mark and Peter, 1997; Juliana and Amvrossios, 2001; Ilaria and Maria, 2003; Anna and Peter, 2004; Ilaria et al., 2012; Liu et al., 2021). The contamination factors mainly occur convection, dispersion and microbial reactions after the contaminants are released into subsurface (Jordi and Yoram, 1996). While the traceability of contamination sources can be solved as a reverse problem by combining the information of groundwater contamination plume with the law of contaminant migration (Gurarslan and Karahan, 2015), in addition, the most commonly used methods are numerical method and analytical method based on the mathematical model of contaminant migration in saturated-unsaturated porous media.

The numerical simulation of groundwater contamination is mainly to study the temporal and spatial variation of the concentration of various solutes in porous media, and predict the distribution of contaminants qualitatively or quantitatively (Song et al., 2020; Banaei et al., 2021). For example, the convection-dispersion model has a wide range of applications, which can be used for isotropic or anisotropic, homogeneous or heterogeneous porous media (Wu et al., 1997; Zhu and Liu, 2001). It can reflect the movement process of solute in groundwater comprehensively under the initial conditions and boundary conditions, and it has become a very important method to solve the problem of groundwater contamination with the continuous and rapid development of science technology. In addition, it is widely used in the field of hydrogeology with its convenient, efficient and flexible characteristics (Xue, 2010). However, the establishment of numerical model requires much higher accuracy of hydrogeological data than the analytical method, and more detailed data are needed for the model identification and verification. For example, the number of monitoring wells in the field investigation stage is relatively small in the internal area of chemical plants which facilities have been completed, thus, it is often not desirable to drill new monitoring wells, therefore, the analytical method is still widely used under above conditions.

In this paper, taking the actual site as an example, mathematical models are established through the generalization of practical problems, and the analytical method is applied to trace the emission process of contamination sources, and then the location and emission process of contamination sources are inverted. In addition, the influence of observation point layout, hydrodynamic dispersion coefficient and actual velocity on the traceability results is discussed by numerical simulation.

Then, the numerical method and analytical method are used to predict the spatial range and diachronic process of chloride in contamination sources, and the results are verified by the geophysical prospecting and drilling sampling analysis, moreover, the diffusion range and diachronic process of chloride are determined based on the analysis of the difference between the predicted results and the measured results. Finally, the suitability of the analytical method in this region is discussed, indicating that the method proposed in this paper is effective, and also it provides a feasible tool for solving the problem of contamination source research in-scale sites, furthermore, it provides a feasible technically and reasonable economical method for contamination source traceability and remediation design under such hydrogeological conditions.

2 Materials and methods

2.1 Study area overview

The research site is located in the central and eastern part of Hefei, Anhui Province, China (Figure 1). In order to investigate the stratigraphic characteristics of the region, high-density resistivity method and ground penetrating radar method were used in this detection, and the hydraulic crawler multifunctional engineering investigation rig was used for drilling. The soil core samples were collected and the corresponding soil samples were obtained. According to the above survey results, the target area is mainly divided into two layers, 1) the principal component of miscellaneous fill layer is clay, surface soil plant roots are more developed and the layer thickness is about 2 m. 2) the thickness of clay layer exceeds 10 m under natural conditions.

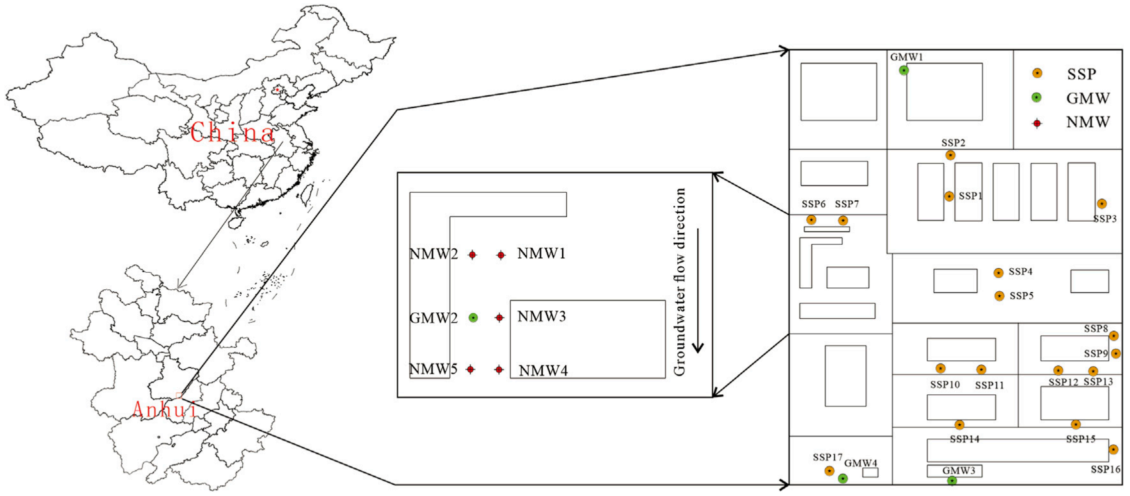

FIGURE 1
Locations of the soil sampling points and groundwater monitoring wells in the study.

2.2 Analytical method

According to the actual survey and test data, the migration trend of chloride in GMW2 monitoring point is mainly vertical migration. Therefore, the analytical solution of one-dimensional migration model is applied with constant concentration in porous media. The main conditions of the model are as follows: 1) The research domain is a semi-infinite porous medium column, and the medium is homogeneous and isotropic. 2) The flow field is uniform with constant velocity, and the actual groundwater velocity is constant. 3) There is no contaminant in the study area at the initial time. 4) The initial contaminant concentration is constant (C_0) without considering adsorption and decay. 5) Water content, seepage velocity and dispersion coefficient are constants. The selected model is as follows:

$$
(\mathrm{I})\begin{cases}
\dfrac{\partial C}{\partial t} = \dfrac{\partial}{\partial z}\left(D_z \dfrac{\partial C}{\partial z}\right) - v_z \dfrac{\partial C}{\partial z} & (0 < z < +\infty, t > 0) \quad (1) \\
C(z,t)|_{t=0} = 0 & (z > 0) \quad (2) \\
C(z,t)|_{z=0} = c_0 & (t > 0) \quad (3) \\
C(z,t)|_{z=\infty} = 0 & (t > 0) \quad (4)
\end{cases}
$$

For the selected mathematical model (I), where C (mg/L) is pollutant concentration, C_0 (mg/L) is continuous point source concentration under Dirichlet boundary condition, D_z (m^2/d) is vertical dispersion coefficient, v_z (m/d) is vertical seepage velocity, z (m) is vertical transport distance.

The analytical solution of the above model by Laplace transform is:

$$
C = \frac{C_0}{2} erfc\left(\frac{z - v_z t}{2\sqrt{D_z t}}\right) + \frac{C_0}{2}\exp\left(\frac{v_z z}{D_z}\right) erfc\left(\frac{z + v_z t}{2\sqrt{D_z t}}\right) \tag{5}
$$

where, erfc ( ) is a residual error function. For formula (5), the larger the distance between the calculated point and the boundary, the smaller the error of the second item at the right end (Chen et al., 2016; Shi et al., 2018), when the contribution of the second item is ignored, formula (5) is changed as,

$$
C = \frac{C_0}{2} erfc\left(\frac{z - v_z t}{2\sqrt{D_z t}}\right) \tag{6}
$$

For contaminant risk screening criteria or detection criteria λ, let $Cs\ (z_j, t_j) = \lambda C_0$, u is set as,

$$
u = \frac{z - v_z t}{2\sqrt{D_z t}} \tag{7}
$$

In addition, erfc (u) is a monotonically decreasing function. According to formulas, it can be determined that the smaller the u value is, the larger the λ becomes, which reflects the role of erfc(u) function.

By formula (7), the traceability of contamination sources can be solved as a reverse problem,

$$
z_{tj} = 2u\sqrt{D_z t_j} + v_z t_j \tag{8}
$$

where, z_{tj} is defined as the maximum vertical migration depth corresponding to the migration time t_j. In practical problems, t_j can be used as the survival time of the contamination source. For any standard λ, the contamination source is not detected beyond the area, when the migration distance satisfy $z > z_{tj}$.

2.3 Numerical method

The scope of the simulation area is mainly determined according to the hydrogeological conditions and the groundwater flow field. Taking GMW2 as the center, the model is set around the fixed head boundary, the east-west boundary is basically perpendicular to the contour line, and the north-south boundary is roughly horizontal with the contour line (Figure 1). In addition, the model is generalized to two layers. The first layer is miscellaneous fill and the thickness is 2 m. The second layer is mainly clay, and the thickness is more than 15 m, which its bottom is an impervious boundary. The vertical source-sink term is atmospheric precipitation infiltration and phreatic evaporation. The groundwater flow direction is from north to south, the water depth is about 1.5 m, and the average annual precipitation is about 1,100 mm (rainfall infiltration coefficient is 0.3).

The three-dimensional unsteady seepage mathematical model of groundwater flow can be described as in Equation (II):

$$
(\mathrm{II})\left\{\begin{array}{lll}
S_s\dfrac{\partial H}{\partial t}=\dfrac{\partial}{\partial x_i}\left(K_{ij}\dfrac{\partial H}{\partial x_j}\right)+W & (i,j=x,y,z) & (9)\\
H(x,y,z,t)\big|_{t=0}=H_0(x,y,z) & (x,y,z)\in\Omega & (10)\\
H(x,y,z,t)\big|_{\Gamma_1}=H_1(x,y,z,t) & (x,y,z)\in\Gamma_1,t>0 & (11)\\
K_{ij}\dfrac{\partial H}{\partial n}\bigg|_{\Gamma_2}=q(x,y,z,t) & (x,y,z)\in\Gamma_2,t>0 & (12)
\end{array}\right.
$$

where, H (m) is the groundwater head, H_0 (m) is the initial head, H_1 (m) is the head of the first boundary Γ_1, q is the flow of the second boundary Γ_2, S_s (1/m) is the water storage rate, W is the source and sink term, Ω is the research domain, K_{ij} (m/d) is the permeability coefficient tensor, n is the outer normal direction of the boundary Γ_2.

The three-dimensional mathematical model of solute transport without considering adsorption and attenuation can be described as in Equation (III):

$$
(\mathrm{III})\left\{\begin{array}{lll}
R\theta\dfrac{\partial C}{\partial t}=\dfrac{\partial}{\partial x_i}\left(\theta D_{ij}\dfrac{\partial C}{\partial x_j}\right)-\dfrac{\partial(\theta v_i C)}{\partial x_i}+I & (i,j=x,y,z) & (13)\\
C(x,y,z,t)\big|_{t=0}=C_0(x,y,z) & (x,y,z)\in\Omega & (14)\\
C(x,y,z,t)\big|_{\Gamma_1}=C_1(x,y,z,t) & (x,y,z)\in\Gamma_1,t>0 & (15)\\
\theta D_{ij}\dfrac{\partial C}{\partial n}\bigg|_{\Gamma_2}=f(x,y,z,t) & (x,y,z)\in\Gamma_2,t>0 & (16)
\end{array}\right.
$$

where, C (mg/L) is the contaminant concentration, C_0 (mg/L) is the initial contaminant concentration, C_1 (mg/L) is the concentration of the first boundary Γ_1, f is the dispersion flux of the second boundary Γ_2, R is the retardation coefficient, θ is the porosity, v_i (m/d) is the actual groundwater flow rate, I is the source and sink phase, D_{ij} (m^2/d) is the dispersion coefficient tensor.

The FEMWATER module in Groundwater Modeling System (GMS) software is selected for this calculation. Hydrogeological parameters are mainly determined according to the field test and geological exploration results, the values of hydrogeological parameters of the model are shown in Table 1.

3 Results

3.1 Field investigation

According to the building layout and production process, soil sampling (SSP) and groundwater sampling (GMW) points were set in Figure 1, where GMW2 was the monitoring point of soil and groundwater. In the later period, five soil and groundwater monitoring points (NMW) were added. The above sampling results showed that only the chloride concentration in GMW2 exceeded the standard value of class III (250 mg/L) in Chinese groundwater quality standards. In order to identify the contamination status of chloride, it is necessary to study the traceability and migration range of potential contaminant source.

Magnetotelluric method is an electromagnetic technique that uses the earth's natural field to map the electrical resistivity changes in subsurface structures. The Magnetotelluric data is used to investigate the shallow to deep subsurface geoelectrical structures and their dimensions for the high penetration depth of the electromagnetic fields in this method (Filbandi Kashkouli et al., 2016). Thus, two geophysical methods of high density electrical method (DUK-2A MIS-60 system) and ground penetrating radar method (GSSI-SIR20 geological radar system TG1067) were used to verify the vertical distribution of strata, and the representative results are shown in Figures 2A,B and Figures 3A,B.

In Figures 2A,B, according to the apparent resistivity results, the depth within 1.5 m shows high resistance, and the apparent resistivity is 10–60 Ω▪m. The apparent resistivity changes widely, indicating that the soil in this layer is inferior in uniformity and contains impurities. It is speculated that this layer is a mixed fill soil layer. The depth below 1.5 m within the detection range shows low resistance, and the apparent resistivity is 5–10 Ω▪m. The variation range of apparent resistivity is relatively small, and the distribution of apparent resistivity in the layer is not obviously layered, which indicates that the soil quality of the layer is relatively uniform, and there is no obvious horizontal stratification of apparent resistivity distribution of artificial plain fill layer. It is inferred that the soil layer is a natural soil layer, and the water content of the soil layer is larger than that of the upper miscellaneous fill layer.

In Figures 3A,B, according to the radar detection results, the radar reflected wave intensity within the detection range is inferior, and the same axis is relatively continuous without obvious abnormal reflection, indicating that the stratum in the field is relatively uniform. From Figures 3A,B, it is clearly shown that the distribution depth of miscellaneous fill layer is less than 1.5 and 2.5 m, respectively, and the average depth of upper layer

TABLE 1 The value of hydrogeological parameters.

Layer	Hydraulic conductivity		Porosity	Storage rate	Dispersion coefficient	Molecular diffusivity
	K_H (m/d)	K_V (m/d)	θ	S_s (1/m)	D_z (m²/d)	D^* (m²/d)
First layer	0.17	1.7	0.42	0.010	0.0036	1.73×10^{-4}
Second layer	0.15	1.5	0.34	0.006	0.0034	

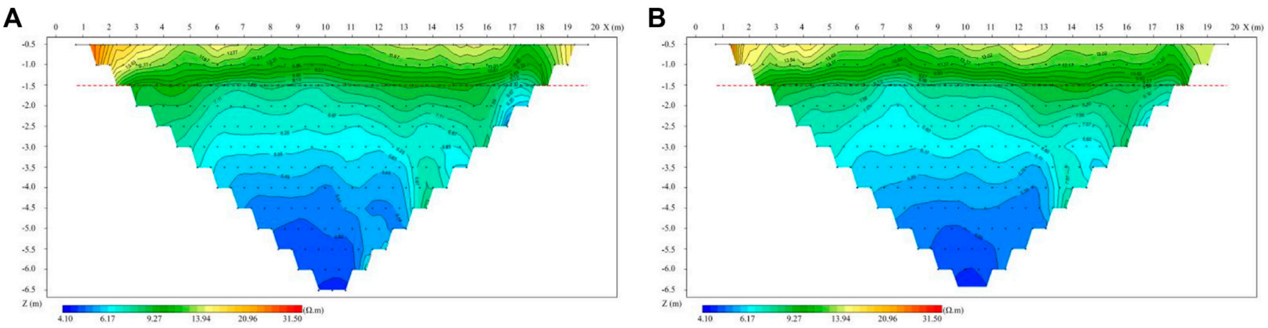

FIGURE 2
The test results of typical high density electrical method (the red dotted line represents the tested stratigraphic boundary).

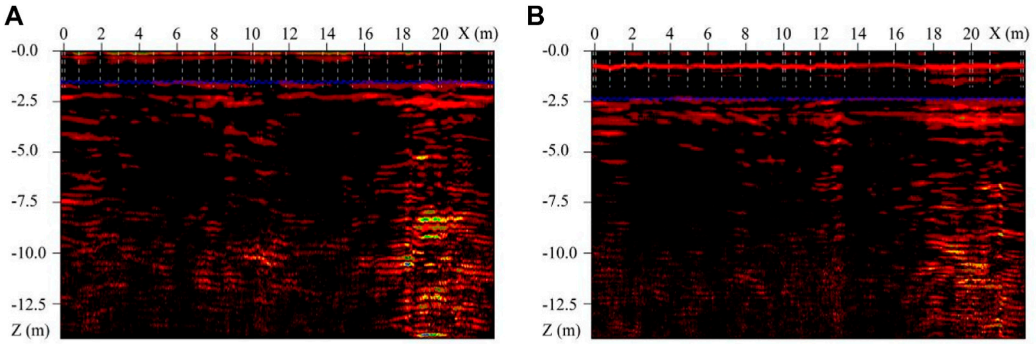

FIGURE 3
The test results of typical ground penetrating radar method (the purple dotted line represents the tested stratigraphic boundary).

is 2 m. The clay layer is distributed below the depth of 1.5 m, and the soil is uniform. It is speculated that the soil layer is natural.

According to the detection results of high density electrical method and ground penetrating radar method, it is speculated that there are miscellaneous fill soil layers and cohesive soil layers distributed from top to bottom within the detection depth of the site. 1) The distribution depth of miscellaneous filling soil layer is within 2 m, and the soil quality of this layer is inferior and contains impurities. 2) The cohesive soil layer is distributed below the depth of 2 m, and the soil quality of this layer is relatively uniform. The apparent resistivity distribution of the artificial fill layer is characterized by

FIGURE 4
Drilling site and soil core sampling process.

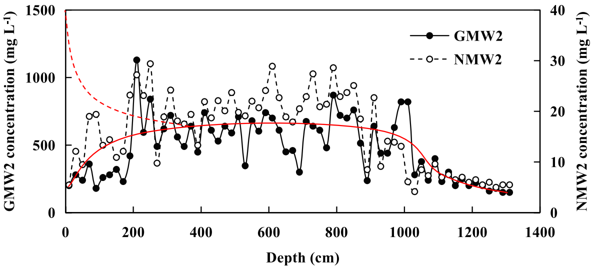

FIGURE 5
Curve diagram of measured vertical concentration change of chloride ions (the red dotted line is traceable historical contamination curve, and the red solid line is measured concentration change trend after surface disturbance).

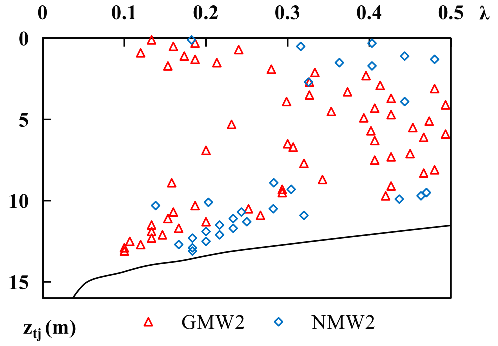

FIGURE 6
Relationship between maximum vertical migration depth (z_{tj}) and measured values of chloride ions under different detection criteria. (△) and (◇) represent the measured chloride ions depth of GMW2 and NMW2, respectively; The black solid line represents z_{tj} under different detection criteria.

obvious horizontal stratification. It is speculated that this layer is a natural soil layer, and the water content of the soil layer is larger than that of the upper miscellaneous fill layer.

The above results are based on the analysis results of high density electrical method and ground penetrating radar detection results. In addition, in order to further verify the stratigraphic characteristics, the depth of soil sampling was about 15 m in this study. The hydraulic crawler multifunctional engineering survey rig was used for drilling, the soil core was sampled and the corresponding soil samples were obtained, the process is shown in Figure 4. According to the drilling sampling analysis, the results are basically consistent with the geophysical survey results.

It can be seen from Figure 5, chloride ions content curve that the values of chloride content are mainly above 400 mg/L at GMW2 sampling point, and are basically concentrated in the range of 2–10 m. The sampling curves of GMW2 and NMW2 showed the same concentration variation trend, that is, it increased with the increase of depth in the range of 0–2 m, while it decreased with the increase of depth in the range of 2–10 m, in which NMW2 is the background sampling. The imaginary line in the diagram is a traceable historical contamination curve, and the regional construction caused the inverted triangle area in the shallow range of 0–2 m. The measured concentration of the surface layer is relatively lower due to the development of the plant's root system and microorganisms influence, in addition, the rainfall and contaminant leaching infiltrate into the surface soil after the construction disturbance.

3.2 Analytical method

In the actual site, there are six soil and groundwater monitoring points (NMW1—5 and GMW2). Due to the limitation of site scale and the monitoring results, the position of GMW2 is the center area of potential contamination sources, and vertical dispersion coefficient and vertical penetration velocity are the main parameters according to the analytical

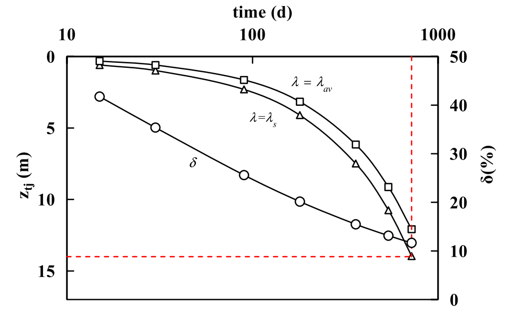

FIGURE 7
Vertical migration depth of chloride ions under different detection standards, δ is the relative deviation between λ_{av} and λ_s.

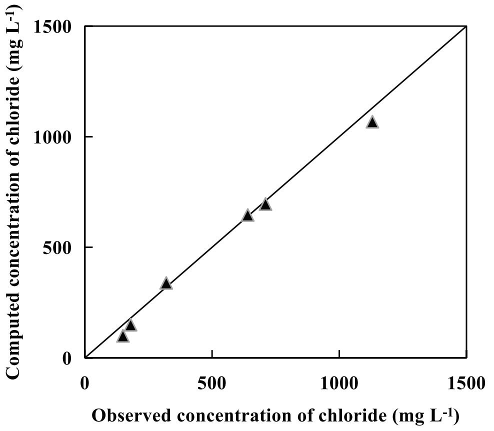

FIGURE 8
The fitting results of chloride ions measured concentration and calculated concentration.

formula (8). From the field test, the value of vertical dispersion coefficient D_z is 0.0034–0.0036 m^2/d. The value of vertical penetration velocity v_z is 0.015–0.017 m/d based on the observation data and model parameters calibration. Then, the z_{tj} of chloride is calculated by Formula (8). The calculation results are shown in Figure 6.

Figure 6 shows that the calculation results accord with the actual situation according to two groups of chloride ions vertical concentration values, and NMW2 is used as the background value for verification. The vertical dispersion coefficient D_z is 0.0035 m^2/d and the vertical penetration velocity v_z is 0.016 m/d, at this time, the source concentration value of GMW2 was about 1,500 mg/L (the measured value was 1,130 mg/L), and the z_{tj} was about 14 m after 720 days. Since the corresponding depths of all measured values were located within the z_{tj} curve of chloride ions, the calculation method proposed was effective by analytical method of z_{tj}.

In order to study the z_{tj} under different screening standards or detection standards, two typical standards were selected for comparative analysis. For example, the groundwater quality class III standard value is 250 mg/L (λ_s = 0.17) and the average chloride concentration is 600 mg/L (λ_{av} = 0.40) in the depth of 2–10 m range, and the calculation results are shown in Figure 7.

From Figure 7, the z_{tj} is about 14 m after 720 days when $\lambda_s = 0.17$, while z_{tj} is about 12 m when $\lambda_{av} = 0.40$, and the z_{tj} is larger by the former calculation standard, that is, the smaller the detection standard, the safer the calculation results. In addition, the relative deviation decreases with the extension of source longevity time. The relative deviation is about 10% when the source longevity time reaches 900 days. In addition, the red dotted line in Figure 7 represents the maximum penetration depth of chloride ions with the corresponding time in the actual site, which can reflect the comprehensive characteristics of the site. Therefore, in the practical application of the analytical method, it is necessary to clarify the screening standard or the detection standard, and then calculate the z_{tj} under different source concentrations and migration time.

3.3 Numerical method

According to the hydrogeological generalization model, the mathematical model has been adjusted and fitted to reflect the actual conditions. Since the source concentration, migration time and z_{tj} are determined by analytical method, six observation points (OBS1-6) have been added with the groundwater flow direction.

In order to meet the accuracy requirements of actual project, the simulation results are combined with the measured values, and the fitting result is shown in Figure 8.

The fitting result shows that the calculated chloride ions concentration is basically consistent with the measured value. Moreover, the plane and vertical distribution of chloride ions concentration were predicted after 720 days with GMW2 as the source center, the results are shown in Figure 9.

From the numerical simulation results (Figure 9), the influence distance of chloride ions is about 6 m along the groundwater flow direction from the source center, the lateral distance is about 4 m, and the z_{tj} is about 15 m at the end of 720 days, in this condition, the groundwater quality class III standard value is used as the detection standard. The above prediction results are consistent with the measurement results, which shows that the numerical method is basically correct and can reflect the simulation process. In addition, the sources distribution characteristics can be basically reflected by arranging observation points

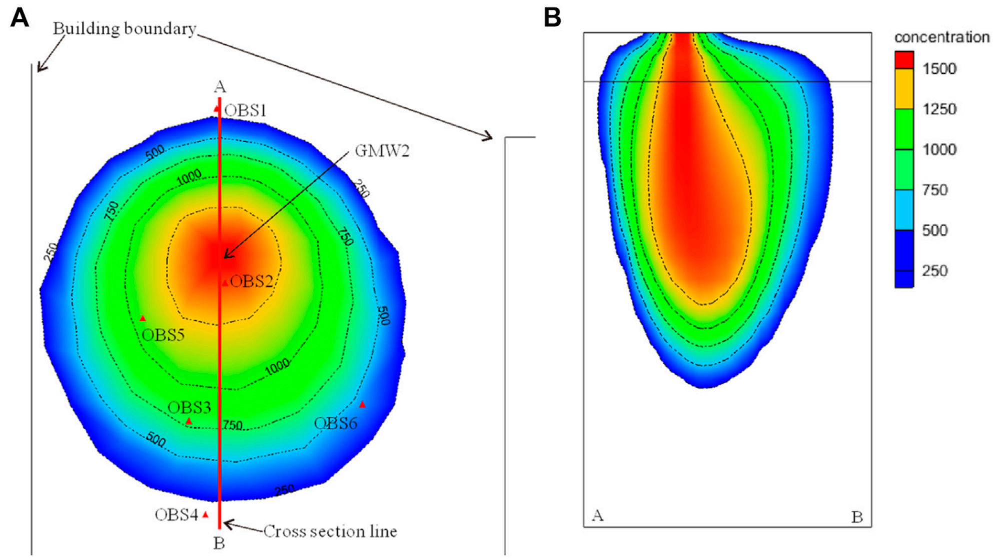

FIGURE 9
Prediction results of chloride ions concentration: **(A)** plane distribution; **(B)** vertical distribution.

upstream, downstream and laterally of groundwater flow direction, respectively.

4 Discussion

In the actual site, given that many decision variables are needed to be identified, two relatively simple methods are applied for the prediction of chloride migration range and duration process in source area, then the geophysical prospecting and drilling sampling analysis are also used for the verification, moreover, the source center is determined based on the difference between predicted results and measured results. Based on the above study, three main points are discussed as follows:

1) The influence of observation point layout on traceability position. The detailedness of the observed data is an important factor affecting the difficulty of solving the traceability problem (Mirghani et al., 2009). In practical applications, the number and location of observation points are restricted by construction site or costs. In order to design the appropriate number and location of observation points, it is necessary to analyze the influence of the number and location of observation points on the traceability effect. In this study, the observation points are arranged along the direction and vertical direction of groundwater flow, then the predicted results are verified by the specific observation points.
2) The influence of model parameters on traceability effect. The hydrodynamic dispersion coefficient is determined by the dispersion of medium parameters, the actual water velocity and the molecular diffusion coefficient of contaminant in the medium. Although the hydrodynamic dispersion coefficient can be obtained by experimental method, which is often determined in the process of calibration of mathematical model (Zheng and Gordon, 2009; Fetter et al., 2011), moreover, the actual average velocity affects the convection and dispersion, because the corresponding measurement error and model uncertainty will be introduced into the traceability processes (Xue, 2007). Therefore, it is necessary to consider both the measured data and the model parameter adjustment method, so as to obtain better traceability results.
3) Comparative analysis of different calculation methods. The traceability problem in the analytical method is a typical inverse problem, and the small changes of important factors will cause great differences in the calculation results. While in the simulation calculation method, the accuracy generalized model can reflect the actual solute migration, and key hydrogeological parameters determined is more important in the model calculation, therefore, it is necessary to verify the results of multiple methods.

5 Conclusion

In this paper, taking the actual site as an example, the numerical, analytical and geophysical method are used to predict and study the spatial range and diachronic process of chloride ions from source area.

The main conclusions are as follows, firstly, analytical method is simple and suitable for relatively simple hydrogeological conditions. Although the calculation results basically meet the requirements of single-point source analysis, however, for the application scope of the proposed analytical method, comparative analysis and research with existing models are required, and the error size needs to be explained in the future applications. Secondly, in the process of practical application, the traceability results are greatly affected by regional factors (groundwater flow rate, dispersion coefficient, observation point layout and concentration measurement error, etc.), and the above factors often affect the accuracy of the traceability and prediction results, thus, it is necessary to further study the parameter sensitivity in the future. Finally, the combined application of analytical method and numerical method is more conducive to the study of contamination source tracing and the range simulation. The proposed method can meet the actual situation better, and provide reference for source effective control and subsequent remediation design under the similar hydrogeological conditions.

Data availability statement

The original contributions presented in the study are included in the article/supplementary material, further inquiries can be directed to the corresponding author.

Author contributions

Conceptualization, FL and HR; methodology, JY; software, FL; validation, FL and HR; formal analysis, FL and HR; investigation, FL and HR; resources, JY and BK; data curation, FL and JY; writing—original draft preparation, FL, HR, and BK.; writing—review and editing, FL, HR, and JY; supervision, YL and YT. All authors have read and agreed to the published version of the manuscript.

Funding

This research was funded by the National Key Research and Development Program of China, grant number 2018YFC1802700; the Open Research Fund Program of State Key Laboratory of Hydroscience and Engineering, Tsinghua University, grant number sklhse-2020-D-06; the National Natural Science Foundation of China, grant number 42107162; the Natural Science Foundation of Anhui Province, grant number 1908085QD168 and the Fundamental Research Funds for the Central Universities of China, grant number PA2021 KCPY0055.

Acknowledgments

The authors would like to thank the editor and reviewers for their constructive and valuable comments and suggestions, which significantly improved the quality of this work.

Conflicts of interest

The authors declare that the research was conducted in the absence of any commercial or financial relationships that could be construed as a potential conflict of interest.

Publisher's note

References

Alexander, Y. S., Scott, L. P., and Gordon, W. W. (2006). A constrained robust least squares approach for contaminant release history identification. *Water Resour. Res.* 42 (4), W4414. doi:10.1029/2005wr004312

Anna, M. M., and Peter, K. K. (2004). Application of geostatistical inverse modeling to contaminant source identification at Dover AFB, Delaware. *J. Hydraulic Res.* 42 (Suppl. 1), 9–18. doi:10.1080/00221680409500042

Banaei, S., Javid, A. H., and Hassani, A. H. (2021). Numerical simulation of groundwater contaminant transport in porous media. *Int. J. Environ. Sci. Technol. (Tehran).* 18 (1), 151–162. doi:10.1007/s13762-020-02825-7

Bashi-Azghadi, S. N., Kerachian, R., Bazargan-Lari, M. R., and Solouki, K. (2010). Characterizing an unknown pollution source in groundwater resources systems using PSVM and PNN. *Expert Syst. Appl.* 37 (10), 7154–7161. doi:10.1016/j.eswa.2010.04.019

Chakraborty, A., and Prakash, O. (2020). Identification of clandestine groundwater pollution sources using heuristics optimization algorithms: A comparison between simulated annealing and particle swarm optimization. *Environ. Monit. Assess.* 192 (12), 791–819. doi:10.1007/s10661-020-08691-7

Chen, Y. M., Xie, H. J., and Zhang, C. H. (2016). Review on penetration of barriers by contaminants and technologies for groundwater and soil contamination control. *Adv. Sci. Technol. Water Resour.* 36 (01), 1–10.

Ellen, M., and Pierre, P. (2007). Simultaneous identification of a single pollution point-source location and contamination time under known flow field conditions. *Adv. Water Resour.* 30 (12), 2439–2446. doi:10.1016/j.advwatres.2007.05.013

Fetter, C. W., Fei, T., Zhou, N. Q., et al. (2011). *Contaminant hydrogeology*. Beijing, China: Higher Education Press.

Filbandi Kashkouli, M., Kamkar Rouhani, A., Moradzadeh, A., et al. (2016). Dimensionality analysis of subsurface structures in magnetotellurics using different methods (a case study: Oil field in southwest of Iran). *J. Min. Environ.* 7 (1), 119–126.

Gongsheng, L., Tan, Y. J., Cheng, J., and Wang, X. Q. (2006). Determining magnitude of groundwater pollution sources by data compatibility analysis. *Inverse Problems Sci. Eng.* 14 (3), 287–300. doi:10.1080/17415970500485153,

Gurarslan, G., and Karahan, H. (2015). Solving inverse problems of groundwater-pollution-source identification using a differential evolution algorithm. *Hydrogeol. J.* 23 (6), 1109–1119. doi:10.1007/s10040-015-1256-z

Ilaria, B., and Maria, G. T. (2003). A geostatistical approach to recover the release history of groundwater pollutants. *Water Resour. Res.* 39 (12), 1372. doi:10.1029/2003wr002314

Ilaria, B., Maria, G. T., and Andrea, Z. (2012). Simultaneous identification of the pollutant release history and the source location in groundwater by means of a geostatistical approach. *Stoch. Environ. Res. Risk Assess.* 27 (5), 1269–1280. doi:10.1007/s00477-012-0662-1

Jordi, G., and Yoram, C. (1996). Contaminant migration in the unsaturated soil zone: The effect of rainfall and evapotranspiration. *J. Contam. Hydrology* 23 (3), 185–211. doi:10.1016/0169-7722(95)00086-0

Juliana, A., and Amvrossios, C. B. (2001). State of the art report on mathematical methods for groundwater pollution source identification. *Environ. Forensics* 2 (3), 205–214. doi:10.1006/enfo.2001.0055

Lapworth, D. J., Baran, N., Stuart, M. E., and Ward, R. (2012). Emerging organic contaminants in groundwater: A review of sources, fate and occurrence. *Environ. Pollut.* 163 (Apr), 287–303. doi:10.1016/j.envpol.2011.12.034

Li, J. L., Long, Y. Q., and Wu, C. Y. (2017). A groundwater pollution source identification method based on the simple genetic algorithm. *Adv. Environ. Prot.* 7 (01), 35–40. doi:10.12677/aep.2017.71005

Liu, J. B., Jiang, S. M., Zhou, N. Q., et al. (2021). Groundwater contaminant source identification based on QS-ILUES. *J. Groundw. Sci. Eng.* 9 (1), 73–82. doi:10.19637/j.cnki.2305-7068.2021.01.007

Long, Y. Q., Wu, C. Y., and Wang, J. P. (2014). The influence of estimated pollution range on the groundwater pollution source identification method based on the simple genetic algorithm. *Appl. Mech. Mater.* 3308, 836–841. doi:10.4028/www.scientific.net/amm.587-589.836

Mahar, P. S., and Datta, B. (1997). Optimal monitoring network and groundwater-pollution source identification. *J. Water Resour. Plan. Manag.* 123 (4), 199–207. doi:10.1061/(asce)0733-9496(1997)123:4(199)

Mahsa, A., and Bithin, D. (2013). Identification of contaminant source characteristics and monitoring network design in groundwater aquifers: An overview. *J. Environ. Prot. (Irvine, Calif.* 4 (5A), 26–41. doi:10.4236/jep.2013.45a004

Mangold, D. C., and Tsang, C. F. (1991). A summary of subsurface hydrological and hydrochemical models. *Rev. Geophys.* 29 (1), 51–79. doi:10.1029/90rg01715

Manish, J., and Bithin, D. (2013). Three-dimensional groundwater contamination source identification using adaptive simulated annealing. *J. Hydrol. Eng.* 18 (3), 307–317. doi:10.1061/(asce)he.1943-5584.0000624

Mark, F. S., and Peter, K. K. (1997). A geostatistical approach to contaminant source identification. *Water Resour. Res.* 33 (4), 537–546. doi:10.1029/96wr03753

Mirghani, B. Y., Mahinthakumar, K. G., Tryby, M. E., Ranjithan, R. S., and Zechman, E. M. (2009). A parallel evolutionary strategy based simulation–optimization approach for solving groundwater source identification problems. *Adv. Water Resour.* 32 (9), 1373–1385. doi:10.1016/j.advwatres.2009.06.001

Nigro, A., Sappa, G., and Barbieri, M. (2017). Application of boron and tritium isotopes for tracing landfill contamination in groundwater. *J. Geochem. Explor.* 172, 101–108. doi:10.1016/j.gexplo.2016.10.011

Palau, J., Marchesi, M., Chambon, J. C., Aravena, R., Canals, A., Binning, P. J., et al. (2014). Multi-isotope (carbon and chlorine) analysis for fingerprinting and site characterization at a fractured bedrock aquifer contaminated by chlorinated ethenes. *Sci. total Environ.* 475, 61–70. doi:10.1016/j.scitotenv.2013.12.059

Rashid, A., Khattak, S. A., Ali, L., Zaib, M., Jehan, S., Ayub, M., et al. (2019). Geochemical profile and source identification of surface and groundwater pollution of District Chitral, Northern Pakistan. *Microchem. J.* 145, 1058–1065. doi:10.1016/j.microc.2018.12.025

Shi, S., Wei, Z., Shengwei, W., Ng, C. W. W., Chen, Y., and Chiu, A. C. F. (2018). Leachate breakthrough mechanism and key pollutant indicator of municipal solid waste landfill barrier systems: Centrifuge and numerical modeling approach. *Sci. Total Environ.* 612, 1123–1131. doi:10.1016/j.scitotenv.2017.08.185

Song, K., Ren, X., Mohamed, A. K., Liu, J., and Wang, F. (2020). Research on drinking-groundwater source safety management based on numerical simulation. *Sci. Rep.* 10 (1), 15481–15517. doi:10.1038/s41598-020-72520-7

Sturchio, N. C., Beloso, A., Jr, Heraty, L. J., Wheatcraft, S., and Schumer, R. (2014). Isotopic tracing of perchlorate sources in groundwater from Pomona, California. *Appl. Geochem.* 43, 80–87. doi:10.1016/j.apgeochem.2014.01.012

Subba Rao, N. (2006). Seasonal variation of groundwater quality in a part of Guntur District, Andhra Pradesh, India. *Environ. Geol.* 49 (3), 413–429. doi:10.1007/s00254-005-0089-9

Wang, H., and Zhang, Q. (2019). Research advances in identifying sulfate contamination sources of water environment by using stable isotopes. *Int. J. Environ. Res. Public Health* 16, 1914. doi:10.3390/ijerph16111914

Wu, J. C., Xue, Y. Q., Zhang, Z. H., et al. (1997). Numerical simulation of groundwater pollution in Taiyuan basin. *J. Nanjing Univ. Nat. Sci.* 33 (3), 70–79.

Xiao, C. N., Lu, W. X., Zhao, Y., et al. (2016). Optimization method of identification of groundwater pollution sources based on radial basis function model. *China Environ. Sci.* 36 (7), 2067–2072.

Xue, Y. Q. (2007). *Groundwater numerical simulation*. Beijing, China: Science Press.

Xue, Y. Q. (2010). Present situation and prospect of groundwater numerical simulation in China. *Geol. J. China Univ.* 16 (01), 1–6.

Yu, Q. L., Wei, L., and Ju, H. (2012). Advance of optimization methods for identifing groundwater pollution source porperties. *Appl. Mech. Mater.* 1802, 603–608. doi:10.4028/www.scientific.net/amm.178-181.603

Zheng, C. M., and Gordon, G. B. (2009). *Applied contaminant transport modeling*. Beijing, China: Higher Education Press.

Zhu, X. Y., and Liu, J. L. (2001). *Numerical study of contaminants transport in fracture-karst water in Dawu well field, Zibo city, Shandong province. Earth Science Frontiers*. Beijing: China University of Geosciences, 171–178.01

Zimmermann, J., Halloran, L. J., and Hunkeler, D. (2020). Tracking chlorinated contaminants in the subsurface using compound-specific chlorine isotope analysis: A review of principles, current challenges and applications. *Chemosphere* 244, 125476. doi:10.1016/j.chemosphere.2019.125476

Zoi, D., and George, F. P. (2009). Optimal search strategy for the definition of a DNAPL source. *J. Hydrology* 376 (3), 542–556. doi:10.1016/j.jhydrol.2009.07.062

frontiers | Frontiers in Environmental Science

TYPE Original Research
PUBLISHED 03 October 2022
DOI 10.3389/fenvs.2022.1005290

EDITED BY
Zifu Li,
University of Science and Technology Beijing, China

REVIEWED BY
Wenbing Tan,
Chinese Research Academy of Environmental Sciences, China
Zhihua Xiao,
Hunan Agricultural University, China

*CORRESPONDENCE
Tao Zhang,
taozhang@cau.edu.cn

SPECIALTY SECTION
This article was submitted to Water and Wastewater Management, a section of the journal Frontiers in Environmental Science

RECEIVED 28 July 2022
ACCEPTED 16 September 2022
PUBLISHED 03 October 2022

CITATION
Xie S, Zhang T, Mishra A, Tiwari A and Bolan NS (2022), Assessment of catalytic thermal hydrolysis of swine manure slurry as liquid fertilizer: Insights into nutrients and metals.
Front. Environ. Sci. 10:1005290.
doi: 10.3389/fenvs.2022.1005290

Assessment of catalytic thermal hydrolysis of swine manure slurry as liquid fertilizer: Insights into nutrients and metals

Shiyu Xie[1], Tao Zhang[1]*, Anshuman Mishra[2], Ashutosh Tiwari[2] and Nanthi S. Bolan[3,4]

[1]Beijing Key Laboratory of Farmland Soil Pollution Prevention and Remediation, Key Laboratory of Plant-Soil Interactions of Ministry of Education, College of Resources and Environmental Sciences, China Agricultural University, Beijing, China, [2]Institute of Advanced Materials, IAAM, Ulrika, Sweden, [3]School of Agriculture and Environment, The University of Western Australia, Perth, WA, Australia, [4]The UWA Institute of Agriculture, The University of Western Australia, Perth, WA, Australia

The recovery of nutrients from livestock manure has generated a lot of interest in biosolids value-adding. There is now more research on manure with high solids content but less study on manure with lower solids content. This study used swine manure slurry as the research object and comprehensively examined the characteristics of organic matter conversion, nitrogen, phosphorus, and metals release during the catalytic-thermal hydrolysis (TH) process. It was found that ammonia nitrogen showed a continuous increase with increasing temperature while inorganic phosphorus showed a rising and then decreasing trend. The addition of HCl and H_2O_2 (TH-HCl-H_2O_2) promoted the hydrolysis of organic matter, showing the best nitrogen and phosphorus release performance, releasing 62.2% of inorganic phosphorus and 50.8% of nitrogen. The release characteristics of nutrients and metals from the TH process were significantly affected by the addition of HCl and H_2O_2, according to structural equation modelling study. The data analysis demonstrated that the liquid fertilizer produced by TH did not surpass the environmental risk associated with nutrients or the ecological risk associated with heavy metals. This study would offer theoretical justification for biowaste conversion for agricultural applications.

KEYWORDS

swine manure slurry, thermal hydrolysis, catalytic, nutrients, metals

1 Introduction

Resource shortage has become an inevitable common problem for human beings in the current era of rapid population, economic and technical growth (Zhang et al., 2020a). Nitrogen and phosphorus, as nutritional resources, are essential elements for the life activities of living organisms. Among them, phosphorus is a non-renewable resource, phosphate resources may be depleted in the coming decades with the increase in consumption (Karunanithi et al., 2015). With the development of scale and intensification of livestock and poultry farming, a huge number of livestock and poultry manure is produced (Bolan et al., 2010; Pan and Chen, 2021). China's swine production accounts for 50% of the world, and China produces 3.8 billion tons of swine manure every year (Song et al., 2020), which have high nitrogen and phosphorus contents and can pose a threat to the environment and lead to eutrophication of water bodies (He et al., 2021). Therefore, the recovery of nitrogen and phosphorus from swine manure is of great significance for environmental pollution control and nutrient recycling.

The main conversion processes used today to treat livestock manure are biological and thermochemical. Biological conversion is based on aerobic composting and anaerobic digestion (Khatun et al., 2020; Zheng et al., 2022), but the composting cycle is long, occupies a large area of land and releases large amounts of greenhouse gases (Joardar et al., 2020; Li et al., 2022). There are many thermochemical conversion methods (Wu et al., 2020), such as gasification, direct combustion, thermal hydrolysis, and liquefaction. The recovery of nitrogen and phosphorus from manure resources is currently hampered by two issues. First, it is necessary to release nitrogen and phosphorus into the supernatant to facilitate recovery, such as proteins, amino acids (Bolyard and Reinhart, 2017), DNA, phospholipids, simple phosphate monoesters and phytic acid (Ekpo et al., 2016). Moreover, a recovery method with high selectivity for nitrogen and phosphorus is required because livestock manure contains a variety of complex substances. The use of thermal conversion technology allows the recovery of large amounts of nutrient resources, deodorization and elimination of pathogens. Among them, thermal hydrolysis (TH) (Zhang et al., 2019; Zhang et al., 2020b; Zhang et al., 2020c) to recover nitrogen and phosphorus from swine manure has now become a targeted area of research.

In recent years, TH has received widespread attention in livestock manure treatment because of its direct treatment of wet waste biomass (Deng et al., 2019; Shi et al., 2018). Nevertheless, energy consumption has become a major limiting factor in the promotion and application of TH technology. According to some studies, adding chemicals like acids, bases, or oxidants (H_2O_2) can effectively reduce energy consumption by facilitating the release and conversion of nitrogen and phosphorus (Ding et al., 2021; Xu et al., 2021; Zhang et al., 2020d). Previous studies have confirmed that HCl-assisted degradation (Zhang et al., 2020d) as well as H_2O_2-assisted oxidation (He et al., 2022; Zhang et al., 2020a) can catalyze the TH process to improve the release of nitrogen and phosphorus in the liquid phase and reduce energy consumption.

In addition, liquid fertilizer is an economical, environmentally-friendly and efficient fertilizer. Liquid fertilizer has the characteristics of low production cost, pollution-free production process, convenient application, high fertilizer efficiency and easy absorption and utilization by plants (Lu et al., 2021). It is well known that three main plant nutrients used for soil fertilization are nitrogen, phosphorus, and potassium. Furthermore, nitrogen and phosphorus can now be used as liquid organic fertilizer because TH treatment has been shown to increase their solubility in the liquid phase. Studies have demonstrated the fertilizer potential of hydrolysis liquor produced from thermal hydrolysis of food waste (Gao et al., 2021). Therefore, with the improvement of production technology, liquid fertilizer has broad development and application prospects.

TABLE 1 Physical and chemical properties of swine manure.

Items	Value (%)
Moisture content	3.23 ± 0.8
Organic dry matter	41.8 ± 0.2
TP	2.59 ± 0.05
TN	2.63 ± 0.03
C	42.2
H	5.93
S	0.88
Al	0.05
Ca	1.80
Mg	1.04
Fe	0.27
Cu	0.02
Cr	0.01
Zn	0.08

Our hypothesis is that the addition of chemicals to the TH process for catalytic oxidation may enhance the efficiency of nitrogen and phosphorus release in manure slurries. We used a combination of geochemical, and integrated spectroscopic and microscopic approaches to verify our hypothesis and ultimately provide an understanding of the fundamental mechanisms that control the nitrogen and phosphorus recovered by TH processes. In this study, the TH processes was used to optimize the nutrient and metal release transformation processes by varying temperature and adding chemicals. The structural equation modelling was used to study the effects of temperature and chemicals on the release of nitrogen, phosphorus, and metals. Finally, environmental risk analyses were performed to evaluate the ecological risk of nutrients and metals. These investigations can provide new insights into the optimization of TH processes and the use of liquid fertilizers in crop production.

2 Materials and methods

2.1 Materials

Swine manure was collected from a swine farm in the suburb of Beijing. The samples were dried, ground, sieved through

40 mesh and sealed in a dry place for later use. The physical and chemical properties of swine manure are shown in Table 1.

2.2 Methods

12.0 g of dried swine manure was accurately weighed in a high-pressure reaction kettle, and 200 ml of deionized water was added to prepare swine manure slurry with a solids content of 6%. The transformation of swine manure in liquid phase during TH processes is studied under different HCl concentrations, H_2O_2 concentrations, and temperatures.

2.2.1 Thermal hydrolysis (TH) process

Prepared samples with a solids content of 6%, fixed HCl (2.5 M) addition ratio of 5%, and set corresponding seven reaction temperature gradients, i.e., 60°C, 80°C, 100°C, 120°C, 140°C, 160°C, 180°C, reaction time of 0.5 h after reaching the corresponding temperature and rotation speed of 400 rpm. Configured the sample with a solids content of 6%, fixed reaction temperature of 140°C, no H_2O_2, 0%–13% volume fraction of HCl (2.5 M), reaction time of 0.5 h after reaching the corresponding temperature, and rotation speed of 400 rpm. Samples with a solids content of 6% were prepared, the fixed reaction temperature was 140°C, HCl (2.5 M) addition ratio was 5%, H_2O_2 (30%) with a volume fraction of 0%–13% were added respectively reaction time was set to 0.5 h after reaching the corresponding temperature, and the rotation speed was set to 400 rpm. After a batch of experiments was finished, the samples were uniformly filtered and the supernatant was taken for subsequent analysis.

2.2.2 Chemical analysis

The total nitrogen and ammonia nitrogen content were determined according to the Kjeldahl method and Naxalite reagent spectrophotometry, respectively (Mahimairaja et al., 1990). The analysis for total phosphorus and inorganic phosphorus concentration was referred to the molybdenum-antimony anti-spectrophotometry (Murphy and Riley, 1962). Metal ions were analyzed by ICP-OES after digestion in Aqua Regia (3: 1 HCl/HNO_3).

2.2.3 The fluorescence excitation-emission, EEM spectral analysis

Swine manure water samples were analyzed by three-dimensional fluorescence (EEM, F-7000, Hitachi, Japan) spectroscopy. All the analyzed samples were diluted 125 times. The actual measurement wavelength ranges Ex and Em were 200–700 nm and 200–600 nm, respectively, scanning interval was 10 nm, scanning speed was 12,000 nm/min, slit width was 5 nm, scanning voltage was 600 V, and blank water samples were ultrapure water. The fluorescence region integration method (FRI), proposed by (Chen et al., 2003), can be used to qualitatively analyze the fluorescence spectrum of water. The three-dimensional fluorescence spectrum data formed by emission and excitation wavelengths are divided into five regions, representing five different types of organic substances, including aromatic protein I, aromatic protein II, fulvic acid, soluble microbial metabolites, and humic acid.

2.2.4 Input electrical energy calculation

The thermal hydrolysis process of dissolving swine manure organic matter to release nutrients requires energy consumption, and the electrical energy (EE/O) consumed by each process can be used to calculate the energy consumption in the TH process. The total EE/O includes the sum of the electrical energy of the TH process (EE/O_{TH}) and the electrical energy consumed by the catalyst ($EE/O_{Catalyst}$). The equations were modified as follows (Guo et al., 2018).

$$EE/O = EE/O_{TH} + EE/O_{Catalyst}\,(KW\,h\,m^{-3}) \tag{1}$$

$$EE/O_{TH} = \frac{CM\Delta T/3600 \times 1000}{V \times -\log(N/N_0)}\,(KW\,h\,m^{-3}) \tag{2}$$

$$EE/O_{Catalyst} = Eq_{Catalyst} \times \frac{C_{Catalyst} \times 1000}{-\log(N/N_0)}\,(KW\,h\,m^{-3}) \tag{3}$$

where C is the specific heat capacity of the liquid ($4.2\ KJ\ kg^{-1}{}^{\circ}C^{-1}$), M is the mass of the liquid (kg), ΔT is the change in temperature of the TH system (°C), V(L) is the total volume of the system, (N/N_0) is the percentage solubility of the nutrient P or N, $C_{Catalyst}$ (M) is the concentration of the catalyst, and $Eq_{Catalyst}$ is the equivalent electrical energy consumption per mole of catalyst produced. More detailed information is provided in Supplementary Appendix Section 2.2.4.

2.2.5 Environmental risk evaluation

The environmental risk evaluation method for fertilizers was designed and optimized by the environmental risk assessment method for heavy metal pollution proposed by Hakanson (1980). The model designed by Lars Hakanson produces a composite environmental risk index that is a positive number greater than 1. The larger the value, the higher the risk level, and there is no upper limit, so it is not easy to compare the environmental risk of pollution of different types of ions. In contrast, the environmental risk index model (Cai et al., 2018) used in this work has a value between 0 and 1, with upper and lower limits of the risk level, which facilitates the understanding and comparison of the risk level. The environmental risk index values are calculated using the following calculation equations:

$$R_t = \sum_{i=1}^{n} q_i R_i \tag{4}$$

$$R_i = \left(\frac{F_i}{F_i + mT_i}\right)^{2u_i} \tag{5}$$

where R_t is the total index of environmental risk index of fertilizer; R_i represents the environmental risk index of

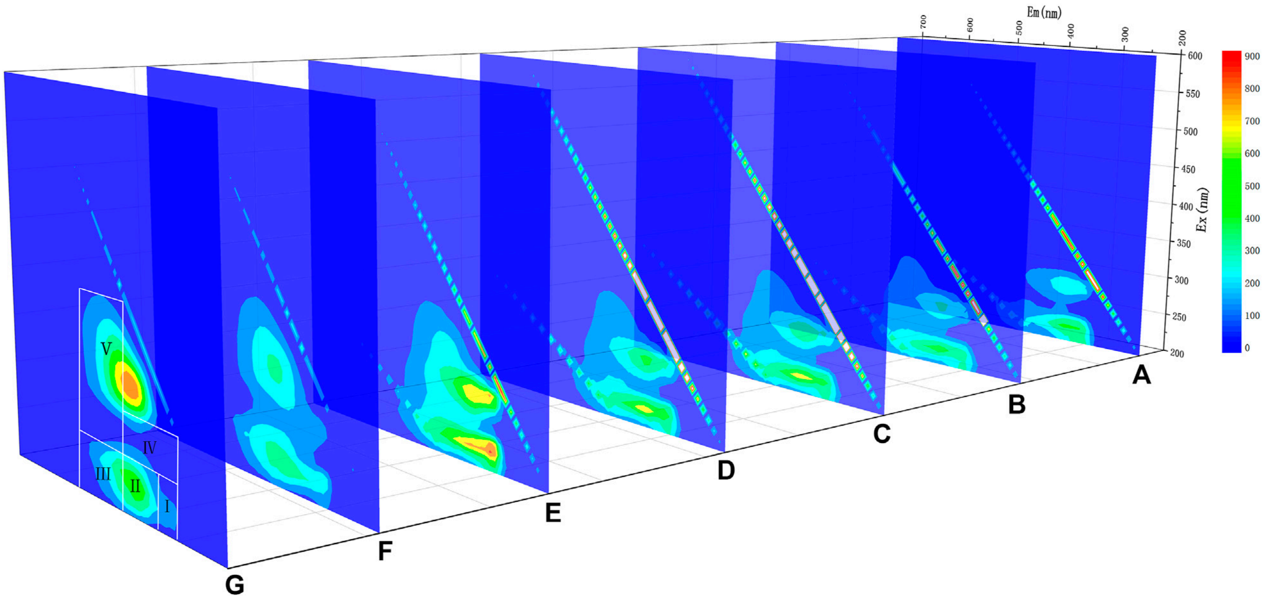

FIGURE 1
3D-EEM analysis in TH systems at different temperatures [**(A)** 60°C; **(B)** 80°C; **(C)** 100°C; **(D)** 120°C; **(E)** 140°C; **(F)** 160°C; **(G)** 180°C].

nitrogen and phosphorus, (i = N, P); q_i is the weighting coefficient of environmental pollution of nitrogen and phosphorus. T_i is the safety threshold of nitrogen and phosphorus fertilizer application. F_i is the intensity of nitrogen and phosphorus fertilizer use in a certain year, which is the actual fertilizer used in agricultural production in that year. u_i represents the fertilizer utilization efficiency (50%) and m represents the replanting index (1). From Eqs 4, 5, we can see that R_i and R_t are between 1 and 0. When $R_i = 0.5$, F_i and T_i are equal, which is the critical point for environmental safety. In this study, the fertilizer use intensity of 250 kg ha^{-1} was set as the environmental safety threshold, and with reference to the current nitrogen, phosphorus and potash fertilization ratio of 1:0.5:0.5 in developed countries, the environmental safety thresholds for nitrogen and phosphorus were determined to be 125, 62.5 kg ha^{-1}, respectively (Kulikowska and Gusiatin, 2015).

The potential ecological risk factor (E_r) for metals was calculated using the Eq. 6:

$$\boldsymbol{E_r = T_{ri} \times \left(\frac{C_i}{C_{ni}}\right)} \tag{6}$$

where T_{ri} is the toxic-response factor for a given metal (Zn = 1; Cr = 2; Cu = 5); C_i is the total metal concentration and C_{ni} is the threshold limit value for a given metal (Cu = 500 mg kg^{-1}, Zn = 1,200 mg kg^{-1}, Cr = 150 mg kg^{-1}) (Kulikowska and Gusiatin, 2015).

2.3 Statistical analysis

Structural equation modelling (SEM) was used to test the effects of temperature, H_2O_2 concentration and HCl concentration on total phosphorus (TP), total nitrogen (TN) and metals. SEM analysis was carried out the maximum likelihood evaluation method of AMOS 24.0 (AMOS, IBM, United States). All statistical analyses were performed with SPSS 25.0 (SPSS, IBM, United States).

3 Results and discussion

3.1 Influence of different temperature treatments on swine manure

3.1.1 3D-EEM analysis

The 3D-EEM of the manure slurry treated at different temperatures is shown in Figure 1. It can be seen that the position of fluorescence peak altered with the change of temperature. The fluorescence peaks were mainly located in the regions I, II, III, and IV under the treatment conditions with lower temperatures. With the increase of temperature, the fluorescence intensity of regions I, II and IV firstly increased and then decreased from 160°C, while the fluorescence intensity of regions III and V increased gradually, which indicates that the substance concentrations of aromatic protein I, aromatic protein II and soluble cell metabolic by-products increased first and then

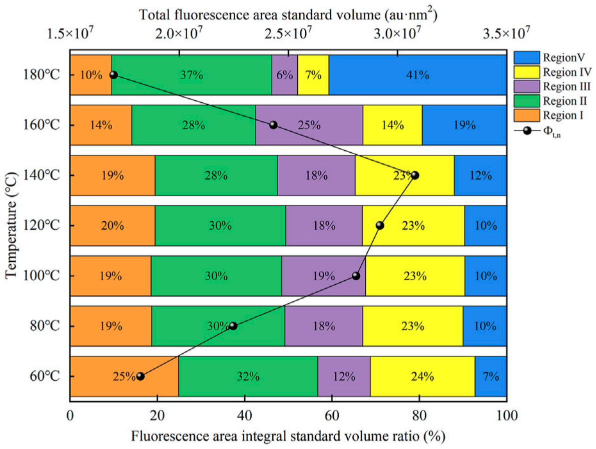

FIGURE 2
The distribution of organic matter in TH systems at different temperatures.

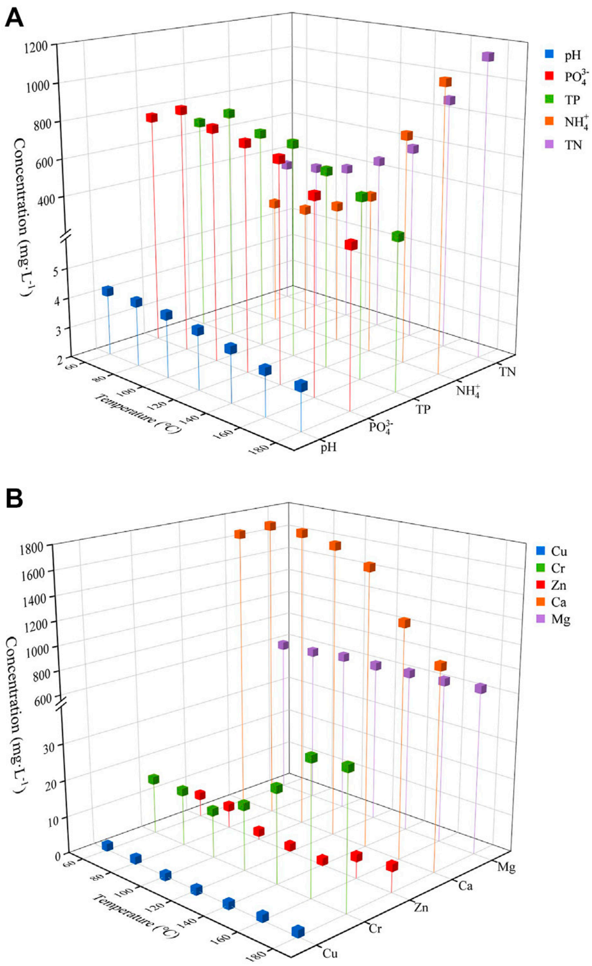

FIGURE 3
Effects of temperature on different elements [**(A)** nitrogen and phosphorus release, **(B)** metal cations].

decreased during the reaction process. Starting from 160°C, aromatic protein was degraded in large quantities, and humic acid and fulvic acid-like substances increased significantly.

The integral standard volume of fluorescence region and integral standard volume ratio of fluorescence region were estimated using FRI calculation method (Figure 2). Through the analysis, the integral standard volumes $\varnothing_{t,n}$ of the total fluorescence region can be obtained, showing a trend of increasing first and then decreasing, which indicates that the relative content of organic matters in manure slurry increases first and then decreases with the change of temperature. At the same time, the relative content of humic acid and fulvic acid-like substances increased greatly with the increase of temperature.

3.1.2 Nitrogen release

The experimental results of nitrogen release with different temperatures are shown in Figure 3A, the thermodynamic model of the release process is shown in Supplementary Appendix Section 3.1. At 60°C–140°C, the change of ammonia nitrogen with temperature is not obvious. After reaching 140°C, the concentration of ammonia nitrogen increases sharply with temperature, with a release rate of 66.4%, which is mainly due to the hydrolysis of soluble proteins in the process of hydrothermal hydrolysis, which generates polypeptides, dipeptides and amino acids. The amino acids were further decarboxylated and deaminated to produce organic acids, ammonia and carbon dioxide (Zhang et al., 2020d). Therefore, the concentration of ammonia nitrogen increases with the increase of hydrothermal hydrolysis temperature and time. From the three-dimensional fluorescence related data, it can be seen that at the temperature range of 60°C–140°C, the aromatic protein in the liquid phase increases greatly with the increase of temperature, and from 140°C–160°C, the aromatic protein in the liquid phase starts to decrease sharply. This reveals that the hydrolysis process is mainly accompanied by: 1) degradation of protein substances in solid increasing soluble protein substances in liquid phase; 2) hydrolysis of soluble organic proteins in liquid phase.

3.1.3 Phosphorus release

As shown in Figure 3A, under the influence of the change of phosphorus release with temperature, pH of manure slurry decreased slightly. This is mainly due to the continuous degradation of organic substances and formation of low molecular acids during the reaction, resulting in the decrease of pH value (Khan et al., 2021). In addition, with the increase of temperature, phosphorus concentration in the aqueous phase tended to increase first and then decrease, similar to the results of the thermodynamic model fitting (Supplementary Appendix

Section 3.1). At 80°C, the phosphorus release concentration reached a maximum, and then started to decrease, and the release rate decreased from 49.5% to 21.0%. The release of phosphorus and calcium (Ca) showed a synchronous change pattern (Figure 3B). Some studies have shown that as the temperature increases, organic phosphorus (phytate, polyphosphate, etc.) hydrolyzes to produce orthophosphate, causing the phosphate concentration in the liquid phase to increase, and as the reaction proceeds, phosphate and multivalent metal cations form precipitates, allowing phosphate to be retained in the solid phase (Deng et al., 2020). However, the pH decreased continuously during the reaction process, which inhibited the precipitation of phosphate as Ca compounds. With the increase of temperature, the proportion of humus in the solution increased continuously (Figure 2). And the abundant Ca, magnesium (Mg) and other metals in solution may react with phosphorus and facilitate the formation of humic acid (HA)- Ca-phosphorus complexes with humic acid, resulting in a simultaneous decrease of Ca and phosphorus in solution (Aragón-Briceño et al., 2021).

3.1.4 Changes in metal cations

Figure 3B shows the variation of metal cations in liquid phase with temperature change. It can be seen that with the change of temperature, the Ca concentration in solution is consistent with the changing trend of phosphorus, and Mg concentration remains constant with temperature. Heavy metals including Zn, Cu, and Cr, in the liquid phase show a regular trend of decreasing at first and then increasing, and the turning point was 100°C. The decrease of heavy metals is related to the increasing humic acid content in the solution, resulting in the complexation of metals. From the 3D fluorescence data, it can be seen that with the increase of temperature, the concentration of humic acid substances in the solution increases continuously.

Studies have shown that humic acid contains a variety of oxygen-containing functional groups, mainly in the form of carboxyl, alcoholic hydroxyl, phenolic hydroxyl, carbonyl and methoxy, which can interact with metal cations in the environment through adsorption, complexation, redox, etc. (Du et al., 2020). Studies have shown that humic acid can passivate heavy metals (Chassapis et al., 2009), and its saturated adsorption capacity for heavy metals changes with pH change. With the increase of reaction temperature, a large number of humic acids are continuously produced. Humic acid surface functional groups provide a large number of active sites, with which heavy metals are combined, thus reducing the concentration of heavy metals in solution (Bolan et al., 2011). With the further increase of temperature, the pH in the liquid phase decreases, resulting in the increased competition of H^+ with heavy metals for binding sites, thus causing heavy metals in the solution to increase.

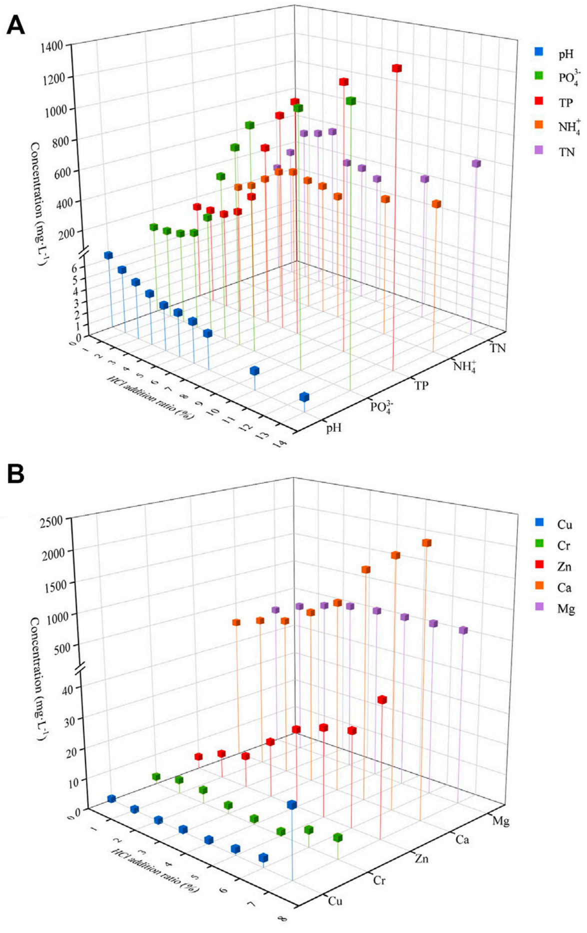

FIGURE 4
Effects of HCl addition on different elements [**(A)** nitrogen and phosphorus release, **(B)** metal cations].

3.2 Influence of different acidity treatments on swine manure

3.2.1 Nitrogen release

Figure 4A shows the results of ammonia nitrogen concentration with HCl addition. With increasing concentration of HCl addition, it can be seen that ammonia nitrogen concentration shows a trend of first rising, then falling, and then rising. The increase in ammonia nitrogen concentration in the initial rising stage is mainly due to the addition of acid which promoted the breakdown of organic particle structure of swine manure. With the rapid decrease of pH, the concentration of ammonia nitrogen began to decrease, reaching the lowest value when HCl was added at 7%, but it was still higher than that without HCl. Then the concentration of ammonia nitrogen increased with the amount of HCl added.

Analyzing the reasons for the change in ammonia concentration with increasing HCl addition, when the HCl addition is in the range of 0%–4%, the structure of organic particles in swine manure is effectively destroyed by HCl, increasing the soluble protein in the solution and promoting the hydrolysis of ammonia nitrogen. When the HCl addition is in the range of 4%–6%, the pH reached a range of 3.03–3.75. Proteins are amphoteric electrolytes, and the dissociation state and degree of protein molecules are affected by the pH value of the solution. By changing the pH value of the solution, the charge property of the solution can be altered, the double electric layer and the hydration membrane on the surface of the protein molecule can be destroyed, this will result in an increase in the intermolecular gravitation, so that the solubility of the protein decreases, causing the precipitation of protein. Pan et al. (2022) showed that the solubility of the protein in sewage sludge is the lowest at about pH 3.3. At this point, the pH value is close to the isoelectric point of the protein, which affects the dissolution of the protein, so even the released protein is precipitated in the solid, thus affecting its hydrolysis and causing the concentration of ammonia nitrogen to drop. When the HCl content is 7%–13%, the acidity of the solution is too strong, which will further promote the destruction of organic particles, and at the same time will promote the hydrolysis process of a large number of soluble proteins to amino acids and to ammonia nitrogen (Yadav et al., 2020).

3.2.2 Phosphorus release

Figure 4A shows the liquid phase phosphate concentration at different HCl additions. The inorganic phosphate release ratio was maximized at 79.6% when the addition amount (v/v%) of HCl was 13%. The phosphate content rapidly increased as HCl addition was raised from 3% to 6%, and then the rate of increase decreased until the phosphate release amount gradually reached the maximum value under our experimental condition. The trend of total phosphorus content is consistent with inorganic phosphate. It illustrated that the HCl addition had a significant influence on the phosphate release as reported by other research work (Zhang et al., 2020d).

Phosphorus in manure is mainly present as solid-phase P, as shown by the strong linear relationships between manure P content and solids content. And various phosphorus fractions in manure have remarkably different chemical characteristics. For the first stage of the phosphate release content curve, the insoluble organic phosphorus (phospholipids and phosphate monoesters) can be decomposed to PO_4^{3-}-P, which increases the concentration of PO_4^{3-}-P in the liquid phase. In the second stage, it could be surmised that when the addition amount of HCl was over 4%, the structure of the phosphorus-containing solid manure particles began to be significantly broken and dispersed. The formation of protons (H^+) by HCl increased as the HCl content continued to increase, resulting in an enhanced dissolution and degradation reaction of organic matter in the liquid phase (Wang et al., 2017). On the one hand, protons (H^+) lead to chain reactions, resulting in continuous degradation of organic phosphate (Zhang et al., 2020a). On the other hand, these protons react with inorganic chemical components of P (Ca/P, Fe/P, Al/P) to release phosphate and metal ions. The organic substances released in the liquid with the TH-HCl process, such as humic acid-like substances could react with metal ions (Ca^{2+}) to form complexes, and promote the dissolution reaction to continue.

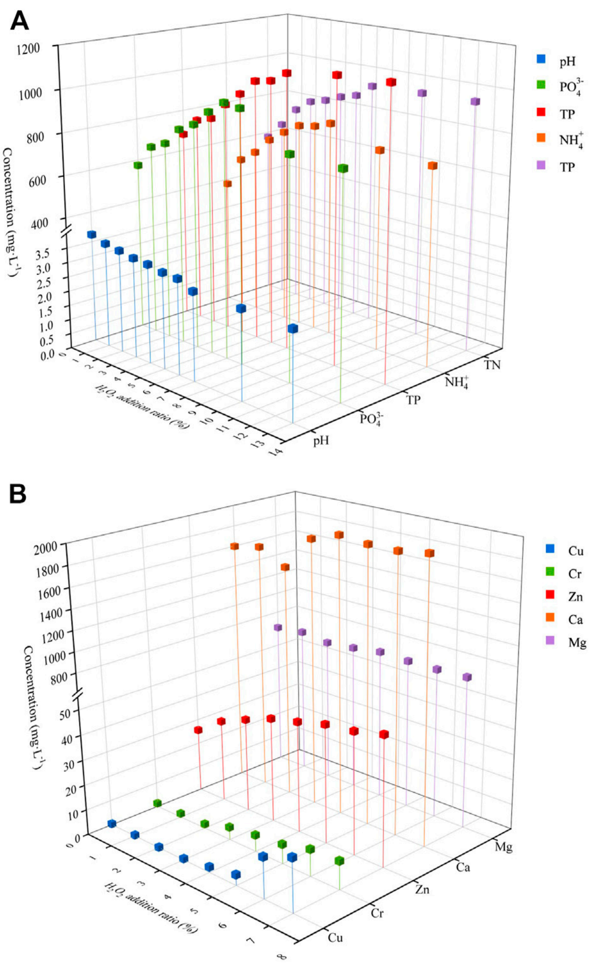

FIGURE 5
Effects of H_2O_2 addition on different elements [**(A)** nitrogen and phosphorus release, **(B)** metal cations].

3.2.3 Changes in metal cations

From the results in Figure 4B, it can be seen that the content of metal cations, Ca and Mg increased continuously with the increase of HCl addition, which on the other hand indicates that phosphorus in swine manure may form corresponding precipitates with metal cations. However, due to the increase of acidity the phosphate precipitation is likely to dissolve to release metal ions (Song et al., 2020). After the thermal reaction, it can be seen that the release of Cu, Zn, and Cr did not increase much and remained relatively constant.

3.3 Influence of H_2O_2 on the properties of swine manure

3.3.1 Nitrogen release

Figure 5B shows the change of ammonia nitrogen concentration with the addition of H_2O_2. It can be seen that the ammonia nitrogen concentration also increases first and then decreases with the concentration of hydrogen peroxide. The ammonia nitrogen concentration reaches the maximum rate of 50.8% when the H_2O_2 addition amount was 7%. Then ammonia nitrogen concentration began to decline, which shows that with the increase of H_2O_2 concentration, the organic nitrogen in the solution is continuously hydrolyzed, thus increasing the ammonia nitrogen. Compared to the TH-HCl process (Figure 4A), the addition of H_2O_2 resulted in a more than 3 times increase in the concentration of ammonia nitrogen, indicating that the chemical oxidant can further promote the conversion and dissolution of nitrogen. Then due to the increase of hydrogen peroxide concentration, it will undergo hydroxyl radical scavenging reaction, thus reducing the ammonia nitrogen concentration, as discussed further in Section 3.3.2.

3.3.2 Phosphorus release

The change of phosphorus concentration with the addition of hydrogen peroxide is depicted in Figure 5A. As can be seen, as the addition of hydrogen peroxide increased, so did the phosphorus release. When the addition amount reached 6%, the concentration of P release reached the maximum of 62.2%., and the concentration of phosphate then started to decline. The concentration of phosphate was still higher even with the addition of 13% hydrogen peroxide than in the absence of hydrogen peroxide addition.

In the process of hydrothermal hydrolysis, the organic matter is degraded mainly by the generation of free radicals (Liu et al., 2021). Adding an appropriate amount of hydrogen peroxide in the process of hydrothermal hydrolysis could significantly increase the oxidation of free radicals in the liquid phase and start a chain reaction (Eqs 4–6); As the amount of hydrogen peroxide increases, the oxidative radicals generated also have more decomposition effect on organophosphorus. When the amount of hydrogen peroxide is too much, the self-decomposition effect of hydrogen peroxide will take place, releasing ·OH, and when the amount of ·OH in the reaction system is too much, the hydroxyl radical scavenging reaction will take place (Han et al., 2022). Moreover, it has been shown that the coupling of HCl and H_2O_2 can reduce the capture of ·OH by OH- and ensure the oxidation efficiency (Zhang et al., 2020a).

$$\boldsymbol{H_2O \rightarrow \cdot H + \cdot OH} \tag{7}$$

$$\boldsymbol{\cdot OH + Organophosphorus\ compounds \rightarrow PO_4^{3-} + H_2O + CO_2} \tag{8}$$

$$\boldsymbol{\cdot H + \cdot OH \rightarrow H_2O} \tag{9}$$

$$\boldsymbol{\cdot H + \cdot H \rightarrow H_2} \tag{10}$$

$$\boldsymbol{H_2O_2 + \cdot OH \rightarrow \cdot H_2O + HO_2 \cdot} \tag{11}$$

$$\boldsymbol{HO_2 \cdot + \cdot OH \rightarrow H_2O + O_2} \tag{12}$$

3.3.3 Changes in metal cations

The concentration of metal cations increased gradually with the increase of hydrogen peroxide addition (Figure 5B). The concentration of Mg did not change with the increase of hydrogen peroxide, while Ca increased slightly with the increase of hydrogen peroxide, and the concentration of Cu did not increase at 0%–5%. When the concentration of H_2O_2 is 7%, the concentrations of Cu, Zn and Cr increased by 98.1%, 49.8% and 88.0%, respectively. This is mainly because the addition of H_2O_2 under high temperature and pressure reaction conditions generates more free radicals, which could effectively promote the oxidative decomposition of the organic particle structure of swine manure (Zhang et al., 2020d), thus releasing the heavy metals from the organic particles. In addition, with the addition of hydrogen peroxide, the organic substances in the liquid phase are continuously degraded into low molecular organic acids (Kulikowska and Gusiatin, 2015), and the pH in the liquid phase is synchronously reduced, which also promotes the release of heavy metal cations.

3.3.4 Input electrical energy

As mentioned earlier, thermal hydrolysis of swine manure can dissolve the nutrients in the liquid phase and be used as a liquid fertilizer. To be commercialized as a fertilizer product, its economic feasibility must be considered. As measured by the consumption of electrical energy per unit of phosphorus released, it was calculated that the TH process consumed more electrical energy as the temperature increased, ranging from 102.35–1462.46 KW h m^{-3}. At 140°C, the TH-HCl-H_2O_2 process consumed a total electrical energy (EE/O) of 1314.79 KW h m^{-3}, with the energy consumption followed: EE/O_{H2O2} (552.60 KW h m^{-3})>EE/O_{HCl} (387.57 KW h m^{-3}) >EE/O_{TH} (374.62 KW h m^{-3}), with the catalyst H_2O_2 consuming the largest equivalent electrical energy contribution. Previous studies have shown that the addition of alkaline reagents leads to a significant increase in the input electrical energy (Zhang et al., 2020d). At a unit price of \$0.07 for 1 KW h, the TH-HCl-H_2O_2 process costs \$92.04 to treat one ton of swine manure, which is more economical than other processes, such as the extraction of phosphorus from anaerobic sludge by the HIR sequence, which costs \$114.01 per ton of sludge treated (Vardanyan et al., 2018).

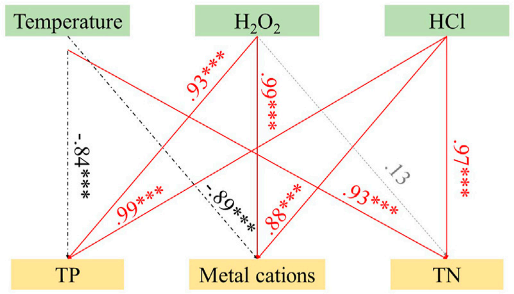

FIGURE 6
Effects of reaction conditions on nutrients and metal ions during thermal hydrolysis.

3.4 The relationship between nutrients, metals and reaction conditions

Structural equation modelling (SEM) can link multiple causal variables to form a composite system and test the hypothesis of relationships in the system (Yang et al., 2022). In this study, the effects of thermal hydrolysis temperature, H_2O_2 concentration and HCl concentration on TP, TN and metals were investigated using SEM (Figure 6). The overall goodness of fit of the model fit is indicated by the chi-square value/degree of freedom (Chi/DF = 1.501), relative fit index (NFI = 0.928), and root mean square error of approximation (RMSEA = 0.268) (Zhang et al., 2017). The continuous arrows, dashed arrows, and dot underlined arrows indicate positive significant relationship, non-significant relationship and negative significant relationship, respectively.

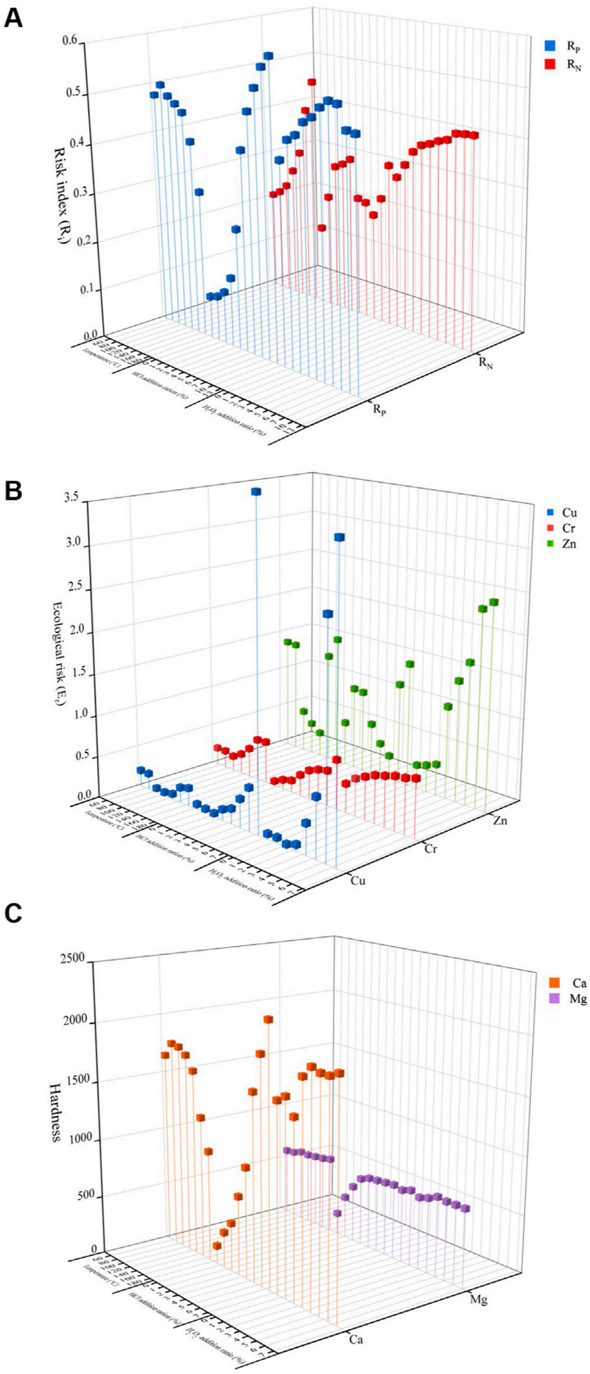

FIGURE 7
Environmental risk under different treatment conditions [**(A)** Risk index, **(B)** Ecological risk, **(C)** Hardness].

The results of structural equation modelling showed that H_2O_2 and HCl concentrations showed significant positive correlation with TP content in aqueous phase ($\lambda = 0.93$, $p < 0.001$; $\lambda = 0.99$, $p < 0.001$), which may be attributed to the decomposition of organic matter of swine manure and release phosphorus with increasing H_2O_2 and HCl concentrations (Chen et al., 2003); while temperature showed a significant negative correlation with TP in aqueous phase ($\lambda = -0.84$, $p < 0.001$), which may be attributed to the gradual transfer of phosphorus from the liquid phase to the solid phase with increasing temperature. Both the increase in temperature and HCl concentration significantly increased the release of TN ($\lambda = 0.93$, $p < 0.001$; $\lambda = 0.97$, $p < 0.001$), probably prompting the hydrolysis of soluble proteins (Zhang et al., 2020a), however, the addition of H_2O_2 had no significant effect on TN content. The influence of the thermal hydrolysis process on the content of the metals mainly results from three aspects: temperature, H_2O_2 concentration and HCl concentration, as shown in Figure 6. Temperature showed a significant negative correlation with metals ($\lambda = -0.89$, $p < 0.001$), which is attributed to the generation of a large amount of humic acid, which adsorbs metals and makes the content of the metals decrease in aqueous phase. H_2O_2 and HCl showed a significant positive correlation with metals ($\lambda = 0.99$, $p < 0.001$; $\lambda = 0.88$, $p < 0.001$), however, the processes of metals release promoted by H_2O_2 and

HCl were different. The addition of H_2O_2 may promote the deconstruction of organic substances during thermal hydrolysis (Kulikowska and Gusiatin, 2015), thus releasing metals, while the addition of HCl may make the content of the metals increase by dissolving the phosphate precipitation produced during thermal hydrolysis. Therefore, to regulate the elemental release characteristics during thermal hydrolysis, multiple influencing factors need to be considered simultaneously.

3.5 Environmental risk evaluation

The ultimate purpose of thermal hydrolysis is to dissolve the nutrients in swine manure into the liquid phase and then apply it to agricultural soil as a liquid fertilizer. To avoid excessive application of fertilizer, which may cause water and air pollution by leaching, fixation and volatilization of nutrients into the environment, it is necessary to conduct environmental risk assessment of fertilizer to accurately grasp the risk level of fertilizer application and strengthen the management of fertilizer application. The nutrients environmental risk index (R_i) and the total risk index (R_t) were calculated for different reaction conditions assuming 60 kg of swine manure to be treated for the preparation of liquid fertilizer and 100 m^2 of test soil (i.e., 6,000 kg swine manure per hectare). As seen in Figure 7A, phosphorus in liquid fertilizers generates greater environmental risk, with excess hydrochloric acid (HCl addition ratio >6%) causing phosphorus fertilizer intensity to exceed environmental thresholds and reach light risk ($R_i = 0.5$) (Hakanson, 1980).

To ensure stable and efficient crop growth and to avoid possible environmental risks, heavy metal content in fertilizers is often regulated in agriculture. The ecological risk factor (Er) of heavy metals was calculated for different temperatures, different acidity and different catalyst concentrations (Wu et al., 2021). As seen in Figure 7B, the ecological risks associated with thermal hydrolysis were mainly due to Zn and Cu. The ecological risk factor (Er) inevitably changed with the increase of temperature due to the decrease and then increase of the heavy metal content, as explained in the previous section. At the end of thermal hydrolysis, the ecological risk factors (Er) for the three treatment groups were 2.32, 5.91, and 6.66, respectively, none of which exceeded the low ecological risk threshold (<40) (Qu et al., 2020), and these values suggest that metals in liquid fertilizers after catalytic thermal hydrolysis exhibit low ecological risk and can be used as soil conditioners.

Similarly, when liquid fertilizers are applied to the soil, Mg^{2+} and Ca^{2+} may combine with CO_3^{2-} in the soil to form precipitates, thus affecting their uptake and utilization by plants and reducing their biological effectiveness (Broadley and White, 2010), therefore, attention should be paid to soil characteristics when applying liquid fertilizers. It is important to note that the risk of soil erosion may lead to an increase in water hardness due to ions entering the water body, therefore, the evaluation of the ecological risk indicator for liquid fertilizers Mg^{2+} and Ca^{2+} can be analogous to the hardness indicator for water, which in engineering practice is defined as the sum of Mg^{2+} and Ca^{2+} concentrations (Tang et al., 2021). The hardness of the liquid fertilizer was calculated for different conditions (Figure 7C), but the concentration of Mg^{2+} and Ca^{2+} decreases significantly after absorption and utilization by plants, thus reducing their environmental pollution due to the risk of loss.

4 Conclusion

Thermal hydrolysis (TH) of swine manure resulted in the hydrolysis of organic matter in swine manure and promoted the release of phosphate and ammonia nitrogen. The addition of HCl and H_2O_2 further accelerated the hydrolysis process of organic phosphorus and protein, compared to the TH process (140°C), the release rates of phosphate and ammonia nitrogen were increased by 17.5% (5% HCl, 6% H_2O_2) and 26.9% (5% HCl, 7% H_2O_2), respectively. According to SEM analysis, the concentrations of nutrients and metals increased significantly when the concentrations of HCl and H_2O_2 were increased. Moreover, calculations showed that applying the thermally hydrolysed swine manure liquid phase to the soil as a liquid fertilizer does not cause environmental risks. It should be emphasized that metal cations show an increasing trend during TH process of swine manure, but still do not exceed the minimum ecological risk threshold. In order to recover the nutrients nitrogen and phosphorus, this study demonstrates a possible route for the TH of livestock manure as a liquid fertilizer. Thus, TH process of animal manures is may be a feasible and sustainable strategy to add value to this waste resource.

Data availability statement

The original contributions presented in the study are included in the article/Supplementary Material, further inquiries can be directed to the corresponding author.

Author contributions

SX: Conceptualization, Investigation, Analysis, Data Curation, Methodology, Writing—original draft. TZ: Supervision, Scientific concept, Guiding, Technical facilities, Foundation, Writing—review and editing. AM: Writing—review and editing. AT: Writing—review and editing. NB: Writing—review and editing.

Funding

The research was sustained by the grant from Government Purchase Service Project of Ministry of Agriculture and Rural Affairs of China (Grant number 202205510310600), the National Key Technology Research and Development Program of China (Grant number 2017YFD0800202), the National Natural Science Foundation of China (Grant Number 31401944).

Acknowledgments

The authors are thankful to International Association of Advanced Materials (IAAM), Sweden for providing international network for carrying out this research.

Conflict of interest

Authors AM and AT were employed by the company Institute of Advanced Materials.

The remaining authors declare that the research was conducted in the absence of any commercial or financial relationships that could be construed as a potential conflict of interest.

Publisher's note

Supplementary material

The Supplementary Material for this article can be found online at: https://www.frontiersin.org/articles/10.3389/fenvs.2022.1005290/full#supplementary-material

References

Aragón-Briceño, C. I., Pozarlik, A. K., Bramer, E. A., Niedzwiecki, L., Pawlak-Kruczek, H., and Brem, G. (2021). Hydrothermal carbonization of wet biomass from nitrogen and phosphorus approach: A review. *Renew. Energy* 171, 401–415. doi:10.1016/j.renene.2021.02.109

Bolan, N. S., Adriano, D. C., Kunhikrishnan, A., James, T., McDowell, R., and Senesi, N. (2011). Dissolved organic matter. *Adv. Agron.* 110, 1–75. doi:10.1016/B978-0-12-385531-2.00001-3

Bolan, N. S., Szogi, A. A., Chuasavathi, T., Seshadri, B., Rothrock, M. J., and Panneerselvam, P. (2010). Uses and management of poultry litter. *World's. Poult. Sci. J.* 66 (4), 673–698. doi:10.1017/S0043933910000656

Bolyard, S. C., and Reinhart, D. R. (2017). Evaluation of leachate dissolved organic nitrogen discharge effect on wastewater effluent quality. *Waste Manag.* 65, 47–53. doi:10.1016/j.wasman.2017.03.025

Broadley, M. R., and White, P. J. (2010). Eats roots and leaves. can edible horticultural crops address dietary calcium, magnesium and potassium deficiencies? *Proc. Nutr. Soc.* 69, 601–612. doi:10.1017/S0029665110001588

Cai, J., Xia, X. L., Chen, H. B., Wang, T., and Zhang, H. L. (2018). Decomposition of fertilizer use intensity and its environmental risk in China's grain production process. *Sustainability* 10, 498–515. doi:10.3390/su10020498

Chassapis, K., Roulia, M., and Tsirigoti, D. (2009). Chemistry of metal-humic complexes contained in megalopolis lignite and potential application in modern organomineral fertilization. *Int. J. Coal Geol.* 78, 288–295. doi:10.1016/j.coal.2009.03.004

Chen, W., Westerhoff, P., Leenheer, J. A., and Booksh, K. (2003). Fluorescence excitation - emission matrix regional integration to quantify spectra for dissolved organic matter. *Environ. Sci. Technol.* 37, 5701–5710. doi:10.1021/es034354c

Deng, Y., Zhang, T., Clark, J., Aminabhavi, T., Kruse, A., Tsang, D. C. W., et al. (2020). Mechanisms and modelling of phosphorus solid-liquid transformation during the hydrothermal processing of swine manure. *Green Chem.* 22, 5628–5638. doi:10.1039/D0GC01281E

Deng, Y., Zhang, T., Sharma, B. K., and Nie, H. (2019). Optimization and mechanism studies on cell disruption and phosphorus recovery from microalgae with magnesium modified hydrochar in assisted hydrothermal system. *Sci. Total Environ.* 646, 1140–1154. doi:10.1016/j.scitotenv.2018.07.369

Ding, Y. F., Sabatini, D. A., and Butler, E. C. (2021). Phosphorus recovery and recycling from model animal wastewaters using materials prepared from rice straw and corn cobs. *Water Sci. Technol.* 83, 1893–1906. doi:10.2166/wst.2021.094

Du, Q., Zhang, S. S., Song, J. P., Zhao, Y., and Yang, F. (2020). Activation of porous magnetized biochar by artificial humic acid for effective removal of lead ions. *J. Hazard. Mat.* 389, 122115. doi:10.1016/j.jhazmat.2020.122115

Ekpo, U., Ross, A. B., Camargo-Valero, M. A., and Fletcher, L. A. (2016). Influence of pH on hydrothermal treatment of swine manure: Impact on extraction of nitrogen and phosphorus in process water. *Bioresour. Technol.* 214, 637–644. doi:10.1016/j.biortech.2016.05.012

Gao, S. M., Lu, D., Qian, T. T., and Zhou, Y. (2021). Thermal hydrolyzed food waste liquor as liquid organic fertilizer. *Sci. Total Environ.* 775, 145786. doi:10.1016/j.scitotenv.2021.145786

Guo, K. H., Wu, Z. H., Yan, S. W., Yao, B., Song, W. H., Hua, Z. C., et al. (2018). Comparison of the UV/chlorine and UV/H2O2 processes in the degradation of PPCPs in simulated drinking water and wastewater: Kinetics, radical mechanism and energy requirements. *Water Res.* 147 (15), 184–194. doi:10.1016/j.watres.2018.08.048

Hakanson, L. (1980). An ecological risk index for aquatic pollution control.a sedimentological approach. *A sedimentol. approach. Water Res.* 14, 975–1001. doi:10.1016/0043-1354(80)90143-8

Han, Z. P., Li, Z., Li, Y., Shang, D. H., Xie, L. B., Lv, Y., et al. (2022). Enhanced electron transfer and hydrogen peroxide activation capacity with N, P-codoped carbon encapsulated CeO_2 in heterogeneous electro-fenton process. *Chemosphere* 287, 132154. doi:10.1016/j.chemosphere.2021.132154

He, G., Liu, X. S., and Cui, Z. L. (2021). Achieving global food security by focusing on nitrogen efficiency potentials and local production. *Glob. Food Sec.* 29, 100536. doi:10.1016/j.gfs.2021.100536

He, X., Zhang, T., Niu, Y., Xue, Q., Ali, E. F., Shaheen, S. M., et al. (2022). Impact of catalytic hydrothermal treatment and Ca/Al-modified hydrochar on lability, sorption, and speciation of phosphorus in swine manure: Microscopic and spectroscopic investigations. *Environ. Pollut.* 299, 118877. doi:10.1016/j.envpol.2022.118877

Joardar, J. C., Abdus Salam, A. B., Ashrafuzzaman, M., Sikder, S., and Mahmud, A. (2020). Influence of municipal solid waste compost on yield of tomato applied solely and in combination with inorganic fertilizer where nitrogen is the only variable factor. *Malays. J. Sustain. Agric.* 5 (1), 29–33. doi:10.26480/mjsa.01.2021.29.33

Karunanithi, R., Szogi, A. A., Bolan, N., Naidu, R., Loganathan, P., Hunt, P. G., et al. (2015). Phosphorus recovery and reuse from waste streams. *Adv. Agron.* 131, 173–250. doi:10.1016/bs.agron.2014.12.005

Khan, N., Mohan, S., and Dinesha, P. (2021). Regimes of hydrochar yield from hydrothermal degradation of various lignocellulosic biomass: A review. *J. Clean. Prod.* 288, 125629. doi:10.1016/j.jclepro.2020.125629

Khatun, A., Sikder, S., and Joardar, J. C. (2020). Effect of co-compost made from cattle manure and sawdust on the growth and yield of okra (Abelmoschus Esculentus L.) *Malays. J. Sustain. Agric.* 4 (1), 36–39. doi:10.26480/mjsa.01.2020.36.39

Kulikowska, D., and Gusiatin, Z. M. (2015). Sewage sludge composting in a two-stage system: Carbon and nitrogen transformations and potential ecological risk assessment. *Waste Manag.* 38, 312–320. doi:10.1016/j.wasman.2014.12.019

Li, H., Zhang, T., Shaheen, S. M., Abdelrahman, H., Ali, E. F., Bolan, N. S., et al. (2022). Microbial inoculants and struvite improved organic matter humification and stabilized phosphorus during swine manure composting: Multivariate and multiscale investigations. *Bioresour. Technol.* 351, 126976. doi:10.1016/j.biortech.2022.126976

Liu, Y. Y., Sun, Y. Q., Wan, Z. H., Jing, F. Q., Li, Z. X., Chen, J. W., et al. (2021). Tailored design of food waste hydrochar for efficient adsorption and catalytic degradation of refractory organic contaminant. *J. Clean. Prod.* 310, 127482. doi:10.1016/j.jclepro.2021.127482

Lu, D., Qian, T. T., Le, C. C., Pan, C. Z., Cao, S. B., Ng, W. J., et al. (2021). Insights into thermal hydrolyzed sludge liquor-identification of plant-growth-promoting compounds. *J. Hazard. Mat.* 403, 123650. doi:10.1016/j.jhazmat.2020.123650

Mahimairaja, S., Bolan, N. S., Hedley, M. J., and Macgregor, A. N. (1990). Evaluation of methods of measurement of nitrogen in poultry and animal manures. *Fertilizer Res.* 24 (3), 141–148. doi:10.1007/BF01073582

Murphy, J., and Riley, J. P. (1962). A modified single solution method for the determination of phosphate in natural waters. *Anal. Chim. Acta X.* 27, 31–36. doi:10.1016/S0003-2670(00)88444-5

Pan, D., and Chen, H. (2021). Border pollution reduction in China: The role of livestock environmental regulations. *China Econ. Rev.* 69, 101681. doi:10.1016/j.chieco.2021.101681

Pan, W. K., Tang, S., Zhou, J. J., Liu, M. J., Xu, M., Kuzyakov, Y., et al. (2022). Plant-microbial competition for amino acids depends on soil acidity and the microbial community. *Plant Soil* 475, 457–471. doi:10.1007/s11104-022-05381-w

Qu, J., Zhang, L., Zhang, X., Gao, L., and Tian, Y. (2020). Biochar combined with gypsum reduces both nitrogen and carbon losses during agricultural waste composting and enhances overall compost quality by regulating microbial activities and functions. *Bioresour. Technol.* 314, 123781. doi:10.1016/j.biortech.2020.123781

Shi, Y., Zhang, T., Ren, H., Kruse, A., and Cui, R. (2018). Polyethylene imine modified hydrochar adsorption for chromium (VI) and nickel (II) removal from aqueous solution. *Bioresour. Technol.* 247, 370–379. doi:10.1016/j.biortech.2017.09.107

Song, C., Yuan, W., Shan, S., Ma, Q., Zhang, H., Wang, X., et al. (2020). Changes of nutrients and potentially toxic elements during hydrothermal carbonization of pig manure. *Chemosphere* 243, 125331. doi:10.1016/j.chemosphere.2019.125331

Tang, C., Rygaard, M., Rosshaug, P. S., Kristensen, J. B., and Albrechtsen, H. (2021). Evaluation and comparison of centralized drinking water softening technologies: Effects on water quality indicators. *Water Res.* 203, 117439. doi:10.1016/j.watres.2021.117439

Vardanyan, A., Kafa, N., Konstantinidis, V., Shin, S. G., and Vyrides, I. (2018). Phosphorus dissolution from dewatered anaerobic sludge: Effect of pHs, microorganisms, and sequential extraction. *Bioresour. Technol.* 249, 464–472. doi:10.1016/j.biortech.2017.09.188

Wang, T., Zhai, Y., Zhu, Y., Peng, C., Wang, T., Xu, B., et al. (2017). Feedwater pH affects phosphorus transformation during hydrothermal carbonization of sewage sludge. *Bioresour. Technol.* 245, 182–187. doi:10.1016/j.biortech.2017.08.114

Wu, J., Chen, W., Zhao, Z., Zhang, K., Zhan, Y., Wu, J., et al. (2021). Give priority to abiotic factor of phosphate additives for pig manure composting to reduce heavy metal risk rather than bacterial contribution. *Bioresour. Technol.* 341, 125894. doi:10.1016/j.biortech.2021.125894

Wu, Q., Wang, H., Zheng, X., Liu, F., Wang, A., Zou, D., et al. (2020). Thermochemical liquefaction of pig manure: Factors influencing on oil. *Fuel* 264, 116884. doi:10.1016/j.fuel.2019.116884

Xu, H. Q., Guo, L., Zhao, Y. G., Gao, M. C., Jin, C. J., Ji, J. Y., et al. (2021). Accelerating phosphorus release from waste activated sludge by nitrilotriacetic acid addition during anaerobic fermentation process and struvite recovery. *Process Saf. Environ. Prot.* 147, 1066–1076. doi:10.1016/j.psep.2021.01.033

Yadav, B., Chavan, S., Atmakuri, A., Tyagi, R. D., and Drogui, P. (2020). A review on recovery of proteins from industrial wastewaters with special emphasis on pha production process: Sustainable circular bioeconomy process development. *Bioresour. Technol.* 317, 124006. doi:10.1016/j.biortech.2020.124006

Yang, X. C., Liu, D. P., Fu, Q., Li, T. X., Hou, R. J., Li, Q. L., et al. (2022). Characteristics of greenhouse gas emissions from farmland soils based on a structural equation model: Regulation mechanism of biochar. *Environ. Res.* 206, 112303. doi:10.1016/j.envres.2021.112303

Zhang, J. Y., Wang, Z. Y., Wang, Y. W., Zhong, H., Sui, Q. W., Zhang, C. P., et al. (2017). Effects of graphene oxide on the performance, microbial community dynamics and antibiotic resistance genes reduction during anaerobic digestion of swine manure. *Bioresour. Technol.* 245, 850–859. doi:10.1016/j.biortech.2017.08.217

Zhang, T., He, X., Deng, Y., Tsang, D. C. W., Jiang, R., Becker, G. C., et al. (2020). Phosphorus recovered from digestate by hydrothermal processes with struvite crystallization and its potential as a fertilizer. *Sci. Total Environ.* 698, 134240. doi:10.1016/j.scitotenv.2019.134240

Zhang, T., He, X., Deng, Y., Tsang, D. C. W., Yuan, H., Shen, J., et al. (2020). Swine manure valorization for phosphorus and nitrogen recovery by catalytic–thermal hydrolysis and struvite crystallization. *Sci. Total Environ.* 729, 138999. doi:10.1016/j.scitotenv.2020.138999

Zhang, T., Wu, X., Fan, X., Tsang, D. C. W., Li, G., and Shen, Y. (2019). Corn waste valorization to generate activated hydrochar to recover ammonium nitrogen from compost leachate by hydrothermal assisted pretreatment. *J. Environ. Manage.* 236, 108–117. doi:10.1016/j.jenvman.2019.01.018

Zhang, T., Wu, X., Li, H., Tsang, D. C. W., Li, G., and Ren, H. (2020). Struvite pyrolysate cycling technology assisted by thermal hydrolysis pretreatment to recover ammonium nitrogen from composting leachate. *J. Clean. Prod.* 242, 118442. doi:10.1016/j.jclepro.2019.118442

Zhang, T., Wu, X., Shaheen, S. M., Zhao, Q., Liu, X., Rinklebe, J., et al. (2020). Ammonium nitrogen recovery from digestate by hydrothermal pretreatment followed by activated hydrochar sorption. *Chem. Eng. J.* 379, 122254. doi:10.1016/j.cej.2019.122254

Zheng, X., Zou, D., Wu, Q., Wang, H., Li, S., Liu, F., et al. (2022). Review on fate and bioavailability of heavy metals during anaerobic digestion and composting of animal manure. *Waste Manag.* 150, 75–89. doi:10.1016/j.wasman.2022.06.033

frontiers | Frontiers in Environmental Science

TYPE Original Research
PUBLISHED 03 October 2022
DOI 10.3389/fenvs.2022.945192

OPEN ACCESS

EDITED BY
Tao Zhang,
China Agricultural University, China

REVIEWED BY
Fang Li,
Donghua University, China
Chamindra L. Vithana,
Southern Cross University, Australia

*CORRESPONDENCE
Kun Bai,
baikun@hfuu.edu.cn

SPECIALTY SECTION
This article was submitted to Water and Wastewater Management,
a section of the journal
Frontiers in Environmental Science

RECEIVED 16 May 2022
ACCEPTED 05 August 2022
PUBLISHED 03 October 2022

CITATION
Bai K, Liu W, Zhao M, Li K and Tian Y (2022), Numerical simulation study of oil–water separation based on a super-hydrophilic copper net.
Front. Environ. Sci. 10:945192.
doi: 10.3389/fenvs.2022.945192

Numerical simulation study of oil–water separation based on a super-hydrophilic copper net

Kun Bai*, Weinan Liu, Maoyu Zhao, Kaifang Li and Yiming Tian

School of Advanced Manufacturing Engineering, Hefei University, Hefei, China

Green and environmentally friendly oil–water separation is an important technique for reducing environmental pollution. In this study, the oil–water separation effect of the super-hydrophilic copper net was optimized through numerical simulation and orthogonal experiments. To be specific, a super-hydrophilic copper net was prepared using the solution etching method to perform oil–water separation experiments, and a favorable oil–water separation effect was achieved. First, the influences of oil–water flow velocity, copper net mesh size, and surface wettability on the oil–water separation effect of the super-hydrophilic copper net were explored via single-factor experiments. The results showed that the oil resistance of the super-hydrophilic copper net degraded, and its oil–water separation effect became poor due to the increasing oil–water flow velocity, enlarged copper net mesh size, and reduced oil contact angle on the surface of the super-hydrophilic copper net. On this basis, the optimized oil–water separation parameters were obtained through orthogonal experiments. The optimized process parameters were as follows: velocity = 0.1 m/s, copper net mesh size = 30 μm, oil contact angle = 150°, and oil removal rate = 95.7%. Furthermore, the copper net was etched using sodium hydroxide and sodium persulfate mixed solution to prepare a 500-mesh super-hydrophilic copper net for the oil–water separation experiment and then the oil removal rate reached 96.4%. The study results provide a theoretical basis, method, and means for the practical application of super-hydrophilic copper nets.

KEYWORDS

super-hydrophilic, copper net, oil–water separation, numerical simulation, contact angle

1 Introduction

With economic development, oily wastewater discharge and treatment difficulties are continuously aggravated. The economical and efficient treatment of oily wastewater can not only save resources and promote resource recycling but also be conducive to environmental protection (Zhang and Zhang, 2018; Chen, 2019; Lu et al., 2020).

Oily wastewater mainly comes from the petroleum industry and food processing industry (Song and Wang, 2011; Yu, 2015; Hu et al., 2021; Xu, 2021; Liu et al., 2022). Oil–water separation technology mainly includes gravity separation, centrifugal separation, membrane separation, electrolysis separation, and air flotation separation (Hu et al., 2015; Shao and Zhong, 2015; Zhang et al., 2017; Zhang et al., 2021). The membrane separation technology is more effective and less costly to operate, but it is prone to blockage when treating oily wastewater with a high oil content, resulting in membrane contamination. Superwetting materials are capable of rapid efficient oil–water separation by virtue of oil–water wettability difference, without secondary pollution, which has been deeply investigated by scholars. Zhang et al. (2018a) experimentally prepared a stainless steel net with super-hydrophobic and super-oleophilic characteristics to explore its oil–water separation ability and self-cleaning ability; Jung and Bhushan (2009) established a model and used to predict the oil drop contact angle in water by studying the wetting behaviors of water drops and soil in a three-phase interface; Zhang et al. (2018b) ablated the Al, Fe, Cu, Mo, and stainless steel surfaces using lasers and prepared rough micro-nanocomposite surfaces. With the inherently high surface energy, Al, Fe, Cu, Mo, and stainless steel surfaces all showed super-hydrophilic and underwear super-oleophobic properties. The previously mentioned scholars used the prepared super-wettable materials to separate oil and water and achieved excellent results. However, the actual oil–water separation environment is often harsh and superwetting materials do not give good oil–water separation results in practice. With further research, more and more results showed that when the superwetting material is impacted, the oil–water separation effect will be affected (Pi et al., 2017; Zhao et al., 2018). In recent years, computer simulation theories of fluid and material properties have been gradually developing. Liu and Yu, (2010) constructed a super-hydrophobic microchannel flow model and studied its flow characteristics via the numerical simulation technique; Qin (2013) explored the oil–water separation effect of a super-hydrophobic membrane-based spiral oil–water separator through the numerical simulation technique.

In this study, the flow field conditions on the water drop–oil drop contact surface of a super-hydrophilic copper net were simulated via FLUENT software. The influences of three factors—oil–water flow velocity, copper net mesh size, and oil contact angle—on oil–water separation were mainly studied. On this basis, the aforementioned influencing factors were subjected to an orthogonal experiment, and optimized process parameters were obtained. The super-hydrophilic copper net was prepared according to the process parameters, and oil–water separation experiments were conducted to verify the reasonableness of the simulation results.

2 Materials and methods

2.1 Procedure of the simulation study

2.1.1 Modeling

The wettability of materials is greatly influenced by their surface microstructure. Periodic rough surfaces, aperiodic rough surfaces, and composite rough surfaces can be prepared through laser ablation and chemical etching (Pan et al., 2010; Cui et al., 2017). In this study, the surface microstructure of the super-hydrophilic copper net was simplified into a periodically distributed groove to simplify the calculation, and a 2D structure of its cross section was taken to establish a 2D model through Gambit software, as shown in Figure 1.

FIGURE 1
Schematic diagram of the groove structure for the super-hydrophilic copper net.

When simulating the oil–water separation of the super-hydrophilic copper net, the influences of three factors—velocity, net mesh size, and oil contact angle on the copper net surface—on the oil–water separation effect were mainly explored. The volume of fluent model (VOF model) (Feng and Yao, 2012; Zhang and Yan, 2013) can be used to acquire clear interfaces between different phases by setting their surface tension and wall surface contact angle. Hence, the VOF model was chosen to simulate the oil–water separation of this super-hydrophilic copper net by abiding by the conservation law of mass, momentum, and energy, with the basic governing equation as follows:

The continuity equation of the VOF model is:

$$\frac{\partial \rho}{\partial t} + \nabla(\rho v) = 0. \tag{1}$$

The continuity equation of the volume fraction is:

$$\frac{\partial \alpha_i}{\partial t} + v\nabla(\alpha_i) = 0. \tag{2}$$

The momentum conservation equation is:

$$\frac{\partial(\rho v)}{\partial t} + \nabla(\rho v v) = -\nabla P + \nabla\left[\mu\left(\nabla v + \nabla v^T\right)\right] + \rho g + F, \tag{3}$$

where ρ is the density, kg/m^3; v denotes the velocity vector, m/s; t represents time, s; ∇ is a mathematical operator notation; α_i is the volume fraction of phase i ; is the dynamic viscosity of fluid; g is the gravitational acceleration, m/s^2; P is the pressure intensity, Pa; and F represents the equivalent body force form of surface tension, N.

2.1.2 Numerical calculation method and boundary conditions

In this study, the flow field condition on the oil drop–water drop contact surface of a super-hydrophilic copper net was simulated. To simplify the calculation, a laminar flow model was selected. Given that a transient problem was the simulation object, pressure-implicit with the splitting of operators (PISO) algorithm was selected to accelerate the convergence rate of single iterative steps during

TABLE 1 Experimental reagents and substrates.

Reagent	Specification
$Na_2S_2O_8$	Analytically pure
Na(OH)	Analytically pure
C_2H_6O	Analytically pure
H_2O	-
Cu	500-mesh

transient calculation, harvesting a good convergence effect. As for the selection of the discretization method, the body force weighted scheme was chosen for pressure, second-order upwind discretization format for momentum, and geometric reconstruction format for the volume fraction. The initialization value of the sub-relaxation factor was set to default.

In this simulation, gravitational acceleration was set at 9.8 m/s^2, initial operating pressure at 101,325 Pa, and water contact angle at 0°. Three-phase (oil, water, and air) fluids were involved in the simulation of oil–water separation for a super-hydrophilic copper net. To clearly observe the flow field conditions on the oil drop–water drop contact surface of this super-hydrophilic copper net, the three-phase computational domains were divided through patch function, where air was set as the primary phase, and the volume fractions of all the three phases in their respective computational domains were set at 1. The tensions on oil and water surfaces were set at 0.029 and 0.072 N/m, respectively.

2.1.3 Range analysis

Range analysis was performed according to the orthogonal experimental results. The experimental results corresponding to the m level of factors in column j as well as K_{jm} and its mean value $_{jm}$ were calculated. Moreover, the range R_j of factors in column j was calculated based on the $_{jm}$ value:

$$\eta = \frac{C_1 - C_2}{C_1} \tag{4}$$

Here, R reflects the variation range of experimental results in case of changes in the factors in column j. A greater R-value manifested a greater influence of this factor on experimental indexes, so the sequence of influencing factors could be judged according to R.

2.2 Procedure of Cu net mesh and oil–water separation

The reagents required for the preparation of the super-hydrophilic copper net and super-hydrophobic copper net experiments are shown in Table 1.

FIGURE 2
Surface contact angle of the super-hydrophilic copper net.

A 500-mesh red copper net with a mesh size of 30 μm was selected as the substrate, and an etching solution was prepared by mixing 25 ml of 1 mol/L sodium hydroxide solution and 25 ml of 0.15 mol/L $Na_2S_2O_8$ solution. The dried red copper net was placed in the etching solution for reaction at room temperature for 60 min and then taken out and washed using deionized water. Subsequently, it was dried up in a blast air oven to prepare a super-hydrophilic copper net. The hydrophilicity of the super-hydrophilic copper net was examined using the OCA15EC optical contact angle meter and SU8010 scanning electron microscope, and the testing process was as follows: when measuring the contact angle of the prepared copper net surface, the SNS syringe needle was selected, and the dosing volume was set to 3 μL. The water was dropped at a dosing rate of 1 μL/s, and a thin film was formed on the surface of the copper net. The indirect contact angle was measured to be 0°, indicating that the copper net is super-hydrophilic, as shown in Figure 2.

The copper net was cut into 10 mm × 10 mm specimens, and the surface morphology of the prepared copper net was characterized using a cold field emission scanning electron microscope electron gun at an acceleration voltage of 15 KV. The surface morphologies of this super-hydrophobic copper net were characterized as shown in Figure 3. After etching through the mixed solution, many tiny clusters attached on the copper net matrix and presented ordered growth around. It could be observed that micrometer needle-like structures were generated on the surface of the copper net substrate, which was mutually crossed and grew around in an unordered way. These clusters and micrometer needle-like structures formed composite micro-nanostructures on the copper net surface, thus greatly increasing the roughness of the copper net surface and endowing it with super-hydrophilicity.

To test the oil–water separation effect of this 500-mesh super-hydrophilic copper net, an oil–water separation device was designed

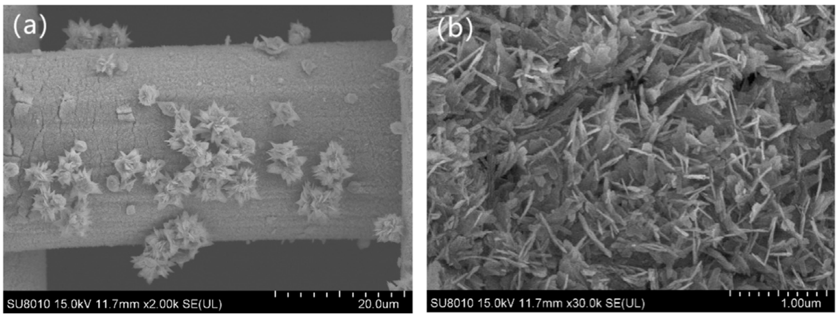

Particles attached to the copper net

Particle morphologies

FIGURE 3
Surface morphologies of the super-hydrophilic copper net.

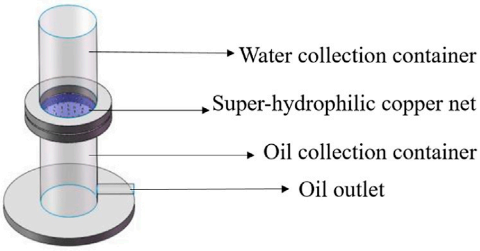

FIGURE 4
Schematic diagram of the oil–water separation device.

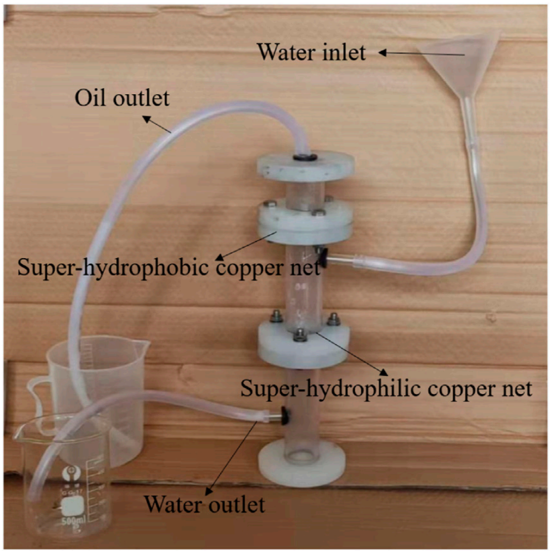

FIGURE 5
Experimental separation device.

as shown in Figures 4, 5. Using restaurant oily wastewater as the separation object, it was first treated by air flotation and the measured animal and vegetable oil content was 54.5 mg/L, and the oil content was still high. Then, the secondary treatment of this oily wastewater was carried out by using a super-hydrophilic copper net. Before the oil–water separation experiment, the super-hydrophilic copper net was fully wetted using water. Next, 500 ml of oily restaurant wastewater pretreated through air flotation was taken and made to flow into the vessel slowly along the inner wall to prevent the oil–water separation effect from being impacted by too high oil–water flow velocity.

3 Results and discussion

3.1 Calculated results and analysis of the simulation study

3.1.1 Oil–water flow velocity

The flow field conditions when oil and water drops contacted the super-hydrophilic copper net were simulated at simulation velocities of 0.1, 0.5, and 1 m/s under the net mesh size of 10 μm and oil contact angle of 150°. At the left was the aqueous phase and at the right was the oil phase, as shown in the following Figure 6.

It could be known from Figure 6 that water drops could completely wet and penetrate through this super-hydrophilic copper net. At a velocity of 0.1 m/s, oil drops failed to wet the super-hydrophilic copper net and were intercepted above it, thus realizing the goal of efficient oil–water separation. As the velocity was elevated to 0.5 m/s, the dynamic pressure was elevated, and oil drops were forcibly extruded into the groove structure on the partial copper net surface, but they did not completely wet the copper net, which was still oleophobic to some extent. When the velocity was increased to 1 m/s, oil drops were forcibly extruded into the groove structure on the copper net surface and passed

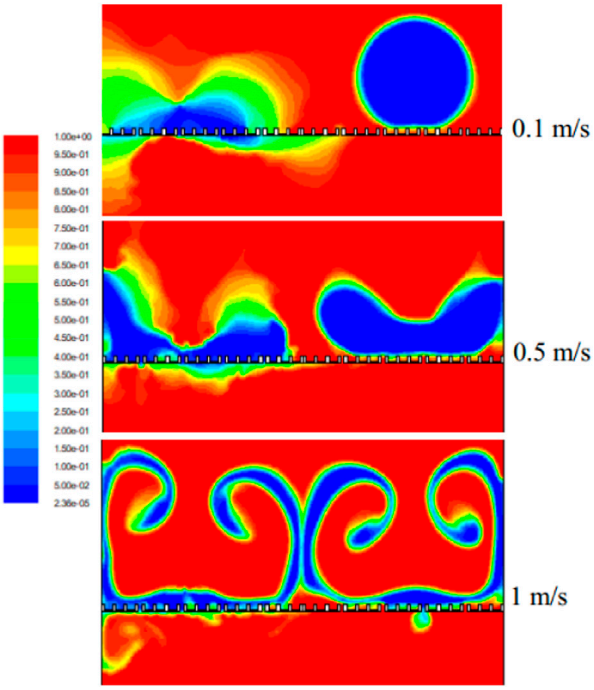

FIGURE 6
Cloud picture of the oil–water volume fraction at a velocity of 0.1, 0.5, and 1 m/s.

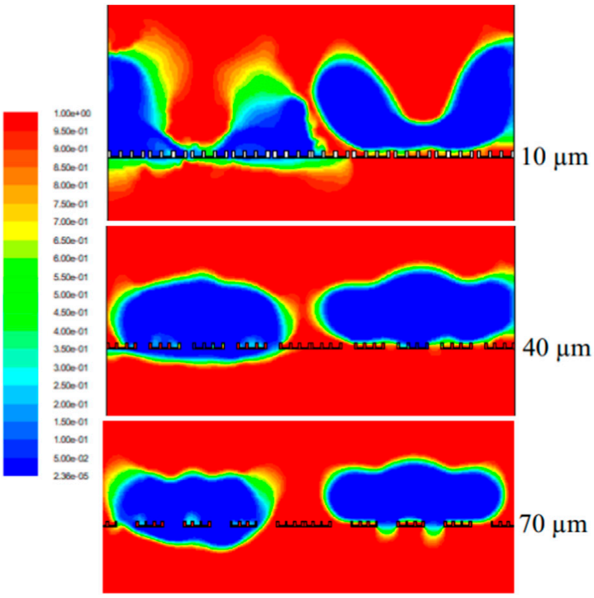

FIGURE 7
Cloud picture of the oil–water volume fraction under the copper net mesh size of 10, 40, and 70 μm.

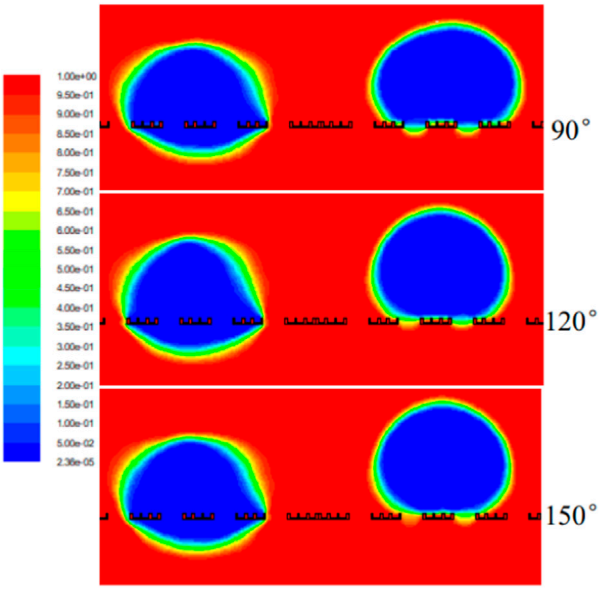

FIGURE 8
Cloud picture of the oil–water volume fraction under the oil contact angle of 90°, 120°, and 150°.

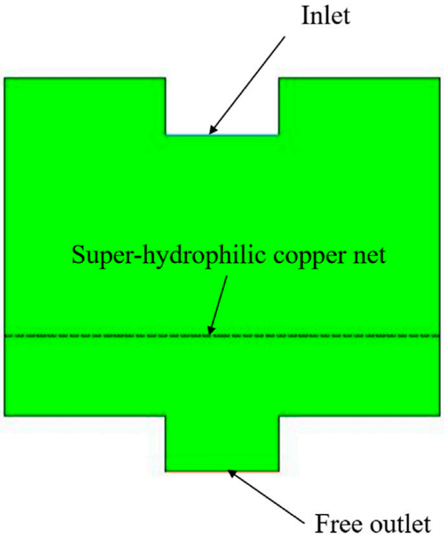

FIGURE 9
2D model drawing of the super-hydrophilic copper mesh.

TABLE 2 Factor levels in the orthogonal experiment.

Level	Copper net mesh size (μm)	Velocity (m/s)	Oil contact angle (°)
1	100	0.1	90
2	70	0.5	120
3	30	1	150

TABLE 3 Orthogonal experiment and results.

No.	Copper net mesh size (μm)	Velocity (m/s)	Oil contact angle (°)	Oil removal rate (%)
1	100	0.1	90	28.3
2	100	0.5	120	24.6
3	100	1	150	35.3
4	70	0.5	150	43.2
5	70	0.1	120	64.7
6	70	1	90	10.1
7	30	0.5	90	26.7
8	30	1	120	31.6
9	30	0.1	150	95.7

through the net via meshes, and this super-hydrophilic copper net could not realize efficient oil–water separation under this circumstance.

3.1.2 Copper net mesh size

The flow field conditions when oil and water drops contacted the super-hydrophilic copper net were simulated at the velocity of 0.5 m/s under the oil contact angle of 150° and the copper net mesh size of 10, 40, and 70 μm, respectively, as shown in the following Figure 7.

It could be known from Figure 7 that the copper net mesh size had a bearing on its oleophobic properties. When the copper net mesh size was continuously enlarged, oil drops would finally pass through this super-hydrophilic copper net. As the copper net mesh size gradually increases, the area of the super-hydrophilic copper mesh also increases, and its impact resistance will be weakened, so the effect of oil–water separation will become worse. Hence, it is important to select an appropriate copper net mesh size in order to enhance the oil–water separation effect.

3.1.3 Contact angle

The flow field conditions when oil and water drops contacted the super-hydrophilic copper net were simulated at the velocity of 0.1 m/s under a copper net mesh size of 70 μm and oil contact angles of 90°, 120°, and 150°, respectively, as shown in the following Figure 8.

As shown in Figure 8, at the velocity of 0.1 m/s and copper net mesh size of 70 μm, water drops could freely pass through the super-hydrophilic copper net at contact angles of 90°, 120°, and 150°. As the oil contact angle was gradually enlarged, the contact area between oil drops and super-hydrophilic copper net was smaller. At the oil contact angle of 90°, partial oil drops penetrated through this super-hydrophilic copper net. When the oil contact angle increased to 150°, oil drops were nearly completely obstructed above the super-hydrophilic copper net, with its oleophobic properties gradually enhanced, which was better for improving the oil–water separation effect.

3.1.4 Three-factor three-level orthogonal experimental analysis

The aforementioned simulation results revealed that velocity, net mesh size, and oil contact angle exerted important influences on the oil–water separation effect of this super-hydrophilic copper net. Based on the simplified 2D super-hydrophilic copper net surface structure, a 2D numerical simulation model of this super-hydrophilic copper net was constructed (Figure 9). Then, a three-factor three-level orthogonal experiment was carried out to further explore the influencing degrees of velocity, copper net mesh size, and contact angle on the oil–water separation effect of the super-hydrophilic copper net. The factor levels in the orthogonal experiment are listed in Table 2, and the orthogonal experiment and its results are presented in Table 3.

TABLE 4 Range analysis of orthogonal experimental results.

Index	Level	Copper net mesh size (μm)	Velocity (m/s)	Oil contact angle (°)
	1	88.2	188.7	65.1
	2	118	94.5	120.9
	3	154	77	174.2
	1	29.4	62.9	21.7
	2	39.3	31.5	40.3
	3	51.3	25.7	58.1
Optimal level		3	1	3
		21.9	37.2	36.4
Sequence	Velocity > oil contact angle > copper net mesh size			

During numerical simulation, outlet flow monitoring was set in FLUENT software. A stable outlet flow indicated that the oil–water separating flow field of this super-hydrophilic copper net was stable. In this case, the mass flow data of inlet and outlet oil were, respectively, recorded, and the oil removal rate was calculated accordingly through the following formula:

$$R_j = \max(K_{j1}, K_{j2}, ...K_{jm}) - \min(K_{j1}, K_{j2}, ...K_{jm}) \quad (5)$$

where η oil removal rate;

C1 mass flow of inlet oil, kg/s; and

C2 mass flow of outlet oil, kg/s.

The range analysis of orthogonal experimental results is presented in Table 4. It could be known from the range analysis that the sequence of factors influencing the oil removal effect of this super-hydrophilic copper net was as follows: oil–water flow velocity > oil contact angle > copper net mesh size. The orthogonal experimental results reflected that the oil removal rate reached the highest value (95.7%) at the velocity of 0.1 m/s, oil contact angle of 150°, and copper net mesh size of 30 μm. Figure 10 is drawn under the aforementioned process parameters. As shown in Figure 10, oil was basically intercepted above the super-hydrophilic copper net, while only a small quantity of oil passed through this net, which showed good oil resistance and water drainage functions under this circumstance.

3.2 Results of the oil–water separation experiment using the newly synthesized Cu net mesh

The animal and vegetable oil concentrations in water before and after the experiment were measured using an infrared oil meter

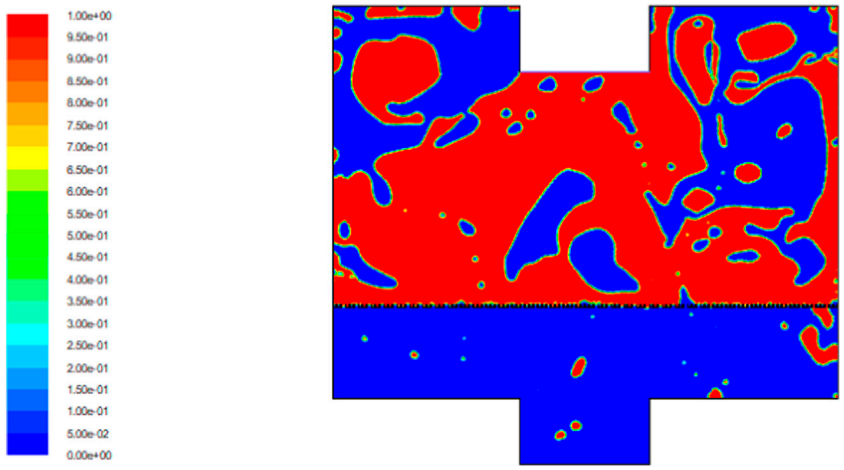

FIGURE 10
Cloud picture of the oil-phase volume fraction.

TABLE 5 Results of the oil–water separation experiment.

Water sample before the experiment (mg/L)	Water sample after the experiment (mg/L)	Oil removal rate (%)
54.5	1.98	96.4

(Table 5). Through the treatment using a 500-mesh super-hydrophilic copper net, a good oil removal effect was achieved at a reasonable oil–water flow velocity, and the content of animal and vegetable oils was reduced to 1.98 mg/L, with the oil removal rate reaching 96.4%, which was approximate to the numerical simulation result. The water qualities before and after the treatment were compared as shown in Figure 11.

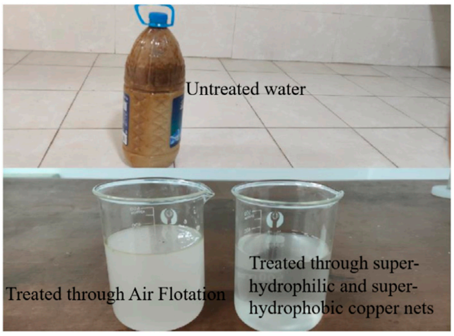

FIGURE 11
Comparison diagram of water qualities before and after treatment.

The oil removal rates mentioned in Sun et al. (2018) were 98.8, 98.75, 99, 99.5, and 99.95%. Further experiments were conducted with three such oil–water separation devices connected in series, and it was measured that the content of animal and vegetable oils was reduced to 0.34 mg/L, and the oil removal rate could reach 99.4%, which is better or close to several membrane separation techniques mentioned in the reference (Sun et al., 2018).

4 Conclusion

In this study, the surface structure of the super-hydrophilic copper net was simplified and three single-factor simulation experiments of oil–water flow rate, copper mesh pore size, and oil contact angle were conducted separately using FLUENT software. The simulation results show that all three factors have an important effect on the oil–water separation effect of the super-hydrophilic copper net. On this basis, the process parameters of oil–water separation using the super-hydrophilic copper net were optimized by orthogonal tests. The super hydrophilic copper net was prepared by etching the copper mesh with a mixture of sodium hydroxide and sodium persulfate, and the oil–water separation experiment was conducted, and then a better oil–water separation effect was obtained. The main conclusions are as follows:

1) With the increase in the oil–water flow velocity and copper net mesh size and the reduction of the oil contact angle on the surface of this super-hydrophilic copper net, its oil resistance performance is degraded, thus failing to achieve efficient oil–water separation.
2) The range analysis of orthogonal experimental results reveals that the oil–water flow velocity has the greatest influence on the oil–water separation effect, followed by the oil contact angle and the copper net mesh size. The optimized process parameters were as follows: velocity was 0.1 m/s, copper net mesh size was 30 μm, oil contact angle was 150°, and oil removal rate reached 95.7%.
3) Through the oil–water separation experiment through 500-mesh super-hydrophilic and super-hydrophobic copper nets, the oil removal rate reached 96.4%, being approximate to the numerical simulation result. Therefore, the reasonability and feasibility of the simulation experiment were further proved.
4) The oil removal rate can reach 99.4% by connecting three super-hydrophilic copper net oil–water separation devices in series. This technology has a high oil removal rate and a simpler method of membrane material preparation.

Data availability statement

The original contributions presented in the study are included in the article/Supplementary Material; further inquiries can be directed to the corresponding author.

Author contributions

Conceptualization, KB and WL; methodology, KB, WL, and MZ; software, KB and WL; validation, WL and KL; formal analysis, KB and WL; investigation, KB, MZ, and KL; resources, KB and WL; writing—original draft preparation, KB; writing—review and editing, WL and YT; supervision, KB, WL, and MZ; and project administration, KB. All authors have read and agreed to the published version of the manuscript.

Conflict of interest

The authors declare that the research was conducted in the absence of any commercial or financial relationships that could be construed as a potential conflict of interest.

Publisher's note

References

Chen, Y. M. (2019). Review of treatment of oily wastewater by combined process. *Ningxia Eng. Technol.* 18 (03), 271–274. [in Chinese]. doi:10.1016/j.arabjc.2013.07.020

Cui, Q. Z., Li, C. X., and Ye, X. M. (2017). Effect of structural parameters on the turbulent resistance characteristics of superhydrophobic microchannels. *Electr. Power Sci. Eng.* 33 (07), 52–57. [in Chinese]. doi:10.1063/5.0056952

Feng, L., and Yao, Q. Y. (2012). Numerical simulation of gas-liquid two-phase flow based on the VOF model in pump station pressure piping. *China Rural Water Hydropower* (12), 124–126+130. [in Chinese].

Hu, H., Wang, F., He, W. Z., and Li, G. M. (2015). Research on oil separation from catering swill by microwave and centrifugation. *Environ. Eng.* 33 (10), 77–80+125. doi:10.13205/j.hjgc.201510017

Hu, T. Y., Tang, J., and Chen, Z. L. (2021). Progress of oily wastewater treatment in petroleum industry. *Technol. Water Treat.* 47 (06), 12–17. doi:10.1016/j.arabjc.2013.07.020

Jung, Y. C., and Bhushan, B. (2009). Wetting behavior of waterand oil droplets in three-phase interfaces for hydropho-bicity/philicity and oleophobicity/philicity. *Langmuir* 25 (24), 14165–14173. doi:10.1021/la901906h

Liu, Y., Sun, Y., Sun, Y. X., Guo, J., Liang, P., Xu, B. W., et al. (2022). Mechanism and experiment of micro-channel filtration by heterostructure media particles for oily wastewater treatment. *Chin. J. Environ. Eng.* 16 (02), 506–514. doi:10.12030/j.cjee.20210108

Liu, Z., and Yu, Z. J. (2010). Numerical simulation of water flow in the super-hydrophobic micro-tube. *Liaoning Chem. Ind.* 39 (9), 897–900. [in Chinese]. doi:10.3969/j.issn.1004-0935.2010.09.001

Lu, H., Liu, Y. Q., Dai, P. Y., Pan, Z. C., Li, Y. D., Wu, S. H., et al. (2020). Process intensification technologies for oil-water separation. *Chem. Industry Eng. Prog.* 39 (12), 4954–4962. [in Chinese]. doi:10.16085/j.issn.1000-6613.2020-0985

Pan, G., Huang, Q. G., Hu, H. B., and Liu, Z. Y. (2010). Wettability of superhydrophobic surface through tuning microcosmic structure. *Polym. Mater. Sci. Eng.* 26 (07), 163–166. [in Chinese].

Pi, P. H., Hou, K., Zhou, C. L., Li, D. G., Wen, X. F., Xu, S. P., et al. (2017). Superhydrophobic Cu2S@Cu2O film on copper surface fabricated by a facile chemical bath deposition method and its application in oil-water separation. *Appl. Surf. Sci.* 396, 566–573. doi:10.1016/j.apsusc.2016.10.198

Qin, J. X. (2013). *Design of spiral flow oil-water separator based on superhydrophobic membrane*. China: Southwest Petroleum University. [in Chinese].

Shao, Y. F., and Zhong, L. W. (2015). The improvement of oil-water separation technique based on gravitational sedimentation. *Telecom Power Technol.* 32 (06), 174–177+193. doi:10.1023/B:WATE.0000038874.85413.05

Song, H. T., and Wang, R. (2011). Analysis of water quality and survey on oily waste water from universities' canteen. *J. Hubei Univ. Sci. Ed.* 33 (03), 323–327. doi:10.3969/j.issn.1000-2375.2011.03.013

Sun, Y., Zhou, L., Bian, T., Tian, X. X., Ren, W. K., Lu, C., et al. (2018). Efficacy evaluation of two commercial modified-live virus vaccines against a novel recombinant type 2 porcine reproductive and respiratory syndrome virus. *Vet. Microbiol.* 45 (8), 176–182. [in Chinese]. doi:10.1016/j.vetmic.2018.02.016

Xu, K. P. (2021). Research status and prospect of oily wastewater treatment methods. *Chem. Enterp. Manag.* (24), 21–22. doi:10.3390/w11122517

Yu, Z. Q. (2015). *Pollution status and prevention countermeasures of oily waste water in catering trade*. china: China Environmental Protection Industry, 47–49.07

Zhang, D., Wang, G., Zhi, S., Xu, K., Zhu, L. J., Li, W. W., et al. (2018). Superhydrophilicity and underwater superoleophobicity TiO2/Al2O3 composite membrane with ultra low oil adhesion for highly efficient oil-in-water emulsions separation. *Appl. Surf. Sci.* 458 (15), 157–165. doi:10.1016/j.apsusc.2018.07.052

Zhang, G. J., and Yan, Y. J. (2013). Numerical simulation method of water-entry impact at low speed for a missile based on VOF model. *J. Air Force Eng. Univ. Nat. Sci. Ed.* 14 (06), 23–26. [in Chinese]. doi:10.1088/1742-6596/1507/10/102028

Zhang, J. X., Ma, Y. Y., Zhou, M., Zhang, X. X., and Wang, C. C. (2017). Advances in oil-water separation technologies. *Water Purif. Technol.* 36 (12), 50–54+61.

Zhang, L. L., Chen, Q., Yin, M. H., Zheng, S. X., and Yang, X. Q. (2021). Emulsified wastewater treatment using membrane separation technique: A review. *Appl. Chem. Ind.* 50 (10), 2791–2796. doi:10.1088/1742-6596/1507/10/102028

Zhang, R., and Zhang, F. (2018). Development of oily wastewater treatment technology. *Contemp. Chem. Ind.* 47 (08), 1695–1697+1701. doi:10.13840/j.cnki.cn21-1457/tq.2018.08.044

Zhang, Z. H., Wang, H. J., Liang, Y. H., Li, X. J., Ren, L. Q., Cui, Z. Q., et al. (2018). One step fabrication of robust superhydrophobic and supero leophilic surfaces with self-cleaning and oil/water separation function. *Sci. Rep.* 8 (1), 3869. doi:10.1038/s41598-018-22241-9

Zhao, Z. E., Sun, S. H., Hu, Y. M., and Zhu, Y. (2018). Research progress on durability and evaluation methods of superhydrophobic surface. *Adv. Material Chem.* 6 (3), 56–65. doi:10.12677/amc.2018.63007

frontiers | Frontiers in Environmental Science

TYPE Original Research
PUBLISHED 11 October 2022
DOI 10.3389/fenvs.2022.967775

OPEN ACCESS

EDITED BY
Shengsen Wang,
Yangzhou University, China

REVIEWED BY
Guohua Hu,
East China Normal University, China
Chengjia Su,
Sun Yat-sen University, China

*CORRESPONDENCE
Qiannan Yang,
yangqiannan@xhsysu.edu.cn

SPECIALTY SECTION
This article was submitted to Water and Wastewater Management,
a section of the journal
Frontiers in Environmental Science

RECEIVED 13 June 2022
ACCEPTED 27 September 2022
PUBLISHED 11 October 2022

CITATION
Zhou Y, Liu Z, Zhang B and Yang Q (2022), Evaluating water resources carrying capacity of Pearl River Delta by entropy weight-TOPSIS model.
Front. Environ. Sci. 10:967775.
doi: 10.3389/fenvs.2022.967775

Evaluating water resources carrying capacity of Pearl River Delta by entropy weight-TOPSIS model

Yueying Zhou[1], Zufa Liu[2], Bowei Zhang[1] and Qiannan Yang[1]*

[1]School of Resources and Planning, Guangzhou Xinhua University, Guangzhou, China, [2]School of Civil Engineering, Sun Yat-sen University, Guangzhou, China

To understand the spatio-temporal changes in the water resources carrying capacity (WRCC) of Pearl River Delta (PRD), 19 indicators were selected from three subsystems (water resources, socio-economic, and eco-environment), and the entropy weight-TOPSIS model was employed to analyze the WRCC of each cities in PRD from 2015 to 2020. As the result shows, the water resources subsystem (WRS) had the largest weight in the evaluation system, followed by the socio-economic subsystem (SES), and the eco-environmental subsystem (EES); among these indicators, economic density, water resources per capita, annual precipitation, and new soil erosion treatment area had the highest weights; the PRD had a low WRCC score overall, with considerable regional differences; the capacity score changed with time, but the ranking of cities remained largely the same, with Shenzhen, Zhaoqing, and Huizhou marking higher scores, whereas Zhongshan, Foshan, and Zhuhai achieving lower scores. It was also found that Shenzhen had a high score for SES, which made up for the shortage of natural water resources there; cities like Huizhou, Jiangmen, and Zhaoqing which boast rich water resources and extensive development achieved high scores for WRS and EES. As the PRD develops, it is important to optimize dispatch of water resources, boost green economy, and promote ecological wellbeing.

KEYWORDS

entropy weight-TOPSIS model, Pearl River Delta, water resources carrying capacity, regional differences, green economy

Introduction

Water resources play a significant role in national economy and living-standard improvement. “Water resources-based planning” is a planning strategy that takes water resources as the primary constraint in control of urban area expansion and restructuring of industry layouts. Though cities often boast rich water resources in the early stage of development, problems like water shortage, water pollution, and ecological degradation rear their ugly heads as the economy takes off and the population grows, hobbling urban development (Wu et al., 2020). Researches show that there is no consensus on the definition of water resources carrying capacity (WRCC) among researchers, and relevant studies often have varied focuses. For instance, Falkenmark and Lundqvist (1998) put forward the term “available water,” and probed into the problem of water security from the perspectives of policy determination and human adaptation. Clarke (2002) maintained that WRCC is closely related to population growth and resource depletion. Milano et al. (2013) used the “water supply/demand ratio” to assess whether the water resources in the Ebro basin would meet the current and future demands of water in the region. Given our research goals, WRCC is defined as the capacity of water resources to meet the needs of human activities in a region within a given time frame, which is subject to impacts from comprehensive factors including water resources abundance, economic-technological strength, and ecological quality (Lin et al., 2020; Zhao et al., 2020; Wang et al., 2022). Evaluating the regional WRCC is a crucial step in urban planning and construction (Buckerfield et al., 2020).

WRCC has been extensively studied. In terms of the research object, most of these studies focused on regions with a certain economic scale like basins, provinces, cities, and economic circles, which rely heavily on water resources and are likely to suffer water shortage, whether rich or lack of natural water resources. As reported by Kang et al. (2019), the Haihe River basin has a low agricultural WRCC; the agricultural WRCC in Shanxi, Inner Mongolia, and Liaoning is also small, though there is no overload problem; the WRCC in Beijing, Tianjin, Hebei, Henan, and Shandong is overloaded, and hence it is necessary to optimize groundwater development and adjust the effective irrigation area. Magri and Berezowska-Azzag (2019) evaluated the water carrying capacity (WCC) of Oran, Algeria, based on four scenarios from the aspects of urban water resources sustainability, urban economy, society and environment, and believed that compared with improving water supply, rational development and recycling of water resources is the solution to maintain WCC. Wang et al. (2022) found that under the scenario of rapid economic development, the WRCC and coupling coordination degree of Guangzhou city are the worst, the water environment protection scenario and water conservation scenario are better, and the comprehensive scenario performs the best. Wang et al. (2021) analyzed the current and future WRCC of the Chang-Ji economic circle, and pointed out the major problems of water resources there—water shortage and poor water quality.

Studies that built WRCC evaluation indicator systems turn out to be similar as most involve indicators in the subsystems such as the water resources, the socio-economic, the eco-environmental and so on, though these indicators differ from each other in the natural and social conditions of the studied area or their research focuses (Li et al., 2021; Meng et al., 2021; Wei et al., 2021). Regarding the research methods, as WRCC evaluation involves many indicators that play varied roles in the evaluation system, researchers often need to assign weights to the indicators and then obtain a comprehensive WRCC score based on the weighted mean. Such methods are legion. Wang et al. (2014a) simulated the impact of economic advances and population growth on water consumption in Tongzhou District, Beijing by the system dynamics (SD) model, and found that the region suffered from severe water shortage and the current water supply could not meet the future needs. Peng et al. (2021) proposed the Driver-Pressure-Engineering water shortage-State-Ecological Basis-Response-Management (DPESBRM) concept, and employed the cloud model to calculate the weights of WRCC indicators, which fully considers the randomness and fuzziness of the evaluation object; their method was used to evaluate the WRCC of karst areas in Guiyang, China, and the evaluation results were found to be in line with the TOPSIS-based evaluation outcomes. Deng et al. (2021) quantified the WRCC of Han River basin in 2010–2016 by set-pair analysis, and forecasted the WRCC of the basin in 2035 by the soil and water assessment tool (SWAT) model. Other evaluation methods include analytic hierarchy process (AHP) (Lu et al., 2017), system dynamics (SD) models, neural networks (Wang et al., 2014b), and TOPSIS models (Lin et al., 2020).

Despite the extensive studies on WRCC, few probed into the WRCC in the urban agglomeration of Pearl River Delta (PRD), and even less combined the spatial and temporal dimensions for comprehensive analysis (Xu et al., 2019). Compared with northern China, the PRD is rich in water resources, however, due to the large population, water resources-reliant industries, urban area expansion, and monotonous water sources in the eastern part, the PRD is plagued by water shortage as it develops. To strike a balance between water resources, environment, and economy, manage water resources in a scientific manner, and promote ecological wellbeing the PRD, we believe it is imperative to comprehensively analyze the spatio-temporal changes in the WRCC of the PRD. Based on the present work, collect data from 2015 to 2020 in the PRD, taking into account the differences in water resources, economic development and ecological environment, an WRCC evaluation index model was established, and the entropy weight-TOPSIS model was employed to perform empirical research from spatial and temporal dimensions. Suggestions were proposed based on the research findings and the differences of each cities, to provide a basis for sustainable and quality development of the PRD, and to expand the meaning of WRCC to a certain extent.

Research area overview

The PRD (111.35°E–115.43°E, 21.56°N–24.40°N), located in the mid-south of Guangdong province and the lower reaches of Pearl River (Figure 1), borders on South China Sea and is subject to the subtropical monsoon climate, with an annual average temperature of 21.4°C–22.4°C, and annual

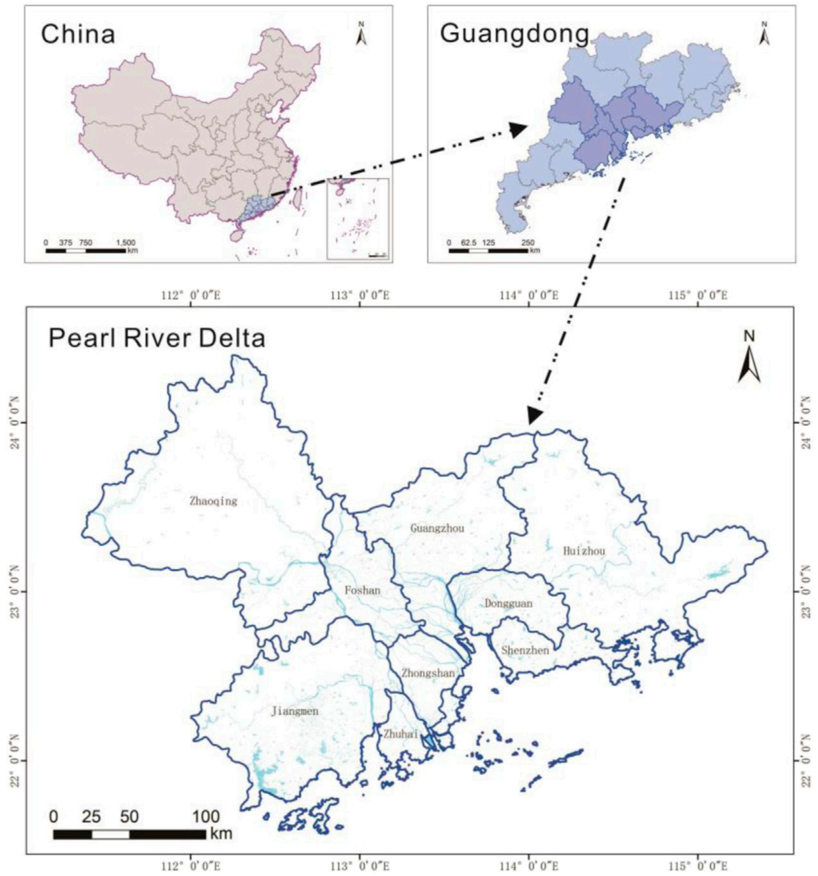

FIGURE 1
Geographical location of the PRD.

precipitation of 1,600–2,300 mm. The PRD accommodates nine cities, i.e., Guangzhou, Shenzhen, Zhuhai, Foshan, Huizhou, Dongguan, Zhongshan, Jiangmen, and Zhaoqing, taking up an area of 55,400 km^2, which is less than one-third of the total area of Guangdong province. As one of the earliest regions that were opened up to the outside world in China, the PRD remains an economic hub for the country and the major part of the Guangdong-Hong Kong-Macau Greater Bay Area. In 2020, the PRD reached an urbanization rate of 85%, and the GDP there reached $1.4 trillion (over 80.8% of the total of Guangdong province). The PRD is at the confluence of Xijiang River, Beijiang River, and Dongjiang River, with rich dense network of waterways.

Research methodology

In the present work, WRCC evaluation index system is constructed, the entropy weight method is used to calculate the weight of each indicator, and the TOPSIS model is used to calculate the annual WRCC and scores of the three subsystems of each city from 2015 to 2020. The weights of indicators, the spatio-temporal changes in the WRCC, and the spatio-temporal changes in the subsystems are discussed, and suggestions for improving the WRCC of PRD is proposed.

Constructing the water resources carrying capacity evaluation index system

Water resources are a vital form of natural resources that social and economic advances hinge on. Developing and utilizing water resources need financial support, and a good environment is the foundation for regeneration of water resources. Thus, to assess regional WRCC, we need to build a multi-layered evaluation system that fully considers factors of water resources, economy, and the natural environment. By referring to relevant works (Xu et al., 2019; Lin et al., 2020; Zhao et al., 2020; Wang et al., 2022) and considering data availability, we constructed a WRCC evaluation indicator

TABLE 1 WRCC evaluation index system for PRD.

Objective layer	Rule layer	Indicator layer	Calculation	Code	Attribute
WRCC evaluation index system	Water resources subsystem (WRS)	Volume of water resources per capita (m3/person)	Total volume of water resources/total population	C1	P
		Water yield modulus (10,000 m^3/km^2)	Total volume of water resources/total area	C2	P
		Water supply per capita (m^3/person)	Volume of water supply/total population	C3	P
		Surface water ratio (%)	Volume of surface water resources/total volume of water resources	C4	P
		Water resources utilization rate (%)	Volume of water supply/total volume of water resources	C5	N
		Annual precipitation (100 million m^3)	—	C6	N
	Socio-economic subsystem (SES)	Population density (person/km^2)	Total population/total area	C7	N
		Natural population growth rate (‰)	—	C8	N
		GDP per capita (10,000 CNY)	GDP/total population	C9	P
		Economic density (100 million CNY/km^2)	GDP/total area	C10	P
		Urbanization rate (%)	Urban population/total population	C11	P
		Water consumption per 10,000 CNY of GDP (m^3)	Total water consumption/GDP	C12	N
		Water consumption per 10,000 CNY of industrial production (m^3)	Industrial water consumption/10,000 CNY industrial production	C13	N
		Urban domestic water consumption per capita (L/d)	Urban water consumption/total population	C14	N
	Eco-environmental subsystem (EES)	Water quality control rate of water functional zone (%)	—	C15	P
		Forest coverage rate (%)	—	C16	P
		Domestic sewage discharge per capita (L/d)	Volume of domestic sewage discharge/total population	C17	N
		Ecological water use rate (%)	Volume of ecological water use/total water consumption	C18	N
		New soil erosion treatment area (km^2)	—	C19	P

Note: P means positive, N means negative; "—" indicates that the indicator is directly extracted from relevant references.

system for PRD. PRD is the confluence of three rivers, where cities vary considerably from each other in terms of local water yield and inflow water volume, and it is challenging to develop inflow water resources, so the water resources subsystem discussed in the present work focuses on the volume and development potential of local water resources, with the volume of water resources per capita and water yield modulus as the evaluation indicators for this subsystem. Population growth and increased water consumption will pose pressure to water resources, but development of water resources utilization facilities and protection of water resources require large economic investment, so such indicators as population density and economic density as selected to assess the socio-economic subsystem of WRCC. Factors that affect water quality like water quality control rate of water functional zone and forest coverage are selected to assess the eco-environmental subsystem of WRCC. Table 1 shows the 19 indicators selected in the present work.

Determining indicator weight by the entropy weight method

A diverse and complex collection of factors contribute to WRCC. The weights should be assigned to the indicators in an objective manner to avoid subjectivity in calculation of weights. In the present work, the entropy weight method that could objectively reflect information in the indicators was employed to resolve the problem of subjectivity of weight assignment. Generally, a smaller entropy of the indicator means a larger entropy weight and hence more importance of the indicator (Kang et al., 2019). With the dimension of time considered, the weight of indicator is calculated as follows:

1) Normalization of the indicators

The primary evaluation matrix of regional WRCC is set as follows:

$$X = \left\{x_{tij}\right\}_{p\times m\times n} (1 \leq t \leq p, 1 \leq i \leq m, 1 \leq j \leq n \tag{1}$$

There are both positive and negative indicators for WRCC evaluation. These indicators are normalized as follows:

For positive indicators:

$$y_{tij} = \left(x_{tij} - \min x_j\right) \Big/ \left(\max x_j - \min x_j\right) \tag{2}$$

And for negative indicators:

$$y_{tij} = \left(\max x_j - x_{tij}\right) \Big/ \left(\max x_j - \min x_j\right) \tag{3}$$

where x_{tij} is the j-th indicator for the city i and the year t; maxx_j and minx_j mean the maximum and minimum of the j-th indicator.

2) The weight of each indicator is:

$$Y_{tij} = y_{tij} \Big/ \sum_{t=1}^{p} \sum_{i=1}^{m} y_{tij} \tag{4}$$

3) The entropy of each indicator can be obtained by the following equation:

$$e_j = -\frac{1}{\ln(p \times m)} \sum_{t=1}^{p} \sum_{i=1}^{m} Y_{tij} \, ln \, Y_{tij} \tag{5}$$

And if $Y_{tij} = 0$, then $Y_{tij} \ln Y_{tij} = 0$.

4) The weight of each indicator can be obtained by the following equation:

$$W_j = \left(1 - e_j\right) \Big/ \sum_{j=1}^{n} \left(1 - e_j\right) \tag{6}$$

where W_j means the entropy weight coefficient; a larger W_j means more information the corresponding indicator conveys, and a more important role this indicator plays in comprehensive evaluation.

TOPSIS model

The technique for order of preference by similarity to ideal solution (TOPSIS) model is a comprehensive evaluation method which can make the best of all primary information to accurately reveal the gaps between different evaluation schemes. The TOPSIS modelling process is as follows:

1) Positive processing is performed on the primary evaluation matrix: $x_{ij} \rightarrow x'_{ij}$ and the normalized decision-making matrix b_{ij}can be obtained by the following equation:

$$b_{tij} = x'_{tij} \Big/ \sqrt{\sum_{i=1}^{m} x'^{2}_{tij}} \tag{7}$$

2) The weighted normalization matrix can be obtained as follows:

$$c_{tij} = w_j \cdot b_{tij} \tag{8}$$

3) The positive ideal solution and the negative ideal solution can be calculated:

$$c_j^+ = \left\{\max c_{tij}\right\} \tag{9}$$

$$c_j^- = \left\{\min c_{tij}\right\} \tag{10}$$

4) The Euclidean distance is employed to calculate the distance of the evaluation object from the positive ideal solution and the negative ideal solution:

$$s_{ti}^+ = \sqrt{\sum_{j=1}^{n} \left(c_{tij} - c_j^+\right)^2} \tag{11}$$

$$s_{ti}^- = \sqrt{\sum_{j=1}^{n} \left(c_{tij} - c_j^-\right)^2} \tag{12}$$

5) The closeness between the evaluation object and the positive and negative ideal solutions is calculated as follows:

$$f_{ti} = s_{ti}^- / \left(s_{ti}^- + s_{ti}^+\right) \tag{13}$$

And the closer f_{ti} is to 1, the better the evaluation object is, which means the score of WRCC is higher.

Data source

The data used in the present work are from the water resources bulletins, annual statistical year books for cities in the PRD, as well as the water resources bulletins, and soil and water conservation bulletins of Guangdong Province in 2015–2020. The calculation method of some indicators is in Table 1.

Results and analysis

Indicator weight

Based on primarily processed data, the entropy weight method was employed to calculate the weight of each indicator, as shown in Table 3. The weights for the WRS, the SES, and the EES are 0.4052, 0.3470, and 0.2478, respectively. The WRS has the largest weight, which means the natural reserve of water resources and water supply engineering capacity are the major contributors to the WRCC of the PRD, and although the geographical distribution of natural water resources cannot be changed, a reasonable WRCC can be maintained through scientific development of water resources and control of population; the SES has the second largest weight, only

TABLE 2 Weights of the 19 indicators for WRCC evaluation of the study area.

Indicator	C1	C2	C3	C4	C5	C6	C7
Weight	0.1169	0.0386	0.0384	0.0550	0.0489	0.1078	0.0128
Indicator	C8	C9	C10	C11	C12	C13	C14
Weight	0.0184	0.0640	0.1496	0.0320	0.0214	0.0347	0.0140
Indicator	C15	C16	C17	C18	C19		
Weight	0.0196	0.0622	0.0475	0.0245	0.0939		

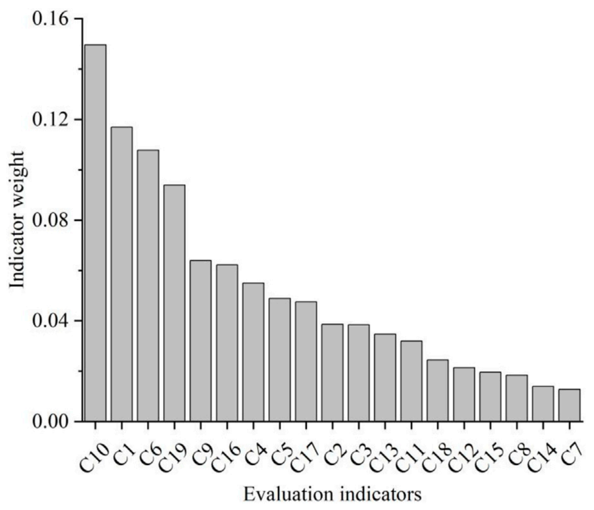

FIGURE 2
Ranking of WRCC evaluation indicators for the PRD.

0.06 less than WRS, which means economic growth not only relies on the natural reserve of water resources, but plays a role in improving the regional WRCC; the EES has the smallest weight, which may be because the impact of changes in the ecological environment on the WRCC is lagging, but a good ecology can sustain the regular water cycle and promote rational development of water resources, and hence the EES is an indispensable part in WRCC evaluation. Indicators with the largest weights in each subsystem are C1, C10, and C19. In this logic, rational development of water resources, acceleration of economic growth, and ecological improvement initiatives are effective measures to improve WRCC.

Table 2 shows the 19 indicators selected in the present work for WRCC evaluation; these indicators are sequenced, as shown in Figure 2. The top-ranking six indicators, C10, C1, C6, C19, C9, and C16, are positive indicators, and two for each subsystem. The weight of C10 is the largest, and C9 ranks fifth, indicating that in the relatively developed PRD, economic investment is particularly important for the utilization and protection of water resources. C1 and C6 take the second place, indicating that natural water resources are the most basic component of WRCC. The treatment of soil erosion and the improvement of forest coverage are conducive to maintaining a good watershed ecology and normal hydrological cycle. That is to say, to improve the WRCC of PRD, we need to fully consider the three subsystems.

Analysis of water resources carrying capacity evaluation results of Pearl River Delta

1) The TOPSIS model was employed to calculate the mean scores of WRCC of the PRD in 2015–2020. The natural breaks method is used to divide the nine cities into three grades according to the scores. With reference to Lin et al. (2020), the connotation and status of WRCC of each grade are explained, as shown in Table 3 and Figure 3 presents the annual changes in WRCC there. As Table 3 reveals, the overall WRCC of the PRD remained small, and the mean score of each city ranges from 0.137 to 0.479; only Shenzhen and Zhaoqing scored higher, followed by Huizhou, Jiangmen and Guangzhou, while Dongguan, Zhuhai, Foshan, and Zhongshan scored relatively lower. As Figure 3 shows, cities along the borders of the PRD including Zhaoqing, Huizhou, Jiangmen, and Shenzhen had the highest WRCC, whereas the five cities in the central region of the PRD had a lower WRCC, demonstrating considerable regional differences. Shenzhen, due to its economic strength, reaches the highest score (0.497), and Zhaoqing, with its rich reserve of water resources and good ecology, has the second largest score of WRCC (0.425), whereas Zhongshan has the lowest score (0.137), and Foshan has the second smallest score (0.174). As Figure 4 shows, in 2015–2020, despite the changes in the WRCC of each city, the ranking of cities remained the same; Foshan, Zhaoqing, and Guangzhou showed stable changes, whereas Shenzhen, Dongguan, and Haizhu presented an upward trend in the evaluation score. As the PRD witnessed a normal and relatively dry year in 2020, with the annual precipitation staying at merely 1,609 mm, all cities in the PRD had a smaller WRCC score in 2020 than in 2019; except Shenzhen and Zhongshan, all other cities had a larger WRCC in 2016 and 2019 than in other years, which is attributed to the rich rainfall in these 2 years and hence a high volume of water resources per capita. The WRCC of the PRD is positively correlated to the precipitation, especially in Guangzhou, Huizhou, Zhongshan, Jiangmen and Zhaoqing, the correlation coefficient is more than 0.72, while Zhuhai is 0.57. To resolve the problem of overdependence of WRCC on natural rainfall, we need to reserve water in the wet years to resolve water shortage in the dry years.

2) The TOPSIS model was used to calculate the score of each subsystem in the WRCC evaluation system for the PRD, and the mean score from 2015 to 2020 was obtained: the mean score for

TABLE 3 Mean WRCC of cities in the PRD from 2015 to 2020.

City	Evaluation score	Evaluation level	Ranking	Connotation	Capacity
Shenzhen	0.497	I	1	Reasonable supply of water resources	The WRCC is moderate, and there is still some potential for further development
Zhaoqing	0.425	I	2	Reasonable supply of water resources	
Huizhou	0.352	II	3	Water shortage	The WRCC reaches the warning threshold, and the potential for further development is limited
Jiangmen	0.332	II	4	Water shortage	
Guangzhou	0.271	II	5	Water shortage	
Dongguan	0.195	III	6	Severe water shortage	The WRCC reaches the upper limit, and there is very limited potential for further development
Zhuhai	0.179	III	7	Severe water shortage	
Foshan	0.174	III	8	Severe water shortage	
Zhongshan	0.137	III	9	Severe water shortage	

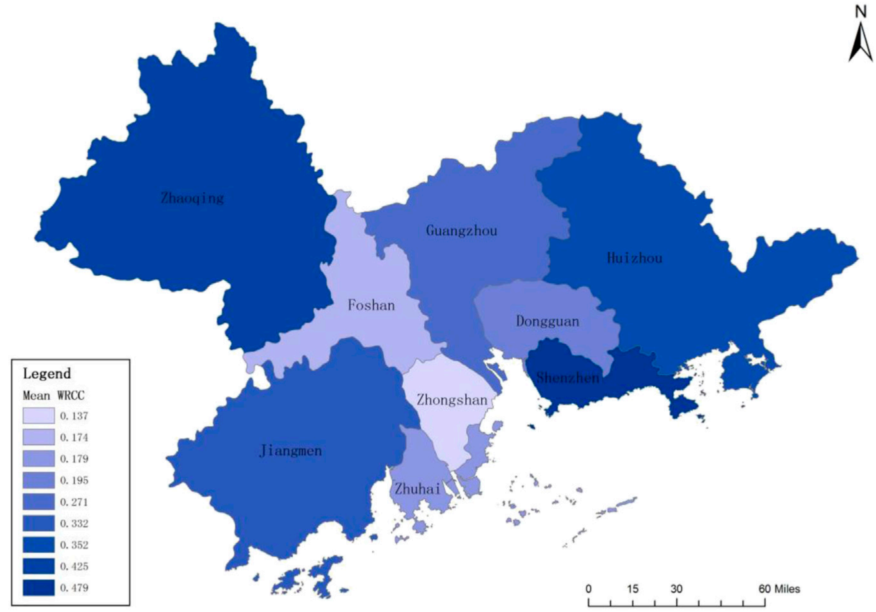

FIGURE 3
Distribution of mean WRCC in PRD in 2015–2020.

WRS, SES, and EES was 0.329, 0.220, and 0.331, respectively. Figure 5 shows the mean WRCC score of each city in the PRD from 2015 to 2020. For cities including Guangzhou, Zhuhai, Foshan and Zhongshan, the score for each subsystem shows little difference; for Shenzhen, however, the SES has a far larger score than the other two subsystems; for Huizhou, Jiangmen, and Zhaoqing, the scores for WRS and EES are far higher than that for the SES. Though Shenzhen had a low volume of water resources per capita (C1), a small annual precipitation (C6), a high population density (C7), and a high ecological water utilization rate (C18), it ranked top among all cities in the PRD in terms of the economic density (C10), urbanization rate (C11), water use volume per 10,000 yuan of GDP (C12), and water use volume per 10,000 yuan of industrial production (C13), which makes up for the lows in WRS and EES. In future urban planning of Shenzhen, it is necessary to better allocate water resources, maintain water diversion projects, improve the ecology, and seek new sources of water supply. For Huizhou and Zhaoqing, the score for SES is far smaller than that for WRS and EES. Thus, these two cities should make the fullest of their rich water resources and good environment

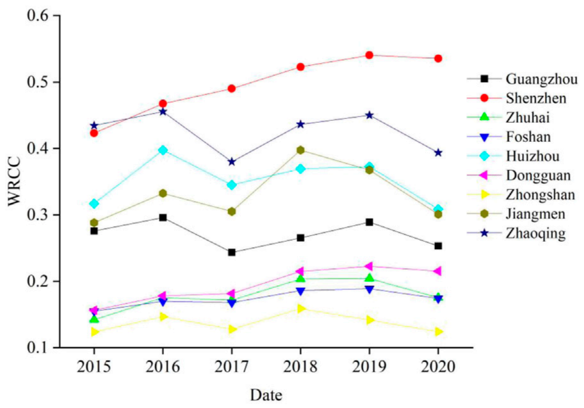

FIGURE 4
Changes in WRCC of cities in the PRD in 2015–2020.

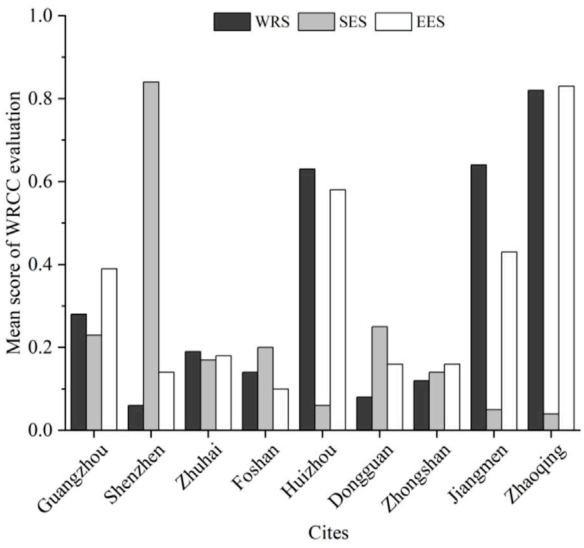

FIGURE 5
Mean score of subsystems in WRCC evaluation of cities in PRD.

to restructure the industries and boost economic growth. In sum, cities in the PRD, which constitute one the most important urban agglomerations in China, should cooperate with each other to achieve optimized transfer of industries and resources, and join hands to improve the natural environment.

3) The subsystems for WRCC evaluation in the PRD show considerable differences, which implies the problems like uneven distribution of water resources, unbalanced economic growth, and varied efforts for ecological improvement in this region. By the score of the WRS in WRCC evaluation, the cities are ranked as follows: Zhaoqing > Jiangmen > Huizhou > Guangzhou > Zhuhai > Foshan > Zhongshan > Dongguan > Shenzhen, and the gap between the maximum (0.817) and the minimum (0.063) is 0.754, which shows varied possession of water resources among cities. Zhaoqing, Huizhou, and Jiangmen boast rich rainfall, with the volume of water resources per capita reaching 3,700, 2,700, and 2,900 m^3/person; besides, with a low water resources utilization rate, the score for the WRS in these three cities is higher than in other cities, indicating the great potential for development of water resources in these cities. For Guangzhou, despite the high precipitation and water supply per capita, the volume of water resources per capita there is only half that of the PRD, and the water utilization rate is high, so the city achieves a score merely at 0.275. Zhuhai, because of its low volume of water resources per capita and small annual precipitation, reaches a score of mere 0.188 in WRCC evaluation. Foshan, Zhongshan, Dongguan, and Shenzhen feature a low annual precipitation and large population, with a volume of water resources per capita at merely 190–590 m^3/person, and hence achieving small scores in WRCC evaluation, at 0.136, 0.121, 0.080, and 0.063, respectively.

By the score of the SES in WRCC evaluation, the cities in the PRD are sequenced as follows: Shenzhen > Dongguan > Guangzhou > Foshan > Zhuhai Zhongshan > Huizhou > Jiangmen > Zhaoqing. The top ranking four cities have a high urbanization rate, all with a rate higher than 90% except Guangzhou, and the rate in Shenzhen even approaches 100%. Besides, these four cities have a high economic density and a high GDP per capita; in particular, Shenzhen has an economic density of $186 million/$km^2$, and a GDP per capita of $28,000/year; besides, the city's strong initiatives towards green economy and low-carbon economy have contributed to coordinated development of water resources and economy. Zhaoqing, which ranks the last among all the cities in the PRD with a score at mere 0.042, has an urbanization rate lower than 50%, and a per-capita GDP of merely $8,000/year, less than 1/3 of that in Shenzhen. These can be attributed to the low GDP in Zhaoqing, the large area of land, its irrational industrial layout, defective industrial chains for the manufacturing and service sectors, and a low water utilization rate of industries. Therefore, in future planning of Zhaoqing, it is necessary to balance resources and economic growth.

By the score of EES in WRCC evaluation, the cities in the PRD are ranked as follows: Zhaoqing > Huizhou > Jiangmen > Guangzhou > Zhuhai > Zhongshan > Dongguan > Shenzhen > Foshan. The cities have varied degrees of environmental quality and ecological treatment efforts, and cities with a higher score often have a larger area. Jiangmen and Zhaoqing have water functional areas with a high water quality control rate; Zhaoqing and Huizhou has a large forest coverage rate and large areas of new soil erosion treatment. Cities with lower scores generally have a smaller area: Foshan, Zhuhai, and Guangzhou have a high domestic sewage discharge per capita; Zhongshan, Foshan, and Zhuhai have a small forest coverage rate. Therefore, cities with a high score in WRCC evaluation need to maintain good environment, strengthen pollution treatment, and promote the pollution accountability systems; for cities with a large

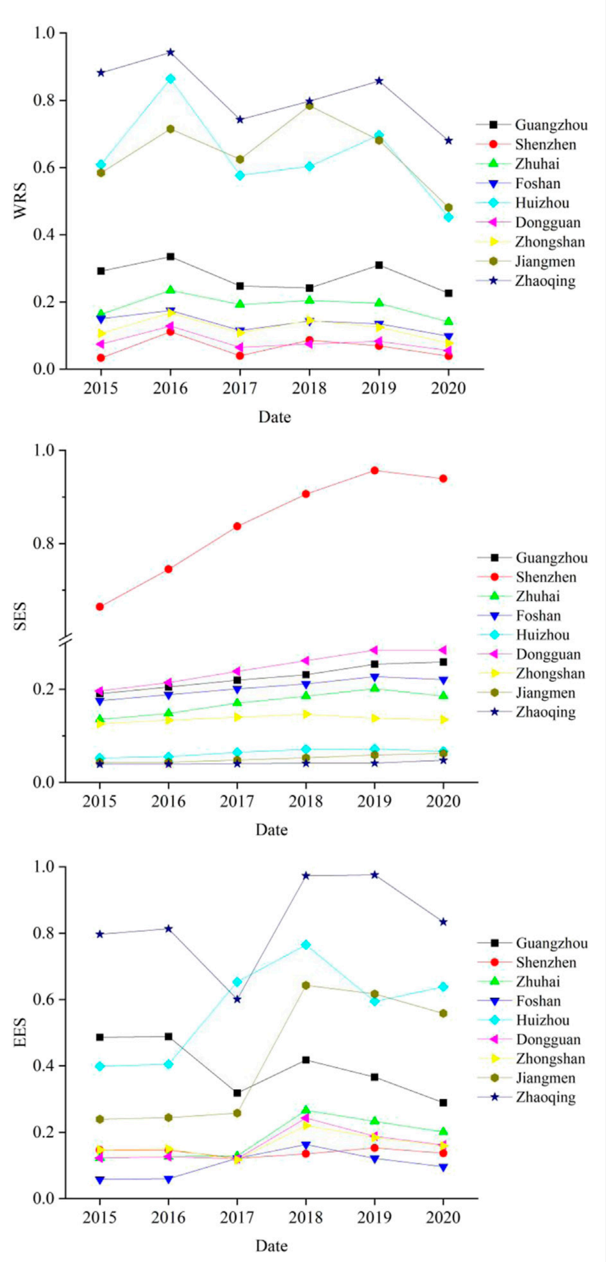

FIGURE 6
Changes in the score of the WRS, SES, and EES in regional WRCC evaluation of cities in PRD from 2015 to 2020.

population and a small area of land, ecological improvement can only play a limited role in increasing the regional WRCC, so it is necessary to find new solutions for environmental treatment and achieve harmony between human and nature.

Analysis of the three subsystems in WRCC evaluation show that cities including Shenzhen, Dongguan, Zhongshan, and Foshan need to make better use of their limited water resources and optimize spatial and temporal allocation of water resources; cities like Zhaoqing, Jiangmen, Huizhou, and Zhongshan should promote industry upgrading, encourage green production and boost economic growth; Cities including Foshan, Shenzhen, Dongguan and Zhongshan need to curb blind expansion of urban areas and reserve more area for the “lucid waters and lush mountains.”

4) As Figure 6 shows, as the time proceeds, the score of the WRS in WRCC evaluation varied from 2015 to 2020, registering a slight decrease overall. The scores for Zhaoqing, Jiangmen, and Huizhou varied considerably, whereas the scores for other cities remained stable. The score for the SES remains stable, with a slight increase; the score for Shenzhen saw a rapid rise, followed by Dongguan and Guangzhou. Under the impact of the Covid-19 pandemic, however, the score for all cities stayed low in 2020. For most cities in the PRD, the score for EES in WRCC evaluation presented an upward trend, though with slight fluctuations; Guangzhou, however, witnessed a dropped score due to its reduced new soil erosion treatment area and increased utilization rate of water for ecological purposes. Though economic growth and ecological treatment can improve regional WRCC, uneven distribution of water resources and increased water demand along with economic growth will still reduce the regional WRCC. Therefore, we need to proceed with strict water resources management policies, encourage water-saving efforts, and transfer water resources in water-rich regions to water-short areas to achieve coordinated development among regions.

Conclusion and suggestions

Conclusion

In the present work, the WRCC of cities in PRD was discussed, and the following conclusion were reached:

1) The three subsystems are sequenced as follows by the weight they have in WRCC evaluation: WRS > SES > EES. Indicators including economic density, C10, C1, C19, C9, and C16 contribute considerably to the regional WRCC of the PRD. Rationally developing water resources, boosting economic growth, and improving the environment are effective measures to improve the regional WRCC.

2) From 2015 to 2020, the WRCC of the PRD remained low overall, with significant regional differences. Cities along the borders of the PRD like Zhaoqing, Huizhou, Jiangmen, and Shenzhen reached a high score in WRCC evaluation, whereas cities in the central area of the PRD achieved a lower score. Though the WRCC of each city changed over time, the ranking of cities by the score of WRCC remained largely the same. The WRCC was found to be positively correlated to precipitation. The scores of WRS, SES, and EES were 0.3288, 0.2202, and 0.3306, respectively. For cities including Guangzhou, Zhuhai, Foshan and Zhongshan, the subsystems achieved similar scores in WRCC evaluation; in Shenzhen, SES achieved a far higher score than the other two subsystems in WRCC evaluation; for Huizhou, Jiangmen, and Zhaoqing, WRS reached a far higher score in WRCC evaluation than the other two subsystems.

3) As further analysis of the three subsystems shows, Zhaoqing, Huizhou, and Jiangmen boast a rich reserve of water resources and considerable potential for further development; Shenzhen, Dongguan, Zhongshan, and Foshan are in short supply of water; Shenzhen, Dongguan, Guangzhou, and Foshan enjoy considerable economic strength, which contributes to coordinated development of the water environment and economy. Zhaoqing, which ranks last in the WRCC evaluation, is less developed than other cities. Zhaoqing, Huizhou, and Jiangmen have a large area of land and good ecology, whereas other cities should pay more attention to promote coordinated development between economic growth and ecological wellbeing.

Suggestions

As the construction of the Guangdong-Hong Kong-Macau Greater Bay Area moved forward, the PRD is bound to see population and economic growth, which will pose tangible challenges to the sustainable development of water resources. In the future, cities in the PRD should cooperate with each other to optimize spatial and temporal allocation of water resources. For example, optimizing the allocation of water resources in the Dongjiang River, and transferring water to water scarce cities in the eastern PRD by Xijiang River diversion project. In order to drive the social-economic development of Zhaoqing, Jiangmen, and Huizhou, green economy and industry configuration should be encouraged. On the basis of comprehensively promotion of the pollution accountability systems, and pursue ecological wellbeing, we should attach importance to the governance of urban rivers in Guangzhou, Zhongshan, and Foshan, and strengthen the monitoring and assessment of environmental health risks. Furthermore, we should push forward the initiatives to build a water-saving society, taking advantage of the economic of the PRD, with further improvement of water resources utilization efficiency. We can also incorporate more data and set thresholds for the evaluation indicators to capture changes in regional WRCC, thereby providing a scientific basis for sustainable development of water resources, economic growth, and ecological improvement in PRD.

Contributions, limitations, and future research

In the present work, 19 indicators were selected, and the entropy weight-TOPSIS model was employed to calculate the WRCC score of cities in the PRD from 2016 to 2020 with relation to WRS, SES, and EES. The distribution pattern of WRCC was analyzed, and contributing factors to regional WRCC were explored on the temporal and socio-economic dimensions. Moreover, suggestions were proposed to promote harmony between water resources and human in PRD.

Nonetheless, there are some limitations in our work. First, the water resources system is complex and constantly changing, and WRCC has such characteristics as diversity, dynamic changes, and fuzziness. Evaluation of WRCC in our work, however, is static evaluation based on historical data and a limited set of indicators; the interactions between subsystems are overlooked; and the results are applicably only to the years between 2015 and 2020. In future works, it is necessary to improve the evaluation indicator system by introducing new indicators related to water conservation and the water environment, increase the basis data to make the research result more scientific and practical; in addition, scientific methods should be adopted to predict the impacts of different urban development plans on the future WRCC of PRD.

Data availability statement

The original contributions presented in the study are included in the article/supplementary material, further inquiries can be directed to the corresponding author.

Author contributions

YZ and QY conceived the conceptualization, acquired the funding and administrated the project; ZL and BZ conducted the investigation, analyzed data and refined the methodology; YZ wrote the original draft; QY reviewed and YZ editing the final paper.

Funding

This study was supported by the Scientific Research Project approved by Department of Education of Guangdong Province (No. 2020KQNCX125) and Scientific Research Foundation of Guangzhou Xinhua University (Nos 2020KYQN01 and 2019KYYB08), Human Geography and Urban-rural Planning, the construction of Guangdong first class undergraduate Program (F22MJ04JY).

Acknowledgments

The authors are grateful for the anonymous referees for their comments and suggestions, which allowed us to improve the quality of this paper.

Conflict of interest

The authors declare that the research was conducted in the absence of any commercial or financial relationships that could be construed as a potential conflict of interest.

Publisher's note

References

Buckerfield, S. J., Quilliam, R. S., Bussiere, L., Waldron, S., Naylor, L. A., Li, S. L., et al. (2020). Chronic urban hotspots and agricultural drainage drive microbial pollution of karst water resources in rural developing regions. *Sci. Total Environ.* 744, 140898. doi:10.1016/j.scitotenv.2020.140898

Clarke, A. L. (2002). Assessing the carrying capacity of the Florida Keys. *Popul. Environ.* 23 (4), 405–418. doi:10.1023/a:1014576803251

Deng, L. L., Yin, J. B., Tian, J., Li, Q. X., and Guo, S. L. (2021). Comprehensive evaluation of water resources carrying capacity in the Han River Basin. *Water* 13, 249. doi:10.3390/w13030249

Falkenmark, M., and Lundqvist, J. (1998). Towards water security: Political determination and human adaptation crucial. *Nat. Resour. Forum* 22 (1), 37–51.

Kang, J., Zi, X., Wang, S. F., and He, L. Y. (2019). Evaluation and optimization of agricultural water resources carrying capacity in Haihe river basin. *Water* 11, 999. doi:10.3390/w11050999

Li, J. X., Ke, L. F., Yang, L., and Qi, H. S. (2021). Research on the county water resources carrying capacity in the new period. *E3S Web Conf.* 276, 01009. doi:10.1051/e3sconf/202127601009

Lin, L. Z., Li, D., and Lin, Z. (2020). Evaluation of water resources carrying capacity in Kubuqi Desert Area based on entropy weight and TOPSIS model. *J. Central China Normal Univ. Nat. Sci.* 54 (4), 640–648. (in Chinese).

Lu, Y., Xu, H. W., Wang, Y. X., and Yang, Y. (2017). Evaluation of water environmental carrying capacity of city in huaihe River basin based on the AHP method: A case in huai'an city. *Water Resour. Industry* 18, 71–77. doi:10.1016/j.wri.2017.10.001

Magri, A., and Berezowska-Azzag, E. (2019). New tool for assessing urban water carrying capacity (WCC) in the planning of development programs in the region of Oran, Algeria. *Sustain. Cities Soc.* 48, 101316. doi:10.1016/j.scs.2018.10.040

Meng, L. H., Liu, Y. C., Ma, W. J., Wang, Q. Y., Mo, X. L., and Tian, J. M. (2021). Variable fuzzy evaluation model for water resources carrying capacity in the Tarim River Basin, China. *Water Supply* 22, 1445–1458. doi:10.2166/ws.2021.341

Milano, M., Ruelland, D., Dezetter, A., Fabre, J., Ardoin-Bardin, S., and Servat, E. (2013). Modeling the current and future capacity of water resources to meet water demands in the Ebro basin. *J. Hydrology* 500, 114–126. doi:10.1016/j.jhydrol.2013.07.010

Peng, T., Deng, H. W., Lin, Y., and Jin, Z. Y. (2021). Assessment on water resources carrying capacity in karst areas by using an innovative DPESBRM concept model and cloud model. *Sci. Total Environ.* 767, 144353. doi:10.1016/j.scitotenv.2020.144353

Wang, G., Xiao, C. L., Qi, Z. W., Liang, X. J., Meng, F. N., and Sun, Y. (2021). Water resource carrying capacity based on water demand prediction in chang-ji economic circle. *Water* 13, 16. doi:10.3390/w13010016

Wang, S., Xu, L., Yang, F. L., and Wang, H. (2014). Assessment of water ecological carrying capacity under the two policies in Tieling City on the basis of the integrated system dynamics model. *Sci. Total Environ.* 472, 1070–1081. doi:10.1016/j.scitotenv.2013.11.115

Wang, W. Y., Zeng, W. H., Yao, B., and Wei, J. (2014). A simulation impact evaluation of social-economic development on water resource use. *J. Water Reuse Desalination* 4 (3), 137–153. doi:10.2166/wrd.2014.050

Wang, X., Liu, L., Zhang, S., and Gao, C. (2022). Dynamic simulation and comprehensive evaluation of the water resources carrying capacity in Guangzhou city, China. *Ecol. Indic.* 135, 108528. doi:10.1016/j.ecolind.2021.108528

Wei, Y. J., Wang, R., Zhuo, X., and Feng, H. Y. (2021). Research on comprehensive evaluation and coordinated development of water resources carrying capacity in qingjiang River basin, China. *Sustainability* 13, 10091. doi:10.3390/su131810091

Wu, C. G., Zhou, L. Y., Jin, J. L., Ning, S. W., Zhang, Z. X., and Bai, L. (2020). Regional water resource carrying capacity evaluation based on multi-dimensional precondition cloud and risk matrix coupling model. *Sci. Total Environ.* 710, 136324. doi:10.1016/j.scitotenv.2019.136324

Xu, Z. Q., Liu, X. Y., Xiao, S. H., Duan, L., Deng, Q. Y., and Li, J. (2019). Evaluation and obstacle factors study of water environmental carrying capacity in the Pearl River Delta. *J. Environ. Eng. Technol.* 9 (1), 44–52. (in Chinese).

Zhao, Y., Wang, Y. Y., and Wang, Y. (2020). Comprehensive evaluation and influencing factors of urban agglomeration water resources carrying capacity. *J. Clean. Prod.* 288, 125097. doi:10.1016/j.jclepro.2020.125097

frontiers | Frontiers in Environmental Science

TYPE Original Research
PUBLISHED 11 October 2022
DOI 10.3389/fenvs.2022.1023356

Comprehensive recycling of fresh municipal sewage sludge to fertilize garden plants and achieve low carbon emission: A pilot study

Xianke Lin[1], Canming Chen[1], Huashou Li[2], Liang Hei[3], Luping Zeng[4], Zebin Wei[1], Yangmei Chen[1] and Qi-Tang Wu[1]*

[1]Guangdong Provincial Key Laboratory of Agricultural and Rural Pollution Abatement and Environmental Safety, College of Natural Resources and Environment, South China Agricultural University, Guangzhou, China, [2]Key Laboratory of Tropical Agro-Environment, Ministry of Agriculture, South China Agricultural University, Guangzhou, China, [3]Key Laboratory of the Pearl River Estuarine Dynamics and Associated Process Regulation, Ministry of Water Resources, Pearl River Hydraulic Research Institute, Pearl River Water Resource Commission, Guangzhou, China, [4]National Key Laboratory of Water Environmental Simulation and Pollution Control, South China Institute of Environmental Sciences, Ministry of Environmental Protection of the People's Republic of China, Guangzhou, China

OPEN ACCESS

EDITED BY
shengsen wang,
Yangzhou University, China

REVIEWED BY
Guodi Zheng,
Institute of Geographic Sciences and Natural Resources Research (CAS), China
jose navarro pedreño,
Miguel Hernández University of Elche, Spain

*CORRESPONDENCE
Qi-Tang Wu,
wuqitang@scau.edu.cn

SPECIALTY SECTION
This article was submitted to Water and Wastewater Management,
a section of the journal
Frontiers in Environmental Science

RECEIVED 19 August 2022
ACCEPTED 26 September 2022
PUBLISHED 11 October 2022

CITATION
Lin X, Chen C, Li H, Hei L, Zeng L, Wei Z, Chen Y and Wu Q-T (2022), Comprehensive recycling of fresh municipal sewage sludge to fertilize garden plants and achieve low carbon emission: A pilot study.
Front. Environ. Sci. 10:1023356.
doi: 10.3389/fenvs.2022.1023356

Recycling nutrients in municipal sewage sludge (MSS) to soil would support sustainable development. In this study, a comprehensive recycling using specific plants able to grow in the fresh MSS and an indirect application technique was developed. Fresh MSS was placed in permeable containers next to *Handroanthus chrysanthus* plants to provide indirect fertilization. Sludge treatment plants (*Alocasia macrorrhiza* and *Pennisetum hybridum*) were grown directly on the Fresh MSS to produce plant biomass and treat MSS. The basal diameters of the *H. chrysanthus* plants were markedly increased by the treatment. Nutrients were extracted from MSS more readily and more biomass was produced by the *P. hybridum* than the *A. macrorrhiza* plants. The heavy metal contents of the soil did not increase significantly and not generate potential ecological risk, but the organic matter, nitrogen, and phosphorus contents increased markedly. The fresh MSS leachate met the relevant fecal coliform and heavy metal irrigation water standards. At the end of the treatment, the MSS mass had markedly decreased and the treated MSS was used as a seedling substrate for two garden plant seedlings. The net carbon emissions from the comprehensive recycling are estimated as -15.79 kg CO_2e (CO_2 equivalent) per ton fresh sludge, in contrast, the emissions from composting treatment are estimated as 8.15 kg CO_2e. The method allows nutrients in MSS to be recycled without causing heavy metal pollution and without net carbon emission, while gives gardening products with commercial value.

KEYWORDS

municipal sewage sludge, indirect application, garden plant, greenhouse gas emissions, sludge treatment plant

1 Introduction

Municipal sewage sludge (MSS) is a solid waste produced during sewage treatment processes and contains large amounts of nutrients that could be utilized. However, MSS also contains relatively large amounts of harmful substances, and appropriate disposal of MSS is challenging but must be achieved to protect human and environmental health. Researchers around the world have been developing methods for treating and disposing of MSS for many years (Parr et al., 1978). Such methods involve phosphorus recovery, co-incineration, building material production, and anaerobic fermentation (Chang et al., 2020; Liang S. et al., 2021; Liang Y. et al., 2021; Iglesias-Iglesias et al., 2021; Zat et al., 2021; Ottosen et al., 2022). There are many excellent techniques for treating and disposing of MSS, but many are too expensive to be used in developing areas. The focus has previously been on disposing of MSS in economically developed areas, but MSS disposal in developing areas should not be ignored.

It is expensive to use advanced MSS treatment methods. Installing a MSS dehydration and incineration plant in China costs US$ 578,000/ (t MSS) before operating costs (Hao et al., 2019). There are additional costs involved in using MSS ash. Yu et al. (2021) calculated the cost of recovering phosphorus from MSS ash and found that, excluding the cost of producing the MSS ash and building a phosphorus recovery system, the reagents required to produce 1 kg of hydroxyapatite ($Ca_5(PO_4)_3OH$) cost US$ 32.2 whereas producing 1 kg of hydroxyapatite from phosphate ore cost only US$ 1.0 ± 0.3. These methods may be able to be used in large developed cities but cannot be afforded in developing areas. Many areas in China and other developing countries are economically developing. Local economic conditions clearly need to be considered when selecting a MSS disposal technique (Lu et al., 2019).

Applying MSS to land is a cheap disposal technique that has been used for a long time (Guoqing et al., 2019). This returns soil-derived nutrients in MSS to the soil and creates a circular flow of nutrients (Gronman et al., 2016). Sludge applications in forests can be environmentally sound if application rates are matched to site characteristics (Zasoski et al., 1984). Badza et al. (2020) assessed the use of MSS in agricultural processes using the characteristics of MSS from 18 wastewater treatment plants in South Africa and found that applying MSS to land was the best option. However, hazardous substances in MSS pose risks to soil, plants, and humans. In particular, heavy metals in MSS tend to accumulate in soil (Zhang et al., 2021), can enter the food chain through surface water and groundwater, and can be absorbed by crops (Zeng et al., 2019), so direct application of MSS to land is controversial (Hei et al., 2016). Composting MSS does not decrease the total amount of heavy metals in the MSS (Wei Y. et al., 2020), so heavy metals can be released into the soil when MSS compost is applied to soil. Riaz et al. (2018) found Cd concentrations higher than the relevant limits in rice grown in soil to which MSS compost and MSS had been applied at an application rate of 1% of the soil mass.

The heavy metals contamination issue is being attracted much attention in China because the soils in south China are acid and the capacity for heavy metals is low. This was why the MSS compost is being banned since 2021 by the Chinese Ministry of Agriculture to be an “organic fertilizer” to apply to agricultural lands *via* the organic fertilizer standards (NY/T 525–2021). Accordingly, an indirect application technique (IAT) allowing MSS to be used to fertilize crops while preventing heavy metal contamination of the soil was proposed (Lin et al., 2021b). This technique uses permeable bags to contain the sludge and, after the release of nutrients such as N, *p*, K *via* leaching by rainfall or spread irrigation, the most part of heavy metals (less soluble than major nutrients) is recovered and taken away from agricultural lands with the solid residue of sludge. It has previously been found that nutrients leached more readily than heavy metals from MSS (Xu et al., 2015; Lin et al., 2021a). Considerably less heavy metal pollution therefore occurs when the IAT is used than when normal MSS application methods are used. It was found in a nine-year study that the IAT is a cheap and simple method for using MSS to fertilize crops that provides nutrients for plants such as bananas, papayas, and corn and does not cause the soil to become contaminated with heavy metals (Lin et al., 2021b). It has been found that specific plants (later called sludge treatment plants) can be grown on fresh MSS and that the plant products can safely be harvested and used. Samake et al. (2003) found that *Alocasia macrorrhiza* can be grown on MSS. It has been found that *A. macrorrhiza* stabilized MSS in ~5 months, during which time the number of *Escherichia coli* markedly decreased and the cress seed germination index reached 100%. Hei et al. (2016) found that *Pennisetum hybridum* seedlings transplanted with substrate into fresh MSS survived and that the harvested *P. hybridum* was economically valuable. Combining the IAT with sludge treatment plants could allow MSS to be used to cheaply generate economic benefit while disposing of the MSS.

In this study, we developed a comprehensive recycling method to recycle MSS using the IAT and sludge treatment plants. The aim was to develop a low-carbon, cheap, and safe MSS disposal technique that will allow MSS to be treated of in developing areas. The fertilization effect and safety of the IAT were assessed at a high MSS application rate (720 t/ha fresh MSS) using the garden tree species *Handroanthus chrysanthus*. Sludge treatment plants (*A. macrorrhiza* and *P. hybridum*) were concurrently grown in the MSS and the products were harvested to give additional value. The treated MSS was then recycled and used as a substrate in a plant nursery to ensure that the resource was completely utilized. Finally, the carbon emission or the greenhouse gas emissions

TABLE 1 Municipal sewage sludge (MSS) and soil characteristics.

Index	MSS I	MSS II	Soil
^{a} WC (%)	^{b} 87.98 ± 0.70	86.69 ± 0.50	-
^{a} FC	0.0300 ± 0.0100	0.0005 ± 0.0003	-
^{a} GI	0.08 ± 0.09	1.32 ± 0.16	-
pH	6.82 ± 0.11	5.84 ± 0.02	5.41 ± 0.15
^{a} OM (g/kg)	435.6 ± 18.3	364.2 ± 9.8	17.9 ± 2.5
N (g/kg)	42.55 ± 0.76	34.25 ± 0.84	0.94 ± 0.08
p (g/kg)	30.09 ± 1.02	26.87 ± 0.59	0.61 ± 0.11
K (g/kg)	10.95 ± 0.06	5.37 ± 0.32	15.07 ± 2.83
Cd (mg/kg)	0.841 ± 0.075	1.466 ± 0.018	0.037 ± 0.008
Cu (mg/kg)	120.5 ± 2.2	3602.1 ± 99.8	14.1 ± 3.2
Pb (mg/kg)	44.72 ± 6.82	77.58 ± 2.49	57.15 ± 2.86
Zn (mg/kg)	389.9 ± 61.8	880.0 ± 19.5	75.6 ± 7.8

^{a}WC, is water content in fresh weight (FW) basis; FC, is fecal coliform value (g^{-1}. FW); GI, is germination index of Chinese cabbage seeds; OM, is organic matter content; OM, and elements contents are all in dry weight (DW) basis.

^{b}All data values represent the means ± standard error (n = 3).

(GHGE) of the comprehensive recycling of MSS were also estimated.

2 Materials and methods

2.1 Experiment one: comprehensive treatment of MSS on land in a garden

2.1.1 Experimental site and materials

The experimental site, which had mountainous lateritic red soil, was in a forest of one-year-old *H. chrysanthus*. The site was ~900 m2 and was far from any heavily populated areas (N 23°19′32.05″, E 113°46′5.79″). The MSS used in the experiment, later called MSS I, was collected at a sewage treatment plant in a residential area near the BYD Auto Co. Plant in Huizhou, Guangdong Province, China. The sewage treatment plant used the A^2/O method to treat domestic sewage, and the MSS was dehydrated through mechanical compression. The physicochemical properties of MSS I are shown in Table 1. In southern China, there are less Hg and As in MSS, the main heavy metals with high contamination risk are Cd, Cu, Pb, and Zn (Guo et al., 2014), so this study focuses on these four heavy metals.

The *P. hybridum* plants were obtained from the Ecological Experiment Base of the South China Agricultural University (Guangzhou, Guangdong Province, China). Old stems of *P. hybridum* with similar diameters and strengths were selected, and stem segments with two tillering nodes were cut. Seedlings were cultivated in small pots for 2 weeks and then transplanted with the nursery substrate into the MSS used in the experiment. The *A. macrorrhiza* plants were obtained from the green belt of the South China Agricultural University. Newly grown *A. macrorrhiza* seedlings were selected and grown in small pots. Two weeks later, the seedlings were transplanted with nursery substrate into fresh MSS.

The MSS utilization method that was used is called an indirect application technique (IAT; Lin et al., 2021b). Briefly, a permeable mesh was laid over the soil, then a cylindrical container was formed on the permeable mesh using a root controlling material that is commonly used in gardens (Peter, 2000). MSS was added to the container to allow the MSS to indirectly fertilize the *H. chrysanthus* plants. Sludge treatment plants (*A. macrorrhiza* and *P. hybridum*) were planted in the MSS to further utilize the nutrients in the MSS (Figure 1).

The experimental design is shown in Figure 1. The ~900 m^2 forested land containing *H. chrysanthus* was divided into nine rows. Treatments were randomly assigned to the rows. Three rows were used for each treatment, and there were three treatments (control (CK), AM (indirect fertilization of *H. chrysanthus* and planting with *A. macrorrhiza* on MSS), and PM [(indirect fertilization of *H. chrysanthus* and planting with *P. hybridum* on MSS)]. The CK rows received no treatment, meaning natural *H. chrysanthus* growth occurred. For the AM and PM treatments, a black fiber mesh was laid on the ground and four sludge containers, each with a diameter of 1 m, were placed around each tree. Fresh MSS (250 kg) was added to each container, and 4 *A. macrorrhiza* or *P. hybridum* seedlings were planted in the fresh MSS (about five plants per m^2 of sludge surface). The surface of the fresh MSS was covered with 1 kg of mature composted MSS after planting to prevent harmful organisms and gases being released to the air. MSS was applied to 48 trees, and 48 t of MSS was used to treat the trees. The basal diameter, diameter at breast height, height, and crown width of each *H. chrysanthus* tree were determined before and after the experiment to assess growth.

2.1.2 Sample collection and analysis

Surface soil (0–20 cm) and MSS samples were collected from the experimental area before and after the experiment. The N and *p* contents of the soil and MSS samples were determined using established methods (Lu, 2000). The Cd, Cu, Pb, and Zn contents of the soil and MSS were determined by atomic absorption spectrophotometry after digestion in a microwave according to a Chinese environmental standard method (HJ 832–2017, HJ means the method is certified by Ministry of Environmental Protection of China) and using the standard substance (GBW-07405: GSS-5) for analysis quality control. The germination index (GI) of MSS was determined using a method proposed by the Chinese sludge standards (GB/T 23,486–2009) using the Chinese cabbage seed germination test. This test is similar to the cress seed germination test, which is internationally recognized as a measure of the phytotoxicity of the sludge material (Zucconi et al., 1981), and calculates this parameter using the following equation:

GI = (seed germination rate (%) X root length) of treatment/(seed germination rate (%) X root length) of water control.

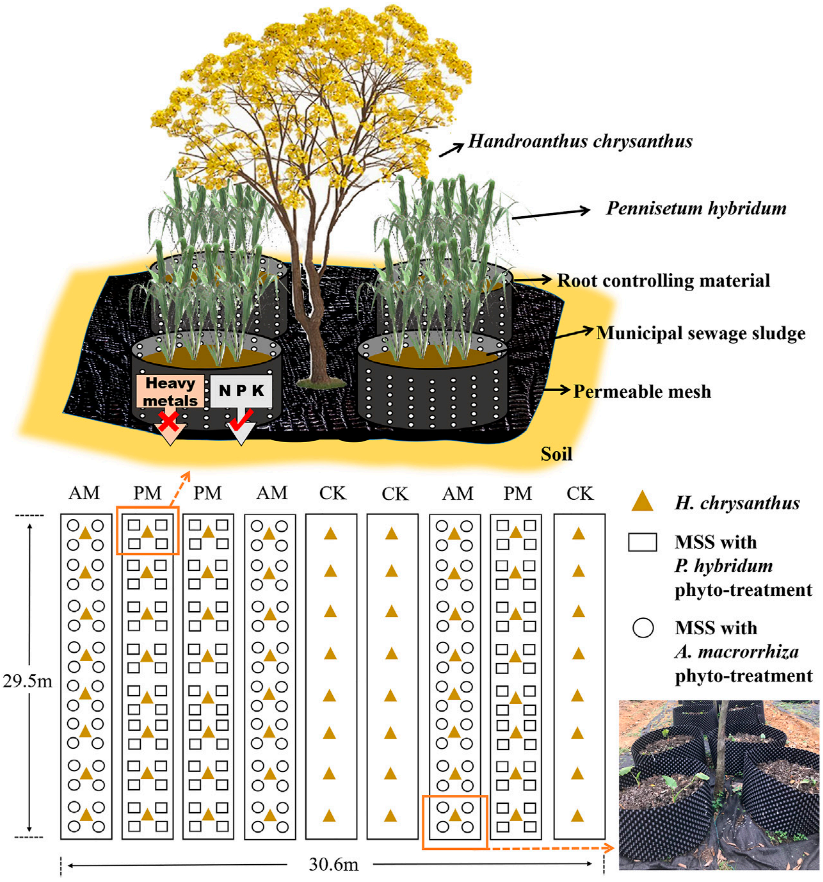

FIGURE 1
Layout of the experimental site and treatments (CK: control without MSS addition; AM: added MSS with *A. macrorrhiza* phyto-treatment; PM: added MSS with *P. hybridum* phyto-treatment).

The fecal coliforms in MSS were detected using the fermentation method (GB 7959–2012, GB means the method is National Standard Method of China).

Once the experiment had started, samples of *A. macrorrhiza* and *P. hybridum* grown on MSS were collected from random four sludge container under two *H. chrysanthus* trees per treatment in months 1, 2, 3, and 6 to allow the optimal harvest times for *A. macrorrhiza* and *P. hybridum* to be determined. Plant samples collected in month 6, were deactivated at 105°C for 30 min, and then dried at 65°C for 48 h. The dry samples were ground and then the nutrient and heavy metal contents were determined. The plant samples were digested in H_2SO_4 and H_2O_2 and then the N and *p* contents were determined using the methods proposed by Chinese Society of Soil Science (Lin et al., 2021b). The K and heavy metal contents (Cd, Cu, Pb, and Zn) of the plant samples were determined by atomic absorption spectrophotometry (GB/T 5009.15–2014) and using a standard substance (GBW-10013: GSB-4) for quality control.

2.1.3 Evaluation of the potential ecological risk of soil heavy metals

Hakanson potential ecological risk assessment was used to assess the risk of heavy metal pollution in the soil (Hakanson, 1980). The potential ecological risk index for single heavy metal (E) and all heavy metals (RI) were calculated using the following equation:

$$E = T_i \times \frac{C_i}{C_s} \tag{1}$$

$$RI = \sum\nolimits_{i=1}^{n} E_i \tag{2}$$

where Ci is the measured value of soil heavy metal i; Cs is the reference value (the natural background value of soil in Guangzhou city, they are 0.14, 13.6, 42.9, and 58.1 mg/kg for Cd, Cu, Pb, and Zn, respectively); and T_i is the toxicity coefficient of heavy metal i (Cd = 30, Cu = 5, Pb = 5, and Zn = 1).

The heavy metals evaluated in this study were different from the original method, so a correction was required (Li et al., 2015). Among the four heavy metals, Cd has the largest T (30),

TABLE 2 Potential ecological risk index grading criteria.

Category	Hakanson		Corrected	
	E	RI	E	RI
Low	<40	<150	<30	<50
Moderate	40–80	150–300	30–60	50–100
High	80–160	300–600	60–120	100–200
Very high	160–320	≥600	120–240	≥200
Extremely strong	≥320	-	≥240	-

according to which the limit value of the first grading standard (Low) of E in this study is 30, and the limit value of the grading standard of each grade of E is obtained by multiplying by two in turn. In the original method, the first level limit value of RI (150) is divided by the sum of all heavy metals E (133) to obtain the coefficient 1.13. The sum of four heavy metals E in this study is 41, multiplying 41 by 1.13 and taking tens place, the first level limit value of RI in this study can be obtained ($1.13 \times 41 = 46.33\tilde{}$ 50), which is multiplied by two in turn to obtain each level of RI. The corrected grading criteria used to define ecological risk of this study are shown in Table 2.

2.2 Experiment 2: simulation of leaching from MSS

MSS I contained a relatively low number of fecal coliforms, so it did not represent the health risks posed by IAT of most MSS. A leaching experiment was therefore performed using a sample called MSS II that contained larger amounts of harmful microorganisms (with a fecal coliform bacteria value of <0.01; Table 1). Fecal coliforms and the heavy metal concentrations in the leachate samples were determined and compared with the Chinese national standard for irrigation water quality (GB 5084–2021) to indirectly determine whether fresh MSS that did not meet sanitary indicator standards could be used in the IAT.

MSS II was collected from the Heshan Sewage Treatment Plant in Jiangmen, Guangdong Province. The experimental site was at the Ecological Farm of the South China Agricultural University in Tianhe District, Guangzhou (N 23°09′57.21″, E 113°21′37.78″). The experimental system (shown in Supplementary Figure S1) consisted of a leachate collection vessel with an upper surface area of 0.12 m^2 on which 5 kg of fresh MSS II in a black fiber mesh bag was placed. Three control vessels without MSS bag were also set-up to collect rainwater. The experiment started on 13 April and rainwater was collected for the first time on 16 April. Leachate was collected three times in 30 days. The pH, chemical oxygen demand, fecal coliform concentration, and Cd, Cu, N, *p*, Pb, and Zn concentrations in the rainwater and leachate samples were determined. The pH was determined using a glass electrode. Fecal coliforms were detected using a rapid paper strip method (HJ 755–2015). The chemical oxygen demand was determined using the dichromate method (HJ 828–2017). The Cd, Cu, Pb, and Zn concentrations were determined by atomic absorption spectrophotometry (GB 7475–1987).

2.3 Experiment 3: investigation of follow-up utilization of MSS

At the end of Experiment one, *Jasminum sambac* and *H. chrysanthus* seedlings were planted in the MSS that had been treated by growing plants in it to investigate follow-up recycling uses of MSS. *J. sambac* seedlings 15 cm tall were purchased from Jianye Jasmine Base in Nanning, Guangxi, China. *H. chrysanthus* seedlings 50–60 cm tall were obtained from the Garden Company of the South China Agricultural University. The *J. sambac* plants were planted on Xinwei Road in Zengcheng District, Guangzhou (N23°19′32.05″, E113°46′5.79″), and the *H. chrysanthus* seedlings were planted at the Ecological Farm of the South China Agricultural University (N23°09′57.21″, E113°21′37.78″).

In the experiment using *J. sambac*, it was grown in two types of treated MSS (AM and PM) (10 kg/pot), one that had previously been used to grow *P. hybridum* (i.e., from the Experiment I PM group) and the other that had previously been used to grow *A. macrorrhiza* (i.e., from the Experiment I AM group). *J. sambac* was also grown in control soil (CK) (10 kg/pot), which was soil collected from a mountain near the experimental site. For each treatment, 10 replicates were performed. The *J. sambac* plants were grown for 3 months. At the end of the experiment, *J. sambac* plant survival and height were recorded.

In the experiment in which *H. chrysanthus* seedlings were planted, 20 kg of the treated MSS was mixed with 20 kg of soil to investigate whether a mixture of MSS and soil could be used as a seedling substrate. Three treatments were performed: 1) CK: Control, soil (40 kg) from local ordinary farmland without fertilizer or sludge. 2) CF: soil (40 kg) fertilized with chemical fertilizers (4 g N, 4 g P_2O_5, and 4 g K_2O added with a 15–15–15 compound fertilizer). 3) PM: mixture of soil and an equal mass of MSS on which *P. hybridum* plants had previously been grown (i.e., from the Experiment I PM group). Four replicates of each treatment were performed. The plants were grown for 6 months. The *H. chrysanthus* plant heights were recorded once each month.

2.4 Net greenhouse gas emissions estimation

Greenhouse gas emissions (GHGE), also called carbon emissions, are generally calculated in terms of carbon dioxide equivalents (CO_2e). Net GHGE consist of three main components: direct carbon emission, indirect carbon emission and carbon emission reduction. The comprehensive treatment proposed in this research use green plants and sunlight, might have less carbon emission, and the *P. hybridum* produced in the treatment process could be used as fuel biomass, which could replace fossil fuels to achieve carbon reduction. Similar to aerobic composting treatment, the comprehensive treated MSS could use as an organic fertilizer. Therefore, comparing the net GHGE of the comprehensive recycling with the aerobic composting treatment can measure the carbon emission level of the integrated method. This study assessed the net GHGE according to the accounting guidelines given in Intergovernmental Panel on Climate Change (IPCC, 2019).

2.4.1 Direct carbon emission

MSS may release CH_4 and N_2O during the treatment process. Therefore, the direct carbon emissions in the treatment process are calculated as follows:

$$E_{D,\,CO_2} = M \times \left(E_{CH_4} \times GWP_{CH_4} + E_{N_2O} \times GWP_{N_2O}\right) \tag{3}$$

Where: $E_{D,\,CO_2}$ is the direct carbon emission, kg CO_2e; M is the mass of treated MSS, t; E_{CH_4} is the CH_4 emission of the treatment, kg/t; GWP_{CH_4} is the 100-year global warming potential (GWP) for CH_4, 25 (IPCC, 2007); E_{N_2O} is the N_2O emissions of the treatment, kg/t; GWP_{N_2O} is the 100-year GWP for N_2O, 298 (IPCC, 2007).

2.4.2 Indirect carbon emission

The treatment of MSS consumes fuel and electricity, which indirectly generates carbon emissions are calculated as follows:

$$E_{I,CO_2} = (M/M_L) \times S \times \varphi_t \times EF_D + W_E \times EF_E \tag{4}$$

Where: E_{I,CO_2} is the indirect carbon emission, kg CO_2e; M is the transport mass of MSS, t; M_L is the transport vehicle load, 10 t; S is the transport distance, km; φ_t is the vehicle fuel consumption, 0.17 kg/km (Wang et al., 2022); EF_D is the carbon emission factor for diesel, 3.0956 kg CO_2/kg (MEE, 2020); W_E is the power consumption of the treatment, kWh/t; EF_E is the carbon emission factor of electricity, 0.8042 kg/kWh (MEE, 2020).

2.4.3 Carbon Reduction

Both treatments are capable of producing fertilizer that can replace the carbon emissions from the production of chemical fertilizers, calculated as follows:

$$E_{N,CO_2} = -(M_{LU} \times w_N \times EF_N) \tag{5}$$

Where: E_{N,CO_2} is the carbon reduction from fertilizer substitution, kg CO_2e; M_{LU} is the mass of treated MSS, kg; w_N is the mass fraction of elemental nitrogen;$EF_N$is the nitrogen fertilizer carbon emission factor, 2.041 kg CO_2e/kg (Chen et al., 2015).

As an energy plant, the use of *P. hybridum* as a fuel can offset carbon emissions from fossil fuel combustion, calculated as follows:

$$E_{P,CO_2} = -\left(\frac{M_P \times Q_P}{Q_s} \times EF_s\right) \tag{6}$$

Where: E_{P,CO_2} is the carbon emission reduction from *P. hybridum* as a fuel, kg CO_2e; M_P is the dry mass of *P. hybridum*, kg; Q_P is the calorific value of *P. hybridum*, which is taken as the average of energy plants, 17,350 kJ/kg (Nazli et al., 2020); Q_s is the calorific value of standard coal, 29,300 kJ/kg (Wang et al., 2022); EF_s is the carbon emission factor of standard coal, which is 2.493 kgCO_2/kg (Wang et al., 2022).

2.5 Statistical analysis

SPSS 22 (SPSS Inc., Chicago, IL, United States) was used to conduct statistical analyses. The normality of distribution and homogeneity of variance were tested before performing ANOVA. Significant differences between the treatments were analyzed using ANOVA and Duncan's multiple range tests. Significance was accepted at $p < 0.05$. For the principal component analysis (PCA), Bray-Curtis dissimilarities were calculated using the vegan package (v.2.5.4) in R (v.3.6.3). Barplot was generated using the ggplot2 package (v.3.3.3).

3 Results

3.1 Growth of *H. chrysanthus*

We measured the basal diameters, diameters at breast height, heights, and crown widths of the *H. chrysanthus* trees before and after the experiment and then calculated the amounts by which the four measurements had increased. The results are shown in Table 3. After a year, the basal diameters and diameters at breast height had increased by only 2.13 and 1.43 cm, respectively, for the trees in the control (CK), but 3.06 and 2.61 cm for the trees in the AM treatment, 3.26 and 2.83 cm for the trees in the PM treatment. The basal diameters and diameters at breast height for the trees in the three treatments were significantly different ($n = 24$, $p = 0.05$). The crown widths and tree heights were also higher for the trees treated with MSS than for the CK trees but the differences were not significant ($n = 24$, $p = 0.05$). We concluded that the IAT and sewage plant treatment had a favorable effect on *H. chrysanthus* growth.

3.2 Effects on the sludge treatment plants

3.2.1 Optimal sludge treatment plants harvest times and yields

The sludge treatment plants needed to be harvested regularly to maximize MSS utilization. The planting times that gave the highest plant yields were identified by harvesting and weighing the sludge treatment plants at different times. The *A. macrorrhiza*

TABLE 3 Changes in growth indicators of *H. chrysanthus*.

Treatment	Basal diameter (cm)	Diameters at breast height (cm)	Crown width (m)	Height (m)
Before treatment				
[a] CK	[b] 9.80 ± 0.64	7.05 ± 0.50	2.86 ± 0.18	4.87 ± 0.02
AM	9.56 ± 0.75	6.81 ± 0.38	2.82 ± 0.16	4.81 ± 0.16
PM	9.44 ± 0.82	6.72 ± 0.51	2.90 ± 0.15	4.75 ± 0.16
After treatment				
CK	12.15 ± 0.84	8.41 ± 0.64	4.21 ± 0.43	6.26 ± 0.23
AM	12.53 ± 1.18	9.42 ± 0.59	4.25 ± 0.47	6.11 ± 0.40
PM	12.61 ± 1.24	9.47 ± 0.89	4.58 ± 0.12	5.97 ± 0.25
Increases in various indicators				
CK	2.13 ± 0.61a	1.43 ± 0.64a	0.69 ± 0.46a	0.76 ± 0.32a
AM	3.06 ± 0.90b	2.61 ± 0.74b	0.95 ± 0.74a	1.16 ± 1.17a
PM	3.26 ± 0.87b	2.83 ± 0.91b	0.76 ± 0.69a	0.88 ± 0.48a

[a] CK: Control without MSS, addition, AM: added MSS, with *A. macrorrhiza* planting, PM: added MSS, with *P. hybridum* planting.

[b] Data are mean ± standard deviation, different lowercase letters indicate that the difference was significant between the treatments according to Duncan's multiple range test ($p = 0.05$, $n = 24$).

and *P. hybridum* plants were harvested and weighed in months 1, 2, 3, and 6. The yields in months 1, 2, 3, and 6 were converted into annual yields by multiplying the yields by factors of 12, 6, 4, and 2, respectively, to allow the yields to be compared. *P. hybridum* harvested in month three gave the highest annual yield (100 ± 25 t/ha). *A. macrorrhiza* harvested in month 6 gave the highest annual yield (9.0 ± 1.4 t/ha). The annual yields at the same harvesting times were significantly higher for *P. hybridum* than *A. macrorrhiza* ($n = 4$, $p = 0.05$). For example, the annual yield was 18.5 times higher for *P. hybridum* than *A. macrorrhiza* when the plants were harvested in month 3 (Supplementary Figure.S2). This indicated that more biomass could be harvested if *P. hybridum* was planted than if *A. macrorrhiza* was planted in the MSS.

3.2.2 Nutrient extraction by the sludge treatment plants

The measured K, N, and *p* contents (dry weight) of the *P. hybridum* biomass were 27.12 ± 7.15, 15.11 ± 3.67, and 5.56 ± 1.42 g/kg, respectively, and the K, N, and *p* contents of the *A. macrorrhiza* biomass were 45.40 ± 10.37, 27.84 ± 1.77, and 5.31 ± 0.07 g/kg, respectively. Under the optimal harvest time as previously mentioned (annual yield 100 and 9.0 t/ha respectively for *P. hybridum* and *A. macrorrhiza*), the *P. hybridum* plants extracted annually 2712, 1511, and 556 kg/ha of K, N, and *p*, respectively, from the MSS. The *A. macrorrhiza* plants extracted 408.6, 250.6, and 47.8 kg/ha of K, N, and *p*, respectively. More than 6.6, 6.0 and 11.6 times of K, N, and *p* were extracted when *P. hybridum* was planted than when *A. macrorrhiza* was planted in the MSS, meaning *P. hybridum* is more suitable than *A. macrorrhiza* for use as a sludge treatment plant to recycle the MSS nutrients into animal feed or organic fertilizer.

3.2.3 Heavy metal contents of the sludge treatment plants

Both *A. macrorrhiza* and P. hybridum are inedible by humans, so the risks posed to humans by directly planting *A. macrorrhiza* and P. hybridum in MSS are relatively low. However, we determined the heavy metal contents (dry weight) of the *A. macrorrhiza* and P. hybridum plants to evaluate possible subsequent uses of the sludge treatment plant biomass. The Cd, Cu, Pb, and Zn contents of the P. hybridum dry biomass were 0.082 ± 0.015, 5.88 ± 0.11, 0.50 ± 0.02, and 38.21 ± 2.22 mg/kg, respectively. The Cd, Cu, Pb, and Zn contents of the *A. macrorrhiza* dry biomass were 0.568 ± 0.121, 9.26 ± 0.90, 2.32 ± 0.97, and 196.53 ± 4.76 mg/kg, respectively. The Cd, Cu, Pb, and Zn contents were lower for *A. macrorrhiza* than P. hybridum. The Cd and Pb contents of the P. hybridum and *A. macrorrhiza* biomass were below the relevant limits for organic fertilizers (Cd ≤ 3 mg/kg, Pb ≤ 50 mg/kg; standard NY 525–2021, Chinese Ministry of Agriculture) and feed (Cd ≤ 1 mg/kg, Pb ≤ 10 mg/kg; standard GB 13078–2017). This indicated that the sludge treatment plant biomass produced on the MSS was safe, in terms of the Cd and Pb contents, for use as animal feed or as raw material for producing organic fertilizer.

3.3 Effects on the soil

3.3.1 Effects on the soil pH and heavy metal contents

After 1 year of the comprehensive treatment, there were no significant differences in the soil pH and the Cd, Cu, Pb, and Zn contents of the soil for the three treatments ($n = 3$, $p = 0.05$, Table 4). The Cd, Cu, Pb, and Zn contents of the soil in the AM

TABLE 4 Characteristics of soils and municipal sewage sludge (MSS) after planting.

Soil	pH	[c] OM g/kg	Cd g/kg	Cu g/kg	Pb g/kg	Zn g/kg	N g/kg	P g/kg	K g/kg
[a] CK	[b] 6.13 ± 0.10a	20.63 ± 2.33a	0.053 ± 0.001a	11.46 ± 1.88a	56.00 ± 1.48 a	75.13 ± 1.76a	1.00 ± 0.06a	0.94 ± 0.05a	15.41 ± 1.77a
AM	6.21 ± 0.53a	25.25 ± 4.47a	0.066 ± 0.007a	12.75 ± 1.06a	48.89 ± 5.60 a	73.75 ± 7.47a	1.30 ± 0.21 ab	1.00 ± 0.05b	12.40 ± 3.42a
PM	5.91 ± 0.33a	29.03 ± 5.11a	0.077 ± 0.021a	14.30 ± 1.18a	51.51 ± 3.46 a	79.56 ± 1.08a	1.56 ± 0.28b	1.61 ± 0.13b	15.25 ± 0.24a
[d] Standards	-	-	≤0.3	≤50	≤90	≤200	-	-	-
MSS							N + P_2O_5+K_2O	[c] FC	[c] GI
Raw sludge	6.82 ± 0.11a	438.83 ± 18.29a	0.841 ± 0.075a	120.5 ± 2.2a	44.72 ± 6.82a	389.9 ± 61.8a	114.25 ± 2.51a	0.03 ± 0.01a	0.08 ± 0.09a
AM	5.40 ± 1.29 ab	415.34 ± 32.55a	0.854 ± 0.056a	140.6 ± 15.1a	67.20 ± 11.29b	570.0 ± 95.3a	94.24 ± 12.01b	0.03 ± 0.00a	0.87 ± 0.16b
PM	4.77 ± 0.39b	395.22 ± 20.97a	0.794 ± 0.050a	136.3 ± 20.6a	65.84 ± 5.90b	549.0 ± 184.1a	94.16 ± 4.28b	0.11 ± 0.05b	0.77 ± 0.24b
[d] Standards	6.5–8.5	≥250	≤5	≤800	≤300	≤2000	≥30	≥0.01	≥0.70

[a] CK: control without sludge addition, AM: added sludge with *Alocasia macrorrhiza* planting, PM: added sludge with *Pennisetum hybridum* planting.

[b] Data are mean ± standard deviation, different letters indicate that the difference was significant between the treatments according to Duncan's multiple range test ($p = 0.05$).

[c] OM, is organic matter content; FC, is fecal coliform value (g/MPN, in fresh weight basis); GI, is germination index of Chinese cabbage seeds.

[d] The soil standard is Soil Environmental Quality Standard of China (GB, 15618–2018); the MSS, standard is Quality of Sludge Used in Gardens or Parks of China (GB/T 2348–2009).

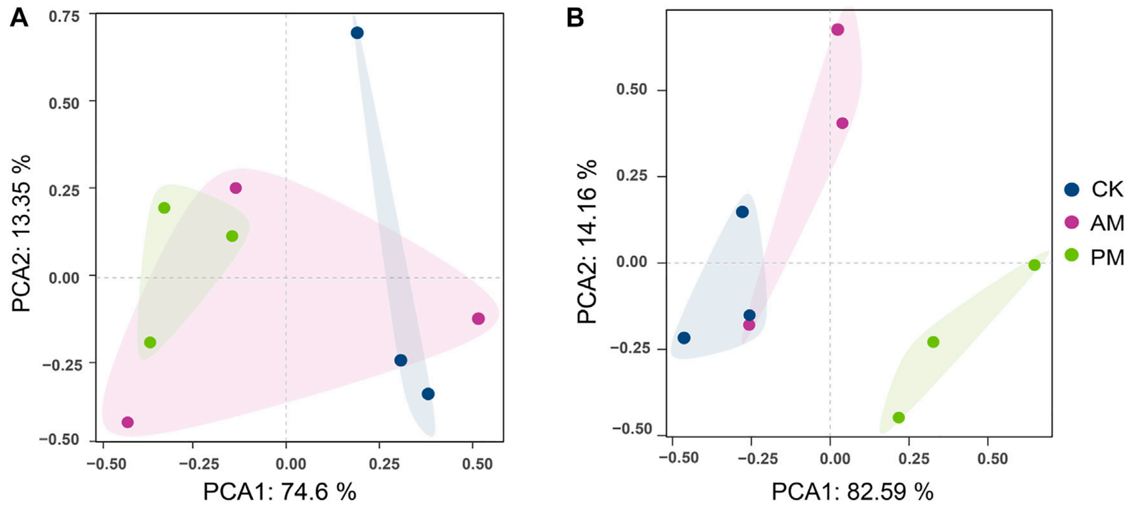

FIGURE 2
The effect of comprehensive treatment on soil, where: **(A)** shows the principal component analysis of heavy metals (Cd, Cu, Pb, Zn) in soil after the experiment; **(B)** shows the principal component analysis of soil nutrients (N, P, OM, K) after the experiment.

and PM treatment areas were all below the relevant Chinese soil environmental quality standard limits (GB 15618–2018). As shown in Figure 2A, principal component analysis indicated that there were no differences between the results for the CK, AM, and PM treatments after 1 year, indicating that the IAT and sludge treatment by plants posed little risk of soil pollution.

The assessment of the potential ecological risk of the soil also indicated that the comprehensive treatment poses little risk of soil contamination. According to Eqs 1, 2, E_{Cd}, E_{Cu}, E_{Pb}, and E_{Zn} for the AM treatment were 14.14, 4.69, 5.70, and 1.27, respectively, and the RI was 25.80; E_{Cd}, E_{Cu}, E_{Pb}, and E_{Zn} for the PM treatment were 16.50, 5.26, 6.00, and 1.37, respectively, and the RI was 29.13. Comparing the corrected grading criteria (Table 2), it can be found that the potential ecological risk to the soil for both treatments is the lowest grade.

3.3.2 Effects on soil nutrients

In the year in which the comprehensive treatment was applied, *H. chrysanthus* grew well while the N and *p* contents of the soil also increased significantly in the PM treatment areas than in the CK area, as shown in Table 4. However, the K content did not follow the same trend because the K content was lower for the MSS than the soil (Table 1). The principal component analysis indicated that, in general, the K, N, OM, and *p* contents of the soil after the experiment were different for the three treatments (Figure 2B) indicating that different amounts of nutrients were leached from the MSS into the soils of the different treatments.

3.4 Changes in MSS properties

3.4.1 Decreases in MSS mass

Each *H. chrysanthus* plant was treated with 1000 kg of MSS. After 1 year, the total remaining MSS masses for the AM and PM treatments were determined and the decreases in the MSS masses were calculated. The MSS masses in the AM and PM treatments had decreased by 84.42% and 85.37%, respectively, at the end of the year. The IAT and sludge treatment plants treatment transformed the fresh MSS into a soil-like substrate (Supplementary Figure.S3) that still had nutrient value, as shown in Table 4, and could be conveniently transported for further use.

3.4.2 Changes in the MSS pH and heavy metal contents

The pH of the MSS I decreased markedly after it had been applied, as shown in Table 4. The change in pH would have been affected by various factors, including precipitation and OM mineralization and nitrification. Plant root exudates could also have changed the MSS pH (Xu and Coventry, 2003). The heavy metal contents of the MSS increased during the experiment, as shown in Table 4. There were no marked differences between the heavy metal contents of the MSS in the AM and PM treatments. *A. macrorrhiza* and *P. hybridum* could have absorbed heavy metals and decreased the heavy metal contents of the MSS. However, *A. macrorrhiza* and *P. hybridum* are not hyperaccumulators, so they would not have absorbed very large amounts of heavy metals. Decomposition of OM and leaching of nutrients would have decreased the MSS mass and would have increased the heavy metal contents of the MSS. However, the Cd, Cu, Pb, and Zn contents of the MSS after the plant treatments were lower than the legal limits for MSS to be used in gardens or parks in China (GB/T 2348–2009).

3.4.3 Nutrient and hygiene indicators

Using the recovered MSS as a substrate for growing seedlings required the nutrient and sanitary indicators of the MSS to be assessed. The OM content of the MSS in the AM and PM treatments after 1 year of indirect MSS utilization and plant treatment was ~400 g/kg (i.e., >250 g/kg; Table 4). The total nutrient (N + P_2O_5+K_2O) content of the treated MSS was ~94 g/kg (i.e., >30 g/kg). There were no significant differences between the OM and total nutrient contents of the AM- and PM-treated MSS. The nutrient contents of the AM- and PM-treated MSS met the requirements for using the treated MSS in landscaping applications.

The seed germination index (GI) was used to indicate the toxicity of the MSS to plants. The AM and PM treatments strongly improved the GI. The GIs for the AM and PM treatments were 0.87 ± 0.16 and 0.77 ± 0.24, respectively, whereas the GI of the raw MSS was 0.08 ± 0.09, as shown in Table 4. The GIs for the AM- and PM-treated MSS met the requirements for the MSS to be used in gardens or parks in China (GB/T 2348–2009).

The fecal coliform bacteria value (FC) is the minimum sample size required to allow coliforms to be detected. The larger the FC the cleaner the MSS. The Chinese "Quality of Sludge Used in Gardens or Parks" standard (GB/T 2348–2009) stipulates that the FC for MSS must be ≥ 0.01 (equivalent to <100 MPN/g). The FCs for the AM- and PM-treated MSS after 1 year were 0.03 ± 0.00 and 0.11 ± 0.05, respectively. The FC for the PM-treated MSS was significantly different from the FCs for the AM-treated and untreated MSS ($n = 3$, $p = 0.05$). This indicated that the PM treatment markedly improved the sanitary level of the MSS.

3.5 Harmful substances in the MSS leachate

It can be seen from Table 1 that the FC for MSS II was above the relevant limit of 0.01 in standard GB/T 2348–2009 and reached 0.0005 ± 0.0003 (equivalent to 2.0×10^3 MPN/g). However, as shown in Table 5, the fecal coliform concentration in the first leachate was only 160 MPN/L. The fecal coliform concentration limit specified in the Chinese standard for irrigation water (GB 5084–2021) is 4.0×10^4 MPN/L. This indicated that microorganisms were retained well by the MSS in the mesh package because the fecal coliform concentration was expected to be higher for the first MSS leachate than for later MSS leachates.

The Cu content of the MSS II, 3602 ± 100 mg/kg (Table 1), was higher than the limit specified in Chinese standard GB/T 2348–2009. The Cu concentration in the leachate caused by rainfall was only 0.584 ± 0.285 mg/L (Table 5), which was lower than the Chinese limit of 1 mg/L for irrigation water (standard GB 5084–2021). The Cd, Pb, and Zn concentrations in the leachates were very low. Similar results were found in a previous study. Xu et al. (2015) performed multiple leaching tests lasting up to 9 months (n = 30) using polluted MSS with a Cd content of 4.92 ± 0.09 mg/kg. They found low Cd concentrations of between 0 and 0.00156 mg/L in the leachate.

3.6 Subsequent MSS utilization

3.6.1 Growth of *J. sambac* planted in treated MSS

The MSS that had been used to grow *A. macrorrhiza* and *P. hybridum* in experiment one (see section 2.1) was used to grow *J. sambac* plants. The *J. sambac* plants grown in the AM- and PM-treated MSS survived well, the survival rates all being 100% ($n = 10$). The *J. sambac* seedlings were ~15 cm tall at the beginning of the experiment. Three months after being planted, the *J. sambac* plants grown in the AM- and PM-treated MSS were >70 cm tall (70.11 ±

TABLE 5 Main properties of municipal sewage sludge leachate of the first collections.

Index	pH	[a] FC	[a] COD (mg/L)	N (mg/L)	*p* (mg/L)	Cd (mg/L)	Cu (mg/L)	Pb (mg/L)	Zn (mg/L)
Rainwater	5.26 ± 0.09	0 ± 0	0 ± 0	0.11 ± 0.19	0.20 ± 0.05	0.0001 ± 0	0.0168 ± 0.001	0.0029 ± 0.0009	0.028 ± 0.018
Leachate	6.59 ± 0.17	160 ± 157	19.3 ± 4.7	16.86 ± 6.12	7.73 ± 1.98	0.0002 ± 0	0.5840 ± 0.285	0.0023 ± 0.0005	0.060 ± 0.017
[b] Standard	5.5–8.5	≤40,000	≤200	-	-	≤0.01	≤1	≤0.2	≤2

[a]FC, is fecal coliform number (MPN/L); COD, is chemical oxygen demand; Data values represent the mean ± standard deviation (n = 3).
[b]The standard is Agricultural Irrigation Water Standard of China (GB, 5084–2021).

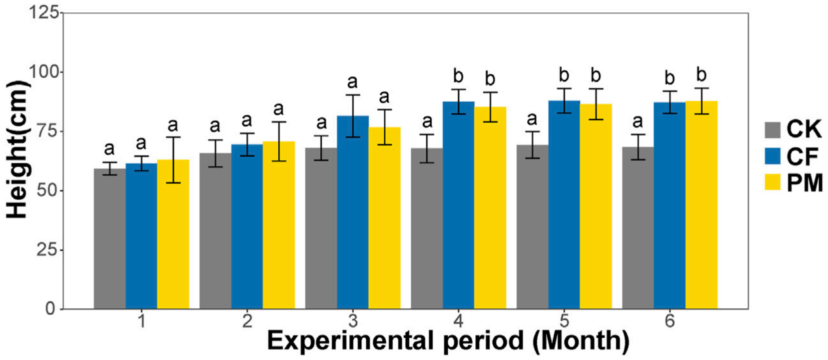

FIGURE 3
Plant heights of *H. chrysanthus* seedlings grown in soil with or without sludge addition (CK: the seedlings were grown in soil; CF: the seedlings were grown in soil with chemical fertilizers; PM: the seedlings were grown in soil amended by an equal mass of *P. hybridum* phyto-treated sludge. Different letters indicate that the difference was significant in the height between the treatments according to Duncan's multiple range test (n = 4, p = 0.05)).

4.58 and 75.35 ± 13.11 cm, respectively) and the plants grown in soil were only ~50 cm tall (49.33 ± 6.66 cm). The *J. sambac* plants grown in the AM- and PM-treated MSS were significantly taller than the *J. sambac* plants grown in soil (n = 10, p = 0.05).

3.6.2 Growth of *H. chrysanthus* seedlings fertilized with treated MSS

The heights of the *H. chrysanthus* plants from the three treatments are shown in Figure 3. The seedling heights were significantly different for the different treatments in month 4 (n = 4, p = 0.05). The plants from the chemical fertilizer treatment and PM (i.e., *P. hybridum* treated MSS) treatment were significantly taller than the plants from the CK treatment, but the plants from the chemical fertilizer and PM treatments were not significantly different (n = 4, p = 0.05). The PM-treated MSS performed as well as or better than the chemical fertilizer treatment, indicating that *P. hybridum* treated MSS provided a good degree of fertilization.

3.7 Carbon emission

The net GHGE is estimated for 1 t fresh MSS. The properties of MSS were referred to MSS I (87.98% water content, 43.56% organic matter, and 4.26% total nitrogen), and the MSS reduction was 85% for the comprehensive recycling and 63% was taken for the composting treatment (Liu et al., 2014). Only the carbon emissions in the treatment processing are considered, excluding the carbon emissions generated during the sludge concentration and dewatering in sewage treatment plant and the subsequent utilization/ application of sludge products.

The emissions of CH_4 from aerobic composting treatment can be taken as 0.2 kg/t (Wang et al., 2022), and are negligible in the comprehensive treatment due to the small volume of MSS in each planting unit. The emission of N_2O during aerobic composting was taken as 0.043 kg/t (Liu et al., 2014). The denitrification of the comprehensive treatment is weak, and the production of N_2O should not exceed that of the composting treatment. The value taken is consistent with that of composting, 0.043 kg/t. Therefore, according to the calculation of Eq. (3), the direct carbon emission from composting treatment is 17.81 kg CO_2e, and the comprehensive treatment is 12.81 kg CO_2e.

The garden forestry site of the comprehensive treatment is usually farer than that of composting site, so the transport distance for the comprehensive treatment is taken as 50 km, while the composting treatment is taken as 30 km. The composting process consumes electrical energy with a

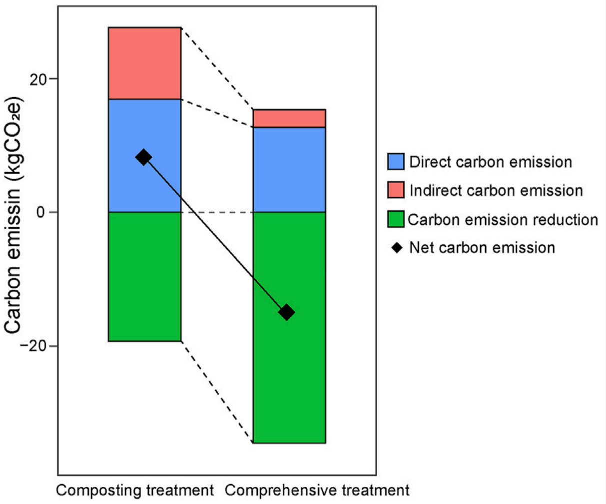

FIGURE 4
Comparison of the carbon emissions of a composting treatment and the comprehensive treatment.

consumption of about 10.06 kWh/t (Liu et al., 2014), while the comprehensive treatment has no electrical energy consumption. Therefore, the indirect carbon emission of composting treatment is 9.67 kg CO_2e and the comprehensive treatment is 2.63 kg CO_2e, calculated according to Eq. (4).

According to the reduction rate of MSS after treatment, the sludge mass after composting is 370 kg, and the comprehensive recycling is 150 kg. The loss rate of N in composting treatment is about 40% (Wang et al., 2019), then the N content of composting treatment is calculated as 2.56%, and the comprehensively treated MSS is measured as 2.60%. In addition, the comprehensive recycling is capable of producing plant products, for example, 1 t fresh MSS can produce about 16 kg of dry matter in the case of *P. hybridum*. Therefore, according to the calculation of Eqs 5, 6, the carbon reduction of composting treatment is -19.33 kg CO_2e and the comprehensive recycling is -31.22 kg CO_2e.

As a result, the carbon emissions of the two treatments are shown in Figure 4. The net GHGE from the composting treatment was 8.15 kg CO_2e and the comprehensive recycling was -15.79 kg CO_2e. This means that the comprehensive recycling of MSS is carbon-negative and contributes to the reduction of carbon emission.

4 Discussion

Comparison between the comprehensive recycling and the conventional land application in environmental benefits.

The comprehensive recycling could fully utilize the nutrients in fresh MSS. A water-permeable material was used to separate the MSS from the soil. Nutrients could be leached from the MSS for use by the *H. chrysanthus* trees but heavy metals were mainly retained by the MSS. The method effectively decreased the amounts of heavy metals that were released from the MSS into the soil (Lin et al., 2021b). In addition, both *A. macrorrhiza* and *P. hybridum* could strongly grow on the MSS, so these species could be used to treat the MSS and therefore offer economic benefits. The conventional method for utilizing MSS on land is the application of composted MSS. Organic pollutants in MSS can be decomposed during the composting process (Zhang et al., 2019) and the bio-availabilities of heavy metals can decrease (Chen et al., 2019). However, composting cannot fundamentally solve the problems caused by heavy metals in MSS. Applying MSS compost can still cause heavy metals to accumulate in soil and plants (Papafilippaki et al., 2015). Repeated applications of MSS compost to soil can markedly increase the amounts of heavy metals leached from the MSS-treated soil and pose the risk of underground water becoming polluted (Fang et al., 2017). The comprehensive treatment could decrease the amounts of heavy metals released into the soil. Our results indicated that the heavy metal contents of the soil did not increase markedly when large amounts of MSS were utilized by comprehensive treatment, as shown in Figure 2A and Table 4.

China has currently proposed two goals of carbon peaking and carbon neutrality, which set a higher standard for how MSS should be treated. The carbon emissions of composting treatment and the comprehensive recycling were also calculated. The emission of N_2O of the comprehensive treatment was set to equal to aerobic composting and the emissions of CH_4 was omitted, due to the lack of available data. Wang et al. (2022) calculated net carbon emissions from different treatment processes for MSS (40–50% OM) and found that composting treatment had lower net carbon emissions than landfills, incineration, pyrolysis, and anaerobic digestion. This study shows that the net carbon emissions of the comprehensive recycling are even lower than those of composting (Figure 4). The comprehensive recycling achieves carbon reduction and is conducive to achieving the dual carbon goals.

In addition, the comprehensive treatment also facilitated the fixation of CO_2 by *H. chrysanthus.* The carbon stock was estimated to be 50% of the total biomass (IPCC 2005) which consist of above ground biomass (AGB) and below ground biomass (BGB). The BGB was estimated from AGB using a root-shoot ratio of 0.26 and the AGB of the trees can be estimated as Khadanga and Jayakumar (2020) proposed. The formula is as follows:

$$AGB\,(kg) = \rho \times \exp\left(-0.667 + 1.784 \times lnD + 0.207 \times (lnD)^2 - 0.0281 \times (lnD)^3\right) \tag{7}$$

where ρ is the wood specific gravity, 1.096 g/cm^3 (Castellanos and Ramón, 2018), ln is the natural logarithm, and D is the diameter at breast height, cm.

According to Table 3, the diameter at breast height was from 7.05 ± 0.50 cm to 8.41 ± 0.64 cm for the CK treatment, and was from

6.72 ± 0.51 cm to 9.47 ± 0.89 cm for the PM treatment. Therefore, according to Eq. (7), the increased biomass of one *H. chrysanthus* tree in the CK treatment can be estimated as 20.41 kg and the PM treatment can be estimated as 43.89 kg. The biomass of each *H. chrysanthus* tree in the PM treatment increased by 23.48 kg over the CK treatment. The planting density of the PM treatment is 800 plants/ha, which means an additional 18.78 t of biomass and 9.39 t of carbon sequestration per hectare of land can be obtained. The comprehensive recycling achieves more carbon fixation, which likewise contributes to the dual carbon goal.

Comparison between the comprehensive recycling and the conventional land application in economic benefits.

The proposed comprehensive recycling does not require a large investment but does require a large area of garden forestry lands (including fruit forestry). However, the garden forestry lands do not affect its productivity by additional sludge phyto-treatment, the garden trees even grow better than the control as shown in this study. In addition, the comprehensive recycling can produce economic benefits in a number of ways: 1) Nutrients for garden plants are provided, meaning smaller amounts of mineral fertilizers need to be purchased; 2) The system markedly improves the nutrient contents of the soil under the indirect application device and improves the soil; 3) Sludge treatment plants growing in the MSS can be used as organic fertilizer or animal feed or plant fuel even for papermaking; 4) After the utilization process is complete, the MSS is fully mature and can be used as organic fertilizer or substrate for garden plants; 5) Carbon emission reductions from MSS treatment can be traded in the carbon trading market.

The main methods to dispose MSS are land application, incineration, disposal in sanitary landfills and making building materials, which accounted for 29.3%, 26.7%, 20.1%, and 15.9%, respectively, of the total amount of MSS disposed of in China in 2019 (Wei L. et al., 2020). The comprehensive recycling used in this study is in the ‘land application’ category. The ultimate goal of any land application system is to make use of the nutrients in MSS, it means less expenditure on chemical fertilizers and more economic value generation. Gouin (1985) reported that composted sewage sludge could replace a complete fertilizer to get comparable growing of Chrysanthemums. The comprehensive recycling reuses directly and comprehensively the nutrients in fresh MSS, and is suitable in gardening developed areas such as Guangdong Province of China.

5 Conclusion

The main conclusions are drawn as follows:

1. The comprehensive recycling increased the growth of *H. chrysanthus*. Good levels of biomass production and nutrient extraction were achieved when *P. hybridum* was planted in fresh sludge and harvested in month 3.
2. The heavy metal contents of the soil did not markedly increase during the experiments but the N, OM, and P contents increased markedly, the comprehensive recycling has little impact on potential ecological risk to the soil.
3. The MSS became mature by the end of the process and was suitable for use as a substrate for cultivating flower seedlings.
4. Even fresh MSS that exceeded the relevant standards gave leachate with fecal coliform and Cu concentrations that met the standards for irrigation water.
5. The comprehensive recycling, which has lower carbon emissions than composting, is carbon-negative and suitable in gardening developed areas.

Data availability statement

The original contributions presented in the study are included in the article/Supplementary Material, further inquiries can be directed to the corresponding author.

Author contributions

XL: Investigation, Writing – original draft, Formal analysis. CC: Investigation. HL: Methodology. LH: Resources. LZ: Visualization. ZW: Formal analysis. YC: Supervision. Q-TW: Conceptualization, Writing – review and; editing, Funding acquisition.

Funding

This study was supported by the R & D program of Guangdong Provincial Department of Science and Technology (Grant No. 2018B030324003, 2021B1212040008, 20220307); Local Innovation and Entrepreneurship Team Project of Guangdong Special Support Program, China (Grant No. 2019BT02L218); the Water Resources Innovation Project of Guangdong Province, China (Grant No. 2017-29); the National Natural Science Foundation of China (Grant No. 21606092).

Acknowledgments

We thank Gareth Thomas, PhD, from Liwen Bianji, Edanz Group China, for editing the English text of a draft of this manuscript.

Conflict of interest

The authors declare that the research was conducted in the absence of any commercial or financial relationships that could be construed as a potential conflict of interest.

Publisher's note

Supplementary material

The Supplementary Material for this article can be found online at: https://www.frontiersin.org/articles/10.3389/fenvs.2022.1023356/full#supplementary-material

References

Badza, T., Tesfamariam, E. H., and Cogger, C. G. (2020). Agricultural use suitability assessment and characterization of municipal liquid sludge: Based on South Africa survey. *Sci. Total Environ.* 721, 137658. doi:10.1016/j.scitotenv.2020.137658

Castellanos, S., and Ramón, J. (2018). Dynamic characteristics of 22 woods determined by the tranverse vibration method. *Rev. Mex. ciencias For.* 9 (48), 181–202. doi:10.29298/rmcf.v8i48.150

Chang, Z., Long, G., Zhou, J. L., and Ma, C. (2020). Valorization of sewage sludge in the fabrication of construction and building materials: A review. *Resour. Conservation Recycl.* 154, 104606. doi:10.1016/j.resconrec.2019.104606

Chen, S., Lu, F., and Wang, X. (2015). Estimation of greenhouse gases emission factors for China's nitrogen, phosphate, and potash fertilizers. *Acta Ecol. sin.* 35 (19), 6371–6383. doi:10.5846/stxb201402210304

Chen, X., Zhao, Y., Zeng, C., Li, Y., Zhu, L., Wu, J., et al. (2019). Assessment contributions of physicochemical properties and bacterial community to mitigate the bioavailability of heavy metals during composting based on structural equation models. *Bioresour. Technol.* 289, 121657. doi:10.1016/j.biortech.2019.121657

Fang, W., Delapp, R. C., Kosson, D. S., Van Der Sloot, H. A., and Liu, J. (2017). Release of heavy metals during long-term land application of sewage sludge compost: Percolation leaching tests with repeated additions of compost. *Chemosphere* 169, 271–280. doi:10.1016/j.chemosphere.2016.11.086

Gouin, F. R. (1985). Growth of Hardy Chrysanthemums in containers of media amended with composted municipal sewage sludge. *J. Environ. Hortic.* 3, 53–55. doi:10.24266/0738-2898-3.2.53

Gronman, K., Ypya, J., Virtanen, Y., Kurppa, S., Soukka, R., Seuri, P., et al. (2016). Nutrient footprint as a tool to evaluate the nutrient balance of a food chain. *J. Clean. Prod.* 112, 2429–2440. doi:10.1016/j.jclepro.2015.09.129

Guo, G., Chen, T., Yang, J., Zheng, G., and Gao, D. (2014). Regional distribution characteristics and variation of heavy metals in sewage sludge of China. *Acta Sci. Circumstantiae* 34 (10), 2455–2461.

Guoqing, X., Xiuqin, C., Liping, B., Hongtao, Q., and Haibo, L. (2019). Absorption, accumulation and distribution of metals and nutrient elements in poplars planted in land amended with composted sewage sludge: A field trial. *Ecotoxicol. Environ. Saf.* 182, 109360. doi:10.1016/j.ecoenv.2019.06.043

Hakanson, L. (1980). An ecological risk index for aquatic pollution control. A sedimentological approach. *Water Res.* 14, 975–1001. doi:10.1016/0043-1354(80)90143-8

Hao, X-D., Chen, Q., Li, J., and Jiang, H. (2019). Ultimate approach to handle excess sludge: Incineration and drying. *CHINA WATER & WASTEWATER* 35 (4), 35–42.

Hei, L., Lee, C. C., Wang, H., Lin, X. Y., Chen, X. H., and Wu, Q. T. (2016). Using a high biomass plant Pennisetum hydridum to phyto-treat fresh municipal sewage sludge. *Bioresour. Technol.* 217, 252–256. doi:10.1016/j.biortech.2016.02.025

Iglesias-Iglesias, R., Portela-Grandío, A., Treu, L., Campanaro, S., Kennes, C., and Veiga, M. C. (2021). Co-digestion of cheese whey with sewage sludge for caproic acid production: Role of microbiome and polyhydroxyalkanoates potential production. *Bioresour. Technol.* 337, 125388. doi:10.1016/j.biortech.2021.125388

IPCC (2019). 2019 refinement to the 2006 IPCC guidelines for national greenhouse gas inventories. Available online at https://www.ipcc.ch/report/2019-refinement-to-the-2006-ipcc-guidelines-for-national-greenhouse-gas-inventories/ (accessed June 5, 2022).

IPCC (2005). Carbon dioxide capture and storage carbon dioxide capture and storage. Available online at https://www.ipcc.ch/report/carbon-dioxide-capture-and-storage/ (accessed July 4, 2022).

IPCC (2007). Climate change 2007: Mitigation of climate change. Available online at https://www.ipcc.ch/report/ar4/wg3/ (accessed June 5, 2022).

Khadanga, S. S., and Jayakumar, S. (2020). Tree biomass and carbon stock: Understanding the role of species richness, elevation, and disturbance. *Trop. Ecol.* 61 (1), 128–141. doi:10.1007/s42965-020-00070-0

Li, Y-M., Ma, J-H., Liu, D-X., Sun, Y-L., and Chen, Y-F. (2015). [Assessment of heavy metal pollution and potential ecological risks of urban soils in Kaifeng City, China]., China. *Environ. Sci.* 36, 1037–1044. doi:10.13227/j.hjkx.2015.03.037

Liang, S., Yang, L., Chen, H., Yu, W., Tao, S., Yuan, S., et al. (2021a). Phosphorus recovery from incinerated sewage sludge ash (ISSA) and reutilization of residues for sludge pretreated by different conditioners. *Resour. Conservation Recycl.* 169, 105524. doi:10.1016/j.resconrec.2021.105524

Liang, Y., Xu, D., Feng, P., Hao, B., Guo, Y., and Wang, S. (2021b). Municipal sewage sludge incineration and its air pollution control. *J. Clean. Prod.* 295, 126456. doi:10.1016/j.jclepro.2021.126456

Lin, X., Chen, X., Li, S., Chen, Y., Wei, Z., and Wu, Q. (2021a). Sewage sludge ditch for recovering heavy metals can improve crop yield and soil environmental quality. *Front. Environ. Sci. Eng.* 15 (2), 22. doi:10.1007/s11783-020-1314-1

Lin, X., Li, S., Wei, Z., Chen, Y., Hei, L., and Wu, Q-T. (2021b). Indirect application of sludge for recycling in agriculture to minimize heavy metal contamination of soil. *Resour. Conservation Recycl.* 166, 105358. doi:10.1016/j.resconrec.2020.105358

Liu, H. T., Zheng, H. X., Chen, T. B., Zheng, G. D., and Gao, D. (2014). Reduction in greenhouse gas emissions from sewage sludge aerobic compost in China. *Water Sci. Technol.* 69 (6), 1129–1135. doi:10.2166/wst.2013.773

Lu, J-Y., Wang, X-M., Liu, H-Q., Yu, H-Q., and Li, W-W. (2019). Optimizing operation of municipal wastewater treatment plants in China: The remaining barriers and future implications. *Environ. Int.* 129, 273–278. doi:10.1016/j.envint.2019.05.057

MEE (2020). 2019 baseline emission factors for regional power grids in China. Available online at https://www.mee.gov.cn/ywgz/ydqhbh/wsqtkz/202012/t20201229_815386.shtml (accessed May 4, 2022).

Nazli, R. I., Kusvuran, A., Tansi, V., Ozturk, H. H., and Budak, D. B. (2020). Comparison of cool and warm season perennial grasses for biomass yield, quality, and energy balance in two contrasting semiarid environments. *Biomass Bioenergy* 139, 105627. doi:10.1016/j.biombioe.2020.105627

Ottosen, L. M., Thornberg, D., Cohen, Y., and Stiernström, S. (2022). Utilization of acid-washed sewage sludge ash as sand or cement replacement in concrete. *Resour. Conservation Recycl.* 176, 105943. doi:10.1016/j.resconrec.2021.105943

Papafilippaki, A., Paranychianakis, N., and Nikolaidis, N. P. (2015). Effects of soil type and municipal solid waste compost as soil amendment on Cichorium spinosum (spiny chicory) growth. *Sci. Hortic.* 195, 195–205. doi:10.1016/j.scienta.2015.09.030

Parr, J. F., Epstein, E., and Willson, G. B. (1978). Composting sewage sludge for land application. *Agric. Environ.* 4, 123–137. doi:10.1016/0304-1131(78)90016-4

Peter, L. (2000). *Fabricated from cuspated sheet plant growth container*. Munich: European Patent Office, EP1241928 A1.

Riaz, U., Murtaza, G., Saifullah, Farooq M., and Farooq, M. (2018). Influence of different sewage sludges and composts on growth, yield, and trace elements accumulation in rice and wheat. *Land Degrad. Dev.* 29 (5), 1343–1352. doi:10.1002/ldr.2925

Samake, M., Wu, Q. T., Mo, C. H., and Morel, J. L. (2003). Plants grown on sewage sludge in South China and its relevance to sludge stabilization and metal removal. *J. Environ. Sci.* 15 (5), 622–627.

Wang, L., Li, D., Liu, Z., and Li, H. (2022). Analysis on carbon emission from sludge treatment and disposal. *China Environ. Sci.* X, 1–10.

Wang, X., Zheng, G., Chen, T., Shi, X., Wang, Y., Nie, E., et al. (2019). Effect of phosphate amendments on improving the fertilizer efficiency and reducing the mobility of heavy metals during sewage sludge composting. *J. Environ. Manage.* 235, 124–132. doi:10.1016/j.jenvman.2019.01.048

Wei, L., Zhu, F., Li, Q., Xue, C., Xia, X., Yu, H., et al. (2020a). Development, current state and future trends of sludge management in China: Based on exploratory data and CO_2-equivaient emissions analysis. *Environ. Int.* 144, 106093. doi:10.1016/j.envint.2020.106093

Wei, Y., Zhao, Y., Zhao, X., Gao, X., Zheng, Y., Zuo, H., et al. (2020b). Roles of different humin and heavy-metal resistant bacteria from composting on heavy metal removal. *Bioresour. Technol.* 296, 122375. doi:10.1016/j.biortech.2019.122375

Xu, R. K., and Coventry, D. R. (2003). Soil pH changes associated with lupin and wheat plant materials incorporated in a red–Brown Earth soil. *Plant Soil* 250 (1), 113–119. doi:10.1023/a:1022882408133

Xu, T., Xie, F., Wei, Z., Zeng, S., and Wu, Q. T. (2015). Phytoremediation of sewage sludge and use of its leachate for crop production. *Environ. Technol.* 36 (23), 3000–3007. doi:10.1080/09593330.2014.955061

Yu, X., Nakamura, Y., Otsuka, M., Omori, D., and Haruta, S. (2021). Development of a novel phosphorus recovery system using incinerated sewage sludge ash (ISSA) and phosphorus-selective adsorbent. *Waste Manag.* 120, 41–49. doi:10.1016/j.wasman.2020.11.017

Zasoski, R. J., Edmonds, R. L., Bledsoe, C. S., Henry, C. L., Vogt, D. J., Vogt, K. A., et al. (1984). Municipal sewage sludge use in forests of the Pacific northwest, U.S.A.: Environmental concerns. *Waste Manag. Res.* 2, 227–246. doi:10.1016/0734-242x(84)90029-6

Zat, T., Bandieira, M., Sattler, N., Segadães, A. M., Cruz, R. C. D., Mohamad, G., et al. (2021). Potential re-use of sewage sludge as a raw material in the production of eco-friendly bricks. *J. Environ. Manag.* 297, 113238. doi:10.1016/j.jenvman.2021.113238

Zeng, L., Lin, X., Zhou, F., Qin, J., and Li, H. (2019). Biochar and crushed straw additions affect cadmium absorption in cassava-peanut intercropping system. *Ecotoxicol. Environ. Saf.* 167, 520–530. doi:10.1016/j.ecoenv.2018.10.003

Zhang, J., Bao, Y., Jiang, Y., Liu, H. T., Xi, B. D., and Wang, D. Q. (2019). Removal and dissipation pathway of typical fluoroquinolones in sewage sludge during aerobic composting. *Waste Manag.* 95, 450–457. doi:10.1016/j.wasman.2019.06.036

Zhang, Q., Zou, D., Zeng, X., Li, L., Wang, A., Liu, F., et al. (2021). Effect of the direct use of biomass in agricultural soil on heavy metals- activation or immobilization? *Environ. Pollut.* 272, 115989. doi:10.1016/j.envpol.2020.115989

Zucconi, F., Pera, A., Forte, M., and De Bertoldi, M. (1981). Evaluating toxicity of immature compost. *Biocycle* 22, 54–57. doi:10.1071/SR9810361

frontiers | Frontiers in Environmental Science

TYPE Original Research
PUBLISHED 31 October 2022
DOI 10.3389/fenvs.2022.1023835

Characteristics of denitrification and anammox in the sediment of an aquaculture pond

Xingguo Liu[1,2]*, Meiyun Gao[3], Jie Wang[1,2], Zhaojun Gu[1,2] and Guo-feng Cheng[1,2]

[1]Fishery Machinery and Instrument Research Institute, Chinese Academy of Fisheries Sciences, Shanghai, China, [2]Key Laboratory of Aquaculture Facilities Engineering, Ministry of Agriculture and Rural Affairs, Shanghai, China, [3]Shanghai Ocean University, Shanghai, China

OPEN ACCESS

EDITED BY
Zheng-Yang Huo,
Renmin University of China, China

REVIEWED BY
Shiyang Zhang,
Wuhan University of Technology, China
Samik Bagchi,
Digested Organics, United States

*CORRESPONDENCE
Xingguo Liu,
liuxg1223@163.com

SPECIALTY SECTION
This article was submitted to Water and Wastewater Management,
a section of the journal
Frontiers in Environmental Science

RECEIVED 20 August 2022
ACCEPTED 14 October 2022
PUBLISHED 31 October 2022

CITATION
Liu X, Gao M, Wang J, Gu Z and Cheng G-f (2022), Characteristics of denitrification and anammox in the sediment of an aquaculture pond.
Front. Environ. Sci. 10:1023835.
doi: 10.3389/fenvs.2022.1023835

Denitrification and anaerobic ammonium oxidation (anammox) are the key processes of nitrogen removal in aquaculture pond sediment. However, the reaction characteristics remain unclear. In this study, considering the sediment of conventional freshwater fishponds as the object, we set the optimal conditions of organic carbon, temperature, and total nitrates for denitrification and anammox. We found that the abundance and diversity of denitrifying bacteria and anammox bacteria in the two groups were significantly different. *Candidatus brocadia* is the most important bacteria in aquaculture pond sediments. The removal efficiencies of nitrite (NO_2^--N), nitrate (NO_3^--N), ammonia nitrogen (NH_4^+-N), and total organic carbon (TOC) in the anammox optimal conditions group were 97.99%, 93.05%, 54.92%, and 58.82%, respectively; however, those in the denitrification optimal conditions group were 99.82%, 86.10%, 45.74%, and 70.76%, respectively. Comparing each optimal condition, the removal efficiency of NO_2^--N and TOC in the denitrification optimal condition groups was higher, whereas those of NO_3^--N and NH_4^+-N were higher in the anammox optimal condition groups. We provide a reference for resolving nitrogen pollution in aquaculture pond sediments.

KEYWORDS

Anammox, denitrification, sediment, pond aquaculture, regulation effect

1 Highlights

1) Denitrification and anammox in pond aquaculture are mainly regulated by organic carbon content, temperature, and nitrite.
2) Denitrification has higher removal efficiency of NO^{2-}-N and TOC, and anammox has a higher removal efficiency of NO^{3-}-N and NH^{4+}-N.
3) In the optimal conditions for denitrification and anammox, denitrification has higher nitrogen removal efficiency, but the role of anammox cannot be ignored.
4) *Candidatus brocadia* is the most important bacteria for nitrogen regulation in aquaculture ponds.

2 Introduction

Nitrogen pollution is the main cause of water quality deterioration in pond aquaculture. The sediment includes pollutants collected from the area of pond aquaculture. Nitrogen cycling in polluted water sediments includes ammoniation, nitrification, denitrification (Table, 1984; Sauthier et al., 1998), and anaerobic ammonium oxidation (anammox) (Van de Graaf et al., 1996). Denitrification and anammox are two transformation pathways which permanently remove fixed nitrogen from the system by converting it to gaseous nitrogen (N) (Castine 2013). Since the nitrogen conversion processes require various microorganisms, the conditions for denitrification and anammox are highly specific. Biological nitrogen removal processes that have been identified to date include denitrification, anammox, and denitrification-dependent anaerobic methane oxidation (Damo) (Hinrichs et al., 1999). Except for a few denitrifying bacteria that can denitrify the sediment in an aerobic environment, almost all denitrification processes are carried out in low oxygen or anaerobic environments; anaerobic ammonia oxidation and denitrifying anaerobic methane oxidation especially can be performed only at oxygen concentrations of <2 μM. The three denitrification processes are collectively referred to as biological anaerobic denitrification (Thamdrup 2012). Denitrifying microorganisms widely exist in marine, river, soil, wetland, and other ecosystems and have a high taxonomic diversity (Tiedje 1988). Ten different families of bacteria, fungi, and archaea exhibit denitrifying properties (Verbaendert et al., 2011). Many studies of denitrification have been reported to date, but they mainly focus on environments such as oceans and wetlands. In recent years, with the increased aquaculture environmental pollution, research on denitrification and anammox in aquaculture environments has gradually increased and become a research hotspot.

Pond aquaculture undeniably offers coniderable potential for food production worldwide. In China, 48.79% aquatical production is from pond aquaculture (FAMA, 2022). However, with the continuous pursuit of high yield, a large number of feeds and fertilizers are used in aquaculture, which leads to the accumulation of organic matter in pond aquaculture sediment and the production of a large amounts of nitrites, ammonia, and other substances, causing a deterioration of water quality and endangering aquaculture animals (Sun et al., 2017; Wei 2017). Sediment is the main sink of eutrophication-related nutrients in pond aquaculture. It results from the sedimentation of particulate matter. In the soil layer below 15 cm, with the increase in the depth of the soil layer, the total phosphorus (TP) content increases, whereas the total nitrogen (TN) shows a downward trend. Organic matter is mainly concentrated at 5–10 cm, and nitrogen-containing organic matter is the main pollutant in the pond sediment (Liu 2011). In ponds with intensive production of staple carp, sludge deposition is ~10–12 cm per year (Zhang 1989). In grass carp aquaculture ponds, the mud (air-dried sample) generally contains 3% organic matter, ~0.01–0.1% available nitrogen, 0.2% of TN, 0.2% of TP, and ~0.7–1% of potassium (Yao 2010). A study showed that the sediment comprises ~14–53% of N and ~39–67% of P from feed (Christopher et al., 2003). The organic matter produced by aquaculture is deposited on the pond bottom, and during denitrification, NO_3^--N is reduced to nitrogen (N_2) and NH_4^+-N. Generally, the lack of oxygen in the sediment is favorable for denitrification and inhibits nitrification, resulting in the accumulation of more NH_4^+-N in the sediment (Yue & Huang 2003). Under the activity of bacteria, excessive NH^{4+}-N, NO^{2-}-N, methane (CH_4), H_2S, and other toxic substances, which are harmful to fish, are produced, affecting the safety of aquaculture (Boyd 1995). Nitrogen cycling in pond sediments is a complex process, and the reaction efficiency greatly varies. Guo et al. (2011) found that the denitrification rate of Grasscarp culture sediment ranges from 0 to 734.15 μmol/(m^2. d), with an ammoniation rate 0–41.25 mmol/(m^2. d) (Guo et al., 2011). The anammox process contributed 1.2%–15.3% to sediment dinitrogen gas production (Shen et al., 2016).

Nitrogen regulation is an important method to maintain a good water environment for pond aquaculture. For example, Wang et al. (2013) found that the aquaculture environment and season have a significant impact on the structure of anammox bacteria in the sediment of ponds (Wang et al., 2013). Gao et al. (2018) found that organic carbon can inhibit anammox bacteria in the sediment of ponds and promote denitrifying bacteria. A temperature of 25–35°C is conducive for denitrification and anammox (Gao et al., 2018). Liao and Wu found that there was a synergistic association between ammonia-oxidizing bacteria and anammox bacteria in the surface sediments of ponds (Liao and Wu, 2013). Nowadays, denitrification has has become a key research topic in the field of water treatment (Shi Y et al., 2022; Shitu A et al., 2022). Numerous studies have shown that organic carbon, temperature, and nitrite are the basic conditions for controlling denitrification and anammox. However, denitrification and anammox have different requirements for organic carbon, temperature, and nitrite. The same organic carbon, temperature, and nitrate conditions cannot meet the needs of denitrification as well as those of anammox (Yu et al., 2016). Under low concentrations of organic carbon, anammox bacteria and denitrifying bacteria can cooperate to remove nitrogen, and excess organic carbon inhibits the activity of anammox bacteria (Liu et al., 2014). Because nitrite controls denitrification and anammox, a higher denitrification effect in the water environment is observed only within a specific concentration range of nitrate. Beyond this concentration range, denitrifying bacteria are inhibited, thereby reducing the denitrification effect (Li et al., 2013). The bacteria in the anammox process are autotrophic, absorbing and fixing CO_2 as a carbon source (Mulder et al., 1995). All studies show that it is difficult to synchronize denitrification and anammox in aquatic environments. Thus, controlling the synchronous reaction of denitrification and anammox is a research challenge.

In this study, we used gene cloning libraries, real-time fluorescence quantitative PCR, and diversity analysis to reveal the characteristics of denitrification and anammox in pond sediments. We hope that our study will provide a theoretical basis for the regulation of nitrogen in sediment and suggest an important way to alleviate nitrogen pollution in aquaculture ponds and improve aquaculture efficiency.

3 Materials and methods

3.1 Sediment collection and processing

The pond sediment was taken from Maogang aquaculture farms (N30°57′1.89″, E 121°08′52.21″), Shanghai, China. The pond aquaculture species were *Ctenopharyngodon Idella* (Grass carp), *Malobrama amblycephala* (Bream), *Hypophthalmichthys molitrix* (Silver carp), and *Aristichys Nobilis* (Bighead carp). The maximum culturing density was 0.82 $\mathrm{kgm^{-3}}$. We collected 0–10 cm surface sediment using a Peterson mud collector, immediately placed the samples in sterile plastic bags after collection, removed air, and transported the samples to the laboratory to be stored in cold storage.

3.2 Experimental equipment and methods

According to the effects of organic carbon, temperature, and nitrite on denitrification and anammox in ponds (Gao et al., 2018), we set up two experimental groups: a denitrification group and an anammox group. Each group consists of three 500-ml triangular flasks. Before the experiment, 100 g of sediment was dried under natural conditions, and 500 ml of purified water was inoculated in each triangular flask of the two groups; in this process, only water was added not inoculated (Van de Graaf et al., 1996). The optimal reaction conditions of the denitrification group were set as 28°C, 150 mg/L $NaNO_2$, and 150 mg/L starch. In the anammox group, the optimal conditions were set as 34°C and 300 mg/L $NaNO_2$. Thereafter, each bottle was purged with N_2 for 10 min to eliminate the influence of O_2 on denitrification and anammox reactions. To control the temperature and other conditions, we put the two groups of experimental triangular flasks in different intelligent artificial climate incubators (RHQ-1000).

According to Chen et al. (2009) and Yang et al. (2012), we set the experimental period as 20 days. After the start of the experiment, three water samples were repeatedly collected in the triangular flasks once a day to measure the physical and chemical indicators. When the nitrite (NO_2^--N) in the denitrification and anammox groups was less than 0.1 mg/L, we added 150 mg/L $NaNO_2$ to the denitrification groups and 300 mg/L $NaNO_2$ to the anammox groups. Two grams of the sediment were collected every 5 days and used to detect physical and chemical indicators and flora. For each experimental system, we collected four types of sediment.

3.3 Physical and chemical indices of water determination

NO_3^--N levels were determined using ultraviolet spectrophotometry, NO_2^--N levels were determined using N-(1-Naphthyl) ethylenediamine spectrophotometry, and NH_4^+-N levels were determined using Nessler's reagent (SEPA and AQSIQ, 2002). TOC was analyzed using the Multi N/C2100 system, with the measurement range being 0–30000 ppm and the maximum carbon content of solids being 150 mg. The spectrophotometer was a Model 721 spectrophotometer produced by Shanghai Precision Scientific Instruments Co., Ltd.

3.4 DNA extraction and PCR amplification

Total DNA was extracted using the FastDNA spin kit for soil (Mpbio, United States) from matrix samples (collected sediments). DNA quality was detected by 1% agarose gel electrophoresis. A total of 8 samples were obtained and divided into 2 parts, one for the analysis of flora structure and diversity, and the other for quantitative analysis.

The *nirS* gene of denitrifying bacteria and the 16S rRNA gene of anammox bacteria were amplified by nested PCR. The primer pair Cd3aF-R3cdR used in the nested denitrification method is referred to in the reported literature (Lipsewers et al., 2016). The primer pair Pla46f-630r was used in the first round of anaerobic ammonia oxidation, and the primer pair Amx368f-Amx820r was used in the second round. The PCR reaction system includes Premix Ex *Taq* 12.5 μl, forward primer 1 μl, reverse primer 1 μl, formwork 1 μl, and ddH_2O 9.5 μl (Zhu et al., 2011).

3.5 Clone library construction and sequencing

After separating the nested PCR sample by agarose gel electrophoresis, a specific fragment size was cut from the gel, purified using the GeneJET Gel Extraction Kit (Thermo), ligated using a pEASY-T1 cloning kit, and then transformed into Trans1-T1 competent cells. Transformed cells carrying the target gene were cultured for 1 h in LB medium without ampicillin and then inoculated on solid LB medium containing ampicillin and the blue spot detection reagent. After overnight culture of each sample, 20 single colonies were obtained. Positive clones were detected by colony PCR, from which 18 were selected, inoculated in 1 ml LB liquid medium with ampicillin, cultured at 37°C for 10 h, and then, sent to Shanghai Invitrogen Co., Ltd. for sequencing.

3.6 Real-time PCR and data analysis

The *nirS* copy numbers in denitrifying bacteria were quantified in eight samples using the *nirS*-specific primers, Cd3aF and R3cdR levels and the 16SrRNA copy numbers in anammox bacteria were quantified using the specific primers, AMX-808-F and AMX-1040-R. The PCR conditions have been described previously (Noredal et al., 2007; Dang et al., 2009). The PCR reaction volume was 20 μl and included the following: 1 μl template DNA, 0.8 μl forward and reverse primers each, 2 × Master mix (Roche) 10 μl, and 7.4 μl ddH_2O.

3.7 Colony structure and diversity analysis

The sequence was edited using DNAStar software; the carrier sequence was removed, and the operational taxonomic units (OTUs) were determined using Mothur software. Each representative OTU sequence was selected as an OTU, and similar sequences were searched and downloaded using the NCBI-BLAST alignment tool. MEGA5.05 was used to align similar sequences with representative sequences through multiple sequence alignments, and a phylogenetic tree was constructed using the neighbor-joining method. The Shannon index (Xu et al., 2011), Simpson index, species richness (Chao) (Cui 2011), and coverage ratio were calculated to analyze microbial diversity.

3.8 Data processing

The diversity level and water index data were analyzed using Statistical Product Service Solutions (SPSS 20.0) software.

4 Results

4.1 Abundance of denitrifying bacteria and anammox bacteria

Through molecular biology experiments, we found that the total abundances of denitrifying bacteria in denitrification and anammox groups under optimal conditions for organic carbon content, temperature, and nitrite were 2.43×10^{11} copies g^{-1} and 2.04×10^{11} copies g^{-1}, respectively, while the abundances of anammox bacteria were 6.16×10^{8} copies g^{-1} and 9.49×10^{8} copies g^{-1}, respectively.

In the denitrification group, the abundances of denitrifying bacteria in the four samples were 2.60×10^{10} copies g^{-1}, 5.86×10^{10} copies g^{-1}, 8.06×10^{10} copies g^{-1}, and 7.78×10^{10} copies g^{-1}, respectively. In the anammox group, the abundances of anammox bacteria in the four samples were 1.35×10^{8} copies g^{-1}, 2.10×10^{8} copies g^{-1}, 4.16×10^{8} copies g^{-1}, and 1.88×10^{8} copies g^{-1}, respectively. The results showed that the total abundance of denitrifying bacteria in the denitrification group was significantly higher than that in the anammox group (Figure 1A). Similarly, the total abundance of anammox bacteria in the anammox group was significantly higher than that in the denitrification group (Figure 1B). Thus, the denitrification group was positive for denitrifying bacteria while the anammox group was suitable for anaerobic ammonia-oxidizing bacteria.

4.2 Diversity of denitrifying bacteria

4.2.1 Diversity level of the *nirS* gene

Using Mothur to analyze the sequence data of denitrifying bacteria in the denitrification and anammox groups, we found the clone coverage rate of the *nirS* gene in the two groups to be over 95%, indicating that the results of this clone library indeed represent the diversity level of denitrifying bacteria. The Shannon index of the denitrifying bacteria in the denitrification group was higher than that of the denitrifying bacteria in the anammox group, whereas the Simpson index showed the opposite trend, indicating that the diversity level of denitrifying bacteria in the denitrification group was relatively high. The diversity of denitrifying bacteria in the four sediments of denitrification and anammox groups did not show an increasing trend with time (Table 1).

4.2.2 Phylogenetic analysis of *nirS* genes

β-Proteobacteria was the most dominant group in the *nirS* gene library. The four sediments collected from denitrification and anammox groups (represented in the table as N1, N2, N3, and N4, and A1, A2, A3, and A4, respectively) were sequenced, and 156 valid sequences were obtained. The OTUs were divided based on Mothur's 3% variance (97% sequence similarity for clustering OTUs), resulting in 20 OTUs. Among them, the number of OTUs from N1, N2, N3, N4, A1, A2, A3, and A4 samples was 4, 5, 5, 4, 2, 4, 6, and 4, respectively, indicating that denitrifying bacteria in the denitrification system showed little difference in OTU numbers at different times.

Phylogenetic analysis was performed to compare and analyze the denitrifying *nirS* genes obtained from denitrification and anammox systems (Figure 2). From the phylogenetic tree, overall, 156 valid sequences could be classified into the

TABLE 1 Diversity level of denitrifying bacteria in the two groups.

Sample name	Simpson/D	Shannon-weiner/H	Chao	Coverage (%)
A1	0.142 ± 0.006^{a}	1.921 ± 0.076^{h}	2	99
A2	0.058 ± 0.002^{abcde}	2.194 ± 0.088^{g}	4	98.5
A3	0.016 ± 0.001^{bce}	2.830 ± 0.113^{a}	6	100
A4	0.053 ± 0.002^{bcde}	2.528 ± 0.101^{d}	4	99.5
N1	0.067 ± 0.003^{abcd}	2.788 ± 0.112^{b}	4	99
N2	0.032 ± 0.001^{bcde}	2.524 ± 0.101^{de}	5	99
N3	0.037 ± 0.001^{bcde}	2.524 ± 0.101^{df}	5	99
N4	0.079 ± 0.003^{abcd}	2.597 ± 0.104^{c}	4	100

Note: The letters in the table represent multiple comparisons ($p < 0.05$). A1, A2, A3, A4, N1, N2, N3, and N4 represent the four sediments collected from anammox and denitrification groups each. Different lowercase letters with shoulder marks in the same column indicate significant differences.

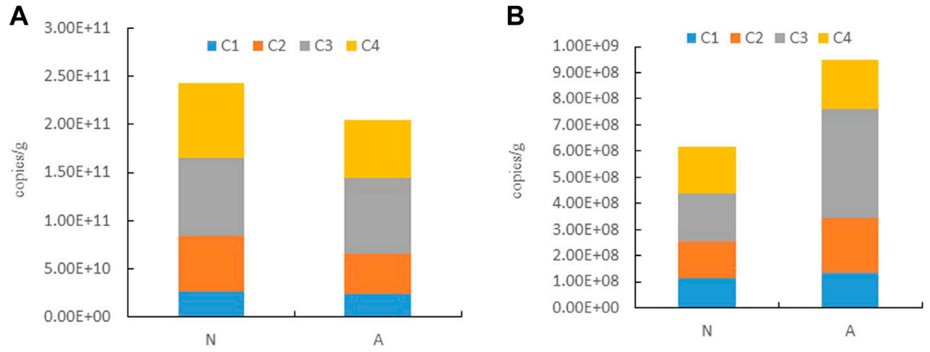

FIGURE 1
Abundance of denitrifying and anammox bacteria in the two conditions **(A)** denitrifying bacteria. **(B)** anammox bacteria. N: denitrification group. A: anammox group. C1, C2, C3, and C4 indicate the four sediments collected.

phylum pseudomonadota, including the classes Alphaproteobacteria, Betaproteobacteria, and Gammaproteobacteria and the genera *Dechloromonas*, Burkholderiaceae, *Thiothrix*, *Thauera*, *Azoarcus*, *Brachymonas*, and *Azospirillum*. In the *nirS* gene cloning library, two OTUs belonged to Alphaproteobacteria and were 98% identical to the most similar *nirS* gene sequence in GenBank. Most of the similar sequences were derived from similar environments, such as the Pearl River estuary in China, the San Francisco Bay estuary (Mosier and Francis, 2010), and the Yangtze River estuary in China (Zheng et al., 2015). Two OTUs belonged to Gammaproteobacteria; the OTU and GenBank strain of the denitrifying bacteria *Thiothrix sp.* AS (KC855765.1) showed 99% sequence similarity with other sequences in the group, the most similar sequence being derived from the estuaries of San Francisco Bay (Mosier and Francis, 2010) and Jiaozhou Bay, China (Dang et al., 2010), and the Haihe River, China.

4.3 Diversity of anammox bacteria

4.3.1 Diversity level of the 16S rRNA gene

The diversity of anammox bacteria in the four sediments of denitrification and anammox groups was analyzed using the Mothur method. Results showed the cloning coverage ratio of the 16S rRNA gene in anammox bacteria to be above 95% in the two groups (Table 2), indicating that the clone library represents the diversity level of anammox bacteria quite well. The Shannon index of anammox bacteria in the anammox group was higher than that in the denitrification group, and the Simpson exponent of the denitrification group was larger, indicating that the diversity of anammox bacteria in the anammox group was relatively high. The diversity levels of anammox bacteria in all four sediments of the anammox group tended to increase with time.

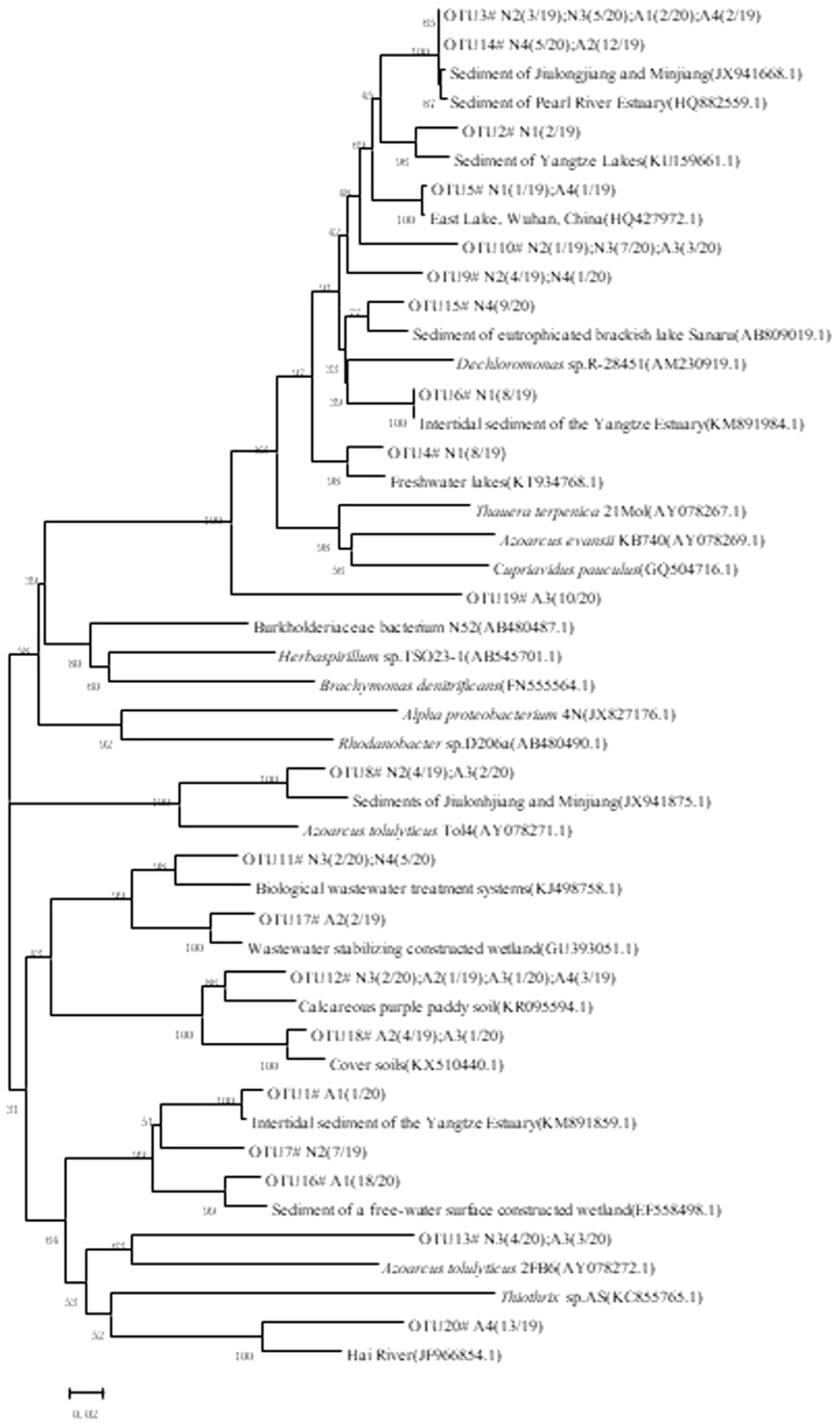

FIGURE 2
Denitrifying nirS genes in the denitrification and anammox groups.

4.3.2 Phylogenetic analysis of 16S rRNA gene

The four sediments collected from the denitrification and anammox groups (represented in the tables as N1, N2, N3, and N4, and A1, A2, A3, and A4, respectively) were sequenced, and 157 effective sequences were obtained. The OTUs were divided into 15 units based on a 3% variance in Mothur. Among them,

TABLE 2 Diversity level of anammox bacteria in the two groups.

Sample name	Simpson/D	Shannon-weiner/H	Chao	Coverage (%)
A1	0.900 ± 0.036^{a}	0.199 ± 0.08^{gh}	3	100
A2	0.300 ± 0.012^{f}	1.192 ± 0.048^{c}	3	98.5
A3	0.237 ± 0.009^{g}	1.488 ± 0.060^{a}	4	99
A4	0.568 ± 0.023^{c}	0.800 ± 0.032^{d}	4	99
N1	0.721 ± 0.028^{b}	0.5180.021 ± ^{f}	2	99
N2	0.363 ± 0.015^{e}	1.340 ± 0.054^{b}	6	100
N3	0.900 ± 0.036^{a}	0.199 ± 0.008^{gh}	2	99
N4	0.479 ± 0.019^{d}	0.688 ± 0.028^{e}	2	99

Note: The letters in the table represent multiple comparisons ($p < 0.05$). A1, A2, A3, A4, N1, N2, N3, and N4 represent the four sediments collected from anammox and denitrification systems each. Different lowercase letters with shoulder marks in the same column indicate significant differences.

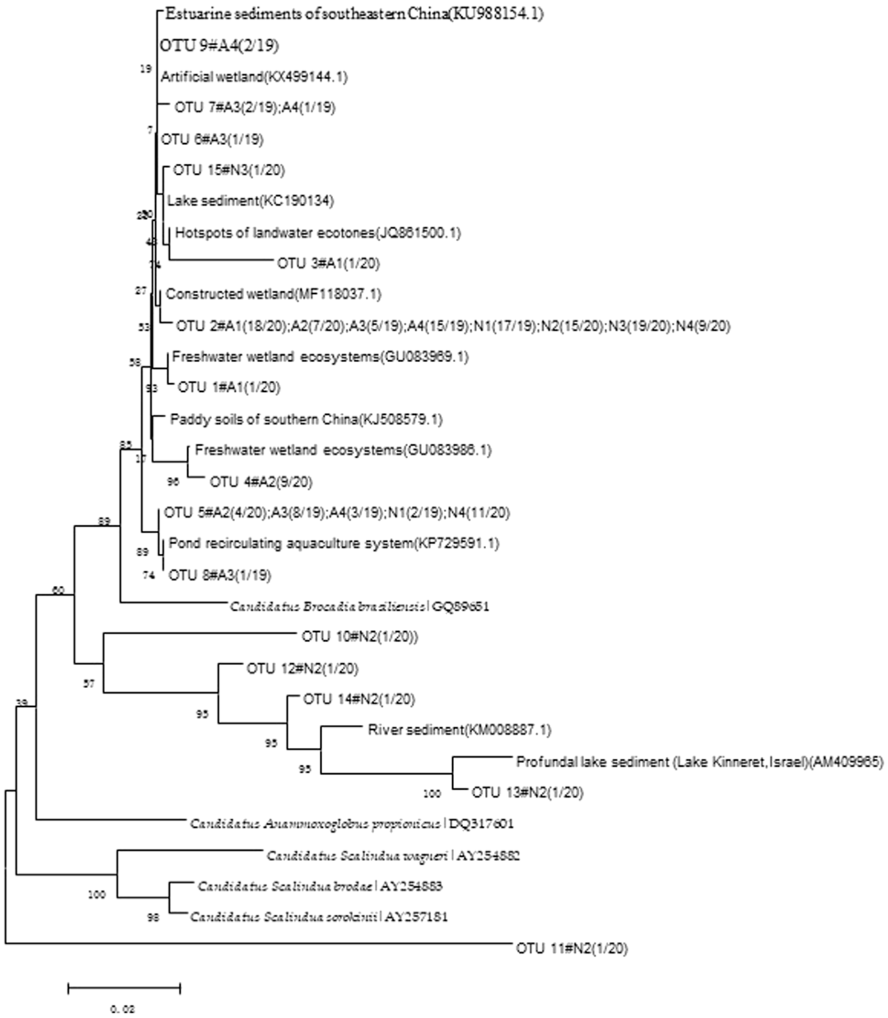

FIGURE 3
The Anammox bacterial 16S rRNA genes in the denitrifying and anammox groups.

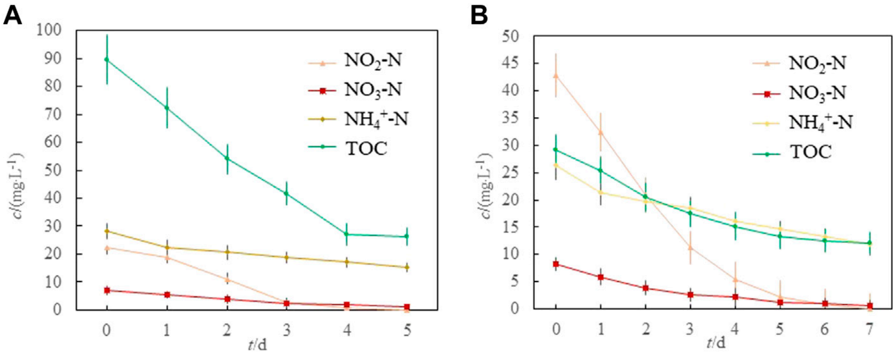

FIGURE 4
The NO_2^--N, NO_3^--N, NH_4^+-N, and TOC in denitrification and anammox groups **(A)** denitrifying group; **(B)**. anammox group.

the number of OTUs in N1, N2, N3, N4, A1, A2, A3, and A4 were 2, 6, 2, 2, 3, 3, 4, and 4, respectively. The results showed that anammox bacteria had differences in OTU numbers at different times in the anammox group and that there were considerable differences with time in the denitrification group. Phylogenetic analysis was used to compare and analyze the anammox bacterial 16S rRNA genes obtained from the denitrifying and anammox groups (Figure 3). The denitrifying and anammox groups mainly contained two types of anammox bacteria: *Candidatus brocadia* and *Candidatus anamomoxoglobus*. Ten OTUs belonged to *Candidatus brocadia*, and their similarity with the most similar 16S rRNA gene sequence in GenBank was 96%. Among them, OTU2 showed the highest abundance across all OTUs in the clone library, similar to that of anammox bacteria found in constructed wetlands, with a similarity of 99% (Lee et al., 2014). A higher abundance of OTU (OTU5) was similar to that of anammox bacteria found in recirculating aquaculture groups, with a similarity of 100% (Van et al., 2011). Most of the similar sequences in the remaining taxa were derived from Chinese estuaries, rivers, and lakes (Wang et al., 2013). Sequence similarity of anammox bacteria among OTU10, OTU12, OTU13, and OTU14 and those in deep-water sediments in the lake was 94–97% (Schwarz et al., 2007).

4.4 Nitrogen removal efficiency of denitrification and anammox groups

Before the experiment, we measured the air-dried sediment samples. The results showed that the contents of NO_2^--N, NO_3^--N, NH_4^+-N, and TOC were 45.87 mgL^{-1}, 14.97 mgL^{-1}, 66.1 $mgL^{-1,}$ and 108.67 mgL^{-1}, respectively. Figure 4 shows the changes in NO_2^--N, NO_3^--N, NH_4^+-N, and TOC in denitrification and anammox groups, respectively. The removal rates ((initial concentration - last concentration)/ initial concentration) for NO_2^--N, NO_3^--N, NH_4^+-N, and TOC in the denitrification group were 99.82%, 86.10%, 45.74%, and 70.76%, respectively (Figure 4A). The removal rates for NO_2^--N, NO_3^--N, NH_4^+-N, and TOC in the anammox group were 97.99%, 93.05%, 54.92%, and 58.82%, respectively (Figure 4B). The removal rates for NO_2^--N and NO_3^--N in the denitrification and anammox groups were over 97% and 85%, respectively. Theoretically, the removal times for NO_2^--N, NO_3^--N, and NH_4^+-N in the denitrification group were approximately 5, 7, and 14 days, respectively, whereas those in the anammox group were approximately 7, 8, and 12 days, respectively. The removal rate for NO_2^--N and TOC were significantly higher in the denitrifying group than in the anammox group, whereas those for NO_3^--N and NH_4^+-N in the anammox group were significantly higher than those in the denitrifying group. In conclusion, the denitrification efficiency was higher in the denitrification group, and ammonia oxidation was higher in the anammox group.

5 Discussion

Sediment is an important part of the aquaculture pond ecosystem. Sediments store nitrogen, phosphorus, and other substances in aquaculture ponds. Excessive accumulation of sediment causes deterioration of water bodies and increases the incidence of diseases in the farmed animals. Sediments are rich in microorganisms, and denitrifying bacteria and anammox bacteria can convert ammonia nitrogen into nitrogen. Thus, the study of the denitrification and anammox of pond sediment has attracted significant attention.

In this study, we found that the Shannon index for denitrifying bacteria in the denitrification group was larger than that in the anammox group, whereas the Simpson index showed the opposite trend. This further indicated the rates of denitrification and anammox to be regulated by organic carbon content, temperature, and nitrite.

In the experiment groups, we found that most sequences of the anammox bacterial 16S rRNA gene clone library belonged to *Candidatus brocadia*, and the most similar sequences were derived from constructed wetlands. This may be attributed to the abundance and diversity of anammox bacteria related to nutrient input from aquaculture ponds (Zeng et al., 2016). Fewer species have been found in these locations compared to those in nearby waters, and this may be attributed to the small scale, and single structure of the aquaculture pond on one hand, and a large number of nutrients added to the aquaculture pond on the other, resulting in the anammox oxidizing bacteria *Candidatus brocadia* becoming the dominant genus in the aquaculture pond. Some sequences in the library constructed in this study belonged to *Dechloromonas*, Burkholderia-ceae, *Thiothrix*, *Thauera*, *Azoarcus*, *Brachymonas*, and *Azospirillum*, which have been reported in other studies. In this study, we found two types of known anammox bacteria, *Candidatus brocade,a* and *Candidatus kuenenia*. It may also be that the aquaculture pond has more nutrients, which makes the *Candidatus brocadia* anammox bacteria become the dominant genus of the aquaculture pond.

In this study, we found that the removal efficiency of NO_2^--N and TOC in the denitrification optimal conditions was higher, whereas that of NO_3^--N and NH_4^+-N was higher in the anammox optimal conditions. This study provided a reference for resolving nitrogen pollution in the aquaculture pond sediment, and it further indicates that the organic carbon, temperature, and nitrate could regulate denitrification and anammox.

This study also suggests that, when regulating pond sediment, in addition to the collaborative application of denitrification and anaerobic ammonia oxidation, we should explore the role of denitrification and anammox, such as establish sequential batch reactions of denitrification and anammox to reduce nitrogen pollution. Overall, our study revealed the characteristics of the denitrification and anammox reactions in pond sediment and provided a reference for resolving nitrogen pollution in the culture environment, which will have great significance in green aquaculture in the future.

Data availability statement

The original contributions presented in the study are included in the article/supplementary material, further inquiries can be directed to the corresponding author.

Author contributions

XL: Conceptualization, Methodology, Formal analysis, Writing-original draft, Validation. MG: Formal analysis, Writing–original draft, Writing–review andamp; editing. JW: Methodology, Validation. ZG: Formal analysis, Investigation, Software. G-FC: Formal analysis, Investigation.

Acknowledgments

The authors would like to thank the “Modern agricultural industrial technology system in China” (grant NO. CARS-46) and the National Key R and D plan of China (grant NO. 2019YFD0900300) for financial support. The authors also thank the reviewer for their contribution in improving our manuscript. We thank www.wileyauthors.com/eeo/preparation for linguistic assistance during the preparation of this manuscript.

Conflict of interest

The authors declare that the research was conducted in the absence of any commercial or financial relationships that could be construed as a potential conflict of interest.

Publisher’s note

References

Boyd, C. E. (1995). *Bottom soils, sediment, and pond aquaculture*. Boston: Springer.

Castine, S. (2013). *Nitrogen removal and reuse in land-based aquaculture*. Townsville, Australia: James Cook University.

Chen, T., Ping, Z., and Hu, B. L. (2009). Species diversity and ecological distribution of anaerobic ammonium-oxidizing bacteria. *Chin. J. Appl. Ecol.* 20 (5), 1229–1235.

Christopher, J., Preston, N., Thompson, P. J., and Burford, M. (2003). Nitrogen budget and effluent nitrogen components at an intensive shrimp farm. *Aquaculture* 218 (1-4), 397–411. doi:10.1016/s0044-8486(03)00014-0

Cui, T. T. (2011). *Intestinal flora diversity study of captive adult pandas in autumn based on 16S rDNA-RFLP technology*. Ya’an, China: Sichuan Agricultural University.

Dang, H., Chen, R., Wang, L., Guo, L., Chen, P., Tang, Z., et al. (2010). Environmental factors shape sediment anammox bacterial communities in hypernutrified Jiaozhou Bay, China. *Appl. Environ. Microbiol.* 76 (21), 7036–7047. doi:10.1128/aem.01264-10

Dang, H., Wang, C., Jing, L., Li T., Fang, Wei, J., et al. (2009). Diversity and distribution of sediment *nirS*-encoding bacterial assemblages in response to environmental gradients in the eutrophied Jiaozhou Bay. *Microb. Ecol.* 58 (1), 161–169. doi:10.1007/s00248-008-9469-5

FAMA (2022). *China fisheries statistics yearbook*. China: China Agricultural Press.

Gao, M. Y., Liu, X. G., Zeng, X. L., and Lu, S. M. (2018). Effects of organic carbon for denitrification and anaerobic ammonium oxidation in sediments of aquaculture pond. *Chin. J. Environ. Eng.* 1, 49–56.

Guo, Y. J., Wang, F., Dong, S. L., Gao, Q. F., Zhang, M. Z., and Tian, X. L. (2011). The rates of denitrification, nitrification and ammoniation in the enclosed sediment of Grasscarp under Different Polyculture Modes. *Chin. Fish. Sci.* 18 (4), 10.

Hinrichs, K., Uwe, H., John, M., Sylva, Sean, Brewer, P., Peter, G., et al. (1999). Methane-consuming archaebacteria in marine sediments. *Nature* 398, 802–805. doi:10.1038/19751

Kiani, S., Kujala, K., Pulkkinen, J. T., Aalto, S. L., Suurnakki, S., Kiuru, T., et al. (2020). Enhanced nitrogen removal of low carbon wastewater in denitrification bioreactors by utilizing industrial waste toward circular economy. *J. Clean. Prod.* 254 (1), 119973. doi:10.1016/j.jclepro.2020.119973

Lee, K. H., Wang, Y. F., Li, H., and Gu, J. D. (2014). Niche specificity of ammonia-oxidizing archaeal and bacterial communities in a freshwater wetland receiving municipal wastewater in Daqing, Northeast China. *Ecotoxicology* 23 (10), 2081–2091. doi:10.1007/s10646-014-1334-3

Li, W. L., Yang, B. Y., Chen, Y. Q., Yin, J., and Xu, S. L. (2015). Study on nitrogen removal characteristics of the denitrifying filter with different additional carbon sources. *Technol. Water Treat.* 41 (11), 82–85.

Li, Y. F., Wang, X., and Gao, Y. (2013). Study on effects of different organic matter, nitrite, e, and pH for denitrification nitrogen and phosphorus removal. *J. Shenyang Archit. Univ. Nat. Sci.* 29 (3), 531–537.

Liao, M. J., and Wu, G. (2013). "Investigation of ammonia-oxidizing microorganisms in aquaculture ponds," in Academic annual meeting of Chinese Society of Environmental Sciences, Chengdu City, Sichuan Province, Oct. 22-23.

Lipsewers, Y. A., Hopmans, E. C., Meysman, F. J., Damsté, J. S. S., and Villanueva, L. (2016). Abundance and diversity of denitrifying and anammox bacteria in seasonally hypoxic and sulfidic sediment of the saline Lake Grevelingen. *Front. Microbiol.* 7, 1–15. doi:10.3389/fmicb.2016.01661

Liu, C., Li, Z., Zhang, Z., Wang, C., and Li, J. (2014). Nitrogen removal performance and sludge characteristics of anammox coupling heterotrophic denitrification. *Chin. J. Environ. Eng.* 8 (8), 3137–3142.

Liu, X. G. (2011). *Study of pollution of pond culture and regulation technology of ecological engineering*. Nanjing, China: Nanjing Agricultural University.

Liu, X. G., Wang, J., Wu, Z. F., Cheng, G. F., and Gu, Z. J. (2021). Anaerobic ammonium oxidation bacteria in a freshwater recirculating pond aquaculture system. *Int. J. Environ. Res. Public Health* 18 (9), 4941. doi:10.3390/ijerph18094941

Mosier, A. C., and Francis, C. A. (2010). Denitrifier abundance and activity across the San Fran cisco Bay estuary. *Environ. Microbiol. Rep.* 2 (5), 667–676. doi:10.1111/j.1758-2229.2010.00156.x

Mulder, A., Graaf, A. A., Robertson, L. A., and Kuenen, J. G. (1995). Anaerobic ammonium oxidation discovered in a denitrifying fluidized bed reactor. *FEMS Microbiol. Ecol.* 16 (3), 177–184. doi:10.1111/j.1574-6941.1995.tb00281.x

Noredal, T. I., Mats, J., Magnus, R., Pell, M., Mikael, H., and Sara, H. (2007). Silver (A_g^+) reduces denitrification and induces enrichment of novel *NirK* genotypes in soil. *FEMS Microbiol. Lett.* 270 (2), 189–194. doi:10.1111/j.1574-6968.2007.00632.x

Sauthier, N., Grasmick, A., and Blancheton, J. P. (1998). Biological denitrification applied to a marine closed aquaculture system. *Water Res.* 32 (6), 1932–1938. doi:10.1016/s0043-1354(97)00406-5

Schwarz, J. I., Eckert, W., and Conrad, R. (2007). Community structure of archaea and bacteria in a profundal lake sediment Lake Kinneret (Israel). *Syst. Appl. Microbiol.* 30 (3), 239–254. doi:10.1016/j.syapm.2006.05.004

SEPA (State Environmental Protection Administration); AQSIQ (State general administration of the people's republic of China for quality supervision and inspection and quarantine) (2002). "Environmental quality standards for surface water," in *National Standard of the People's Republic of China GB3838*.

Shen, L., Wu, H., Gao, Z., Ruan, Y. j., Xu, X. h., Li, J., et al. (2016). Evidence for anaerobic ammonium ox idation process in freshwater sediments of aquaculture ponds. *Environ. Sci. Pollut. Res.* 23 (2), 1344–1352. doi:10.1007/s11356-015-5356-z

Shi, Y., Liu, T., Yu, H., and Quan, X. (2022). Enhancing anoxic denitrification of low C/N ratio wastewater with novel ZVI composite carriers. *J. Environ. Sci.* (2), 12.

Shitu, A., Liu, G., Muhammad, A. I., Zhang, Y., Tadda, M. A., Qi, W., et al. (2022). Recent advances in application of moving bed bioreactors for wastewater treatment from recirculating aquaculture systems: A review. *Aquac. Fish.* 7 (3), 244–258. doi:10.1016/j.aaf.2021.04.006

Sun, Z. D., Wang, Y. Z., and Gao, K. Z. (2017). Biological ecological remediation technology of polluted water. *Shandong Fish.* 4, 52–55.

Table, T. S. (1984). *Turnover of nitrogen compounds in the constructed wetland Oath freshen*. Kassel, Germany: University Kassel Press.

Thamdrup, B. (2012). New pathways and processes in the global nitrogen cycle. *Annu. Rev. Ecol. Evol. Syst.* 43 (1), 407–428. doi:10.1146/annurev-ecolsys-102710-145048

Tiedje, J. M. (1988). Ecology of denitrification and dissimilatory nitrate reduction to ammonium. *Environ. Microbiol. Anger*, 179–244.

Van de Graaf, A. A., de Bruijn, P., Robertson, L. A., Jetten, M. S. M., and Kuenen, J. G. (1996). Autotrophic growth of anaerobic ammonium-oxidizing micro-organisms in a fluidized bed reactor. *Microbiology* 142 (8), 2187–2196. doi:10.1099/13500872-142-8-2187

Van, K., Harhangi, H. R., Flik, G., Jetten, M. S. M., Klaren, P. H. M., and dchjm, O. P. (2011). Anam mox bacteria in different compartments of recirculating aquaculture systems. *Biochem. Soc. Trans.* 39 (6), 1817–1821. doi:10.1042/bst20110743

Verbaendert, I., De Vos, P., Boon, N., and Heylen, K. (2011). Denitrification in gram-positive bacteria: An underexplored trait. *Biochem. Soc. Trans.* 39 (1), 254–258. doi:10.1042/bst0390254

Wang, Z. Y., Wang, C. H., Wang, Z. X., and Pei, Y. S. (2013). Enhancement of anaerobic ammonium oxidation in lake sediment by applying drinking water treatment residuals. *Bioresour. Technol.* 142 (8), 745–749. doi:10.1016/j.biortech.2013.06.016

Wei, L. (2017). Harmful treatment of nitrite in the late stage of prawn culture. *Plant Dr.* 1, 43–44.

Xu, Q., Zhang, F., Zhong-Qi, X. U., Jia, Y. L., and You, J. M. (2011). An analysis of the characteristics and the "dilution effect" of the Simpson index and Shannon-Wiener index. *Pratacultural Sci.* 28 (4), 527–531.

Yang, R. G., Zhang, L. H., and Liu, Q. (2012). Analysis of influence factors on wastewater biological treatment process of shortcut nitrification-denitrification. *J. Northeast China Inst. Electr. Power Eng.* 32 (1), 61–65.

Yao, H. L. (2010). *Study on the ecology of integrated aquaculture pond in China*. Beijing, China: Science Press.

Yu, D. S., Wei, S. J., Li, J., Qi, P. Q., and Guan, Y. J. (2016). Effect of temperature on simultaneous carbon and nitrogen removal by anaerobic ammonium oxidation and denitrification. *China Environ. Sci.* 36 (5), 1384–1391.

Yue, W. Z., and Huang, X. P. (2003). Advance in biogeochemistry studies on nitrogen and phosphorus in offshore sediment. *J. Appl. Oceanogr.* 22 (3), 407–414.

Zeng, X. L., Liu, X. G., Wu, Z. F., Shi, X., and Lu, S. M. (2016). [Community characteristics of ANAMMOX bacteria in subsurface flow constructed wetland (SSFCW) for processing of aquaculture waster water]. *Environ. Sci.* 37 (2), 615–621.

Zhang, Y. Z. (1989). *Chinese pond aquaculture*. Beijing, China: Science Press.

Zheng, Y. L., Hou, L. J., Liu, M., Gao, J., Yin, G. Y., Li, X. F., et al. (2015). Diversity, abundance, and distribution of nirS-harboring denitrifiers in intertidal sediments of the Yangtze estuary. *Microb. Ecol.* 70 (1), 30–40. doi:10.1007/s00248-015-0567-x

Zhu, G., Wang, S., Yu, W., Wang, C., Risgaard-Petersen, N., Jetten, M. S., et al. (2011). Anaerobic ammonia oxidation in a fertilized paddy soil. *Int. Soc. Microb. Ecol.* 5 (12), 1905–1912. doi:10.1038/ismej.2011.63

frontiers | Frontiers in Environmental Science

TYPE Original Research
PUBLISHED 10 January 2023
DOI 10.3389/fenvs.2022.1071963

OPEN ACCESS

EDITED BY
Tao Zhang,
China Agricultural University, China

REVIEWED BY
Changyin Zhu,
Nanjing University, China
Omar Mohammad Atta,
Al-Azhar University, Egypt
Chengcheng Xia,
Sichuan University, China
Tongzhou Liu,
Harbin Institute of Technology, China

*CORRESPONDENCE
Zijun Dong,
✉ dongzijun@szu.edu.cn

SPECIALTY SECTION
This article was submitted to Water and Wastewater Management,
a section of the journal
Frontiers in Environmental Science

RECEIVED 17 October 2022
ACCEPTED 29 December 2022
PUBLISHED 10 January 2023

CITATION
Gu Y, Zhang Y, Jiang C, Dong Z and Bai X (2023), Efficient metformin transformation in sulfite/UV process co-present with oxygen.
Front. Environ. Sci. 10:1071963.
doi: 10.3389/fenvs.2022.1071963

Efficient metformin transformation in sulfite/UV process co-present with oxygen

Yurong Gu[1], Yi Zhang[1], Chengchun Jiang[1], Zijun Dong[2,3]* and Xue Bai[4]

[1]School of Material and Environmental Engineering, Shenzhen Polytechnic, Shenzhen, China, [2]College of Civil and Transportation Engineering, The Underground Polis Academy, Shenzhen University, Shenzhen, China, [3]Shenzhen Key Laboratory of Green, Efficient and Intelligent Construction of Underground Metro Station, Shenzhen, Guangdong, China, [4]School of Civil and Environmental Engineering, Shenyang Jianzhu University, Shenyang, China

UV/sulfite process without oxygen has been extensively explored and used for the degradation of many micro-pollutants. In the present work, a UV/sulfite process in the presence of oxygen was applied to degrade a widely used pharmaceutical compound, metformin (MET). The results showed that the oxygen-involved UV/sulfite process could efficiently degrade MET. At an initial concentration of 2.5 mg/L, 86.0% of MET was removed from the contaminated water within 180 min irradiation at a sulfite dosage of 10 mM, solution pH of 9, and UV intensity of 4,092 μW/cm^2. In addition, sulfate radical ($SO_4{\bullet}^-$), hydroxide radical (•OH), hydrogen atom (•H), and hydrated electron (e_{aq}^-) were found to be the dominant active species contributing to MET removal in the studied process through scavenging experiments. The increase in UV intensity, sulfite dosage, solution pH, and reaction temperature enhanced MET degradation in the investigated process to a certain extent, whereas the introduction of bicarbonate and fulvic acid slightly suppressed MET degradation. Finally, the degradation products of MET were identified. The oxygen-involved UV/sulfite process exhibited a remarkable denitrification capacity (>80%) in MET. The findings of this study may offer a novel approach for treating emerging contaminants.

KEYWORDS

sulfite, UV, oxygen, metformin, AOPs

1 Introduction

Pharmaceutical and personal care products (PPCPs) comprise diverse organic substances, including antibiotics, analgesics, hormones for pharmaceuticals and cosmetics, antibacterial agent, preservatives for personal care products (Zhang et al., 2022). Metformin (MET), a common antidiabetic drug used for type II diabetes treatment, has been ranked among the most widely used PPCPs because more than 200 million people are suffering from diabetes worldwide (Yu et al., 2022). The widespread use of MET inevitably results in its emission into the environment through wastewater discharge as conventional wastewater treatment approaches (i.e., flocculation, activated carbon filtration, and bio-degradation) are ineffective for MET removal (Scheurer et al., 2009). Thus, the occurrence of MET in sewage, effluent in sewage treatment plants, and surface water is frequently reported (Ambrosio-Albuquerque et al., 2021). For example, a relatively high concentration of MET ranging from 70 to 325 μg/L was found in the effluent of a Portuguese sewage treatment plant (Gaffney et al., 2017). The potential bio-toxicity of MET, such as causing estrogenic effects or acting as an endocrine disruptor, has been reported in some literature (Niemuth and Klaper, 2015; Crago et al., 2016). Hence, MET has become an emerging pollutant in aquatic environments.

Several attempts have been made to alleviate MET contamination, including graphene oxide adsorption, photo-oxidation, and electro-oxidation (Zhu et al., 2017; Karimiana et al., 2020). Owing to the operational simplicity and cost-efficiency of light sources, photo-oxidation methods (i.e., UV/Fenton, UV/H_2O_2, and UV/TiO_2) have become the most favored treatment techniques for organic pollutants degradation (Zhou et al., 2017; George et al., 2022).

In recent decades, the UV/sulfite system has gained increasing attention as an often-mentioned advanced reduction process (ARP) because of the production of various reductive species, such as hydrated electron (e_{aq}^-, $E = -2.9$ V) and hydrogen atom (•H, $E = -2.3$ V) (Vellanki et al., 2013; Ding et al., 2022). Several halogenated organic pollutants decomposition by the UV/sulfite system have already been investigated. For instance, Song et al. (2013) reported that perfluorooctanoic acid (PFOA), which is an extremely recalcitrant halogenated contaminant, can be completely decomposed in the UV/sulfite system after 1 h reaction, and a high defluorination efficiency of approximately 90% could be obtained by extending the reaction time to 24 h. Liu et al. (2015) achieved nearly 40% degradation efficiency of atenolol (20 μM) even at a neutral solution pH. In the above-mentioned degradation process, e_{aq}^- was manifested the dominant reductive species contributing to the decomposition of the target pollutants, and oxygen was previously removed from the reaction system by purging nitrogen, because oxygen can react with e_{aq}^- and lead to superoxide radical ($O_2{\bullet}^-$) generation. Nevertheless, once oxygen is applied in the sulfite mediated UV photolysis system, another mild radical, namely sulfite radical ($SO_3{\bullet}^-$), is likely to be transformed into a highly reactive oxidant sulfate radical ($SO_4{\bullet}^-$) (Deister and Warneck, 1990), indicating that the oxygen-involved UV/sulfite system can be regarded as a prospective advanced oxidation process (AOP) (Huang et al., 2018; Li et al., 2020). Recently, (Chen et al. (2021) developed a synergetic-photoelectric sulfite mediated system where oxygen was continuously produced through water electrolysis. The combined effect of electrolysis and photolysis on sulfite brings about a large number of active species generation. The steady-state $SO_4{\cdot}^-$ concentration was determined as ranging from .2 × 10^{-12} to 1.1 × 10^{-12} M. Correspondingly, this reaction system had extraordinary oxidative capacity in removing micro-pollutants such as ibuprofen and bisphenol A. Although several researchers have explored treatment efficiency of the oxygen-involved UV/sulfite system towards some emerging contaminants (i.e., atrazine, bisphenol A, trichlorophenol) (Cao et al., 2021a), the systematic investigation on the degradation efficiency of the antidiabetic drug, namely MET, was still scanty. Furthermore, investigation of the oxygen-involved UV/sulfite system on target pollutant removal in the real water matrix was also scarce.

Herein, a UV/sulfite system with the co-presence of oxygen was built and utilized for MET degradation. The crucial species contributing to MET degradation were ascertained. The impact of several common factors such as pH value of testing solution, reaction temperature, sulfite dosage and co-present compounds on MET degradation was evaluated. In addition, MET degradation in a real water matrix was monitored. The degradation products of MET as well as the bio-toxicity change of the testing solution were also determined. Outcomes in the present work suggests a distinctive treatment technology for emerging contaminants.

2 Materials and methods

2.1 Materials

Metformin hydrochloride (MET, 97.0%, $C_4N_5H_{11}{\bullet}HCl$), sodium sulfite (98.0%, Na_2SO_3), tertiary-butanol (TBA, ≥99.5%, $C_4H_{10}O$), methanol (MeOH, >99.9%, CH_3OH), fulvic acid (85.0%, FA), potassium nitrate (>99.0%, KNO_3), superoxide dismutase (SOD, ≥1,400 units/mg dry weight), and sodium bicarbonate (99.7%, $NaHCO_3$) were purchased from Aladdin Co., LTD. (Shanghai, China) or Sigma-Aldrich Co., LTD. (Guangzhou, China). A Millipore purification system (Millli-Q IQ 7000, Darmstadt, Germany) was employed for the generation of ultrapure water and subsequent preparation for diverse reaction solution.

2.2 MET degradation experiments

MET degradation experiments were conducted in a 3-L cylindrical glass vessel (Supplementary Figure S1). A mixed solution containing MET and sulfite was filled into the vessel and magnetically stirred during the degradation process. In addition, the testing solution was purged with air or nitrogen gas (1 L/min) for 180 min. Apart from investigating the impact of solution pH on MET removal, the solution pH was maintained at approximately 9 with 10 mM phosphate buffer. A monochromatic low-pressure lamp ($\lambda = 254$ nm, 10 W, Dongguan, China) with a quartz sleeve enclosure was used as the irradiation source. The UV lamp was ignited and warmed for 30 min before commencing the irradiation experiments to obtain a stable output. MET batch degradation experiments were carried out at a constant temperature (25°C) through a thermostatic recirculation system (THD-1015, Ningbo, China). KNO_3 (5 mM), $NaNO_2$ (5 mM), MeOH (300 mM), TBA (300 mM), and SOD (3.3 mg/L) were introduced as scavengers to ascertain the contribution of different active species to MET degradation. Sulfite dosage was changed from 2.5 mM to 15 mM to study the impact of the sulfite dosage on MET removal. To reveal the impact of UV intensity on MET degradation efficiency, the UV lamp was wrapped with a few aluminum foil to change UV light emitted into the reaction solution (Li et al., 2014). The maximum UV intensity (100% I_0) entering into the reaction solution was measured to be 4,092 μW/cm^2 using a UV irradiatometer (Linshang Co., LTD., Shenzhen, China). Additionally, effect of the coexisting constituents such as HCO_3^- and natural organic matter (NOM) on MET removal was monitored by adding diverse concentrations of HCO_3^- (0–2.0 mM) and FA (0–15 mg/L) to the reaction system. Additionally, two surface water samples from Dasha River in Nanshan District (Shenzhen, China) was obtained and used to evaluate MET degradation efficiency in a real water matrix. Water quality parameters of the surface water samples were listed in Supplementary Table S1. Samples were withdrawn at the preset intervals for immediate analysis. All experiments were performed in triplicate, and the mean values were presented.

2.3 Analysis procedures

MET concentration was analyzed by using a Waters high-performance liquid chromatography which was equipped with a

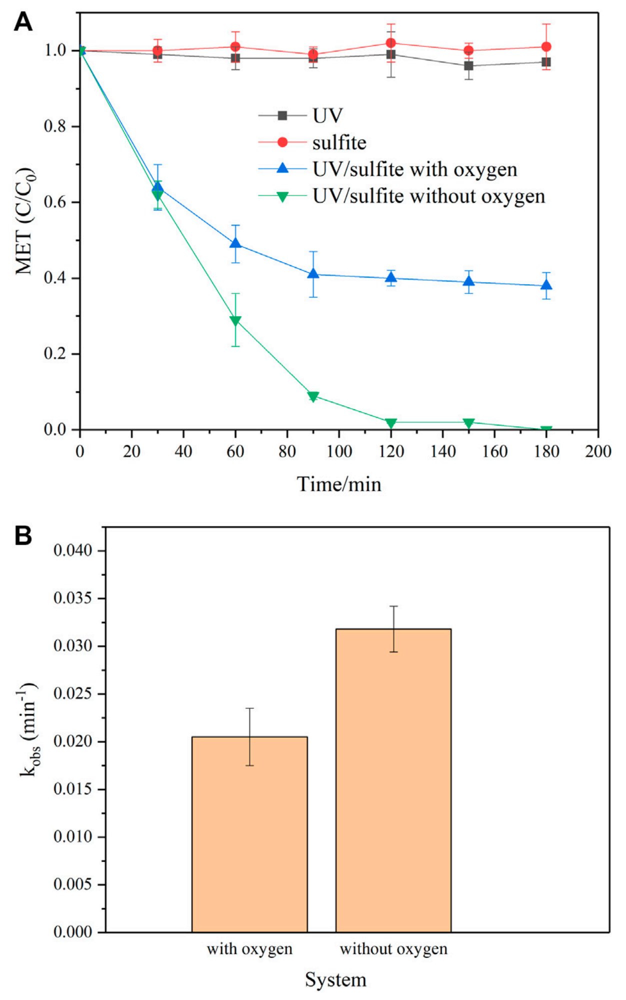

FIGURE 1
(A) MET degradation efficiency in different reaction processes; **(B)** Pseudo first-order rate constants for MET degradation with or without oxygen by the UV/sulfite process. Experimental conditions: $[MET]_0$ = 10 mg/L, $[SO_3^{2-}]_0$ = 10 mM, pH = 9.

reversed C18 column (5 μm, 4.6 × 250 mm, Phenomenex, Torrance, United States) and a UV detector. The separation conditions were set as follows: A mixed solution which contained .1% acetic acid (80%) and MeOH (20%) was employed as mobile phase. The flow rate of mobile phase was determined as 1.0 mL/min. The wavelength of the UV detector for MET concentration measurement was 246 nm.

A pH meter (Mettler Toledo, Shanghai, China) was employed for solution pH determination. Inorganic degradation products of MET such as nitrite and ammonia nitrogen were detected through a colorimetric method. The detection of organic intermediates was performed in a ultra high-performance liquid chromatography (UPLC, Agilent 1290, CA, United States) coupled with time-of-flight mass spectrometry (AB SICEX Tripe TOF 4600, CA, United States). The mobile phase was a mixture of acetonitrile (10%) and .1% formic acid (90%) with a flow rate of .8 mL/min. The column temperature and injection volume of sample were set at 30°C and 10 μL, respectively. Bio-toxicity of the testing solution was determined by the luminescent bacteria toxicity test referring to the guideline from ISO standard (quality, 2007), and the relative inhibition rate towards luminescent bacteria was used as an indicator to reflect bio-toxicity of the testing solution.

3 Results and discussion

3.1 MET degradation in direct UV and UV/sulfite systems

MET degradation in four different reaction systems was monitored, and the results were shown in Figure 1A, B. 62.0% MET removal was obtained after 180 min irradiation in the oxygen-involved UV/sulfite system at sulfite dosage of 10 mM, whereas negligible MET removal (<5%) was achieved in direct UV and sulfite systems, which was ascribed to the weak absorption of MET in the UV-C region and poor reduction capacity of sulfite (Maćerak et al., 2018; Karimiana et al., 2020). Although the oxygen-free UV/sulfite system behaved better MET treatment efficiency, it needed constant purging of nitrogen gas, which made it unpractical for real wastewater treatment. MET degradation kinetics in the two UV/sulfite system were found to fit the pseudo first-order model, and observed rate constants (k_{obs}) were .0205 min^{-1} and .0318 min^{-1}, respectively. Comparison between this work and previous investigations concerning about MET removal by photolytic methods was conducted (Table 1), and k_{obs} of MET degradation in this work was a bit faster than that of previous studies. Additionally, energy consumption needed for MET removal to half of its initial concentration was calculated as .1 kJ/μmol, which was at least 1–2 order of magnitude lower than that of other emerging contaminants (i.e., PFOA, ICMs) degraded by photolytic techniques (Vecitis et al., 2009; Gu et al., 2022). The obtained results suggested the studied oxygen-involved UV/sulfite process was promising for practical MET-containing wastewater treatment.

The extraordinary MET degradation performance in the UV/sulfite system was ascribed to the generation of reactive species. When sulfite undergoes UV photolysis, reactive species like e_{aq}^-,·H, and $SO_3{\cdot}^-$ have been reported to be produced before (Milh et al., 2021). In addition, the studied system was continuously purged with air, thus oxygen was likely to react with $SO_3{\cdot}^-$ and lead to $SO_4{\cdot}^-$ generation (Eqs. 1–4). According to Yang et al. (2015), hydroxyl radical (·OH) can be transformed from $SO_4{\cdot}^-$ in the testing solution. Hence, at least five kinds of reactive species, namely e_{aq}^-,·H, $SO_3{\cdot}^-$, $SO_4{\cdot}^-$, and ·OH, were likely to exist in the studied system. Scavenging reactions were conducted to determine the primary active species that contributed to MET removal.

As shown in Figure 2, the introduction of both MeOH and TBA inhibited MET degradation. However, the inhibition effect of MeOH was more obvious, indicating that both $SO_4{\cdot}^-$ and ·OH contributed to MET degradation. Because MeOH reacted quickly with both $SO_4{\cdot}^-$ and ·OH at a comparable rate constant, whereas TBA merely efficiently quenched ·OH (Supplementary Table S2). Moreover, nitrate and nitrite were employed in the reaction system to uncover the role of reductive species (i.e., e_{aq}^-,·H) played in MET removal, and MET degradation was apparently suppressed in the presence of nitrate and nitrite, where nitrite exhibited a more obvious inhibition. When 5 mM of nitrate and nitrite were introduced into the reaction system individually, MET degradation ratio decreased by 13.0% and 44.7% after 180 min irradiation, respectively. It is well documented that both nitrate

TABLE 1 Summary of previously reported literature for photolysis of MET.

Degradation methods	Reaction conditions	Removal ratio (%)	Time (min)	k_a (min^{-1})	Reference
UV/Fenton	$[MET]_0$ = 1,027 ng/L	43	10	—	Cruz et al. (2012)
	$[H_2O_2]_0$ = 50 mg/L				
	$[Fe^{2+}]_0$ = 5 mg/L pH near neutral				
	light source UV_{254}				
UV/H_2O_2	$[MET]_0$ = 2 μM	≈45	60	.0152	Neamţu et al. (2014)
	$[H_2O_2]_0$ = 300 μM pH 6.5			$\tau_{1/2}$ = 45.6 min	
UV/TiO_2	$[MET]_0$ = 10 mg/L	31	30	—	Quintão et al. (2016)
	$[TiO_2]_0$ = 120 mg/L light source UV_{254}				
$UV/TiO_2/PDS$	$[MET]_0$ = 5 mg/L	91.6	210	.013	Nezar and Laoufi, (2018)
	$[TiO_2]_0$ = 100 mg/L			$\tau_{1/2}$ = 53.3 min	
	$[K_2S_2O_8]_0$ = 1,000 mg/L				
	pH free				
$VUV/Fe^{2+}/PMS$	$[MET]_0$ = 50 mg/L	89.7	30	—	Karimiana et al. (2020)
	$[Fe^{2+}]_0$ = .05 mg/L				
	$[PMS]_0$ = 50 mg/L pH 6.3				
	light source VUV				
Oxygen-involved UV/sulfite system	$[MET]_0$ = 10 mg/L	62.0	180	.0205	This work
	$[SO_3^{2-}]_0$ = 10 mM pH 9			$\tau_{1/2}$ = 33.8 min	
	light source UV_{254}				

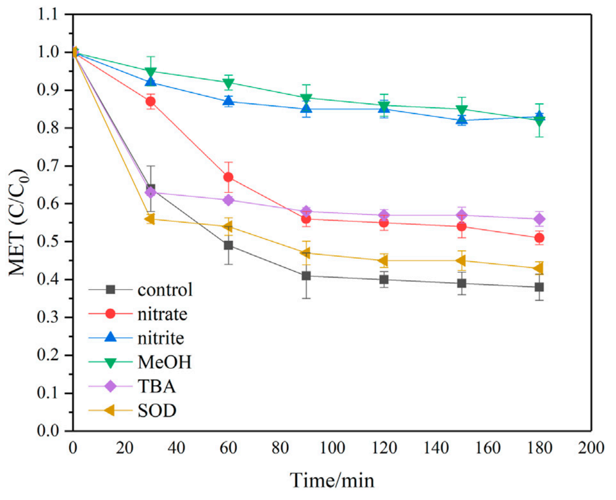

FIGURE 2
The effect of different scavengers on MET degradation. Experimental conditions: $[MET]_0$ = 10 mg/L, $[SO_3^{2-}]_0$ = 10 mM, pH = 9, $[TBA]_0$ = 300 mM, $[MeOH]_0$ = 300 mM, $[KNO_3]_0$ = 5 mM, $[NaNO_2]_0$ = 5 mM, and $[SOD]_0$ = 3.3 mg/L.

and nitrite can efficiently scavenge e_{aq}^- at 10^9 $M^{-1}s^{-1}$ level (Buxton et al., 1988). Nevertheless, nitrite reacts with ·H approximately 500 times as fast as that for nitrate (Buxton et al., 1988), which led to a similar e_{aq}^- concentration but a much lower ·H concentration. The different ·H and e_{aq}^- concentration was thus used to identify their impact on MET removal. Results in Figure 2 indicated both ·H and e_{aq}^- participated in the MET degradation process. Considering another mild oxidant, $SO_3\cdot^-$ (E_0 = .63 V, pH = 7) (Buxton et al., 1988), many studies have reported its negligible contribution to target pollutant decomposition in sufite-based UV photolytic system (Li et al., 2012; Gu et al., 2016). Notably, the generated $SO_3\cdot^-$ can be transformed into highly oxidative $SO_4\cdot^-$ when co-present with oxygen, as demonstrated in the above discussion by alcohol inhibition experiments. Consequently, participation of $SO_3\cdot^-$ in MET degradation can be excluded. In the presence of oxygen, e_{aq}^- may be quickly quenched and resulted in O_2^- generation (Deister and Warneck, 1990). Therefore, SOD was selected as the quencher and applied to the reaction solution to evaluate the contribution of $O_2\cdot^-$ to MET degradation. Negligible MET suppression (<5%) was observed when SOD was introduced into the UV/sulfite process, suggesting an insignificant role of $O_2\cdot^-$. In summary, it is highly probable that reactive species, including $SO_4\cdot^-$, ·OH, ·H and e_{aq}^-, mainly accounted for MET degradation in the oxygen-involved UV/sulfite system.

$$SO_3^{2-} + h\nu \rightarrow SO_3\cdot^- + e_{aq}^- \tag{1}$$

$$HSO_3^- + h\nu \rightarrow SO_3\cdot^- + \cdot H \tag{2}$$

$$SO_3\cdot^- + O_2 \rightarrow SO_5\cdot^- \tag{3}$$

$$SO_5\cdot^- + SO_3^{2-} \rightarrow SO_4\cdot^- + SO_4^{2-} \tag{4}$$

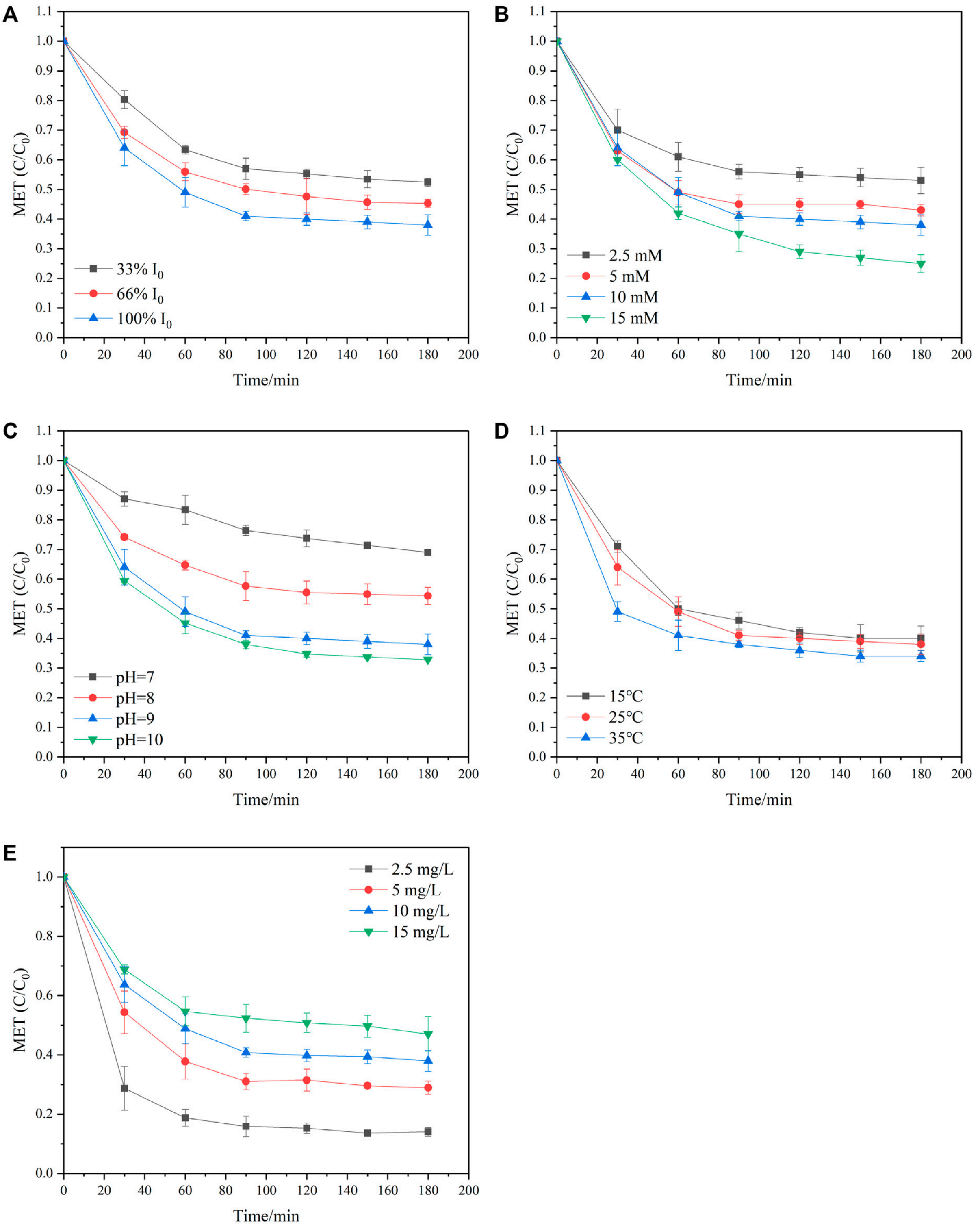

FIGURE 3
The effect of different water quality or operating parameters **(A)** UV intensity; **(B)** sulfite dosage; **(C)** solution pH; **(D)** reaction temperature; **(E)** initial MET concentration on MET degradation by the oxygen-involved UV/sulfite system. Experimental conditions: [MET]$_0$ = 10 mg/L, [SO$_3^{2-}$]$_0$ = 10 mM, pH = 9, T = 25°C.

3.2 Influence of incident UV intensity

In the UV photolytic process, the incident UV intensity is a major factor determining the reaction rate between target pollutant and reactive species generated. Zhang et al. (2013) found methylene blue removal rate in a UV/TiO_2/H_2O_2 system was positively proportional to the UV intensity. Similar results were reported by Liu et al. (2014) A higher UV intensity was found beneficial for enhancing dichloroethane removal in a UV/sulfite system, and the observed rate constant of dichloroethane removal showed a linear relationship with UV intensity (R^2 > .99). MET degradation experiments at different UV intensity were carried out and results were presented in Figure 3A. MET degradation ratio was obviously enhanced by increasing UV intensity. MET degradation efficiency altered from 47.6% to 62.0% after 180 min reaction when UV intensity varied from 33% I_0 to 100% I_0. MET degradation in the UV/sulfite system followed pseudo first-order kinetics (R^2 > .98) (Supplementary Table S2). The observed rate constants of MET degradation at 100% I_0 was almost doubled when compared with that at 33% I_0. When UV intensity entering the testing solution increased, the amount of generated radicals increased accordingly, which in consequence led to a faster MET removal. Referring to previous investigations, the generation rates of e_{aq}^- and $SO_3\cdot^-$ are proportional to UV intensity under alkaline pH conditions when sulfite undergoes UV photolysis (Song et al., 2013). e_{aq}^- and $SO_4\cdot^-$ which was produced through chain reactions between O_2 and $SO_3\cdot^-$, were manifested the governing active species accounting for MET degradation in Section 3.1. Thus an increase in UV intensity would benefit MET transformation in the studied reaction system.

3.3 Influence of sulfite dosage

Different sulfite concentrations were introduced to monitor their influence on MET removal at an initial MET concentration of 10 mg/L, and the results were presented in Figure 3B. MET degradation was apparently enhanced by increasing sulfite dosage. As depicted in Figure 3B, increasing sulfite dosage from 2.5 mM to 15 mM led to a higher degradation ratio of MET, increasing from 46.9% to 75.5% after 180 min irradiation. The obvious promotion on MET removal at higher sulfite dosage further confirmed the negligible role of direct photolysis. If direct photolysis governs the MET degradation process, the augmentation of sulfite dosage may result in a decrease in UV intensity, which otherwise would be absorbed by MET, and thus causing a reduction in k_{obs} (Liu et al., 2014). As depicted in Figure 3B and Supplementary Table S3, the optimal sulfite dosage was 10 mM, and further increasing the sulfite concentration slowed MET degradation rate. At a constant solution pH and UV intensity, the reactive species (i.e., e_{aq}^- and $SO_3\cdot^-$) production was positively correlated with sulfite dosage (Yoon et al., 2014), thereby causing the difference in MET degradation kinetics. When sulfite dosage was changed from 2.5 mM to 10 mM, a 1.1 fold increase in k_{obs} was observed (Supplementary Table S3). Nevertheless, a further increase in sulfite dosage to 15 mM led to a decline in k_{obs} to .0175 min^{-1}. At higher sulfite dosages, the scavenging reactions between the generated reactive species (e.g., ·H, e_{aq}^-) and co-present constituents became vigorous, thus enormous reactive species were quenched, and their use in MET degradation was limited (Fu et al., 2010; Yazdanbakhsh et al., 2018). Consequently, sulfite dosage exhibited less of enhancement effect on MET degradation, which was reflected by the reduction in k_{obs}.

3.4 Influence of solution pH

Apart from sulfite dosage, the solution pH also affected the degradation of target pollutants in the sulfite mediated photolysis process. Figure 3C presented the effect of solution pH on MET removal at a sulfite dosage of 10 mM. MET degradation was substantially facilitated when the solution pH was changed from neutral to alkaline conditions. The optimal solution pH was at 9, further increasing the solution pH brought about slight enhancement both in degradation efficiency and rate of MET. Moreover, MET degradation kinetics in the investigated solution pH range was well depicted by the pseudo first-order model (Supplementary Table S3), which was in accordance with previous studies (Li et al., 2012; Liu et al., 2015).

Two main reasons can be used to explain the impact of solution pH on MET removal in the UV/sulfite system. On one hand, sulfite distribution would change along with the alteration of solution pH. As shown in Supplementary Table S4, the major form of sulfite at neutral pH condition is HSO_3^-, and its proportion gets declined with the increase of solution pH, which means the reactive species generated from HSO_3^- photolysis would accordingly decreased. On the contrary, the production of e_{aq}^- can be enhanced because of the increase of SO_3^{2-} proportion. Therefore, a dramatic promotion on MET degradation was obtained when solution pH was adjusted from pH seven to pH 9. SO_3^{2-} species accounts for more than 98% of sulfite species at pH 9, thus further increase of solution pH shows little effect on target pollutant degradation. On the other hand, solution pH also affected the transformation between ·H and e_{aq}^-. The transformation from ·H to e_{aq}^- was promoted at a higher pH condition (Eq. 5). Since e_{aq}^- was verified an important contributor for MET removal in the investigated system, the higher e_{aq}^- concentration would certainly lead to better MET treatment efficiency.

$$\cdot H + OH^- \rightarrow e_{aq}^- + H_2O \tag{5}$$

Moreover, the distribution of MET molecule was strongly dependent on the solution pH. As reported by (Scheurer et al. (2009), the principal existing form of MET was its neutral molecule when solution pH was above 12, whereas the protonation reaction occurred at two amino groups accompanied with a decrease in solution pH, which was nearly accomplished at pH 8. The change in the charged MET species may also impact its reaction with various oxidative or reductive species in the studied system, and then caused different MET degradation efficiency.

3.5 Influence of reaction temperature

Temperature is of great importance when determining the rates of chemical reactions. Hence the impact of reaction temperature on MET degradation was explored, and the results were shown in Figure 3D. MET degradation was remarkably enhanced with the increase in reaction temperature. When we transformed Figure 3D to semilog plots, it was found that during the studied temperature range, MET degradation was well fitted with a pseudo first-order model (R^2 > .97) (Supplementary Table S3). Additionally, the MET degradation rate increased 1.1–1.8 folds when the reaction temperature was raised by increments of 10°C. Based on the Van't Hoff equation, the reaction rate of a common chemical process increases approximately 2–4 folds when the reaction temperature is increased by 10°C. Apparently, the impact of temperature on MET removal in the oxygen-involved UV/sulfite system was weakened, hinting the photo-chemical process played a key role during MET degradation. Moreover, the activation energy was calculated as 27.8 kJ/mol, which was comparable to that of a commonly used PPCPs, atenolol, treated by the sulfite-mediated UV irradiation process (Liu et al., 2015).

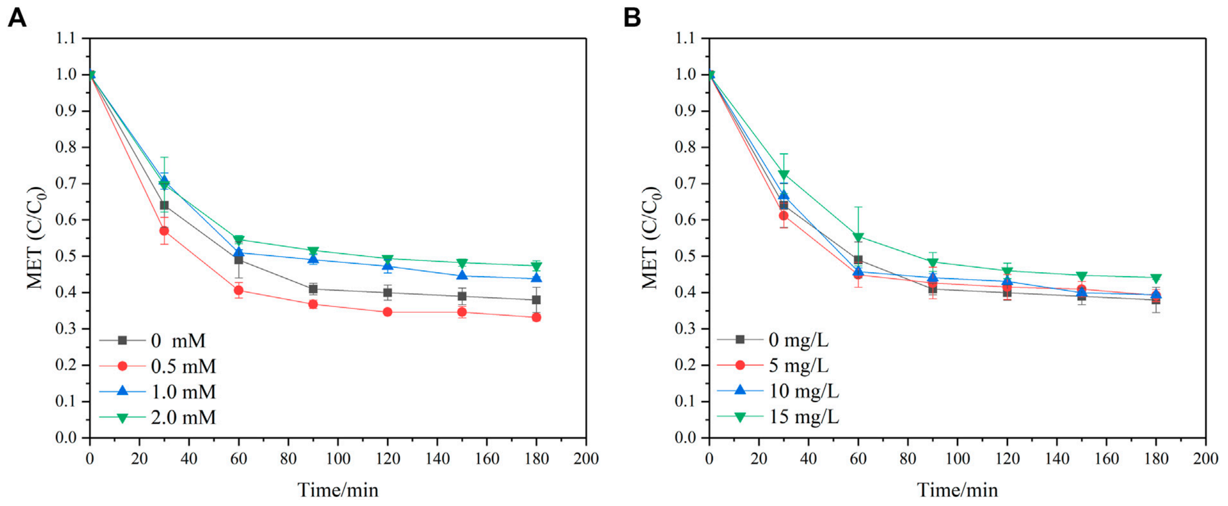

FIGURE 4
MET degradation with co-presence of **(A)** HCO_3^- and **(B)** FA. Experimental conditions: $[MET]_0$ = 10 mg/L, $[SO_3^{2-}]_0$ = 10 mM, UV intensity = 100% I_0, and pH = 9.

3.6 Influence of initial MET concentration

MET concatenation was varied in different water matrix (Ambrosio-Albuquerque et al., 2021), thus it's necessary to evaluate the effect of initial MET concentration on MET degradation in the present system. As depicted in Figure 3E, approximately 86.0% MET was removed from the aqueous media at initial MET concentration of 2.5 mg/L, and the degradation ratio gradually decreased to 53.0% as the initial MET concentration increased to 15 mg/L. Under the circumstance of lower MET concentration, the produced reactive species in the oxygen-involved UV/sulfite system were such sufficient that most of MET could be degraded. As the initial MET concentration increased, the effective collision frequency between MET molecule and the reactive species was decreased. Additionally, more intermediates of MET would be generated when a higher initial MET concentration was employed in the investigated system, which also might compete for the reactive species with MET and accordingly slackened MET degradation (Shah et al., 2014).

3.7 Influence of co-present compounds

In real aqueous environments, many compounds are co-present with MET, and their presence may impact MET degradation capacity in the UV/sulfite system. HCO_3^- and FA are ubiquitously present in natural water, thus they were selected as representative inorganic and organic substance, respectively, to investigate the water quality effect on MET degradation. The results are presented in Figure 4. In general, the introduction of HCO_3^- to the UV/sulfite system slightly suppressed MET removal, and the suppression effect of HCO_3^- was aggravated with an increase in HCO_3^- concentration. MET degradation ratio decreased from 62.0% to 52.6% when HCO_3^- dosage was increased by 2.0 mM after 180 min irradiation. The inhibitory effect of HCO_3^- on MET removal was ascribed to the following reasons. Firstly, it was reported that HCO_3^- can act as a quencher for ·OH (Eq 6) (Buxton et al., 1988), thus the introduction of HCO_3^- to the reaction solution may result in ·OH consumption, which was attested to be responsible for MET degradation and further caused the reduction of MET degradation efficiency. Secondly, HCO_3^- could also react with another vigorous species, e_{aq}^-, in the studied system, thus a certain amount of e_{aq}^- may be consumed by HCO_3^- and consequently cause an inhibition effect on MET removal. Nevertheless, the rate constant between HCO_3^- and e_{aq}^- (or ·OH) was relatively slow ($k \approx 10^6\ M^{-1}\ s^{-1}$) (Buxton et al., 1988), which was at least 10 times smaller than that between perfluorooctanoic acid, a notorious persistent contaminant, and e_{aq}^- (Huang et al., 2007). Therefore, the co-presence of 2 mM HCO_3^- only led to a 10.2% decrease in MET removal in the UV/sulfite process during 180 min reaction.

$$HCO_3^- + \cdot OH \rightarrow CO_3\cdot^- + H_2O \quad k = 8.5 \times 10^6\ M^{-1}\ s^{-1} \tag{6}$$

Similarly, the introduction of FA resulted in a weak suppression on MET degradation. For instance, at the highest FA dosage of 15 mg/L, MET removal ratio was reduced by only 6.2%. These results differed slightly from those of other researches, which reported that the introduction of NOM to the sulfite-mediated UV photolysis process considerably reduced the target pollutant removal. Xiao et al. (2017) stated BrO_3^- removal ratio was evidently reduced in the sulfite-mediated UV photolysis process when humic acid was simultaneously added. They reported that the BrO_3^- removal ratio dramatically decreased from approximately 60.0%–44.8% and 17.0% at humic acid concentrations of 2 mg/L and 5 mg/L, respectively. The distinguishing behavior of the target pollutant removal in the investigated system was caused by the various water characteristics (i.e., DO and pH) and the different NOM used (Peldszus et al., 2004). The slight suppression of NOM in our study can be attributed to the following reasons. Firstly, NOM is rich in chromophores (Lyu et al., 2015), hence behaved competitively for UV light, which resulted in less UV light being absorbed by sulfite and the subsequent reduction of produced oxidative or reductive species. Moreover, several oxidative reactive species (i.e., ·OH, $^1O_2$, H_2O_2) were produced in the process of NOM photolysis, which may react quickly with reductive species such

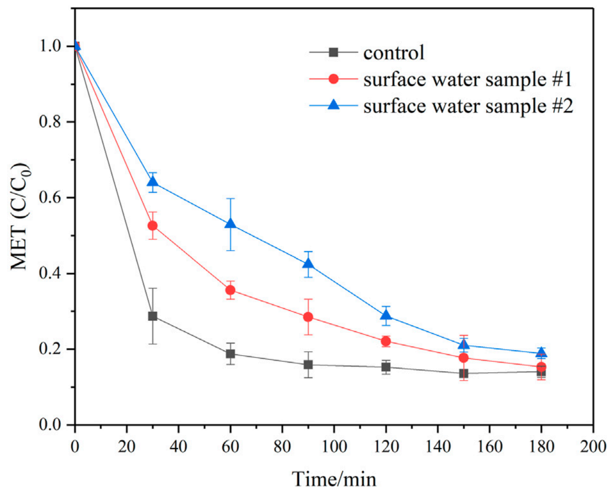

FIGURE 5
MET degradation in the real water matrix. Experimental conditions: $[\text{MET}]_0 = 2.5$ mg/L, $[\text{Sulfite}]_0 = 10$ mM, UV intensity = 100% I_0.

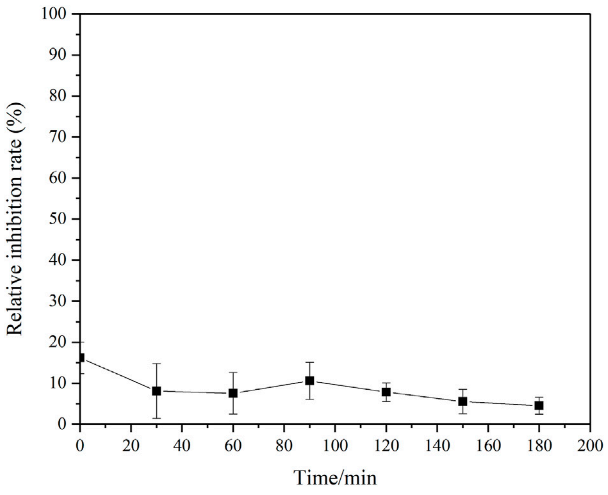

FIGURE 6
Bio-toxicity change of the testing solution during MET degradation process. Experimental conditions: $[\text{MET}]_0 = 10$ mg/L, $[\text{Sulfite}]_0 = 10$ mM, UV intensity = 100% I_0.

as e_{aq}^- (Lester et al., 2013) and reduce the proportion of e_{aq}^- used for MET degradation, thus causing an inhibition effect on MET removal. Nevertheless, some of the generated oxidative reactive species, such as ·OH, have been demonstrated to be beneficial for MET removal in the oxygen-involved UV/sulfite processes. Consequently, the impact of NOM on MET removal during the investigated process is complicated.

MET degradation experiments in a real water matrix were also performed, and the results were portrayed in Figure 5. In general, MET degradation was partly restrained in surface water samples when compared to the previous studied synthetic matrix. Several reasons may account for this phenomenon. Firstly, the solution pH of two surface water samples were less than 9 (Supplementary Table S1), which may result in less sulfite exist in the form of SO_3^{2-} and accordingly less e_{aq}^- generation. Secondly, NOM and inorganic ions were co-present in the surface water samples with certain extent (Supplementary Table S1). Their detrimental effect on target pollutants degradation in the UV/sulfite system has also been reported by other researchers (Cao et al., 2021b; Liu et al., 2022). Hence, MET degradation by the studied process in real water samples was impaired. Nevertheless, nearly 80% of MET was removed after 180 min irradiation, which suggested the studied oxygen-involved UV/sulfite process was prospective for MET-bearing wastewater treatment.

3.8 MET degradation products

In order to investigate the degradation pathway of MET in the oxygen-involved UV/sulfite system, the degradation products were detected. Nitrite and ammonium ions were the dominant inorganic degradation products (Supplementary Figure S2), among which ammonium accounted for the majority. The calculation of nitrogen balance indicated most of the nitrogen (>80%) in MET molecule was transformed into inorganic nitrogen species. Due to the relatively low concentration and small molecule weight, the organic intermediates of MET degradation were difficult to be determined. Therefore, MET degradation experiment at a higher initial MET concentration (1 g/L) and longer reaction time (8 h) was conducted to better ascertain these organic intermediates, and the results were shown in Supplementary Table S5. Three organic N-containing products with lower molecule weight were detected with m/z at 125, 115, and 87, respectively. Referring to previous investigation (Badran et al., 2019; Carbuloni et al., 2020), their molecule structures were also given. The same degradation intermediates were also reported in another literature (Quintão et al., 2016), where MET degradation occurred in three oxidative reaction systems (i.e., sodium hypochlorite, ozonation, photocatalysis). A previous study by Trouillas et al. (2013) have explored the ·OH induced oxidative degradation of MET, in which ·OH was produced through water radiolysis reaction. There were totally four kinds of intermediates determined by using HPLC/MS, which included 4-amino-2-imino-1-methyl-1,2-dihydro-1,3,5-triazine (compound 2 in this study), methylbiguanide (compound 3 in this study), hydroperoxide of metformin and 2-amino-4-methylamino-1,3,5-triazine. ·H abstraction, electron transfer and ·OH addition were three main reaction pathways when MET was primarily attacked by ·OH. The bond dissociation enthalpies at C8 and C9 in MET molecule were very close, which hinted the two methyl functional groups were equal targets for ·OH attacking, and further causing MET converted to methylbiguanide. In addtion, the production of methylbiguanide was reported primarily occurred in the alkaline pH value, which was in good agreement with the reaction condition of our study (pH 9). Additionally, the bio-toxicity of the testing solution during the target pollutant degradation was monitored and presented in Figure 6. The bio-toxicity of the testing solution gradually declined along with MET degradation in general. Overall, the oxygen-involved UV/sulfite process exhibited a remarkable denitrification capacity in MET.

4 Conclusion

This work explored MET degradation in the oxygen-involved UV/sulfite process under different experimental parameters. A relatively higher degradation efficiency and k_{obs} were achieved in the investigated process, where $SO_4 \cdot^-$, ·OH, e_{aq}^- and ·H were manifested the major contributors to MET removal. Alkaline conditions (pH ≥ 9) were favorable to the degradation of MET. The MET degradation efficiency was positively correlated with the incident UV intensity, sulfite dosage and reaction temperature, and negatively correlated with the initial MET concentration. The co-existed bicarbonate and FA slightly suppressed MET degradation. The oxygen-involved UV/sulfite system exhibited an extraordinary denitrification capacity in MET. Nitrite, ammonium ions and three kinds of N-containing organic compounds were detected as the dominant intermediates for MET degradation. This study offered a novel approach for treating emerging contaminants.

Data availability statement

The original contributions presented in the study are included in the article/Supplementary Material, further inquiries can be directed to the corresponding author.

Author contributions

YG Conceptualization, Methodology, Investigation, Software, writing—original draft preparation, Writing—review and editing, Validation, Funding acquisition. YZ Conceptualization, Methodology, Data curation. CJ Conceptualization, Writing—review and editing, Funding acquisition ZD Conceptualization, Methodology, Investigation, Data curation, Writing—review and editing, Supervision. Funding acquisition, Visualization. XB Investigation, Validation, Data curation All authors have read and agreed to the published version of the manuscript.

Funding

We thank the National Natural Science Foundation of China (42107396, 52170007), Shenzhen Science and Technology Program (JCYJ20220531094416037), Shenzhen Sustainable Development Project (KCXFZ202002011006362, KCXFZ20201221173413037) for financial support of the present work.

Conflict of interest

The authors declare that the research was conducted in the absence of any commercial or financial relationships that could be construed as a potential conflict of interest.

Publisher's note

Supplementary material

The Supplementary Material for this article can be found online at: https://www.frontiersin.org/articles/10.3389/fenvs.2022.1071963/full#supplementary-material

References

Ambrosio-Albuquerque, E. P., Cusioli, L. F., Bergamasco, R., Gigliolli, A. A., Lupepsa, L., and Paupitz, B. R. (2021). Metformin environmental exposure: A systematic review. *Environ. Toxi. Col. Phar. Metformin Environ. Expo. A Syst. Rev.* 83, 103588.

Badran, I., Manasrah, A. D., and Nassar, N. N. (2019). A combined experimental and density functional theory study of metformin oxy-cracking for pharmaceutical wastewater treatment. *Rsc. Adv.* 9, 13403–13413. doi:10.1039/c9ra01641d

Buxton, G. V., Greenstock, C. L., Helman, W. P., and Ross, A. B. (1988). Critical review of rate constants for reactions of hydrated electrons, hydrogen atoms and hydroxyl radicals (·OH/$\cdot O^-$) in aqueous solution. *J. Phys. Chem. Ref. Data.* 17 (2), 513–886. doi:10.1063/1.555805

Cao, Y., Qiu, W., Li, J., Jiang, J., and Pan, S. Y. (2021). Review on UV/sulfite process for water and wastewater treatments in the presence or absence of O_2. *Sci. Total. Environ.* 765, 142762. doi:10.1016/j.scitotenv.2020.142762

Cao, Y., Qiu, W., Li, J., Zhao, Y. M., Jiang, J., and Pang, S. Y. (2021). Sulfite enhanced transformation of iopamidol by UV photolysis in the presence of oxygen: Role of oxysulfur radicals. *Water. Res.* 189, 116625. doi:10.1016/j.watres.2020.116625

Carbuloni, C. F., Savoia, J. E., Santos, J. S., Pereira, C. A., Marques, R. G., Ribeiro, V. A., et al. (2020). Degradation of metformin in water by TiO_2–ZrO_2 photocatalysis. *J. Environ. Manage.* 262, 110347. doi:10.1016/j.jenvman.2020.110347

Chen, L., Xue, Y. F., Luo, T., Wu, F., and Alshawabkeh, A. N. (2021). Electrolysis-assisted UV/sulfite oxidation for water treatment with automatic adjustments of solution pH and dissolved oxygen. *Chem. Eng. J.* 403, 126278. doi:10.1016/j.cej.2020.126278

Crago, J., Bui, C., Grewal, S., and Schlenk, D. (2016). Age-dependent effects in fathead minnows from the anti-diabetic drug metformin. *Gen. Comp. Endocr.* 232, 185–190. doi:10.1016/j.ygcen.2015.12.030

Cruz, N. D., Pulgarin, C., Giménez, J., Esplugas, S., Grandjean, D., and Alencastro, L. F. (2012). Degradation of 32 emergent contaminants by UV and neutral photo-fenton in domestic wastewater effluent previously treated by activated sludge. *Water. Res.* 46, 1947–1957. doi:10.1016/j.watres.2012.01.014

Deister, U., and Warneck, P. (1990). Photooxidation of SO_3^{2-} in aqueous solution. *J. Phys. Chem.* 94, 2191–2198. doi:10.1021/j100368a084

Ding, Y. C., Han, J. L., Feng, H. J., Liang, Y. X., Jiang, W. L., Liu, S, H., et al. (2022). Source prevention of halogenated antibiotic resistance genes proliferation: UV/sulfite advanced reduction process achieved accurate and efficient elimination of florfenicol antibacterial activity. *Sci. Total. Environ.* 849, 157844. doi:10.1016/j.scitotenv.2022.157844

Fu, J., Zhang, Z. M., Tang, J. Y., Zeng, Q. F., An, S. Q., and Zhu, H. L. (2010). Photoreduction of reactive brilliant red X-3B by ultraviolet irradiation/potassium borohydride/sodium bisulfite. *J. Environ. Eng.* 136, 1314–1319. doi:10.1061/(asce)ee.1943-7870.0000251

Gaffney, V. J., Cardoso, V. V., Cardoso, E., Teixeira, A. P., Martins, J., Benoliel, M. J., et al. (2017). Occurrence and behaviour of pharmaceutical compounds in a Portuguese wastewater treatment plant: Removal efficiency through conventional treatment processes. *Environ. Sci. Pollut. Res.* 24, 14717–14734. doi:10.1007/s11356-017-9012-7

George, N. K., Wols, B. A., Santoro, D., Borboundakis, M., Bell, K., and Gernjak, W. (2022). A novel approach to interpret quasi-collimated beam results to support design and scale-up of vacuum UV based AOPs. *J. Water. Res.* 17, 100158. doi:10.1016/j.wroa.2022.100158

Gu, Y. R., Dong, W. Y., Luo, C., and Liu, T. Z. (2016). Efficient reductive decomposition of perfluorooctanesulfonate in a high photon flux UV/sulfite system. *Environ. Sci. Technol.* 50, 10554–10561. doi:10.1021/acs.est.6b03261

Gu, Y. R., Qi, Han., Dong, Z. J., Zhu, J. X., Jiang, C. C., and Qi, J. K. (2022). Enhanced degradation and deiodination of diatrizoate in a sulfite mediated photolytic system: Performance, products and possible pathways. *J. Hazard. Maters. Adv.* 8, 100144.

Huang, L., Dong, W. B., and Hou, H. Q. (2007). Investigation of the reactivity of hydrated electron toward perfluorinated carboxylates by laser flash photolysis. *Chem. Phys. Lett.* 436, 124–128. doi:10.1016/j.cplett.2007.01.037

Huang, Y., Han, C., Liu, Y. Q., Nadagouda, M. N., Machala, L., O'Shea, K. E., et al. (2018). Degradation of atrazine by $Zn_xCu_{1-x}Fe_2O_4$ nanomaterial-catalyzed sulfite under UV-vis light irradiation: Green strategy to generate SO_4. *J. Appl. Catal. B* 221, 380–392. doi:10.1016/j.apcatb.2017.09.001

Karimiana, S., Moussavia, G., Fanaeia, F., Mohammadia, S., Shekoohiyana, S., and Giannakis, S. (2020). Shedding light on the catalytic synergies between Fe(II) and PMS in vacuum UV (VUV/Fe/PMS) photoreactors for accelerated elimination of pharmaceuticals: The case of metformin. *Chem. Eng. J.* 400, 125896. doi:10.1016/j.cej.2020.125896

Lester, Y., Sharpless, C. M., Mamane, H., and Linden, K. G. (2013). Production of photo-oxidants by dissolved organic matter during UV water treatment. *Environ. Sci. Technol.* 47, 11726–11733. doi:10.1021/es402879x

Li, G., Wang, C., Yan, Y. P., Yan, X. R., Li, W. T., Feng, X. H., et al. (2020). Highly enhanced degradation of organic pollutants in hematite/sulfite/photo system. *Chem. Eng. J.* 386, 124007. doi:10.1016/j.cej.2019.124007

Li, X. C., Fang, J. Y., Liu, G. F., Zhang, S. J., Pan, B. C., and Ma, J. (2014). Kinetics and efficiency of the hydrated electroninduced dehalogenation by the sulfite/UV process. *Water. Res.* 62, 220–228. doi:10.1016/j.watres.2014.05.051

Li, X. C., Ma, J., Liu, G. F., Fang, J. Y., Yue, S. Y., Guan, Y. H., et al. (2012). Efficient reductive dechlorination of monochloroacetic acid by sulfite/UV process. *Environ. Sci. Technol.* 46, 7342–7349. doi:10.1021/es3008535

Liu, S. H., Han, J. L., Ding, Y. C., Gao, X. X., Chen, H. Y., Wang, H. C., et al. (2022). Advanced reduction process to achieve efficient degradation of pyridine. *Chemosphere* 287, 132240. doi:10.1016/j.chemosphere.2021.132240

Liu, X., Vellanki, B. P., Batchelor, B., and Abdel-Wahab, A. (2014). Degradation of 1, 2-dichloroethane with advanced reduction processes (ARPs): Effects of process variables and mechanisms. *Chem. Eng. J.* 237, 300–307. doi:10.1016/j.cej.2013.10.037

Liu, X. W., Zhang, T. Q., Wang, L. L., Shao, Y., and Fang, L. (2015). Hydrated electron-based degradation of atenolol in aqueous solution. *Chem. Eng. J.* 260, 740–748. doi:10.1016/j.cej.2014.08.109

Lyu, X. J., Li, W. W., Lam, P. K. S., and Yu, H. Q. (2015). Photodegradation of perfluorooctane sulfonate in environmental matrices. *Sep.Purif. Technol.* 151 (13), 172–176. doi:10.1016/j.seppur.2015.07.049

Maćerak, A. L., Kerkez, Đ., Bečelić-Tomin, M., Pilipović, D. T., Kulić, A., Jokić, J., et al. (2018). Removal of diclofenac and metformin from water in laboratory photo reactor. *Digit. Publ. Inst. Proc.* 2 (20), 1288.

Milh, H., Yu, X. Y., Cabooter, D., and Dewil, R. (2021). Degradation of ciprofloxacin using UV-based advanced removal processes: Comparison of persulfate-based advanced oxidation and sulfite-based advanced reduction processes. *Sci. Total. Environ.* 764, 144510. doi:10.1016/j.scitotenv.2020.144510

Neamțu, M., Grandjean, D., Sienkiewicz, A., Faucheur, S. L., Slaveykova, V., Colmenares, J. J., et al. (2014). Degradation of eight relevant micropollutants in different water matrices by neutral photo-Fenton process under UV254 and simulated solar light irradiation - a comparative study. *Appl. Catal. B Environ.* 158-159, 30–37.

Nezar, S., and Laoufi, N. A. (2018). Electron acceptors effect on photocatalytic degradation of metformin under sunlight irradiation. *Sol. Energy.* 164, 267–275. doi:10.1016/j.solener.2018.02.065

Niemuth, N. J., and Klaper, R. D. (2015). Emerging wastewater contaminant metformin causes intersex and reduced fecundity in fish. *Chemosphere* 135, 38–45. doi:10.1016/j.chemosphere.2015.03.060

Peldszus, S., Andrews, S. A., Souza, R., Smith, F., Douglas, I., Bolton, J., et al. (2004). Effect of medium-pressure UV irradiation on bromate concentrations in drinking water, a pilot-scale study. *Water Res.* 38, 211–217. doi:10.1016/j.watres.2003.09.010

quality, Water (2007). *Determination of the inhibitory effect of water samples on the light emission of Vibrio fifischeri (Luminescent bacteria test)-Part 3: Method using freeze-dried bacteria.* Geneva, Switzerland: International Organization for Standardization. ISO 11348-3.

Quintão, F. J., Freitas, J. R., Machado, C. F., Aquino, S. F., Silva, S. Q., and Afonso, R. J. (2016). Characterization of metformin by-products under photolysis, photocatalysis, ozonation and chlorination by high-performance liquid chromatography coupled to high-resolution mass spectrometry. *Rapid. Commun. Mass. Sp.* 30 (21), 2360–2368.

Scheurer, M., Sacher, F., and Brauch, H. J. (2009). Occurrence of the antidiabetic drug metformin in sewage and surface waters in Germany. *J. Environ. Monit.* 11, 1608–1613. doi:10.1039/b909311g

Shah, N. S., Khan, J. A., Nawaz, S., and Khan, H. M. (2014). Role of aqueous electron and hydroxyl radical in the removal of endosulfan from aqueous solution using gamma irradiation. *J. Hazard. Mat.* 278, 40–48. doi:10.1016/j.jhazmat.2014.05.073

Song, Z., Tang, H. Q., Wang, N., and Zhu, L. H. (2013). Reductive defluorination of perfluorooctanoic acid by hydrated electrons in a sulfite-mediated UV photochemical system. *J. Hazard. Mat.* 262, 332–338. doi:10.1016/j.jhazmat.2013.08.059

Trouillas, P., Marchetti, C., Bonnefont-Rousselot, D., Lazzaroni, R., Jore, D., Gardès-Albert, M., et al. (2013). Mechanism of one-electron oxidation of metformin in aqueous solution. *Phys. Chem. Chem. Phys.* 15, 9871–9878. doi:10.1039/c3cp50602a

Vecitis, C. D., Park, H., Cheng, J., Mader, B. T., and Hoffmann, M. R. (2009). Treatment technologies for aqueous perfluorooctanesulfonate (PFOS) and perfluorooctanoate (PFOA). *Front. Environ. Sci. Engin. China.* 3 (2), 129–151. doi:10.1007/s11783-009-0022-7

Vellanki, B. P., Batchelor, B., and Abdel-Wahab, A. (2013). Advanced reduction processes: A new class of treatment processes. *Enivron. Eng. Sci.* 30 (5), 264–271.

Xiao, Q., Ren, Y. F., and Yu, S. L. (2017). Pilot study on bromate reduction from drinking water by UV/sulfite systems: Economic cost comparisons, effects of environmental parameters and mechanisms. *Chem. Eng. J.* 330, 1203–1210. doi:10.1016/j.cej.2017.08.071

Yang, Y., Jiang, J., Lu, X., Ma, J., and Liu, Y. (2015). Production of sulfate radical and hydroxyl radical by reaction of ozone with peroxymonosulfate: A novel advanced oxidation process. *Environ. Sci. Technol.* 49, 7330–7339. doi:10.1021/es506362e

Yazdanbakhsh, A., Eslami, A., Moussavi, G., and Rafiee, M. (2018). Photo-assisted degradation of 2, 4, 6-trichlorophenol by an advanced reduction process based on sulfite anion radical: Degradation, dechlorination and mineralizationPhoto-assisted degradation of 2, 4, 6-trichlorophenol by an advanced reduction process based on sulfite anion radical: Degradation, dechlorination and mineralization. *Chemosphere* 191, 156–165. doi:10.1016/j.chemosphere.2017.10.023

Yoon, S., Han, D. S., Liu, X., Batchelor, B., and Abdel-Wahab, A. (2014). Degradation of 1, 2-dichloroethane using advanced reduction processes. *J. Environ. Chem. Eng.* 2, 731–737. doi:10.1016/j.jece.2013.11.013

Yu, H., Yang, R. T., Wu, J. H., Wang, S. Y., Qin, X. Y., Wu, T., et al. (2022). Association of metformin and depression in patients with type 2 diabetes. *J. Affect. Disord.* 318, 380–385. doi:10.1016/j.jad.2022.09.015

Zhang, Q., Li, C. L., and Li, T. (2013). Rapid photocatalytic decolorization of methylene blue using high photon flux UV/TiO_2/H_2O_2 process. *Chem. Eng. J.* 217, 407–413. doi:10.1016/j.cej.2012.11.106

Zhang, W. Q., Huang, T., Ren, Y., Yang, S., Zhao, X. Y., Yuan, M. S., et al. (2022). A multifunctional chitosan composite aerogel for PPCPs adsorption. *Carbohydr. Polym.* 298, 120102. doi:10.1016/j.carbpol.2022.120102

Zhou, L., Ferronato, C., Chovelon, J. M., Sleiman, M., and Richard, C. (2017). Investigations of diatrizoate degradation by photo-activated persulfate. *Chem. Eng. J.* 311, 28–36. doi:10.1016/j.cej.2016.11.066

Zhu, S., Liu, Y. G., Liu, S. B., Zeng, G. M., Jiang, L. H., Tan, X. F., et al. (2017). Adsorption of emerging contaminant metformin using graphene oxide. *Chemosphere* 179, 20–28. doi:10.1016/j.chemosphere.2017.03.071

frontiers | Frontiers in Environmental Science

TYPE Original Research
PUBLISHED 20 March 2023
DOI 10.3389/fenvs.2023.945884

Water quality variation in the middle route of South-to-North Water Diversion Project, China

Yuanzhu Wang[1,2], Chenglin Wang[2], Chunmei Zhang[1], Jiangkui Liang[3], Wujuan Mi[1], Gaofei Song[1], Yuxuan Zhu[1], Shulei Wang[3], Yuming Shang[3] and Yonghong Bi[1]*

[1]State Key Laboratory of Fresh Water Ecology and Biotechnology, Institute of Hydrobiology, Chinese Academy of Sciences, Wuhan, China, [2]Central Southern Safety & Environmental Technology Institute Company Limited, Wuhan, China, [3]Management Bureau of South to North Water Transfer Canal Project, Beijing, China

OPEN ACCESS

EDITED BY
Zheng-Yang Huo,
Renmin University of China, China

REVIEWED BY
Dongguo Shao,
Wuhan University, China
Renata Augustyniak-Tunowska,
University of Warmia and Mazury in Olsztyn, Poland

*CORRESPONDENCE
Yonghong Bi,
✉ biyh@ihb.ac.cn

SPECIALTY SECTION
This article was submitted to Water and Wastewater Management,
a section of the journal
Frontiers in Environmental Science

RECEIVED 17 May 2022
ACCEPTED 28 February 2023
PUBLISHED 20 March 2023

CITATION
Wang Y, Wang C, Zhang C, Liang J, Mi W, Song G, Zhu Y, Wang S, Shang Y and Bi Y (2023), Water quality variation in the middle route of South-to-North Water Diversion Project, China.
Front. Environ. Sci. 11:945884.
doi: 10.3389/fenvs.2023.945884

The South-to-North Water Division Middle Route Project (MRP) is currently the longest inter-basin water diversion project in the world. It benefits a large population and its water quality has attracted much attention. In this study, seasonal investigations on 11 sampling sites along the MRP were conducted from 2018 to 2019; water temperature, pH, turbidity, transparency, COD_{Mn}, dissolved oxygen, total phosphorus, phosphate, total nitrogen, ammonia, nitrate, and chlorophyll *a* were determined synchronously. Single leakage distance clustering analysis identified the spatio-seasonal heterogeneity of physiochemical parameters. The trophic level index (TLI) and the water quality status were assessed: TLI increased and WQI decreased from south to north; TLI and WQI had seasonal differences ($p < 0.001$), the best water quality was observed in autumn, and the lowest TLI was observed in winter. The trophic level was "oligotrophic to mesotrophic"; water quality status was "good." The multiple linear stepwise regression analysis confirmed that total nitrogen (TN), Chl *a*, and COD_{Mn} were the driving factors in water quality. These factors were applied to build the simplified WQI model, which was confirmed as a reliable method of water quality assessment for the MRP and a fitting substitute for TLI and WQI. The results provided support for the water quality evaluation of the MRP.

KEYWORDS

South-to-North Water Division Middle Route Project, water quality, physiochemical parameters, trophic level index, heterogeneity

1 Introduction

Adequate amounts of sustainable freshwater resources are important to guarantee ecological integrity and the survival of human society (Wu et al., 2018). However, with rapid social and economic development and continuous accretion of the population (Barakat et al., 2016), the increasing consumption of water resources has led to freshwater reserve scarcity. China is facing serious uneven distribution and shortage of water resources, especially in the northern area (Xin et al., 2015). In addition to this, because of multifaceted effects, such as hydraulic alteration (Nazeer et al., 2018), land use change (Giri et al., 2016), and inputs of toxic chemicals and nutrients (Ding et al., 2019), water quality deterioration has also become severe, which has resulted in some water bodies being abandoned as they could not be used as drinking water resources anymore. Thus, water quality determines the ecological service function of water bodies. On this account, monitoring and assessing water quality is necessary to safeguard freshwater resources (Pesce et al., 2000), which could help us instantly understand the status of water quality.

There are multiple statistical approaches to assessing water quality. The simplest index is the single factor index, which is easily compared between different water bodies (Sánchez et al., 2007). Conventional water quality evaluation was based on the comparison of measured water quality parameters with existing standards for kinds of water bodies (Pesce et al., 2000; Chang et al., 2020). Such assessments might not provide a fully accurate water quality evaluation method (Tziritis et al., 2014). Hence, systematic methods, including multi-parameters, must be used to acquire a rational description of the water quality status. A water quality index (WQI) has been widely used as one of the most effective approaches, integrating multiple measured water quality parameters to yield a single dimensionless number formula to perform water quality assessment (Horton et al., 1965). The minimum WQI model (WQI_{min}) applies several key parameters that can express water quality directly and easily to evaluate water quality (Akkoyunlu et al., 2012). Mostly, the parameters chosen for a WQI_{min} calculation ought to represent other unselected environmental parameters and must be easy and quick to measure (Pesce et al., 2000). Furthermore, the trophic level could also indicate water quality conditions and provide information on the structure and function of an ecosystem (Wang et al., 2019). The Carlson method evolved into the trophic level index (TLI) method, which has been established based on Chl *a* and other parameters by desirable, correlation-generated consequences (Burns et al., 2005; Wang et al., 2019). The trophic index has been broadly applied to the eutrophication assessment of surface water, such as the Suez Canal (El-Serehy et al., 2018) and Lake Taihu (Wang et al., 2019). Though there were many assessment methods for water quality, the integrated methods of trophic level and water quality are still needed.

China has built the longest inter-basin water diversion project in the world, the South-to-North Water Division Middle Route Project (MRP) (Wang, et al., 2021), which is a man-made concrete channel with a total length of 1,432 km (including 155 km of Tianjin division) (Huang et al., 2021) that aims to solve the serious water shortage in the northern districts of China. As the MRP has been running, it has alleviated the supply and demand issues of water resources in districts along the MRP, alleviated the groundwater over-exploitation in the water-receiving area, and played a vital role in society by creating economical and ecological benefits. At present, some studies have revealed the spatial and temporal dynamics of the bacterioplankton community structure in the MRP (Luo et al., 2019), eutrophication of water supplied to lakes, heavy-metal pollution (Guo et al., 2020a), fish community structure (Guo et al., 2020b), and physical and chemical statuses of some sections of the MRP (Nong et al., 2019; Nong et al., 2020). However, a comprehensive water quality assessment in the MRP is still lacking. It is necessary to carry out constant water quality monitoring and assessment in the MRP.

The main aims of this study were 1) to illustrate the spatio-temporal variations of parameters in the MRP, 2) to assess the trophic level, and water quality status of the MRP based on TLI and WQI methods, and 3) to address the key factors to establish a fast and cost-effective water quality model. This study was conducted to establish a simple WQI_{min} model for the assessment of water quality after the utilization of the MRP; the WQI_{min} model proved to be the most valuable and reliable evaluation method for long-distance water diversion projects worldwide.

2 Materials and methods

2.1 Study area and sampling stations

The middle route of the South-to-North Water Diversion Project is located between 32.68°N–39.99°N and 111.72°E–116.27°E, which spans eight latitudes and three temperature zones (subtropical zone, warm temperate zone, and temperate zone) from south to north (Luo et al., 2018), with a length of 1,432 km; it needs 2 weeks to divert water from the original reservoir to terminal water bodies. The MRP originates from Danjiangkou Reservoir, which crosses two provinces—Henan (HN) and Hebei (HB), and arrives at Beijing (BJ), the capital of China, and Tianjin (TJ). Water flows aided by gravity along the channel from Danjiangkou Reservoir (whose storage has been expanded) through the intake gate of the Taocha headwater. Along the middle route, canals pass the west Tangbai River region, the watershed between the Yangtze River basin and the Huaihe River–Fangcheng Pass, run across the Yellow River Basin, and finally arrive in BJ. This inter-basin project solves the problem of water shortage and provides clean water for production, living, industry, and agriculture for at least 20 large- and medium-sized cities along the route (Wang, et al., 2021). The MRP canal was closed and separated from the land, so the local catchment cannot influence the water quality, but the rainwater and dry/wet settlement from the air to the channel could affect the water quality. By December 2020, the MRP supplied a total of 34.8 billion cubic meters of water transported northward, benefiting 69 million people (Office of the South-to-North Water Diversion Project Construction Committee, State Council, PRC).

There were 11 monitoring sites chosen to represent the MRP, covering four main provinces including the headstream and terminal places (as shown in Figure 1). The 11 sampling sites were set almost at equal distances; the regional aspect was also considered in the sample site design. S1 (Taocha) was located in the Henan Province, which is the source of headwater. S2 (Shahe), S3 (Lushan), S4 (Chuanhuang South), and S5 (Chuanhuang North) were all located in the HN Province. S6 (Zhanghe North), S7 (Guyunhe), and S8 (Xiheishan) were located in the HB Province. Xiheishan was an intersection site where the main channel divides into two branches: one flows to S9 (Waihuanhe) in TJ and the other flows to S10 (Huinanzhuang station) and S11 (Tuanchenghu) in BJ; the detailed sampling information is given in Supplementary Table S1.

2.2 Sample collection and parameter determination

The investigation was conducted every quarter. Parameters including WT, DO, and pH were obtained using a water quality analyzer (YSI, proplus, United States). Velocity and discharge were recorded using a flowmeter (Flowatch, Switzerland). The turbidity

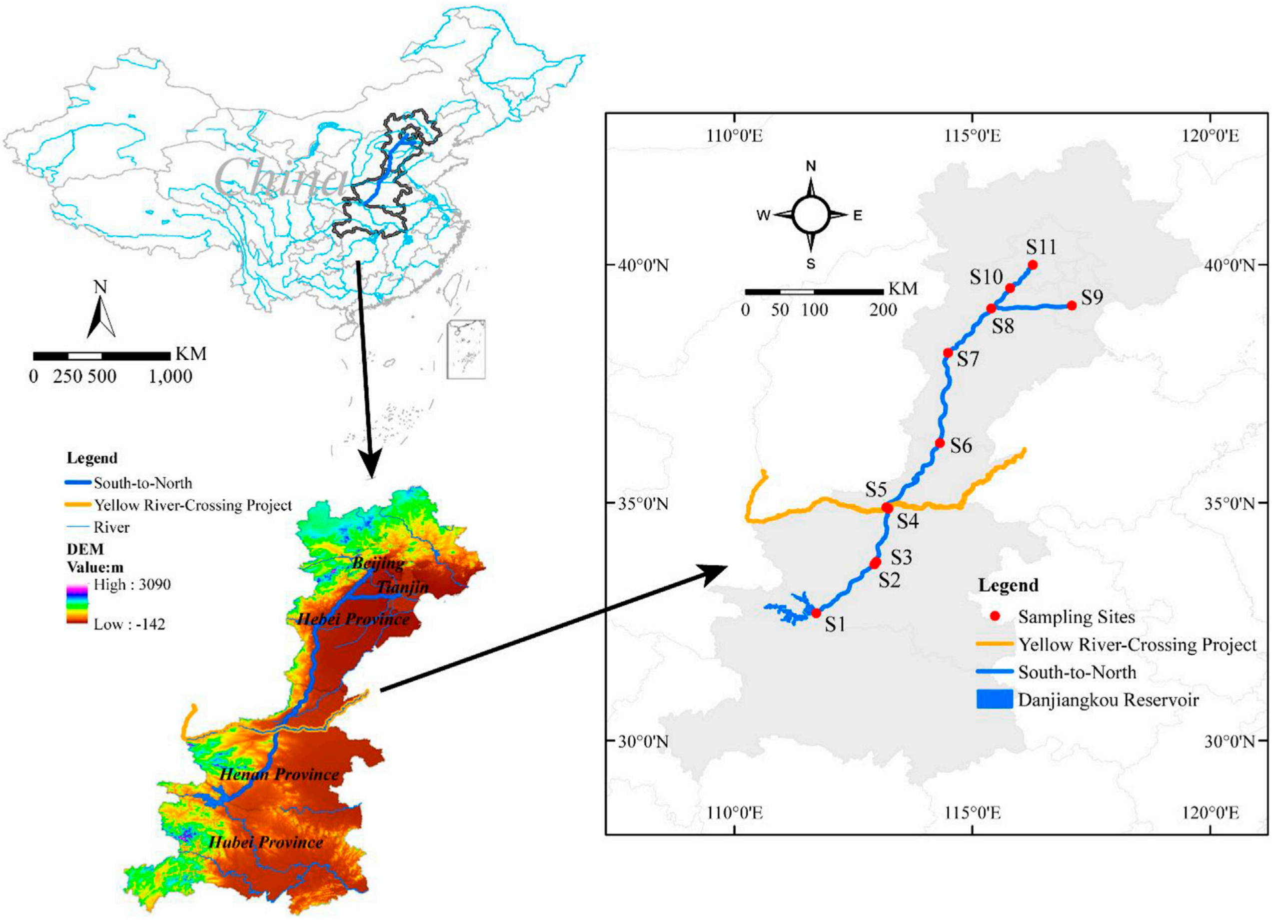

FIGURE 1
Locations of eleven sampling sites for the middle route of the South-to-North Water Diversion Project, China.

was determined using a turbidimeter (WGZ-200S, China). A Secchi disc tool measured SD. The water samples (from a surface depth of 0 cm–50 cm) were collected in 550 mL acid-cleaned plastic bottles and rinsed with surface water before sampling (three replications in each monitoring site). The samples needed to be stored in an icebox and were transferred to the lab to be determined as soon as possible. Samples used for the measurement of PO_4-P, NO_3-N, and NH_4-N were filtered using a GF/C membrane (Whatman GF/C), and then the membrane filters were soaked in 10 mL, 90% acetone solution to extract Chl *a*. Furthermore, TN and TP were digested at 120°C for 30 min and tested using a UV-spectrophotometer (UV-1780), and chemical oxygen demand (COD_{Mn}) was determined; the aforementioned parameters were determined following the standard methods for the examination of water and wastewater (APHA., 2017).

2.3 Trophic level index algorithms

To understand the trophic condition of MRP, TLI values were used, which were given a weighting sum based on the correlation between TP, TN, COD_{Mn}, SD, and Chl *a* (China Environmental Monitoring Station., 2001). These parameters were applied for calculating the TLI, and the qualification formulas of five parameters were established, which was the calculation result of the investigation of 26 major lakes (reservoirs) in China (Jin et al., 1995).

The TLI has a scale from 0 to 100, with a high value indicating a high trophic level, and was used to assess the eutrophication level of monitoring sites of the MRP. The trophic level is classified into five classes according to the score of TLI (∑): the oligotrophic level (TLI (∑) < 30), mesotrophic level (30 ≤ TLI (∑) ≤ 50), light eutrophic level (50 < TLI (∑) ≤ 60), middle eutrophic level (60 < TLI (∑) ≤ 70), and hyper eutrophic level (TLI (∑) > 70) (Wang et al., 2019).

2.4 Water quality index algorithms

The water quality index (WQI) is a widely used method to evaluate water quality and reflect the comprehensive impact of different environmental parameters, as well as obtain an objective assessment of the comprehensive water quality without neglecting the overall water quality status because of the deviation of individual factors that were put forward by Pesce et al. (2000). The WQI has been widely used as one of the most effective approaches to performing water quality assessments, integrating multiple

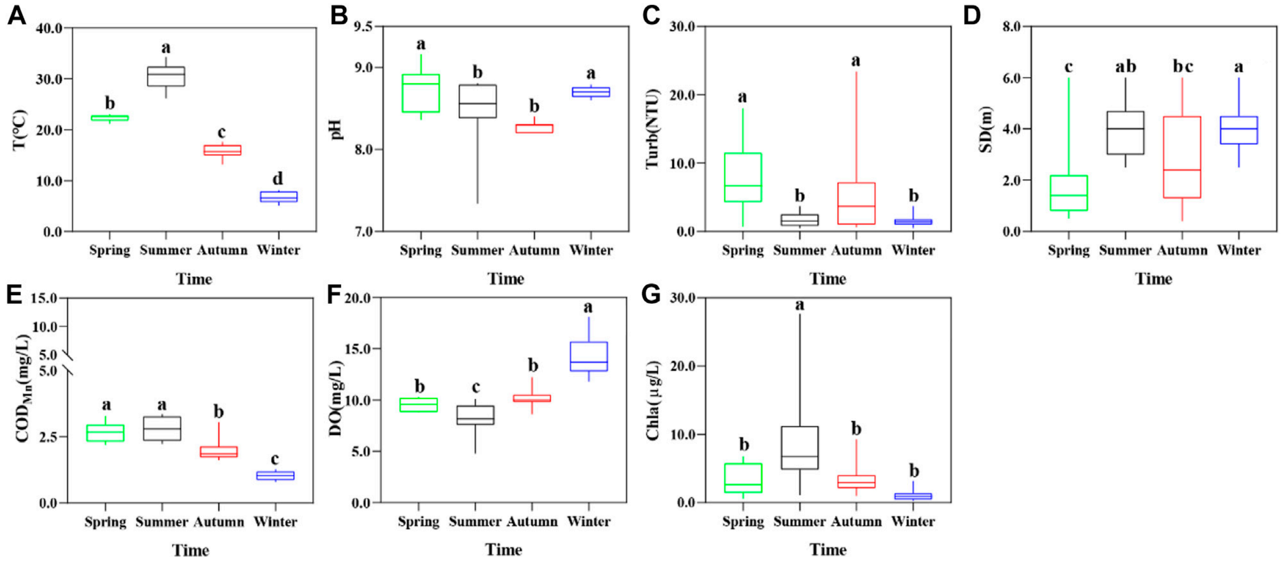

FIGURE 2
Box plots of seasonal variations of environmental parameters in the middle route of South-to-North Water Diversion Project. **(A)** Box plot of T; **(B)** box plot of pH; **(C)** box plot of Turb; **(D)** box plot of SD; **(E)** box plot of COD$_{Mn}$; **(F)** box plot of DO; **(G)** box plot of Chl *a*.

measured water quality parameters. In this study, 15 physicochemical parameters collected from eleven sampling sites were selected as evaluation objects to form a 15 × 11 matrix. The principal component formula was deduced by calculating the eigenvalues and the coefficient matrix to quantify the factors. Then, stepwise multiple linear regression analyses were carried out to figure out the key factors affecting WQI and then develop the WQI$_{min}$ model, which helps to select the influencing key factors.

According to the results of factor analysis and correlation analysis, 11 environmental parameters were selected and weighted. Every single parameter was assigned a weight based on its potential effect on the water quality (Wu et al., 2018). T, DO, pH, COD$_{Mn}$, Tur, Chl *a*, TP, PO$_4$-P, TN, NH$_4$-N, and NO$_3$-N were used to compute the WQI. The formula used was as follows:

$$\mathrm{WQI} = \sum_{i=1}^{n} C_i \times P_i \Big/ \sum_{i=1}^{n} Pi, \qquad (8)$$

where n is the amount of the selected parameters, Ci is the normalized value of parameter I, Pi is the weight of parameter I, the minimum value of P$_i$ was one, and the maximum weight allocated to parameters that influenced the water quality most was four (Supplementary Table S2). These values have been demonstrated in published studies (Koçer et al., 2014; Sun et al., 2016; Tian et al., 2019). The WQI has a scale from 0 to 100, with high values predicting good water quality conditions of each monitoring site of the MRP. Based on the grade of the WQI, the water quality was categorized into five grades: excellent (100–90), good (90–70), medium (70–50), bad (50–25), and very bad (25–0) (Tian et al., 2019).

In order to assess the water quality of the MRP in an easy and effective way, a WQI$_{min}$ model built during a previous research study was used (Pesce et al., 2000). This model usually uses 3–5 important parameters to evaluate the water quality, per the following formula:

$$\mathrm{WQI\ min} = \sum_{i=1}^{n} C_i / n. \qquad (9)$$

Here, n is the total number of parameters included in the study; Ci is the normalized value of parameter i (Supplementary Table S2). The selected parameters were introduced into WQI$_{min}$ on the basis of the results of linear regression analysis. All samples collected from the four seasons were applied for calculating the selected environmental parameters and the relation between WQI with TLI and WQI$_{min}$.

Although the water velocity could influence the water quality significantly, spatio-temporal differences in the water velocity of the MRP were not significant, so the water velocity was not used to compute the WQI.

2.5 Statistical procedures

All data analyses were conducted with SPSS 22.0 (IBM SPSS statistical), PAST 3.0 (Paleontological Statistics), and R (Corrplot). Considering the heterogeneous distribution of sampling sites, inverse distance weighting (IDW) interpolation was applied to reveal the spatial variation of physicochemical parameters. ArcGIS 10.2 (Esri Inc., US) was used for the spatial data treatment. The Kruskal–Wallis method was used to evaluate significant differences between the mean of parameters at the spatial and temporal scales. The variations of environmental parameters in the seasonal changes were found using the Kendall test. For grouping the sampling sites, cluster analysis was carried out using single-linkage distance and square-root data transformation. A Spearman correlation analysis was conducted to study the relationship and dependence between environmental factors. Principal component analysis (PCA) is a quantitative analysis of multi-dimensional factors in the system, which can compress multiple variables into individual comprehensive

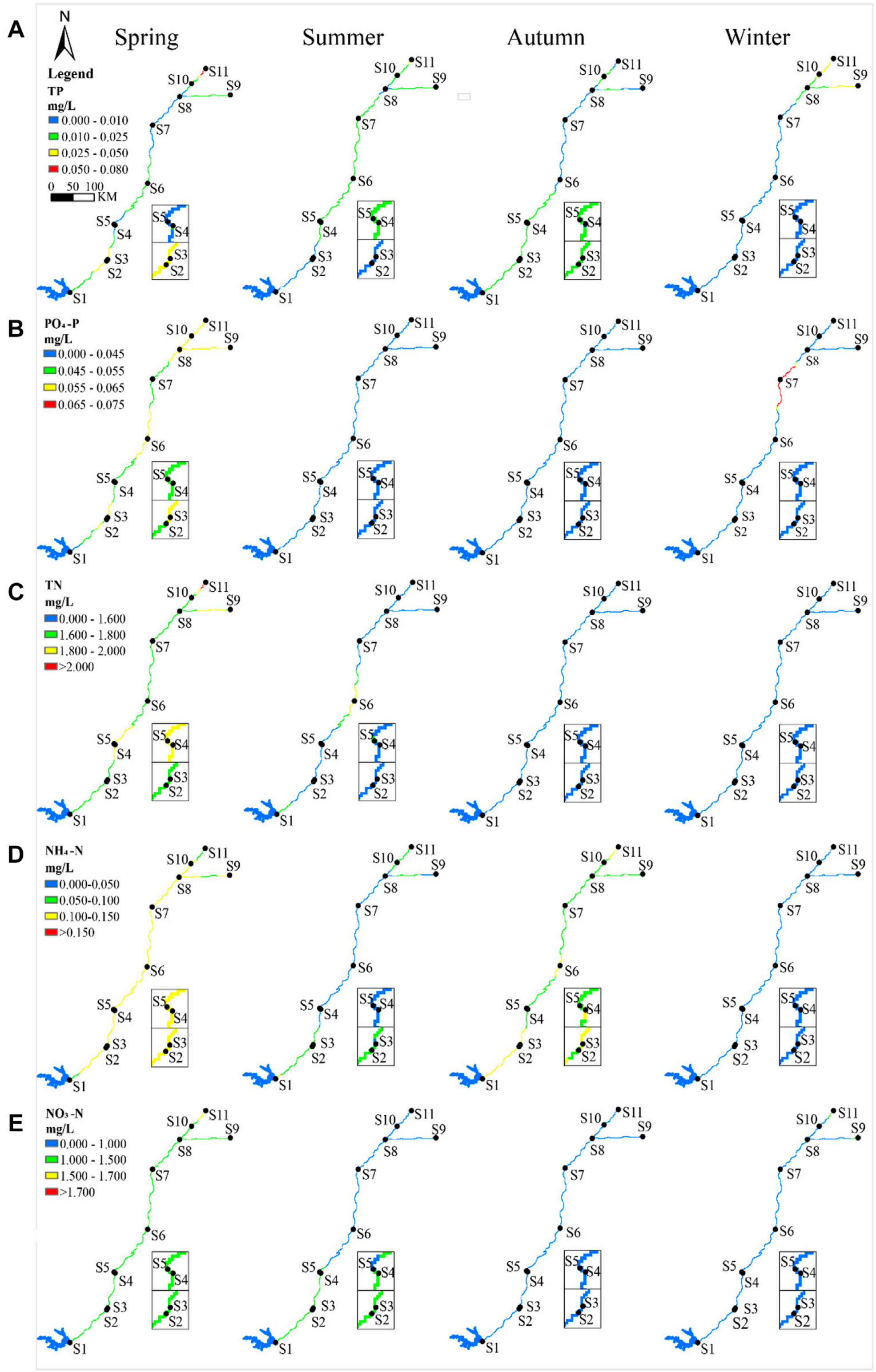

FIGURE 3
Spatio-temporal distribution of phosphorus and nitrogen in the middle route of South-to-North Water Diversion Project. **(A)** Spatio-temporal distribution of TP; **(B)** spatio-temporal distribution of PO_4-P; **(C)** spatio-temporal distribution of TN; **(D)** spatio-temporal distribution of NH_4-N; **(E)** spatio-temporal distribution of NO_3-N.

variables that reflect the problem (Tripathi et al., 2019). Stepwise multiple linear regression analyses were carried out to find the key factors affecting TLI and WQI and to develop the WQI_{min} model, which helps to select the influencing key factors. Based on the Pearson correlation analysis between WQI, TLI, and WQI_{min}, the slope has explanatory significance.

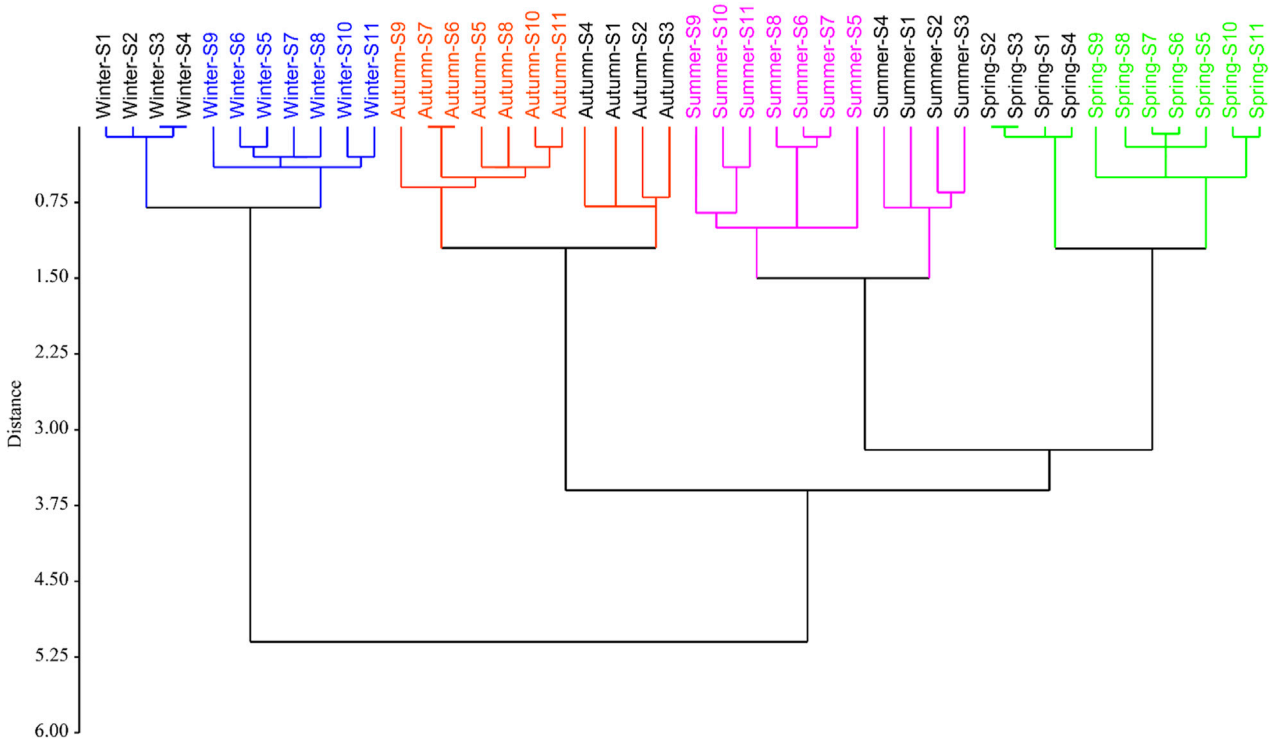

FIGURE 4
Dendrogram showing two clusters of sampling sites in four seasons using a single-linkage distance.

3 Results

3.1 Physicochemical parameters

The average water temperature (WT) was 18.79°C ± 8.78°C, the maximum value was 30.36°C in summer, and the lowest was 6.79°C in winter (Figure 2A). The Kruskal–Wallis test showed significant differences between seasons in WT ($p < 0.001$). The pH ranged from 7.34 to 9.16, and the mean value was 8.56 ± 0.30 (Figure 2B). The average turbidity was 4.32 ± 5.17 NTU, and the maximum was 7.58 NTU in spring (Figure 2C). In addition, SD ranged from 0.40 m to 6.00 m, and the mean value was 3.19 ± 1.68 m (Figure 2D). The Pearson analysis found that the turbidity and SD had a negative relationship ($R^2 = -0.79$) (Supplementary Figure S1).

COD_{Mn} was in the range of 0.80 mg·L^{-1}–3.34 mg·L^{-1}, the mean value was 2.15 ± 0.80 mg·L^{-1}, and the lowest value was 1.02 mg·L^{-1} in winter (Figure 2E). The Kruskal–Wallis test showed that COD_{Mn} in summer had differences in autumn and winter ($p < 0.01$). There were significant differences between values in spring and winter ($p < 0.01$). Pearson correlation analysis illustrated that there was a positive correlation between COD_{Mn} and Chl *a* ($R^2 = 0.57$) (Supplementary Figure S1). DO ranged from 4.76 mg·L^{-1} to 18.10 mg·L^{-1} (Figure 2F). Pearson correlation analysis showed a negative correlation between DO and COD_{Mn} ($R^2 = -0.69$) and WT ($R^2 = -0.83$) (Supplementary Figure S1). The content of Chl *a* was in the range of 0.260 μg·L^{-1}–27.681 μg·L^{-1}, with an average of 4.079 ± 4.760 μg·L^{-1} (Figure 2G); it first increased and then decreased from south to north. The order of Chl *a* concentration by season was summer > spring > autumn > winter ($p < 0.05$). The maximum value of Chl *a* was 27.681 μg·L^{-1} at Chuanhuang North in summer. It could be seen that Chl *a* had notable spatial differences in spring, summer, and autumn ($p < 0.05$).

3.2 Nutrient concentration

TP varied from 0.001 mg·L^{-1} to 0.077 mg·L^{-1}, with a quarterly value of 0.025 ± 0.024 mg·L^{-1} (Figure 3A). TP increased significantly from south to north in spring, with an average of 0.063 ± 0.006 mg·L^{-1}, while it was stable in the other three seasons, with an average value of 0.012 ± 0.010 mg·L^{-1}. The Kruskal–Wallis test showed significant differences between spring and the other three seasons ($p < 0.01$). The concentration of PO_4-P was 0.001 mg·L^{-1}–0.143 mg·L^{-1}, with a quarterly mean value of 0.024 ± 0.028 mg·L^{-1} (Figure 3B), and the maximum was 0.055 ± 0.007 mg·L^{-1} at Lushan in spring.

The maximum value of TN was 2.216 mg·L^{-1}, measured at Tuanchenghu during spring. The average TN was 1.786 ± 0.124 mg·L^{-1} in spring, which was higher than that in summer (1.493 ± 0.190 mg·L^{-1}) (Figure 3C). Meanwhile, TN in the channel showed an increasing variation in spring from south to north (Supplementary Table S3). The range of NH_4-N was 0.001 mg·L^{-1}–0.143 mg·L^{-1}, and the average was 0.068 ± 0.042 mg·L^{-1}. Ammonia (NH_4-N) accounted for 5% of TN (Figure 3D), and there was a notable difference between spring and summer ($p < 0.01$) as well as in the relationship between autumn and winter ($p < 0.01$). NO_3-N

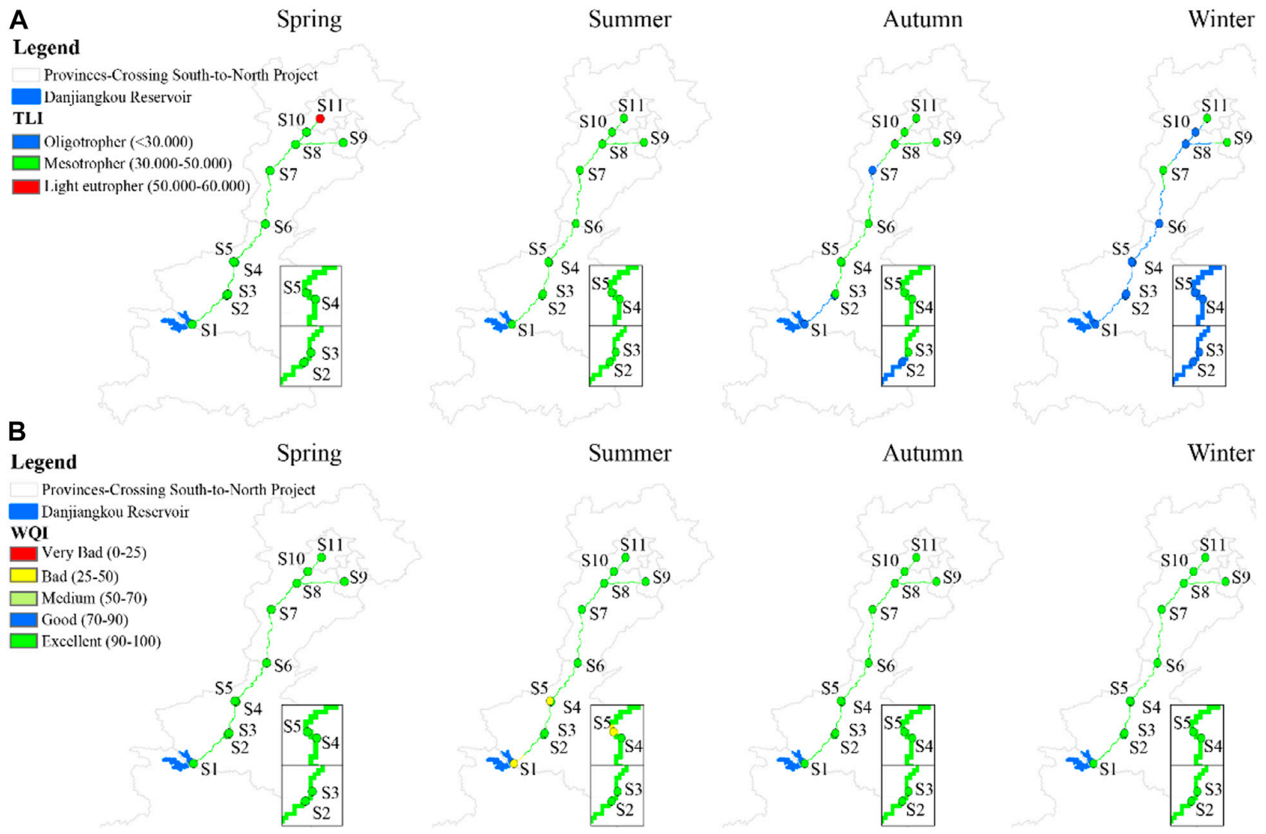

FIGURE 5
Spatio-temporal distribution of TLI and WQI in the middle route of South-to-North Water Diversion Project. **(A)** Spatio-temporal distribution of TLI; **(B)** spatio-temporal distribution of WQI.

occupied 70% of TN, and other forms of nitrogen had a percentage of 30%. NO_3-N varied from 0.155 mg·L^{-1} to 1.696 mg·L^{-1}, with a seasonal average of 0.871 ± 0.457 mg·L^{-1} (Figure 3E). There were differences between summer, autumn, and spring ($p < 0.01$). In terms of spatial variation, there was a notable increase in trend along the MRP in spring (Supplementary Table S3).

3.3 Spatio-temporal heterogeneity of parameters

Single leakage distance clustering analysis showed all samples were clustered into four groups, which reflected a clear seasonal change in the water quality. All samples were bunched into two branches in each season, which indicated notable spatial differences (Figure 4). Thus, water quality has a distinct characteristic of spatio-temporal differences.

3.4 Water quality assessment

3.4.1 Trophic level assessment

The average TLI was 35.00 ± 6.84, and the trophic level was "mesotrophic". The mean value in spring was 42.82 ± 4.64, which was notably higher than that in summer (36.89 ± 4.13), autumn (32.58 ± 3.79), and winter (27.71 ± 3.23) ($p < 0.01$) (Figure 5A). The order of TLI by seasons was spring > summer > autumn > winter. Therefore, TLI first decreased and then slowly increased. The Kendall test results showed that TLI increased significantly in summer, autumn, and winter, except in spring (Supplementary Table S3). Among the samples, only Tuanchenghu in spring had light eutrophication, and 98% of the samples were at the level of "oligotrophic to mesotrophic."

3.4.2 Water quality assessment

There were 11 parameters selected to calculate the WQI. The results showed that the WQI ranged from 66.67 to 89.58, the quarterly average value was 79.53 ± 5.49, and the water quality grade was "good." Among all samples, 93% showed good water quality, 7% of the samples showed medium water quality, and the minimum WQI appeared at Taocha in summer. The order of TLI by season was autumn (86.55 ± 1.87) > winter (83.22 ± 0.99) > summer (74.24 ± 3.62) > spring (74.09 ± 2.12) (Figure 5B). The water quality showed seasonal heterogeneity. In this study, Pearson correlation analysis results showed that TN ($R^2 = -0.92$) and WT ($R^2 = -0.69$) had a significant negative correlation with the WQI.

3.4.3 WQI$_{min}$ model establishment

PCA showed that the two main axes of the principal components explained were 51.74% and 31.40%, respectively

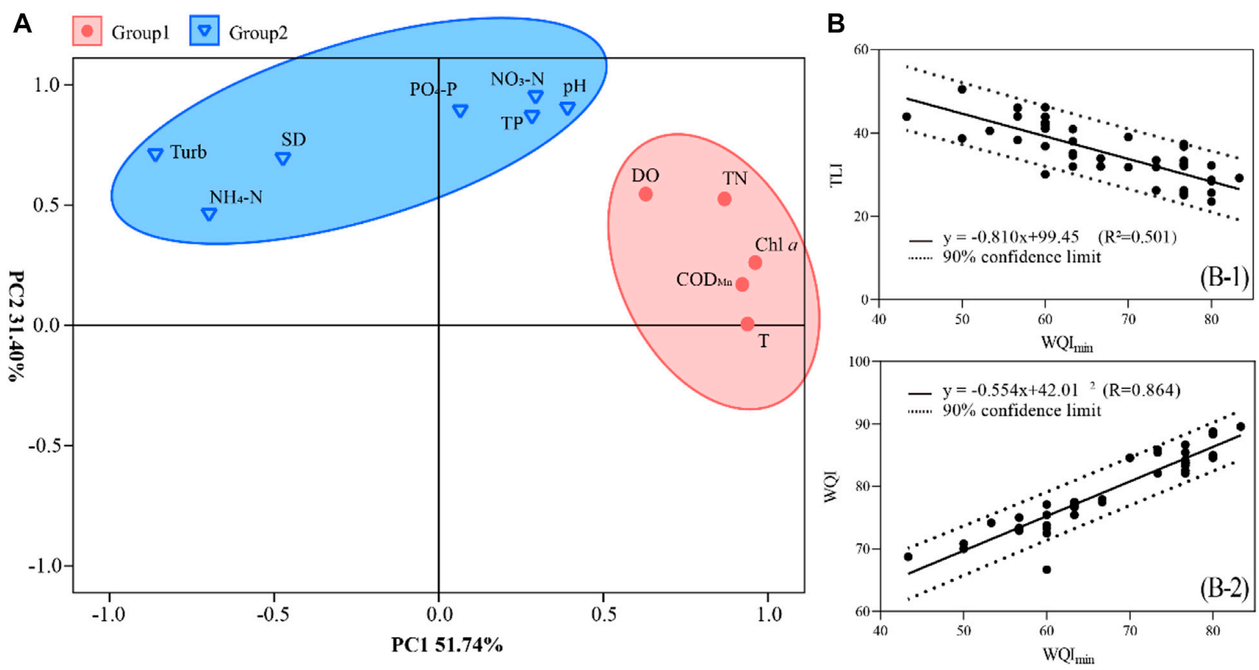

FIGURE 6
Principal component analysis and the relationship between WQI, TLI, and WQI_{min} based on the environmental parameters. **(A)** Principal component analysis; **(B)** linear regression between TLI, WQI, and WQI_{min}: (B-1) TLI with WQI_{min}; (B-2) WQI with WQI_{min}.

(Figure 6A). According to the matrix table, the first principal component (PC1) consisted of TN, WT, Chl *a*, DO, and COD_{Mn}. The second principal component (PC2) described TP, PO_4-P, NO_3-N, NH_4-N, pH, Tur, and SD. It demonstrated that PC1 mostly explained the variation of the environmental parameters among seasons in the MRP.

The multiple stepwise linear regression model was applied to screen the key factors affecting WQI (Table 1). The results showed that TN was the first chosen parameter in the model and contributed the most to WQI in the training ($R^2 = 0.841$, $p < 0.001$). TN values showed an increasing trend. Then, Chl *a* was introduced into the model and increased R^2. COD_{Mn} is an indicator of organic and inorganic oxidizable substances, having the third-highest explanatory power with regard to WQI in the MRP. Therefore, TN, Chl *a*, and COD_{Mn} were selected to calculate the WQI_{min} model.

According to regression analysis, Pearson correlation results indicated that WQI_{min} had a negative relation with TLI ($R^2 = -0.501$, $p < 0.01$) (Figure 6B-1), and the WQI_{min} model also had a strong positive relationship with WQI ($R^2 = 0.864$, $p < 0.001$) (Figure 6B-2)). It showed that the selected key environmental factors had an important impact on the WQI_{min} model, and the results of the WQI_{min} model were accurate.

4 Discussion

4.1 Spatio-temporal pattern of water quality

Water quality describes the state of the aquatic environment and measures the availability and suitability of water (El-Serehy et al., 2018). The status and variations of water quality can be assessed, which is critical for identifying its spatial and temporal pattern (Wu et al., 2018). According to the TLI and WQI assessment, the trophic level index and the water quality status were classified as "mesotrophic" and "good" in the MRP, respectively. However, a study found that the water quality still had a risk of deterioration from upstream to downstream; TLI and WQI in spring were worse than those in other seasons, which indicated the spatio-temporal heterogeneity of the water quality in the MRP.

A previous study also found that spring had the lowest WQI in the MRP (Nong et al., 2019). This was consistent with our results, that the highest TLI and the lowest WQI were in spring (Figure 5), which indicated that the water quality confronted more risks in spring than in other seasons. The water quality was rated as "poor" in the dry season and as "good" in the wet season in the Aksu River (Şener et al., 2017); WQI was higher in summer than in other seasons in the Luanhe River (Tian et al., 2019); TLI in the wet season reached a lightly eutrophic level, which was higher than that in the dry season in Wuli Lake (Wang et al., 2019). The water quality in these waters exhibited a distinct seasonal variation compared to that of the MRP. A concerning result showed the trophic index and the water quality level reflecting temporal heterogeneity in the MRP, especially during spring.

In terms of spatial variation, it was verified that different regions could show distinct water quality characteristics. It was found that high pollution mainly happened at the beginning and the end of rivers, whereas less pollution occurred in the middle parts of rivers (Hajigholizadeh et al., 2017). In the upstream of the Luanhe River, the water quality was rated as "good," which was better than that in the downstream, evaluated as "bad" (Tian et al., 2019). WQI

TABLE 1 Stepwise linear regression of WQI with parameters examined after normalizing.

Model	Linear model	R^2	p
1	-12.1549 TN$+94.683$	0.841	<0.001
2	-11.442 TN-0.314 Chl $a+95.077$	0.900	<0.001
3	-10.601 TN-0.213 Chl $a-1.231$ $COD_{Mn}+96.257$	0.915	<0.050

classified the Dongjiang River as follows: upstream sites as "good" (WQI = 79.1–83.2) and downstream sites as "medium" (WQI = 63.6–64.1) (Sun et al., 2016). This spatial heterogeneity was also observed in our study. The MRP, with a length of 1,432 km, spans different latitudes and tends to form different regions with different aquatic conditions (McLean et al., 2016). TLI increased and WQI decreased from south to north; the end section (Tuanchenghu) had light eutrophication. The water quality might deteriorate from the initial headwater source (upstream) to terminal water bodies (downstream). In addition, the Chuanhuang project was divided into two parts according to the variation of environmental parameters. Previous research studies revealed that the Yellow River crossing projects as a culver tunnel with a length of 4,250 m; an internal diameter of φ7 m (Chuanhuang South to Chuanhuang North) produced a distinguished difference in the water quality before and after. The special hydraulic project might have a certain impact on the aquatic environment (Luo et al., 2019). In summary, both geographical and seasonal effects resulted in the spatio-temporal pattern of the water quality in the MRP.

4.2 Reliability of WQI_{min}

WQI_{min} simplified water quality assessment by using key parameters based on WQI and TLI, contributing to a more rapid and efficient evaluation of water quality statuses (Wu et al., 2018) and making it easy to obtain and represent the major environmental parameters (Pesce et al., 2000). The most influential parameters in the arithmetic of WQI_{min} were N and COD_{Mn} in Lake Taihu (China) (Wu et al., 2018), which were also emphasized in the Dongjiang River (China) (Sun et al., 2016) and the Aksu River (SW-Turkey) (Şener et al., 2017). COD_{Mn} and Chl *a* played important parts and were included in the WQI_{min} of the Luanhe River (China) (Tian et al., 2019). In Dianchi Lake (China), TN, Chl *a*, and COD_{Mn} were selected in the water quality assessment model, which made great contributions (Yang et al., 2018). It concluded that some factors such as TN, Chl *a*, and COD_{Mn} had been widely introduced into WQI_{min} models because of their great impact on water quality assessment.

Comprehensive and full consideration of the weights of selected parameters improved the accuracy of WQI_{min}, which was verified in previous studies (Koçer et al., 2014; Barakat et al., 2016; Tripathi et al., 2019). Compared to other water bodies, the proposed WQI_{min} model in this research was composed of three vital parameters, i.e., TN, Chl *a*, and COD_{Mn}, and evaluated the water quality of the MRP, constructing stricter standards on the spatial and seasonal analysis of the water quality. WQI_{min} could provide simpler measurement methods and lower analytical assumptions (Wang et al., 2019), which has a worthy application for saving testing parameter costs and improving evaluation efficiency.

Conclusion

Water quality in the MRP was "good" throughout the year but was worse in summer than in other seasons. The trophic level was "oligotrophic to mesotrophic"; only Tuanchenghu was in the "mesotrophic" level in spring. WQI decreased and TLI increased significantly from south to north along the MRP. TN, Chl *a*, and COD_{Mn} were the driving factors of the water quality and can be included to establish the reliable WQI_{min} model for water quality assessment.

Data availability statement

The original contributions presented in the study are included in the article/Supplementary Material; further inquiries can be directed to the corresponding author.

Author contributions

Conceptualization: YW, CW, and YB; Data curation: YW and CZ; Funding acquisition: YB; Investigation: YW, YZ, YB, WM, GS, SW, YS, and JL; Supervision: CW and YB; Writing—original draft: YW; Writing—review & editing: YB.

Funding

This work was partially funded by the China National Critical Project for Science and Technology on Water Pollution Prevention and Control (No. 2017ZX07108-001).

Conflict of interest

YW and CW were employed by Central Southern Safety & Environmental Technology Institute Company Limited. JL, SW, and YS were employed by the Management Bureau of the South to North Water Transfer Canal Project.

The remaining authors declare that the research was conducted in the absence of any commercial or financial relationships that could be construed as a potential conflict of interest.

Publisher's note

Supplementary material

The Supplementary Material for this article can be found online at: https://www.frontiersin.org/articles/10.3389/fenvs.2023.945884/full#supplementary-material

References

Akkoyunlu, A., and Akiner, M. E. (2012). Pollution evaluation in streams using water quality indices: A case study from turkey's sapanca lake basin. *Ecol. Indic.* 18, 501–511. doi:10.1016/j.ecolind.2011.12.018

APHA (2017). *Standard methods for the examination of water and wastewater*. 23. Washington DC: American Public Health Association.

Barakat, A., El Baghdadi, M., Rais, J., Aghezzaf, B., and Slassi, M. (2016). Assessment of spatial and seasonal water quality variation of oum Er rbia river (Morocco) using multivariate statistical techniques. *Int. Soil Water Conservation Res.* 4 (4), 284–292. doi:10.1016/j.iswcr.2016.11.002

Burns, N., McIntosh, J., and Scholes, P. (2005). Strategies for managing the lakes of the rotorua district, New Zealand. *Lake Reserv. Manag.* 21 (1), 61–72. doi:10.1080/07438140509354413

Chang, N. N., Luo, L., Wang, X. C., Song, J., Han, J. X., and Ao, D. (2020). A novel index for assessing the water quality of urban landscape lakes based on water transparency. *Sci. Total Environ.* 735, 139351. doi:10.1016/j.scitotenv.2020.139351

China Environmental Monitoring Station (2001). *Lakes (reservoirs) eutrophication assessment methods and classification Technology requirements*. Beijing, China: China Environmental Monitoring Station.

Ding, X. W., Zhu, Q., Zhai, A. F., and Liu, L. (2019). Water quality safety prediction model for drinking water source areas in Three Gorges Reservoir and its application. *Ecol. Indic.* 101, 734–741. doi:10.1016/j.ecolind.2019.01.068

El-Serehy, H. A., Abdallah, H. S., Al-Misned, F. A., Al-Farraj, S. A., and Al-Rasheid, K. A. (2018). Assessing water quality and classifying trophic status for scientifically based managing the water resources of the Lake Timsah, the lake with salinity stratification along the Suez Canal. *Saudi J. Biol. Sci.* 25 (7), 1247–1256. doi:10.1016/j.sjbs.2018.05.022

Giri, S., and Qiu, Z. Y. (2016). Understanding the relationship of land uses and water quality in twenty first century: A review. *J. Environ. Manag.* 173, 41–48. doi:10.1016/j.jenvman.2016.02.029

Guo, C. B., Chen, Y. S., Gozlan, R. E., Liu, H., Lu, Y., Qu, X., et al. (2020b). Patterns of fish communities and water quality in impounded lakes of China's south-to-north water diversion project. *Sci. Total Environ.* 713, 136515. doi:10.1016/j.scitotenv.2020.136515

Guo, C. B., Chen, Y. S., Xia, W. T., Qu, X., Yuan, H., Xie, S. G., et al. (2020a). Eutrophication and heavy metal pollution patterns in the water suppling lakes of China's south-to-north water diversion project. *Sci. Total Environ.* 711, 134543. doi:10.1016/j.scitotenv.2019.134543

Hajigholizadeh, M., and Melesse, A. M. (2017). Assortment and spatiotemporal analysis of surface water quality using cluster and discriminant analyses. *Catena* 151, 247–258. doi:10.1016/j.catena.2016.12.018

Horton, R. K. (1965). An index-number system for rating water quality. *J. Water Pollut. Control Fed.* 37 (3), 300–306.

Kannel, P. R., Lee, S., Lee, Y. S., Kanel, S. R., and Khan, S. P. (2007). Application of water quality indices and dissolved oxygen as indicators for river water classification and urban impact assessment. *Environ. Monit. Assess.* 132 (1-3), 93–110. doi:10.1007/s10661-006-9505-1

Koçer, M. A. T., and Sevgili, H. (2014). Parameters selection for water quality index in the assessment of the environmental impacts of land-based trout farms. *Ecol. Indic.* 36, 672–681. doi:10.1016/j.ecolind.2013.09.034

Luo, Z. X., Li, S. J., Hou, K., and Ji, G. D. (2019). Spatial and seasonal bacterioplankton community dynamics in the main channel of the middle route of SouthSouth-to-North water diversion project. *Res. Microbiol.* 170 (1), 24–34. doi:10.1016/j.resmic.2018.08.004

McLean, D. L., Langlois, T. J., Newman, S. J., Holmes, T. H., Birt, M. J., Bornt, K. R., et al. (2016). Distribution, abundance, diversity and habitat associations of fishes across a bioregion experiencing rapid coastal development. *Estuar. Coast. Shelf Sci.* 178 (5), 36–47. doi:10.1016/j.ecss.2016.05.026

Nazeer, S., Khan, M. U., and Malik, R. N. (2018). Phytoplankton Spatio-temporal dynamics and its relation to nutrients and water retention time in multi-trophic system of Soan River, Pakistan. *Environ. Technol. Innovation* 9, 38–50. doi:10.1016/j.eti.2017.10.005

Nong, X., Shao, D., Xiao, Y., and Zhong, H. (2019). Spatio-temporal characterization analysis and water quality assessment of the SouthSouth-to-North water diversion project of China. *Int. J. Environ. Res. Public Health* 16 (12), 2227. doi:10.3390/ijerph16122227

Nong, X., Shao, D., Zhong, H., and Liang, J. (2020). Evaluation of water quality in the South-to-North Water Diversion Project of China using the water quality index (WQI) method. *Water Res.* 178, 115781. doi:10.1016/j.watres.2020.115781

Pesce, S. F., and Wunderlin, D. A. (2000). Use of water quality indices to verify the impact of Córdoba City (Argentina) on Suquı´a River. *Water Res.* 34 (11), 2915–2926. doi:10.1016/S0043-1354(00)00036-1

Sánchez, E., Colmenarejo, M. F., Vicente, J., Rubio, A., García, M. G., Travieso, L., et al. (2007). Use of the water quality index and dissolved oxygen deficit as simple indicators of watersheds pollution. *Ecol. Indic.* 7 (2), 315–328. doi:10.1016/j.ecolind.2006.02.005

Şener, Ş., Şener, E., and Davraz, A. (2017). Evaluation of water quality using water quality index (WQI) method and GIS in Aksu River (SW-Turkey). *Sci. Total Environ.* 584-585, 131–144. doi:10.1016/j.scitotenv.2017.01.102

Sun, W., Xia, C. Y., Xu, M. Y., Guo, J., and Sun, G. P. (2016). Application of modified water quality indices as indicators to assess the spatial and temporal trends of water quality in the Dongjiang River. *Ecol. Indic.* 66, 306–312. doi:10.1016/j.ecolind.2016.01.054

Tian, Y. L., Jiang, Y., Liu, Q., Dong, M. Y., Xu, D. X., Liu, Y., et al. (2019). Using a water quality index to assess the water quality of the upper and middle streams of the Luanhe River, northern China. *Sci. Total Environ.* 667, 142–151. doi:10.1016/j.scitotenv.2019.02.356

Tripathi, M., and Singal, S. K. (2019). Use of principal component analysis for parameter selection for development of a novel water quality index: A case study of river ganga India. *Ecol. Indic.* 96, 430–436. doi:10.1016/j.ecolind.2018.09.025

Wang, J. L., Fu, Z. S., Qiao, H. X., and Liu, F. X. (2019). Assessment of eutrophication and water quality in the estuarine area of Lake Wuli, Lake Taihu, China. *Sci. Total Environ.* 650, 1392–1402. doi:10.1016/j.scitotenv.2018.09.137

Wu, Z. S., Wang, X. L., Chen, Y. W., Cai, Y. J., and Deng, J. C. (2018). Assessing river water quality using water quality index in Lake Taihu Basin, China. *Sci. Total Environ.* 612, 914–922. doi:10.1016/j.scitotenv.2017.08.293

Xin, X. K., Li, K. F., Finlayson, B., and Yin, W. (2015). Evaluation, prediction, and protection of water quality in Danjiangkou Reservoir, China. *Water Sci. Eng.* 8 (1), 30–39. doi:10.1016/j.wse.2014.11.001

Yang, K., Yu, Z. Y., Luo, Y., Yang, Y., Zhao, L., and Zhou, X. L. (2018). Spatial and temporal variations in the relationship between lake water surface temperatures and water quality - a case study of Dianchi Lake. *Sci. Total Environ.* 624, 859–871. doi:10.1016/j.scitotenv.2017.12.119

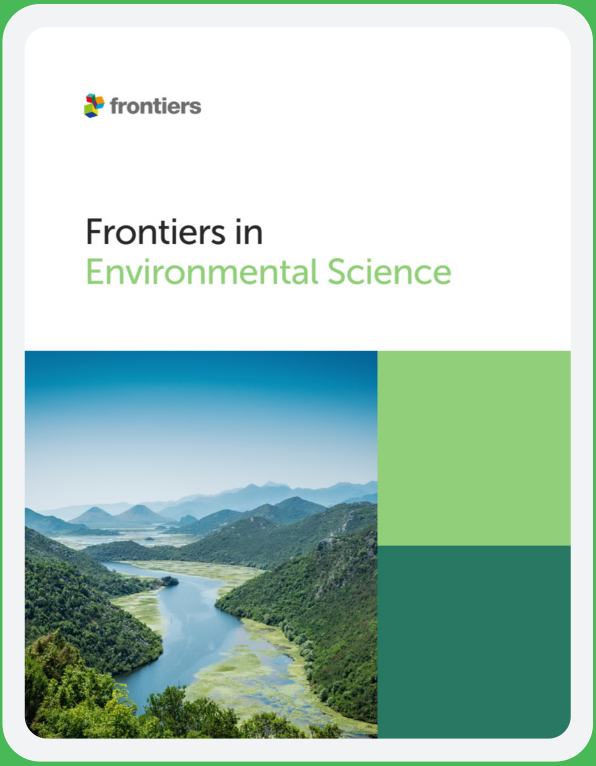
frontiers
Frontiers in
Environmental Science